UC Riverside

UC Riverside Electronic Theses and Dissertations

Title

Magnesium Oxide Based Nanocomposites for Bone Repair

Permalink

https://escholarship.org/uc/item/2x71r348

Author

Wetteland, Cheyann Lee

Publication Date

2017

Peer reviewed|Thesis/dissertation

eScholarship.org Powered by the California Digital Library
University of California

UNIVERSITY OF CALIFORNIA
RIVERSIDE

Magnesium Oxide Based Nanocomposites for Bone Repair

A Dissertation submitted in partial satisfaction
of the requirements for the degree of

Doctor of Philosophy

in

Bioengineering

by

Cheyann Lee Wetteland

September 2017

Dissertation Committee:
Dr. Huinan Liu, Chairperson
Dr. Manuela Martins-Green
Dr. Juchen Guo

Copyright by
Cheyann Lee Wetteland
2017

The Dissertation of Cheyann Lee Wetteland is approved:

_____

_____

_____

Committee Chairperson

University of California, Riverside

ACKNOWLEDGMENTS

My PhD has been a five-year-long struggle and would not have been possible without the support of many people along the way. I would like to thank my Dissertation Chair, Dr. Huinan Liu, as well as Dr. Manuela Martins-Green and Dr. Juchen Guo for their guidance and service on my dissertation committee.

I have immense gratitude for all the current and former members of the Biomaterials and Nanomedicine Lab group at the University of California, Riverside. In particular, I would like to thank Nhu-Y Thi Nguyen as a collaborator but also as a close friend whose support both inside and outside of the lab was (and continues to be) invaluable to my success in all aspects of my life. I truly believe I would not have made it this far without her. I would also like to thank Radha Daya, Catherine Augello, Hayley Ostrin, Naiyin Zhang, and Dr. Qiaomu Tian for their friendship and insight, which made it possible for me to weather the lows and celebrate the highs of research. I want to thank Dr. Ian Johnson for his time and for passing on his knowledge of polymer chemistry to me while finishing his dissertation.

Several undergraduate researches also volunteered their time and energy to help me with my work. I would like to thank Jorge Sanchez, Cole Azevedo, Christine Silken, Sebo Michelle Wang, Elizabeth Ang, Omar Mahmood, Vanessa Guzman, and Hakikat Gil for their contributions from cell counting to developing figures.

Finally, I would like to thank my family, especially my parents, for their unbridled support and for making me who I am today. In particular, I want to thank my

partner, Evan, for his love and patience during the tumultuous times that graduate school brought upon us in the face of the continuous struggles of life.

The text of this dissertation, in part, is a reprint of the material as it appears in:

1. Wetteland, C.L., N.Y. Nguyen, and H. Liu, *Concentration-dependent behaviors of bone marrow derived mesenchymal stem cells and infectious bacteria toward magnesium oxide nanoparticles.* Acta Biomater, 2016. **35**: p. 341-56.

DEDICATION

I dedicate this dissertation to

my partner:

Evan Daniel Bryan

whose love, support, and sacrifice

made it possible for me to complete this work.

ABSTRACT OF THE DISSERTATION

Magnesium Oxide Based Nanocomposites for Bone Repair

by

Cheyann Lee Wetteland

Doctor of Philosophy, Graduate Program in Bioengineering
University of California, Riverside, September 2017
Dr. Huinan Liu, Chairperson

Magnesium oxide (MgO) is a bioactive ceramic of increasing interest for bone applications. However, as MgO is relatively new to medical applications, there are limited publications on the cytocompatibility and bioactivity of MgO. In this work, we explore the properties of MgO nanoparticles (nMgO) in both bare form and as a component of polymeric composites.

Bare nMgO was reactive in simulated physiological environments, creating concentration-dependent effects. Specifically, nMgO has dynamic effect on bone marrow derived mesenchymal stem cells (BMSCs) and cell culture medium, Dulbecco's Modified Eagle Medium (DMEM) with 10% fetal bovine serum (FBS) and 1% penicillin/streptomycin (P/S). At low concentrations, nMgO enhanced the proliferation of BMSCs, but in concentrations exceeding 500 μg/mL there was significant cell death. However, increasing nMgO caused decrease in Ca^{2+} in DMEM, indicating that nMgO may enhance deposition of calcium salts. Much of this activity may be attributed to the dissociation of nMgO which resulted in release of Mg^{2+} and OH^-. MgO nanoparticles

readily dissociated in DMEM and simulated body fluid (SBF) due to pH and biological buffering effects. Developing polymeric nanocomposites with nMgO provided a way to mitigate dissociation of nMgO while maintaining beneficial effects to cells.

Several nMgO nanocomposites were evaluated. First, a method to increase dispersion of nMgO in poly (lactic-co-glycolic acid) (PLGA) using purely mechanical stimulation was developed. These composites were compared with composites of nanophase hydroxyapatite (nHA) in PLGA. Hydroxyapatite is a naturally occurring calcium phosphate, well-established for bone applications. Optical transparency measurements confirmed increased dispersion. However, the release of nMgO from nMgO/PLGA was found to exceed tolerable levels for BMSCs. Less nMgO was utilized in subsequent studies but to maintain the mechanical support from nanoparticle filling in PLGA, triphasic composites of PLGA/HA/MgO were developed. Improved cell response was observed when the amount of nMgO was decreased to 1-5 wt% compared to composites with 30 wt% nMgO, but we did not observe improved cell response when compared to PLGA/HA composites with 30 wt% nHA. However, these solvent-casted nanocomposites served as a guideline for the development of a thermogelling hydrogel containing nHA and nMgO.

PLGA-PEG-PLGA (PLGA block linkage with PEG, PbP) was utilized for its thermogelling properties. The presence of nMgO initially helped to stabilize the hydrogel. However, this property was lost as nMgO hydrated and eventually dissociated leading to loss of structural integrity of the hydrogel. As such, nMgO can be a useful

additive to materials for bone regeneration but its reactivity means that it should be coated to preserve its beneficial properties and mitigate dissociation.

Table of Contents

List of Figures

List of Tables

Chapter 1: Introduction

1.1 Need for Bone Regeneration

In 2011, the life expectancy of men and women in the US was reported to be 76.3 and 81.1 years, respectively [1]. Just eleven years prior, the life expectancy of men and women in the US was reported to be 74.1 and 79.5 years respectively [2]. There has been a consistent increase in life expectancy since 1930 and this trend is likely to continue. As life expectancy increases, doctors and researchers face increasing challenges in treating loss of tissue function due to aging, with a particular emphasis on bone health. Bone mineral density has been found to be relatively stable until age 50, at which point women and men are at risk for developing osteoporosis [3]. Osteoporosis is a degenerative disease that results in a decrease in bone density and an increased risk of fracture. Complications from osteoporosis and similar conditions often lead to the need for bone implants, including fixation devices and joint replacements. Osteoporosis causes more than 8.9 million fractures annually [4]. The increasing aging population creates a great need for methods of bone regeneration to prevent costly and potentially damaging surgeries.

The ability of bone to heal itself can be disrupted by degenerative diseases like osteoporosis or in cases of large defects from trauma [5-8]. Treatments for osteoporotic fractures include invasive procedures such as surgical implants [7, 8]. In the case of large defects, treatments include autografts and allografts. Autografts are bone transplants that take healthy bone from a patient and implant it into a defect site. Allografts are a similar treatment, except the healthy bone tissue comes from a donor or cadaver instead of the

patient, themselves. Autografts result in faster healing and lower immune response as patients are their own donors. However, autografts require two surgical sites. Allografts result in only one surgical site for the patient but require much more time to heal due to immune response to the implanted tissue. Allografts are also in very limited supply due to limited donors and tissue match requirements. Synthetic grafts are an increasingly popular prospect for treatment of bone defects because there is no need for additional surgical sites, they have lower chance of immune response, and they do not require components from biological tissues, which are in limited supply [9, 10].

Successful synthetic scaffolds mimic the native tissue they are meant to help repair. Bone extracellular matrix (ECM) consists of collagen type 1, apatite, and matrix proteins including glycoproteins and proteoglycans [9, 10]. The collagen provides high fracture toughness, the apatite provides compressive strength, and the matrix proteins are involved in extracellular signaling. A synthetic scaffold for bone regeneration should incorporate materials that can mimic each of these properties. This dissertation focuses on the use of magnesium oxide nanoparticles to add bioactivity to synthetic biomaterials for bone regeneration.

1.2 Magnesium Oxide for bone regeneration

1.2.1 Properties of Magnesium oxide

Magnesium oxide (MgO) is a metal oxide ceramic with near perfect cubic crystal structure. It is rarely found in nature due to its hygroscopic nature, as it can hydrate to form magnesium hydroxide ($Mg(OH)_2$) [11-14]. Magnesium oxide has a long history in industrial applications due to its high thermostability. It is often produced by first precipitating magnesium hydroxide from solutions of sodium hydroxide and magnesium

chloride. The magnesium hydroxide can then be converted to magnesium oxide through dehydration at 400 ºC [11]. As a result, the activity of magnesium oxide and magnesium hydroxide in physiological settings is inherently linked. Both MgO and $Mg(OH)_2$, however, are widely considered insoluble.

1.2.2 Magnesium oxide and bone applications

Use of magnesium oxide for medical applications is relatively new. MgO nanoparticles have a history as an antimicrobial agent [15-17]. However, use of MgO for bone applications is fairly recent and as a result, it is still not fully understood.

Magnesium oxide has been used as a dietary supplement to improve bone density. Studies confirm increase in bone density in women who consume MgO and $Mg(OH)_2$ regularly [18, 19]. However, when consuming MgO or $Mg(OH)_2$, the acidic environment of the stomach causes rapid dissociation of MgO and $Mg(OH)_2$ resulting in delivery of Mg^{2+} ions. Magnesium ions have been shown to be cytocompatible and promote osteogenesis [20, 21]. However, the beneficial effects of dietary MgO supplementation is related to its dissociation products, instead of the MgO itself.

Few studies exist on the *in vitro* and *in vivo* activity of MgO in direct contact with bone forming cells. Implantation of MgO powder paste in the bone marrow cavity of rat tibia has been shown to result in a 25% increase in the thickness of compact bone [22]. However, use of bar MgO nanoparticles is limited by the low fracture toughness of MgO. Incorporation into polymer composites is a viable method for delivering MgO while increasing fracture toughness. MgO has been incorporated into poly (methyl methacrylate) cements and carrageenan hydrogels to increase mechanical properties of

these materials [23, 24]. Additionally, a few studies also show increased osteoblast proliferation and alkaline phosphatase expression when cultured on polymer/MgO composites, indicating that this family of composites is viable for further study [25-27].

1.3 Hydroxyapatite as a model ceramic for bone regeneration

Hydroxyapatite (HA) is a naturally occurring form of calcium phosphate that is well-established as a material for bone applications [28-30]. It has been shown to be both osteoconductive and osteoinductive. As a result, HA is a prime candidate for comparison with MgO as well as use with MgO for bone applications.

Naturally occurring bone mineral is a calcium deficient form of HA. In contrast, synthetic HA has a Ca:P ratio of 1.6. As a result, dopants are used to produce HA mineral more similar to natural bone [28-30]. Use of both HA and MgO in composites may result in chemistry more similar to natural bone and therefore aid in bone healing and mineralization.

1.4 Poly (lactic-co-glycolic acid) as a matrix for MgO

Poly (lactic-co-glycolic acid) (PLGA) is a synthetic co-polymer of lactic acid (LA) and glycolic acid (GA). Degradation properties of PLGA can be tuned by altering LA:GA ratio and total chain length, which affects crystallinity and water permeability of PLGA. As a biodegradable polyester, PLGA degrades through hydrolysis of its ester bonds. As a result, PLGA is completely bioresorbable. PLGA is well-established as a biocompatible material and is approved for specific clinical use by the Food and Drug Association (FDA) [31-33]. The tunability of PLGA and the status of PLGA as a well-established biodegradable polymer make it an ideal matrix material for implantable

scaffolds [31-34]. While PLGA is biocompatible, it is not particularly bioactive. Addition of bioactive nanoparticles, such as MgO and HA, is a well-established method to develop scaffolds for tissue engineering. We utilized PLGA and PLGA-based hydrogels as matrices for MgO and HA composites for bone regeneration.

1.5 Overview

This work aims to develop MgO and MgO-based nanocomposites as materials for bone regeneration. Due to the limited publications on MgO as a material for bone regeneration, in Chapter 2, we explored the effects of bare MgO nanoparticles on bone marrow derived mesenchymal stem cells (BMSCs). We also evaluated MgO nanoparticles as an antimicrobial agent against gram positive and gram negative bacteria. This study showed that MgO dissociated in biological media, despite the fact that MgO is widely considered insoluble. In Chapter 3, we sought to better understand the potential reactions of bare MgO in a physiological setting. We evaluated the dissociation of MgO and $Mg(OH)_2$ in a variety of physiologically relevant medias including Dulbecco's Modified Eagle's Medium (DMEM) and simulated body fluid (SBF). The bare MgO nanoparticle studies were used to inform the development of subsequent polymeric composites.

Several PLGA composites with MgO were developed. The first challenge we faced was homogeneous dispersion of MgO and HA nanoparticles in PLGA. In Chapter 4, we discuss a method of utilizing exclusively mechanical stimulation to improve dispersion of both MgO and HA in PLGA. This study also showed increased toxicity of MgO in PLGA with increased dispersion. It was then necessary to develop composites

with less MgO. To maintain the mechanical benefits of ceramic nanoparticles to PLGA, we developed composites containing both HA and MgO to reduce the amount of MgO without reducing the total amount of nanoparticles, as discussed in Chapter 5. We found that PLGA/HA/MgO composites with 29% HA and 1% MgO, by weight, were a viable candidate for further study. However, solvent-casted PLGA scaffolds, such as the ones we developed, would require surgery to implant and would need to be manufactured for each uniquely shaped defect. In Chapter 6, we addressed this issue by developing an injectable, *in situ*-forming hydrogel using triblock polymers of PLGA and polyethylene glycol. The final study presented is PLGA-PEG-PLGA hydrogel loaded with HA and MgO.

1.6 References

1. Hoyert, D.L. and J. Xu, *Deaths: preliminary data for 2011.* Natl Vital Stat Rep, 2012. **61**(6): p. 1-51.
2. Arias, E., *United States life tables, 2000.* Natl Vital Stat Rep, 2002. **51**(3): p. 1-38.
3. Looker, A.C., et al., *Total body bone area, bone mineral content, and bone mineral density for individuals aged 8 years and over: United States, 1999-2006.* Vital Health Stat 11, 2013(253): p. 1-78.
4. Johnell, O. and J.A. Kanis, *An estimate of the worldwide prevalence and disability associated with osteoporotic fractures.* Osteoporos Int, 2006. **17**(12): p. 1726-33.
5. Diab, D.L. and N.B. Watts, *Postmenopausal osteoporosis.* Curr Opin Endocrinol Diabetes Obes, 2013. **20**(6): p. 501-9.
6. Tella, S.H. and J.C. Gallagher, *Prevention and treatment of postmenopausal osteoporosis.* J Steroid Biochem Mol Biol, 2014. **142**: p. 155-70.
7. Garcia-Gareta, E., M.J. Coathup, and G.W. Blunn, *Osteoinduction of bone grafting materials for bone repair and regeneration.* Bone, 2015. **81**: p. 112-21.
8. Pilipchuk, S.P., et al., *Tissue engineering for bone regeneration and osseointegration in the oral cavity.* Dent Mater, 2015. **31**(4): p. 317-38.
9. Hammouche, S., D. Hammouche, and M. McNicholas, *Biodegradable bone regeneration synthetic scaffolds: in tissue engineering.* Curr Stem Cell Res Ther, 2012. **7**(2): p. 134-42.

10. Yunus Basha, R., T.S. Sampath Kumar, and M. Doble, *Design of biocomposite materials for bone tissue regeneration.* Mater Sci Eng C Mater Biol Appl, 2015. **57**: p. 452-63.
11. Amundsen, K., et al., *Magnesium*, in *Ullmann's Encyclopedia of Industrial Chemistry*. 2000, Wiley-VCH Verlag GmbH & Co. KGaA.
12. Fruhwirth, O., et al., *Dissolution and Hydration Kinetics of Mgo.* Surface Technology, 1985. **24**(3): p. 301-317.
13. Mejias, J.A., et al., *The kinetics and mechanism of MgO dissolution.* Chemical Physics Letters, 1999. **314**(5-6): p. 558-563.
14. Refson, K., et al., *Water chemisorption and reconstruction of the MgO surface.* Phys Rev B Condens Matter, 1995. **52**(15): p. 10823-10826.
15. Sawai, J., *Quantitative evaluation of antibacterial activities of metallic oxide powders (ZnO, MgO and CaO) by conductimetric assay.* J Microbiol Methods, 2003. **54**(2): p. 177-82.
16. Sawai, J. and T. Yoshikawa, *Quantitative evaluation of antifungal activity of metallic oxide powders (MgO, CaO and ZnO) by an indirect conductimetric assay.* J Appl Microbiol, 2004. **96**(4): p. 803-9.
17. Wetteland, C.L., N.Y. Nguyen, and H. Liu, *Concentration-dependent behaviors of bone marrow derived mesenchymal stem cells and infectious bacteria toward magnesium oxide nanoparticles.* Acta Biomater, 2016. **35**: p. 341-56.
18. Carpenter, T.O., et al., *A randomized controlled study of effects of dietary magnesium oxide supplementation on bone mineral content in healthy girls.* Journal of Clinical Endocrinology & Metabolism, 2006. **91**(12): p. 4866-4872.
19. Sojka, J.E. and C.M. Weaver, *Magnesium Supplementation and Osteoporosis.* Nutrition Reviews, 1995. **53**(3): p. 71-74.
20. Yoshizawa, S., et al., *Role of magnesium ions on osteogenic response in bone marrow stromal cells.* Connect Tissue Res, 2014. **55 Suppl 1**: p. 155-9.
21. Yoshizawa, S., et al., *Magnesium ion stimulation of bone marrow stromal cells enhances osteogenic activity, simulating the effect of magnesium alloy degradation.* Acta Biomater, 2014. **10**(6): p. 2834-42.
22. Nygren, H., et al., *Increase of Compact Bone Thickness in Rat Tibia after Implanting MgO into the Bone Marrow Cavity.* J Funct Biomater, 2014. **5**(3): p. 158-66.
23. Hezaveh, H. and Muhamad, II, *Effect of MgO nanofillers on burst release reduction from hydrogel nanocomposites.* J Mater Sci Mater Med, 2013. **24**(6): p. 1443-53.
24. Khandaker, M., Y. Li, and T. Morris, *Micro and nano MgO particles for the improvement of fracture toughness of bone-cement interfaces.* J Biomech, 2013. **46**(5): p. 1035-9.
25. Hickey, D.J., et al., *Adding MgO nanoparticles to hydroxyapatite-PLLA nanocomposites for improved bone tissue engineering applications.* Acta Biomater, 2015. **14**: p. 175-84.
26. Pourdanesh, F., et al., *In vitro and in vivo evaluation of a new nanocomposite, containing high density polyethylene, tricalcium phosphate, hydroxyapatite, and*

magnesium oxide nanoparticles. Mater Sci Eng C Mater Biol Appl, 2014. **40**: p. 382-8.
27. Roh, H.S., et al., *Addition of MgO nanoparticles and plasma surface treatment of three-dimensional printed polycaprolactone/hydroxyapatite scaffolds for improving bone regeneration.* Mater Sci Eng C Mater Biol Appl, 2017. **74**: p. 525-535.
28. Cheng, L., et al., *Osteoinduction of hydroxyapatite/beta-tricalcium phosphate bioceramics in mice with a fractured fibula.* Acta Biomater, 2010. **6**(4): p. 1569-74.
29. Koutsopoulos, S., *Synthesis and characterization of hydroxyapatite crystals: a review study on the analytical methods.* J Biomed Mater Res, 2002. **62**(4): p. 600-12.
30. Zakaria, S.M., et al., *Nanophase hydroxyapatite as a biomaterial in advanced hard tissue engineering: a review.* Tissue Eng Part B Rev, 2013. **19**(5): p. 431-41.
31. Gentile, P., et al., *An overview of poly(lactic-co-glycolic) acid (PLGA)-based biomaterials for bone tissue engineering.* Int J Mol Sci, 2014. **15**(3): p. 3640-59.
32. Kapoor, D.N., et al., *PLGA: a unique polymer for drug delivery.* Ther Deliv, 2015. **6**(1): p. 41-58.
33. Ortega-Oller, I., et al., *Bone Regeneration from PLGA Micro-Nanoparticles.* Biomed Res Int, 2015. **2015**: p. 415289.
34. Johnson, I., K. Akari, and H. Liu, *Nanostructured hydroxyapatite/poly(lactic-co-glycolic acid) composite coating for controlling magnesium degradation in simulated body fluid.* Nanotechnology, 2013. **24**(37): p. 375103.

Chapter 2: Concentration-dependent behaviors of BMSCs and infectious bacteria toward magnesium oxide nanoparticles

2.1 Introduction

This article reports the quantitative relationship between the concentration of magnesium oxide (MgO) nanoparticles and its distinct biological activities towards mammalian cells and infectious bacteria for the first time. The effects of MgO nanoparticles on the viability of bone marrow derived mesenchymal stem cells (BMSCs) and infectious bacteria (both gram-negative and gram-positive) showed a concentration-dependent behavior *in vitro*. The critical concentrations of MgO nanoparticles identified in this study provided valuable guidelines for biomaterial design toward potential clinical translation.

The bioactivity and mechanical properties of MgO have recently attracted significant interest for potential biomedical applications, from bone repair to biosensing [1-5]. For bone repair, Nygren *et al.* observed that the thickness of compact bone increased by 25% after implanting MgO powder paste into bone marrow cavity of rat tibia for 3 weeks as compared with sham-operated controls. This suggested that MgO had stimulatory effects on bone healing and regeneration [6]. Clinically, MgO has also been used to improve bone mineral density when taken orally as a dietary supplement [7]. Moreover, MgO is beneficial for improving mechanical properties of poly (methyl methacrylate) (PMMA)-based bone cement. For example, MgO was incorporated into PMMA cement to enhance the fracture toughness of bone-PMMA interface [8]. Additionally, MgO powder was reported to exhibit antimicrobial properties against both gram-negative and gram-positive bacteria *in vitro*, such as *Escherichia coli* (*E. coli*) and

Staphylococcus aureus (*S. aureus*) [9, 10]. These appealing properties of MgO make it a promising material for treating bone-related diseases and injuries, such as osteoporosis (a disease that decreases bone density and increases risk for bone fracture), osteomyelitis (bone infection), bone fracture, or other bone loss induced by trauma or disease.

MgO nanoparticles can further enhance the aforementioned properties considering its high surface area to volume ratio due to its nanometer size, as has been shown for other metal oxide nanoparticles [11]. Before taking advantage of their desirable properties for clinical applications, it is important to determine how MgO nanoparticles affect cellular functions, specifically the functions of relevant bone cells. BMSCs are multipotent stem cells that can differentiate into a variety of mesodermal cells, including osteoblasts (bone forming cells), and play critical roles in bone healing [12, 13]. Thus, BMSC culture provides an excellent model system for studying the cytocompatibility of MgO nanoparticles and determining clinically relevant concentration range.

The culture methods to determine material-cell interactions are not yet standardized. Previous studies have used co-seeding and sequential seeding to study the interactions between BMSCs and other cell lines [14-16]. We were interested in applying the same techniques to study the interactions between BMSCs and MgO nanoparticles. Co-seeding involves seeding the BMSCs with MgO simultaneously. Sequential seeding involves culturing BMSCs for 24 hours prior to exposure to MgO. Through these methods we aimed to model two analogous *in vivo* scenarios: the interactions between MgO nanoparticles and migrating cells (co-seeding) and the interaction between MgO

nanoparticles and well-established cells within the extracellular matrix (sequential seeding).

In addition, to realize the coupled benefits of MgO nanoparticles in promoting bone growth and antimicrobial activity, it is essential to determine how MgO nanoparticles affect viability of infectious bacteria, especially the species causing orthopedic implant infection and osteomyelitis. *E. coli* is one of the most common gram-negative bacteria that cause orthopedic implant infection [17]. *Staphylococcus epidermidis* (*S. epidermidis*) is one of the most common gram-positive infectious bacteria found in osteomyelitis [17, 18]. Thus, we are interested in evaluating the antimicrobial activity of MgO nanoparticles with both bacteria types. It is also important to include both gram-negative and gram-positive bacteria in the study to comprehend overall antimicrobial properties of a material. Minimum bactericidal concentration (MBC) is crucial for fighting clinically relevant bacterial infections and developing antimicrobial biomaterials and surfaces because MBC indicates the lowest concentration required to kill bacteria. Specifically, the MBC is the concentration that results in ≥ 90% decrease in the colony forming units (CFU), with respect to the seeding density. MBC is not yet established for MgO nanoparticles. Krishnamoorthy *et al.* reported that the minimum inhibitory concentration (MIC) of MgO nanoparticles was 500 µg/mL for *E. coli* and 1000 µg/mL for *S. aureus* using a microtitre plate-based assay with resazurin (7-hydroxy-10-oxidophenoxazin-10-ium-3-one, $C_{12}H_7NO_4$) as an indicator for bacterial growth [19]. The previously reported MIC provided the basis for our study to determine the MBC of MgO nanoparticles for *E. coli* and *S. epidermidis.*

Therefore, the objective of this study was to investigate the effects of MgO nanoparticles on the viability of BMSC, *E. coli*, and *S. epidermidis*, and to determine the critical cytotoxic concentrations (CCC) for BMSCs and MBCs for bacteria.

2.2 Materials and Methods

2.2.1 Preparation and Characterization of MgO Nanoparticles

MgO nanoparticles were procured from US Research Nanomaterials Inc. (US3310). The vendor reported that MgO nanoparticles had a 99+% purity, a diameter of 20nm, a specific surface area of > 60 m^2/g, a polyhedral morphology, a bulk density of 0.145 g/cm^3, and a true density of 3.58 g/cm^3. The MgO nanoparticles for BMSC and bacterial cultures were sterilized through heating at 200°C in an oven for one hour. MgO cannot be sterilized through UV irradiation because the UV affects the surface chemistry of the MgO particles by causing adsorption of O_2 and production of superoxide ions [25, 26]. MgO nanoparticles were sterilized prior to characterization so that the particles would be in the same condition during characterization as they were in *in vitro* experiments.

MgO nanoparticles were characterized before their use in cell and bacteria cultures. The morphology of MgO nanoparticles was visualized using a field emission scanning electron microscope (SEM; Philips XL30), with a secondary electron detector, at an accelerating voltage of 30 kV, a working distance of 10 mm, and an original magnification of 250,000x. MgO particle size and distribution were quantified based on SEM images using the quantitative image analysis tools in ImageJ. We also confirmed morphology and crystal structure of the MgO nanoparticles with transmission electron

microscopy (TEM; Titan Themis 300) at an accelerating voltage of 120 kV. Elemental composition of the MgO nanoparticles was confirmed using the energy dispersive X-ray spectroscopy (EDS; EDAX Leap detector attached to Philips XL30 SEM) at a spot size of 3 and an accelerating voltage of 30 kV. Crystalline phase of MgO nanoparticles was characterized using x-ray diffraction (XRD; Empyrean, PANalytical). The XRD spectrum for MgO was obtained using Cu Kα radiation (45 kV, 40 mA) at a step size of 0.006^{o} and dwelling time of 50 seconds using a PIXcel 1D detector (PANalytical). Phase identification was performed using the HighScore software (PANalytical).

2.2.2 BMSC Culture with MgO Nanoparticles and Analyses

2.2.2a: Bone Marrow Derived Mesenchymal Stem Cell Culture

Rat BMSCs were extracted from the femur and tibia of juvenile Sprague Dawley rats according to the established protocol approved by the Institutional Animal Care and Use Committee (IACUC) at the University of California at Riverside [27, 28]. Briefly, the ends of the dissected long bones were cut using a scalpel and cell-containing bone marrow was flushed out of the marrow cavity using Dulbecco's Modified Eagle Medium (DMEM; Corning) supplemented with 10 v/v % fetal bovine serum (FBS; Hyclone) and 1 v/v % penicillin/streptomycin (P/S; Hyclone). Hereafter, DMEM with 10 v/v % FBS and 1 v/v % P/S will be referred to as DMEM. The bone marrow was collected into a sterile 15 mL tube with DMEM and large clusters were broken up using a syringe. The cell suspension was then filtered using a 70 μm nylon strainer (Fisher Scientific, Fisherbrand^{TM} 22363548) to remove aggregates. The filtered cells were centrifuged and cultured in fresh DMEM in a T-75 flask under standard cell culture conditions (that is, a

sterile, 37 °C, 5% CO_2/95% air, humidified environment). After 3 days, the media was changed to wash away non-adhered hematopoietic stem cells, leaving only the adherent mesenchymal stem cells to be cultured until they reached confluency. The pH of DMEM was adjusted to 7.4 before being used in cell culture and addition of MgO nanoparticles. BMSCs at their second passage were used for *in vitro* experiments with MgO nanoparticles.

All the experimental procedures were conducted under sterile conditions using a biosafety II laminar flow hood (Class II Type A2, Labconco) and a cell culture incubator (MCO-19AIC, Sanyo Scientific) in a certified cell culture room.

2.2.2b Co-seeding and Sequential-seeding Methods for Culturing BMSCs with MgO Nanoparticles

Two culture methods, i.e., co-seeding and sequential-seeding, were used to study the effects of MgO nanoparticles on BMSCs *in vitro*. For the co-seeding method, MgO nanoparticles were introduced concurrently into the culture when BMSCs were seeded. Specifically, BMSCs were seeded at a density of 10,000 cells/cm^2 in 2 mL DMEM into each well of a 12-well tissue culture treated plate (Corning, Falcon® 353043). Immediately following, MgO nanoparticle allocations of 0.6, 0.9, 1.5, 2.1, 3.0, 3.6, 4.2, 4.8, and 6.0 mg were suspended in 1mL of DMEM and added into the respective wells. Each well had a total volume of 3mL. The resulting concentrations of MgO nanoparticles in the respective wells were 200, 300, 500, 700, 1000, 1200, 1400, 1600, and 2000 µg/mL.

For the sequential-seeding method, BMSCs were first seeded at a density of 10,000 cells/cm^2 into each well with 3mL of media in the 12-well tissue culture treated

plates, and cultured for 24 hours to allow the BMSCs to attach. Afterwards, the DMEM was replaced with 3mL of fresh media containing the prescribed 200-2000 μg/mL of MgO nanoparticles. The BMSCs were then cultured with MgO nanoparticles at concentrations of 200- 2000 μg/mL for additional 24, 48, and 72 hours. Every 24 hours, 2.5mL of media were collected and replaced with the same volume of fresh media; the rest 0.5 mL of media were not collected in order to avoid disturbing the MgO nanoparticles at the bottom of the wells.

The BMSC cultures without MgO nanoparticles were included as the Cells Only positive control and the DMEM without cells and MgO as the Media Only control (blank reference). All the experimental and control groups were run in triplicate.

2.2.2c Post-culture BMSC Characterization and Media Analyses

After each prescribed culture period, 3mL of media was collected for media analysis and the cells were prepared for fixation and staining. Each culture well was washed with phosphate-buffered saline (PBS) to remove non-adherent or dead cells. Adherent cells were fixed using 4% paraformaldehyde (Electron Microscopy Sciences, 15714-S). The paraformaldehyde was diluted with PBS from a stock of 32% to 4 v/v % prior to fixing. The fixed cells were then stained with 4',6-diamidino-2-phenylindoledilactate (DAPI; Life Technologies) for the nuclei of the cells and Alexa Fluor® 488-phalloidin (Life Technologies) for F-actin. The stained cells in each well were imaged using a fluorescence microscope (Nikon Eclipse T*i*-S) at 10 random locations. For each well, the number of adherent cells was counted using the analysis tools in ImageJ. BMSC adhesion density was calculated as the number of adhered cells

per unit area. Each image represents a known area of the culture plate. We divided the cell count in an image by the area of the image to calculate the cell density. The average cell density calculated from all the images for one sample type was used to represent the cell density of that sample type.

The pH of the post-culture media was measured immediately after collection using a pre-calibrated pH meter (Symphony SB70P, VWR). The concentrations of Mg^{2+} and Ca^{2+} ions were measured using inductively coupled plasma optical emission spectrometry (ICP-OES; PerkinElmer Optima 8000). For the ICP-OES analysis, the collected post-culture media was first diluted to 1:100 in deionized (DI) water, and then fed into the instrument for the measurement using an auto sampler. Concentrations of Mg^{2+} and Ca^{2+} ions were calculated based on the calibration curves generated using Mg and Ca standards (Perkin Elmer) diluted to the ranges of 0.5–5.0 and 0.1–1.0 mg/L, respectively.

2.2.2d Behavior of MgO Nanoparticles in DMEM without BMSCs

MgO nanoparticles were cultured in DMEM in acellular conditions to determine their effects on the media. Specifically, MgO nanoparticles at the prescribed 200-2000 µg/mL concentration were incubated in DMEM without cells under standard cell culture conditions for 24 hours. Subsequently, the media were collected for pH measurements and analyses of Mg^{2+} and Ca^{2+} concentrations using ICP-OES, as described earlier.

Considering the buffering effects of DMEM under standard cell culture conditions, it is necessary to monitor the media pH more frequently within the first 24 hours of incubation. To evaluate the effect of MgO nanoparticles on pH, concentrations

of 0, 200, and 1000 µg/mL of MgO nanoparticles in 3mL of DMEM were selected. The media pH was measured after incubation for 5 minutes, 15 minutes, 30 minutes, 1 hour, 2 hours, 4 hours, and 24 hours. The pH at 0 minutes was the media pH measured immediately after adding MgO nanoparticles but before placing them into the cell culture incubator.

2.2.3 Bacterial Culture with MgO Nanoparticles and Analyses

2.2.3a Bacterial Culture

E. coli (ATCC® 25922) and *S. epidermidis* (ATCC® 35984) were cultured in Luria-Bertani Broth (LBB; Sigma Aldrich, L3022) and Tryptic Soy Broth (TSB; Sigma Aldrich, 22092), respectively. Frozen stocks of each bacterial type were stored at -80ºC. A sterile loop was used to transfer a portion of the frozen stocks to their respective broths. The bacteria were cultured in a shaker incubator (Incu-shaker Mini, Benchmark Scientific) at 37°C and 250 rpm for 16 hours. For *S. epidermidis*, an aliquot of 100 µL from the culture grown overnight was added to 5 ml of fresh broth and cultured for another 4-6 hours. Afterwards, the bacteria were counted using a hemocytometer (Hausser Bright-Line 3200, Hausser Scientific) and diluted to a concentration of $5x10^5$ cells/mL in LBB or TSB because this is the clinically relevant concentration for orthopedic infections [29]. Subsequently, 3 mL of *E. coli* in LBB or *S.* epidermidis in TSB were added to each well of a 12 well non-tissue culture treated polystyrene plate (Corning, Falcon® 351143), and MgO nanoparticles with the prescribed mass of 0.6, 0.9, 1.5, 2.1, 3.0, 3.6, 4.2, 4.8, and 6.0 mg were added immediately after. As a result, *E. coli* and *S. epidermidis* were cultured with 200-2000 µg/mL of MgO nanoparticles, and

incubated for 24 hours in a shaker incubator at 37°C and 120rpm. The co-seeding of the bacteria and MgO mimics the *in vivo* scenario in which bacteria are introduced with medical devices or implants. The shaking speed for the culture plates was reduced from the initial speed of 250 rpm to 120 rpm to prevent spillage between wells. After 24 hours, the respective bacteria in the LBB or TSB were collected for analyses. The *Bacteria Only* group without MgO nanoparticles and the *Broth Only* group without MgO nanoparticles and bacteria were included as the positive control and blank reference, respectively.

2.2.3b Post-culture Bacterial Viability and Broth Analyses

After the respective bacteria were cultured with MgO nanoparticles, the bacterial concentrations in the collected broth were analyzed using two different methods, i.e., measuring optical absorbance using a microplate reader (Infinite M200 Pro, Tecan) and measuring the colony forming units (CFU) plated on agar plates.

Viability of the suspended *E. coli* and *S. epidermidis* was determined through evaluation of colony forming units (CFU) on Luria Bertani (LB) and Tryptic Soy (TS) Agar (Sigma Aldrich) plates, respectively. The *E. coli* in the LBB was serially diluted to $1:10^6$ for the control group and the experimental groups cultured with 200-1200 µg/mL MgO nanoparticles, while the groups with 1400-2000 µg/mL MgO nanoparticles were not diluted. The *S. epidermidis* in the TSB was serial diluted to $1:10^6$ for the control group and the experimental groups cultured with 200 or 300 µg/mL MgO nanoparticles, $1:10^4$ for the groups with 500 µg/mL MgO nanoparticles, $1:10^2$ for the groups with 700 µg/mL MgO nanoparticles, and $1:10^{-1}$ for the groups with 1000-2000 µg/mL MgO nanoparticles. The dilution factor was selected to give a reasonably countable number of

CFUs. Each bacterial suspension was diluted with its respective broth and 100 µL of the diluted suspension was pipetted onto the respective agar plates. The bacterial suspension was then evenly spread across the respective agar plates. The agar plates were inverted so that the agar was on the top side, and then incubated for 16-18 hours. The number of colonies formed on the respective agar plates was counted, and multiplied by the dilution factor to obtain the CFU/ml values.

The pH of the post-culture LBB and TSB was measured using a pre-calibrated pH meter (Symphony SB70P, VWR). The post-culture LBB and TSB was diluted to 1:50 with DI water and analyzed using ICP-OES to determine the $Mg^{2+}$and Ca^{2+} ion concentrations in each broth. All the experimental and control groups were run in triplicate.

2.2.3c Characterization of Bacterial Adhesion and Morphology by SEM

To characterize the bacterial adhesion and morphology after they were cultured with MgO nanoparticles, *E. coli* and *S. epidermidis* was cultured with 200 to 2000 µg/mL MgO nanoparticles and prepared for SEM imaging. Before placing the bacteria or MgO into each culture well, a sterilized $1cm^2$ square borosilicate glass slide (Fisher Scientific, Fisherbrand™ cover glass 12-542-B) was placed into the bottom of each well. The glass slides were previously cut to 1 cm x 1 cm squares, using a diamond saw (DynaCut 1500HD). The bacterial culture method was similar as described above. After the respective bacteria were cultured with the prescribed concentrations of MgO nanoparticles on the glass slides for 24 hours, each well was rinsed with Tris-buffered saline (Sigma Aldrich) to remove the bacteria that did not attach. The bacteria were then

fixed in 10% glutaraldehyde for 1 hour. The 10% glutaraldehyde solution was previously diluted from a 25% glutaraldehyde solution (Sigma-Aldrich) in a Tris-buffered saline. Each sample was then rinsed 3 times with a Tris-buffered saline, and dried in air at room temperature for at least 24 hours. These dried glass slides with adherent bacteria were then coated with Pt/Pd using a sputter coater (108 Auto Sputter Coater, Cressington Scientific.) at 20mA for 60 seconds, in preparation for scanning electron microscopy (SEM; Philips XL30). Representative images were taken using a secondary electron detector, at an accelerating voltage of 10 kV, a working distance of 10 mm, and an original magnification of 10,000x. The bacterial culture with glass and subsequent fixation procedure were intended for SEM imaging of bacterial adhesion and morphology, and were not used for bacterial quantification.

2.2.3d The Effects of MgO Nanoparticles on LBB and TSB without Bacteria

MgO nanoparticles ranging from 200 to 2000 µg/mL were incubated in LBB or TSB in acellular conditions for 24 hours to determine their specific effects on the pH of broth and the ionic concentrations in broth. At the end of 24 hours, the broth was collected for pH measurements and analyses of Mg^{2+} and Ca^{2+} concentrations using ICP-OES, similarly as described earlier.

2.2.3e Bacterial Culture with Increasing pH and Mg^{2+} ion Concentrations

To determine whether the ionic byproducts of MgO nanoparticles (OH^- and Mg^{2+}) contributed to its antimicrobial properties, we cultured *E. coli* and *S. epidermidis* in the respective broth with initial pH adjusted to 7, 7.5, 8, 8.5, 9, 9.5, and 10 or in the respective broth supplemented with 1, 5, 10, 15, 20, 30, 40, and 50 mM of Mg^{2+} ions. For

the pH study, the broth pH was intentionally adjusted to 7-10 using sodium hydroxide (NaOH, Strem Chemicals). For the Mg^{2+} ion dosage study, Mg^{2+} ions were added into the respective broth using a stock solution of magnesium chloride hexahydrate ($MgCl_2 \cdot 6H_2O$, Sigma Aldrich). The stock solution was prepared by dissolving 1.525g of $MgCl_2 \cdot 6H_2O$ in 50mL of LBB or TSB respectively, to achieve the Mg^{2+} ion concentration of 150mM. The 150mM stock solution was diluted with the respective broth to obtain the doping solutions with Mg^{2+} ion concentrations from 1 to 50mM. The doping solutions were added into the respective bacterial culture to give the supplemental Mg^{2+} ion dosages of 1-50 mM. To clarify, the values reported as supplemental Mg^{2+} dosages do not include the Mg^{2+} ions already present in the broth. It is important to note that 0mM does not actually mean there were no Mg^{2+} ions present in the broth, but rather that no additional Mg^{2+} ions were added into the broth to serve as a control group.

After 24 hours of culture, the bacteria and respective broth were analyzed to determine the specific effects of each soluble factor on the total bacterial concentration and bacteria viability, as well as the changes in broth pH and ionic concentrations, using the same method as described earlier.

2.2.4 Statistical Analysis

All experiments were run in triplicate. All data sets were analyzed using one-way analysis of variance (ANOVA) followed by the Tukey highest significant difference post hoc test. Statistical significance was considered at $P < 0.05$.

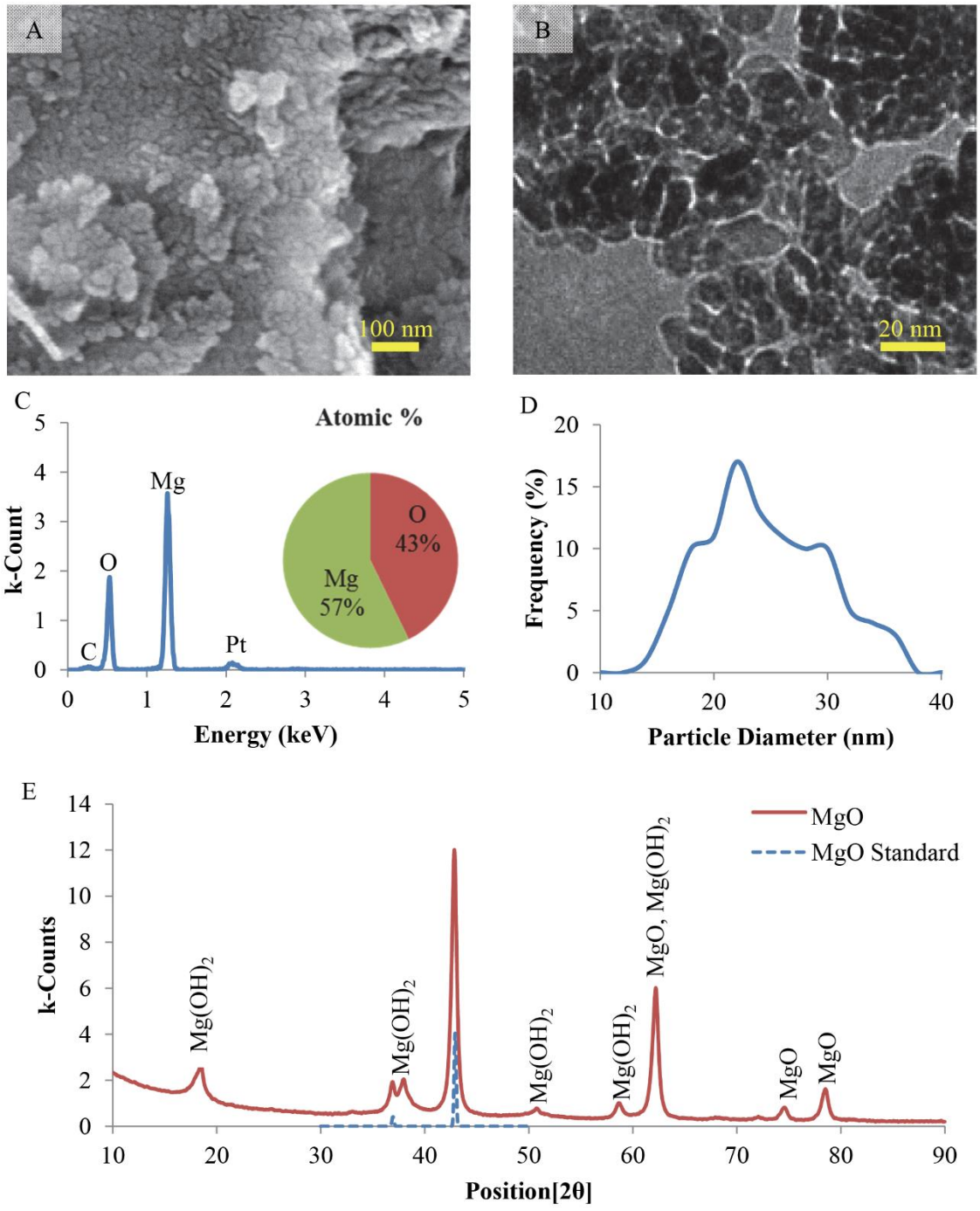

Figure 2.1: Characterization of MgO nanoparticles. (A) SEM image, (B) TEM image, (C) EDS analysis, (D) particle size distribution, and (E) XRD spectrum.

2.3 Results

2.3.1 Characterization of MgO Nanoparticles

SEM images of MgO were taken immediately after sterilization and before BMSC and bacterial culture (Figure 2.1A). The TEM image of MgO revealed that the particles mostly had near spherical morphology and crystalline structure (Figure 2.1B), in agreement with the vendor's characterization [30]. EDS results confirmed the atomic composition was close to MgO (Figure 2.1C). The average particle diameter for MgO was 23 ± 5 nm (Figure 2.1D). The standard peaks for MgO were observed in the XRD spectrum, indicating that the expected crystalline form of MgO was present (Figure 2.1E). Additional peaks in the XRD pattern of the MgO sample also indicated the presence of crystalline phases matching $Mg(OH)_2$. MgO is hygroscopic and can readily react with water in the atmosphere to form $Mg(OH)_2$, which is most likely the reason for the presence of $Mg(OH)_2$ peaks in the XRD spectrum.

2.3.2 BMSC Morphology, Adhesion Density and Respective Media Analyses

2.3.2a BMSC Adhesion Density and Media Analyses with Co-seeding

Based on the prior research, the 0 to 2000 µg/mL concentration range of MgO nanoparticles was studied to determine the CCC for BMSCs [19]. Morphology and density of BMSCs that were cultured with MgO nanoparticles through the co-seeding method was characterized using fluorescence microscopy (Figure 2.2). The BMSC viability significantly reduced after 24 hours of incubation with 200 µg/mL of MgO nanoparticles and near to complete cell death at or above 300 µg/mL, when compared with the positive control (Cells Only), as quantified in Figure 2.2D. Surviving cells

exhibited abnormal morphology after co-seeding with 200 to 300 µg/mL of MgO nanoparticles, appearing smaller and exhibiting signs of possible membrane damage, as highlighted in Figure 2.2 A-B.

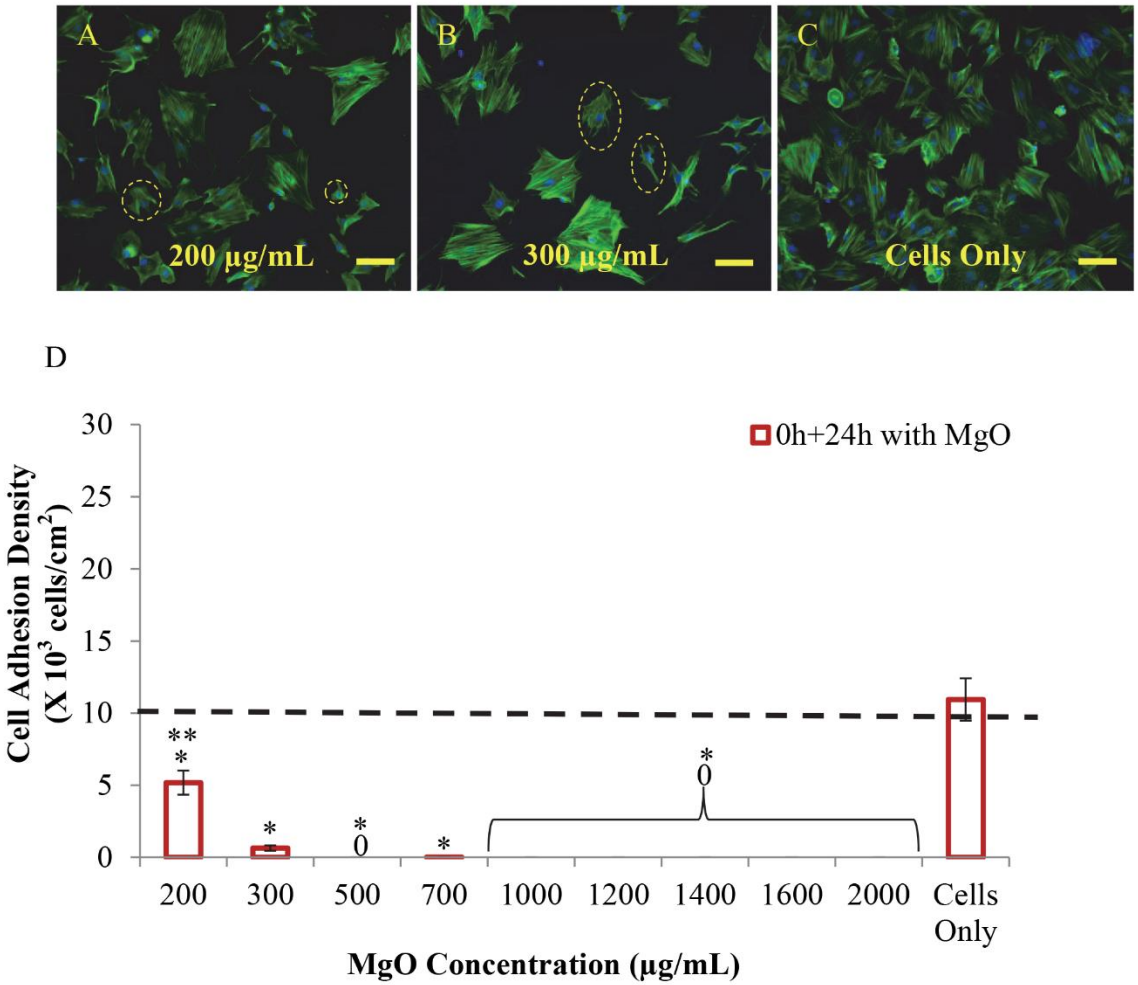

Figure 2.2: Morphology and adhesion density of BMSCs co-seeded in DMEM with MgO nanoparticles at concentrations of 200 – 2000 µg/mL. (A-C) Fluorescence images of BMSCs after 24 hours of incubation with MgO nanoparticles at a concentration of (A) 200 µg/mL and (B) 300 µg/mL, as compared with (C) the Cells Only control. BMSCs were seeded at a density of 10,000 cells/cm2 at time zero (t0) as indicated by dashed line and incubated for 24 hours with 200 to 2000 µg/mL of MgO nanoparticles. Examples of cells with abnormal morphology are circled with a dashed yellow line. Blue stain indicates nuclei and green stain indicates F-actin. (D) BMSC adhesion density quantified from fluorescence images. Values are mean ± standard error; n=30. *p<0.05 compared to the Cells Only control, **p<0.05 compared to 300-2000 µg/mL.

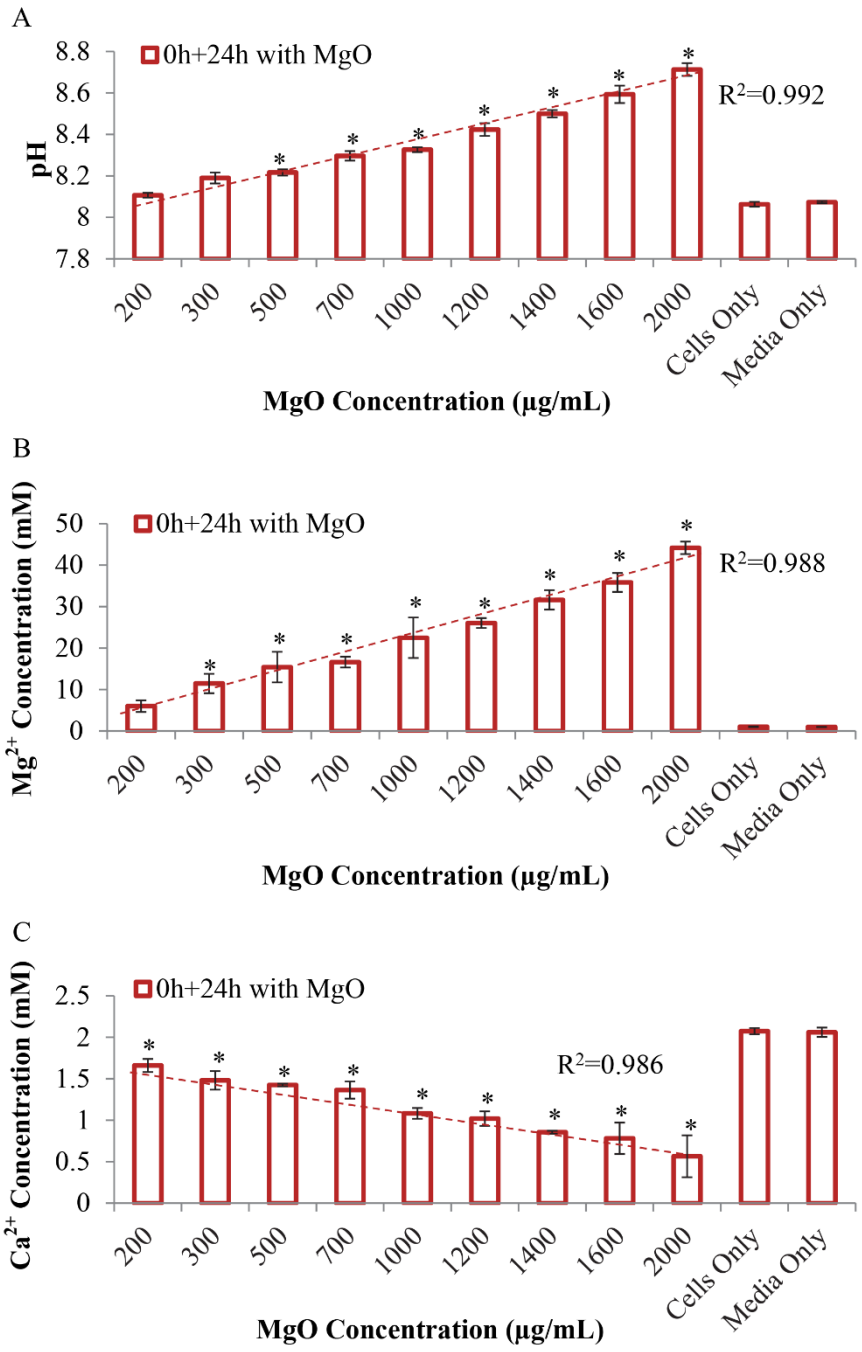

Figure 2.3: Media analyses after co-seeding and 24 hours of incubation of BMSCs with MgO nanoparticles at concentrations of 200 – 2000 µg/mL. (A) post-culture media pH, (B) Mg^{2+} ion concentration in the post-culture media, and (C) Ca^{2+} ion concentration in the post-culture media. Red dashed line indicates the linear fit for the data corresponding to 200-2000 µg/mL MgO nanoparticles. Values are mean ± standard deviation; n=3. *p<0.05 compared to the Cells Only control.

For the co-seeding method, the trends of media analyses were highlighted using linear regression, as shown in Figure 2.3. The average pH of the culture media showed an increasing trend with increasing concentrations of MgO nanoparticles (Figure 2.3A). The average pH of the culture media with 200 and 300 µg/mL MgO nanoparticles were higher than that of the *Cells Only* control, but not statistically significant; the pH for the rest of experimental groups was significantly higher than the Cells Only control. Mg^{2+} concentration showed a similar increasing trend with increasing concentrations of MgO nanoparticles (Figure 2.3B). The average Mg^{2+} concentration in the culture media with 200 µg/mL MgO nanoparticles were higher than that of the *Cells Only* control, but not statistically significant; Mg^{2+} concentration for the rest of experimental groups was significantly higher than the Cells Only control. In contrast, Ca^{2+} concentration showed a decreasing trend with increasing concentrations of MgO nanoparticles (Figure 2.3C). Ca^{2+} concentration for all experimental groups was statistically lower than that of the *Cells Only* control.

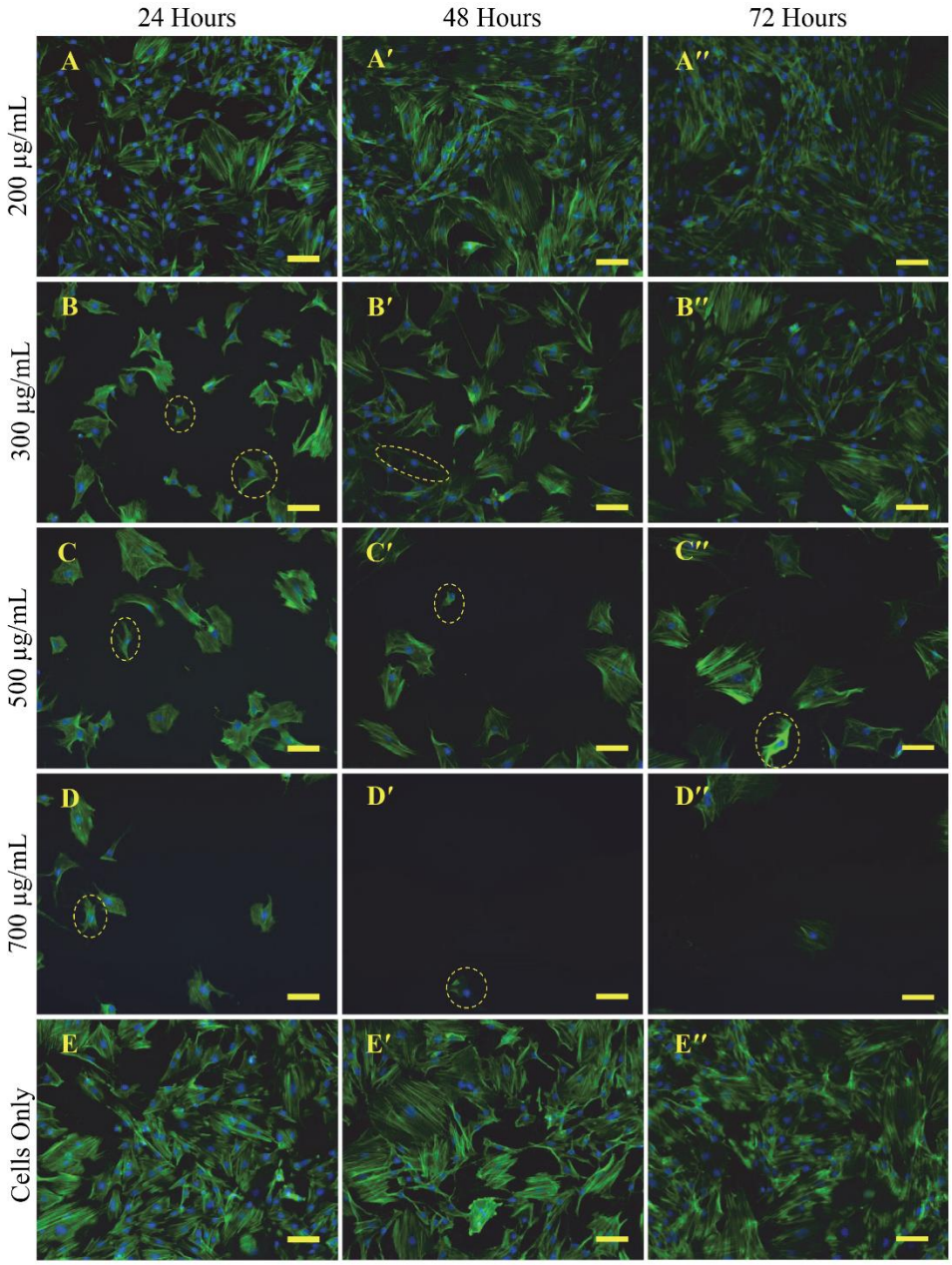

Figure 2.4: Fluorescence images of BMSCs that were sequentially cultured in DMEM with MgO nanoparticles at concentrations of (A-D) 200 – 700 µg/mL for (A-D) 24, (A′-D′) 48, and (A″-D″) 72 hours compared to (E-E″) the respective Cells Only control at each time point. MgO nanoparticles at concentrations of 1000 - 2000 µg/mL caused complete cell death and images are not shown since no viable cells were found. The Cells Only group did not have any MgO nanoparticles. Examples of cells with abnormal morphology are circled with a dashed yellow line. Blue stains nuclei and green stains F-actin. Scale bar = 100 µm.

2.3.2b BMSC Adhesion Density and Media Analyses with Sequential-Seeding

The morphology of BMSCs that were cultured with MgO nanoparticles through the sequential-seeding method was observed using fluorescence microscopy (Figure 2.4). Qualitatively, cells cultured with 200µg/mL MgO exhibited healthy morphology and grew to confluency (Figure 2.4A-A"), similar to the Cells Only control group (Figure 2.4E-E"). At or above 300 µg/mL, the cells appeared smaller and some showed signs of membrane damage, similar to the experimental groups under the co-seeding method. The sequential-seeding method closely represents how cells in the body would react to the use of MgO nanoparticles, since BMSCs in our body would be well established in their extracellular matrix before the introduction of implant materials such as MgO.

The BMSC adhesion density was quantified based on the fluorescence images of sequentially seeded cultures (Figure 2.5). The cell density significantly increased after the cells were incubated with 200 µg/mL of MgO nanoparticles for 72 hours, when compared with all the other conditions. All samples sequentially-seeded with 300 µg/mL or more of MgO showed significant decrease in cell density during the first 24 hours. At 300 µg/mL, no statistical difference was detected at 48 and 72 hours when compared with the *Cells Only* control. This indicated that the cells were able to recover from MgO exposure at 300 µg/mL. The cells cultured with MgO concentrations at or above 500 µg/mL did not recover during 48 and 72 hours of culture; the cell density was significantly lower than the Cells Only control at the respective time points and the experimental groups of 200 and 300 µg/mL at 72 hours.

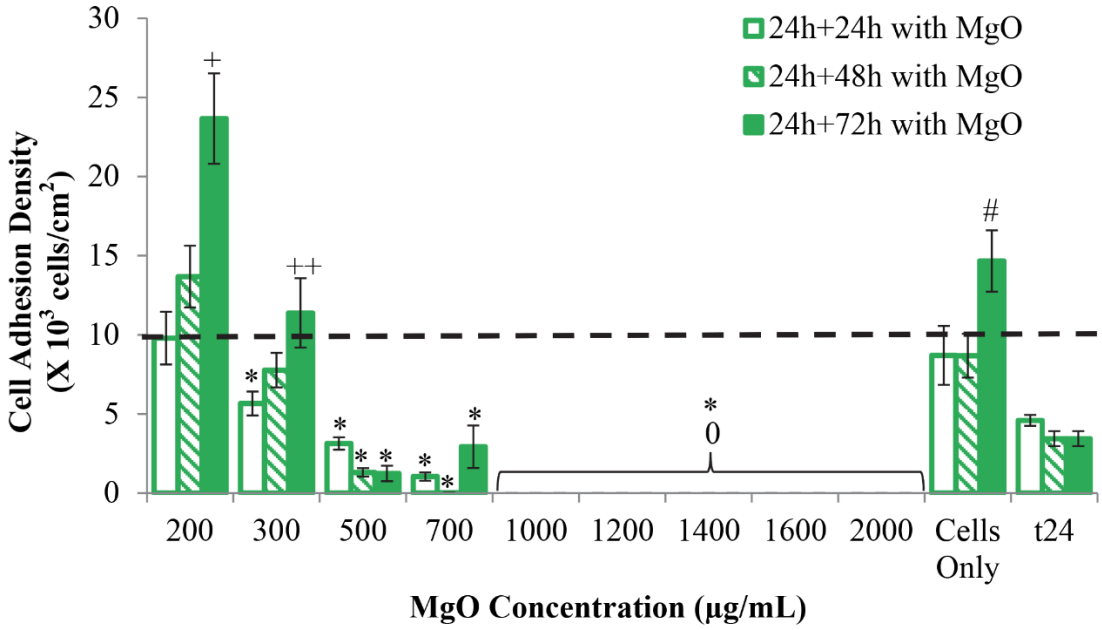

Figure 2.5: Adhesion density of BMSCs after they were sequentially cultured in DMEM with MgO nanoparticles at concentrations of 200 – 2000 µg/mL for 24, 48, and 72 hours, quantified from fluorescence images. BMSCs were seeded at a density of 10,000 cells/cm2 at time zero (t0) as indicated by dashed line. The cell density after incubation for 24 hours but prior to exposure to MgO is represented by the t24 group. Afterwards, 200 to 2000µg/mL of MgO nanoparticles were added into the BMSC culture and incubated for additional 24, 48, 72 hours. Values are mean ± standard error; n=30. *p<0.05 compared to the Cells Only control for respective time points, +p<0.05 compared to the same MgO concentration group at the earlier time points of 24h+24h and 24h+48h, as well as all the other groups with greater than 200 µg/mL MgO concentrations and the Cells Only control at all time points, ++p<0.05 compared to the same MgO concentration group at the earlier time point of 24h+24h, as well as all the groups with greater than 300 µg/mL MgO concentrations at all of the time points, #p<0.05 compared to the Cells Only control group at 24h+24h and 24h+48h time points.

For the sequential-seeding method, the trends for media pH and Mg^{2+} concentration in the media were highlighted using linear regression, as shown in Figure 2.6. During the first 24 hours, the pH of the cell culture media increased as the concentration of MgO increased (Figure 2.6A), similar to the co-seeding method. At 48 and 72 hours, the pH increase was smaller when comparing each condition with their

respective pH at 24 hours. The pH increased to the maximum of 8.7 at the highest MgO concentration being studied, i.e., 2000 µg/mL. The trend of increasing Mg^{2+} concentration with increasing MgO concentration during the first 24 hours of sequential culture (Figure 2.6B) was similar to the co-seeding method. At 48 and 72 hours, Mg^{2+} concentration continued to show an increasing trend with increasing MgO concentration, but the extent of increase was much smaller. The Ca^{2+} concentration showed a decreasing trend during the first 24 hours of sequential culture as MgO concentration increased, but this trend did not continue at 48 and 72 hours (Figure 2.6C). The trends in pH, Mg^{2+} and Ca^{2+} concentrations indicated that the dissolution of MgO or its effect on media occurred mostly within the first 24 hours of culture.

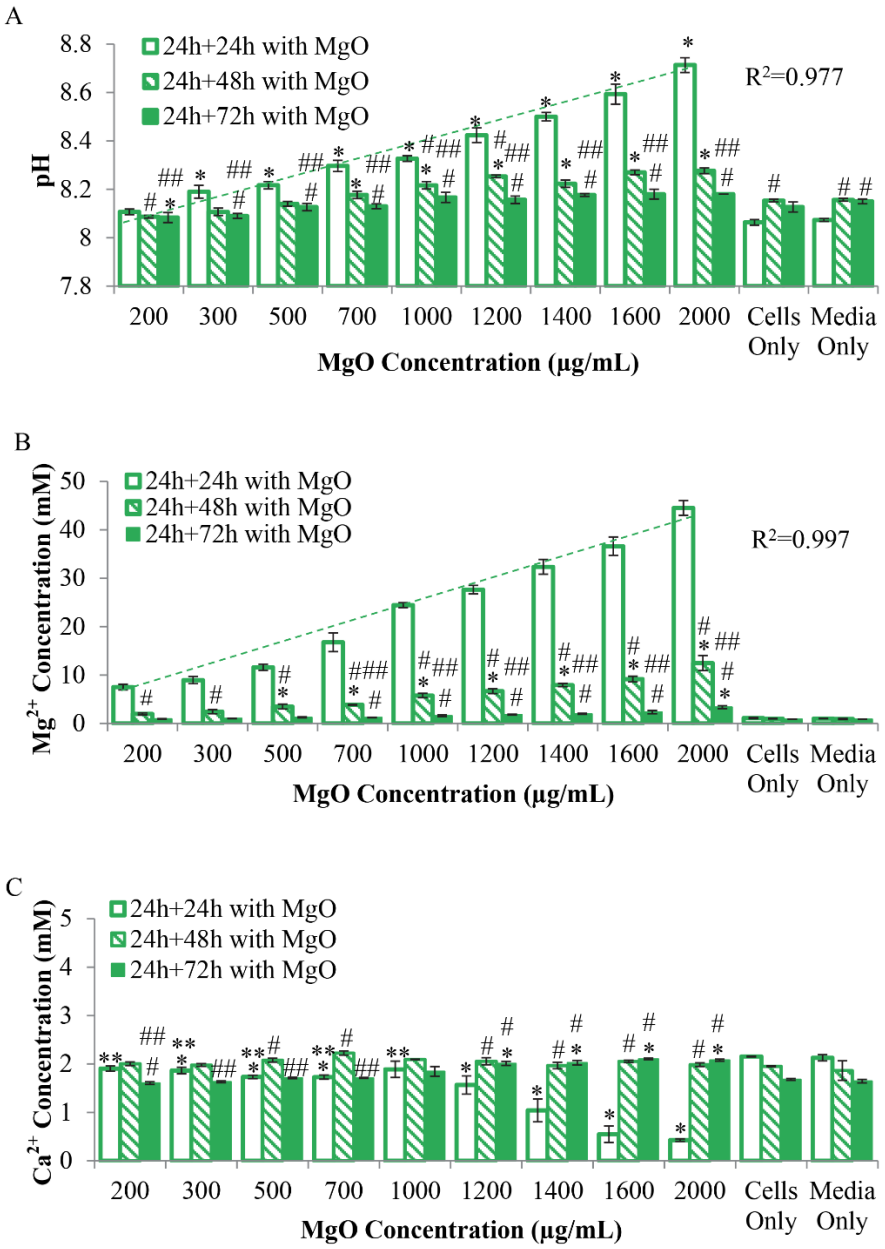

Figure 2.6: Media analyses after BMSCs were sequentially cultured with MgO nanoparticles at concentrations of 200 – 2000 µg/mL for 24, 48, and 72 hours. (A) post-culture media pH, (B) Mg^{2+} ion concentration, and (C) Ca^{2+} ion concentration in the post-culture media at each prescribed MgO concentration and each prescribed time point. Green dashed line indicates linear fit for the data corresponding to the 24h+24h time point with 200-2000 µg/mL MgO. Values are mean ± standard deviation; n=3.*p<0.05 compared to the Cells Only control at respective time points, **p<0.05 compared to 1400-2000 µg/mL MgO, #p<0.05 compared to 24h+24h time point at respective MgO concentration, ##p<0.05 compared to 24h+48h time point at respective MgO concentration.

2.3.2c The Effects of MgO Nanoparticles on DMEM in Acellular Conditions

The addition of MgO into DMEM showed similar effects on the media pH, Mg^{2+} concentration, and Ca^{2+} concentration under acellular conditions (Figure 2.7). As MgO concentration increased, the media pH and Mg^{2+} concentration showed increasing trends. There were no statistically significant differences in pH or Mg^{2+} concentration between 200-300 µg/mL and the Media Only control. At and above 500 µg/mL, both pH and Mg^{2+} concentration were significantly higher than the Media Only control. Conversely, the Ca^{2+} concentration showed a deceasing trend as MgO concentration increased (Figure 2.7C). There were no statistically significant differences in Ca^{2+} concentration in media cultured with 200-300 µg/mL MgO as compared with the Media Only control. At and above 500 µg/mL, there was statistically significant decrease of Ca^{2+} in the media with respect to the Media Only control.

After the addition of MgO nanoparticles of 200 or 1000 µg/mL into the media under acellular conditions, we observed that the average media pH reached its peak at 15 minutes and then decreased over the 24 hours of culture (Figure 2.8). Specifically, at 15 minutes, the mean pH of media with 200 µg/mL MgO was 8.57, and the pH of the media with 1000 µg/mL MgO was 9.37. At the end of 24 hours, the pH for media with 200µg/mL and 1000µg/mL of MgO decreased to 7.78 and 8.01, respectively.

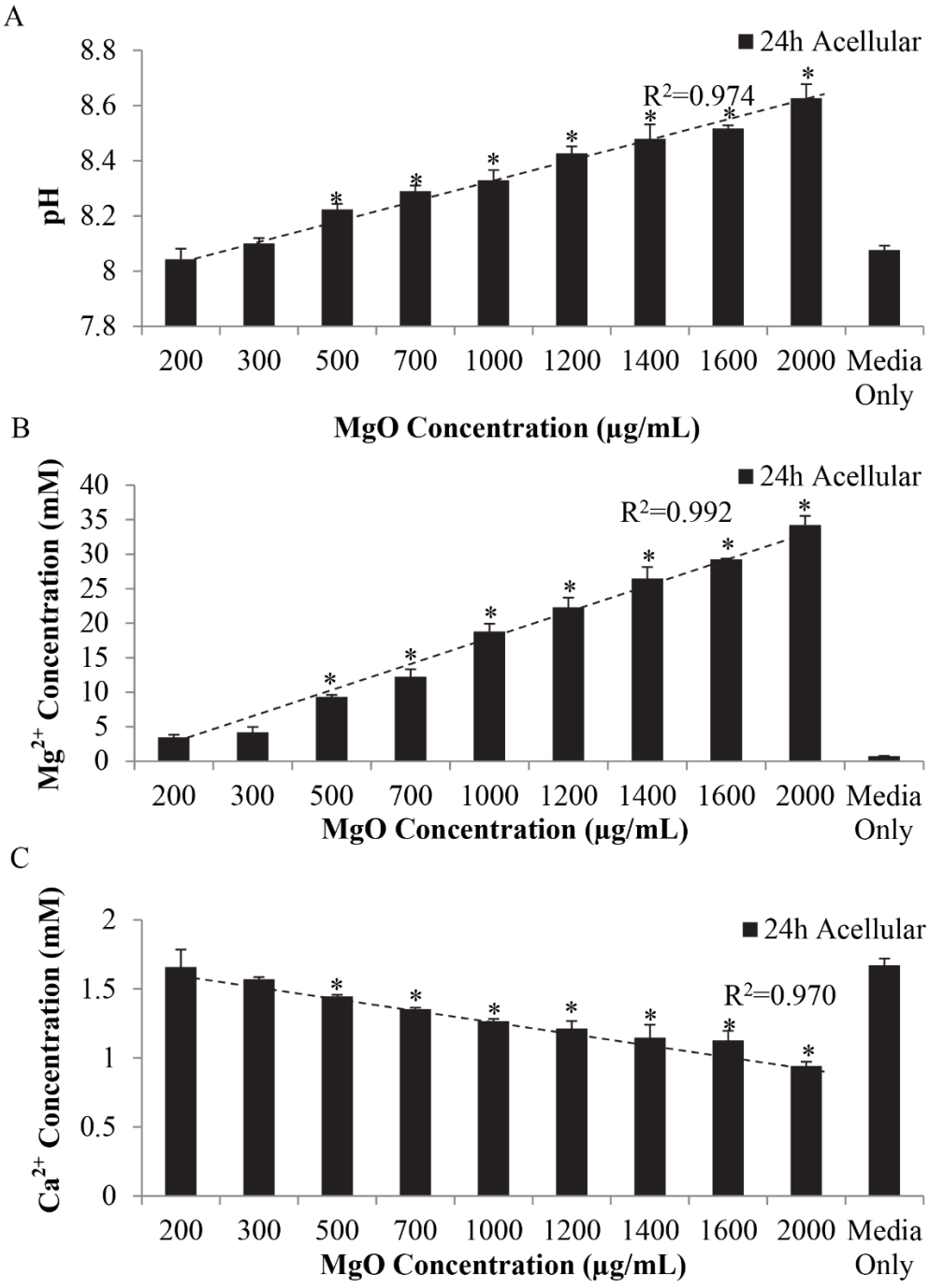

Figure 2.7: Media analyses after 24 hours of incubation of DMEM with MgO nanoparticles at concentrations of 200 – 2000 µg/mL at acellular condition. (A) post-culture media pH, (B) Mg^{2+} ion concentration in the post-culture media, and (C) Ca^{2+} ion concentration in the post-culture media. Black dashed line indicates the linear fit for the data corresponding to 200-2000 µg/mL MgO. Values are mean ± standard deviation, n=3. *p<0.05 compared to the Media Only Control.

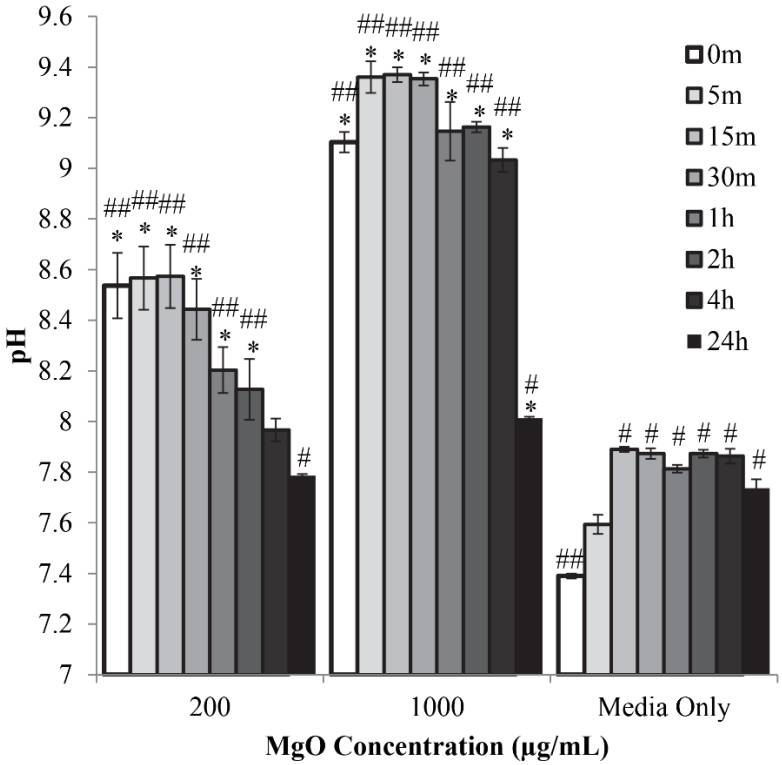

Figure 2.8: The effect of MgO nanoparticles on the pH of DMEM over 24 hours at acellular condition. Values are mean ± standard deviation; n=3*p<0.05 compared to the Media Only control at respective time points, #p<0.05 compared to 0 minute time point of respective concentration group, ##p<0.05 compared to 24 hour time point of respective concentration group.

2.3.3. Bacteria Adhesion, Viability, and Respective Broth Analyses

2.3.3a Bacteria Adhesion and Viability in Exposure to MgO Nanoparticles

E. coli and *S. epidermidis* adhered on the glass slides were visualized using SEM, after culture with MgO nanoparticles at concentrations of 200 - 2000 µg/mL (Figure 2.9). As compared with the Bacteria Only control, *E. coli* appeared to have a normal morphology, but less bacteria and smaller clusters were present when cultured with increasing concentrations of MgO nanoparticles from 200 to 700 µg/mL (Figure 2.9 A$^-$-D$^-$). MgO nanoparticles at concentrations of 1000 - 2000 µg/mL caused complete bacteria death and no bacteria were found on the glass slides (Image not shown). The *S.*

epidermidis showed similar trends as *E. coli* after culture with MgO nanoparticles (Figure 2.9 A^{+}-C^{+}). As compared with the Bacteria Only control, *S. epidermidis* appeared to have a normal morphology, but far less bacteria and fewer clusters were observed as MgO concentrations increased. Qualitatively, the presence of MgO nanoparticles resulted in reduction of adherence for both gram-negative and gram-positive bacteria, beneficial for preventing biofilm formation.

Bacterial viability was quantified through CFU (Figure 2.10). We also quantified live and dead bacteria concentration through optical absorbance measurements, which further confirmed our CFU measurements (Data not shown). The absorbance measurements quantify all bacteria in broth and do not distinguish live or dead bacteria, while CFUs measured from agar plating only quantify viable bacteria. The presence of MgO nanoparticles did not affect the absorbance reading. Based on CFU quantification, *E. coli* viability decreased significantly when cultured with MgO nanoparticles at and above 1200µg/mL, indicating MBC for *E. coli* was 1200 µg/mL (Figure 2.10). *S. epidermidis* viability decreased when cultured with MgO nanoparticles at 500 and 700 µg/mL as compared with the Bacteria Only control, making these concentrations bacteriostatic (Figure 2.10). *S. epidermidis* viability decreased significantly when cultured with MgO nanoparticles at and above 1200µg/mL, indicating MBC for *S. epidermidis* was 1200 µg/mL. At MgO concentrations of 200-300 µg/mL, the CFUs of *E. coli* and *S. epidermidis* were significantly greater than their respective controls, indicating that low concentration of MgO might enhance bacterial growth.

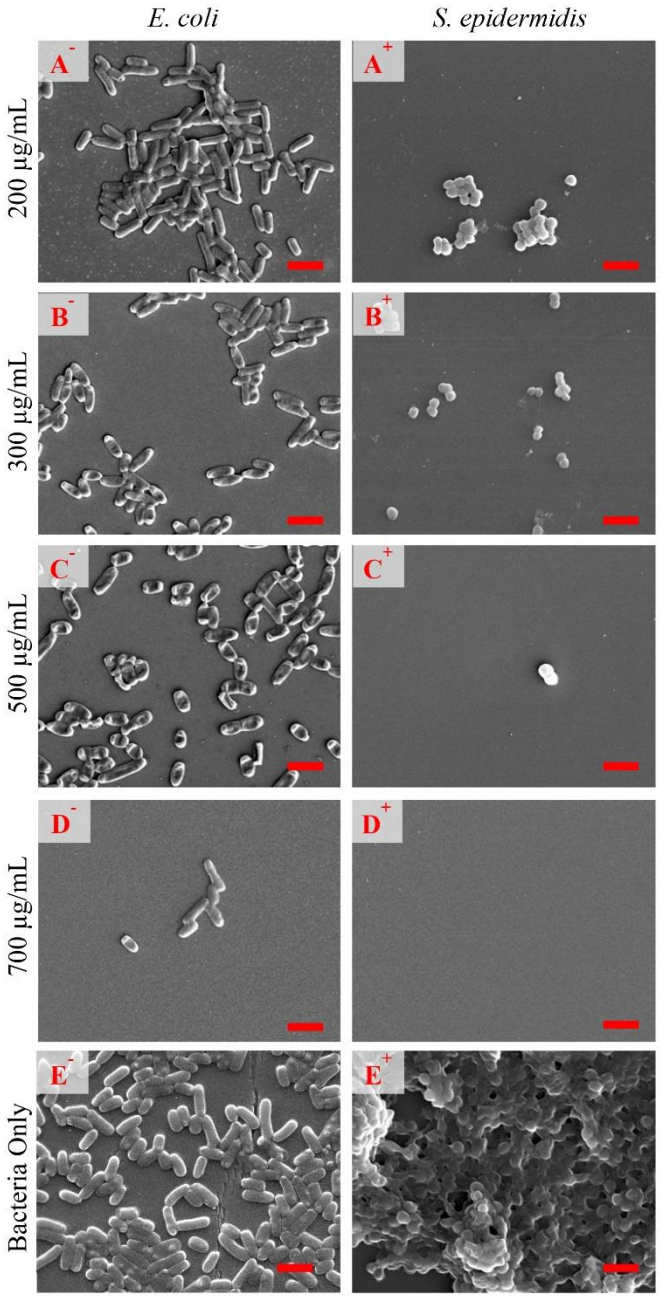

Figure 2.9: SEM images of (A^--E^-) *E. coli* and (A^+-E^+) *S. epidermidis* after culture with MgO nanoparticles at concentrations of (A-D) 200 – 700 µg/mL and (E) Bacteria Only control without MgO nanoparticles. MgO nanoparticles at concentrations of 1000 - 2000 µg/mL caused complete bacterial death and thus images are not shown since no viable bacteria were found. Scale bar = 2 µm.

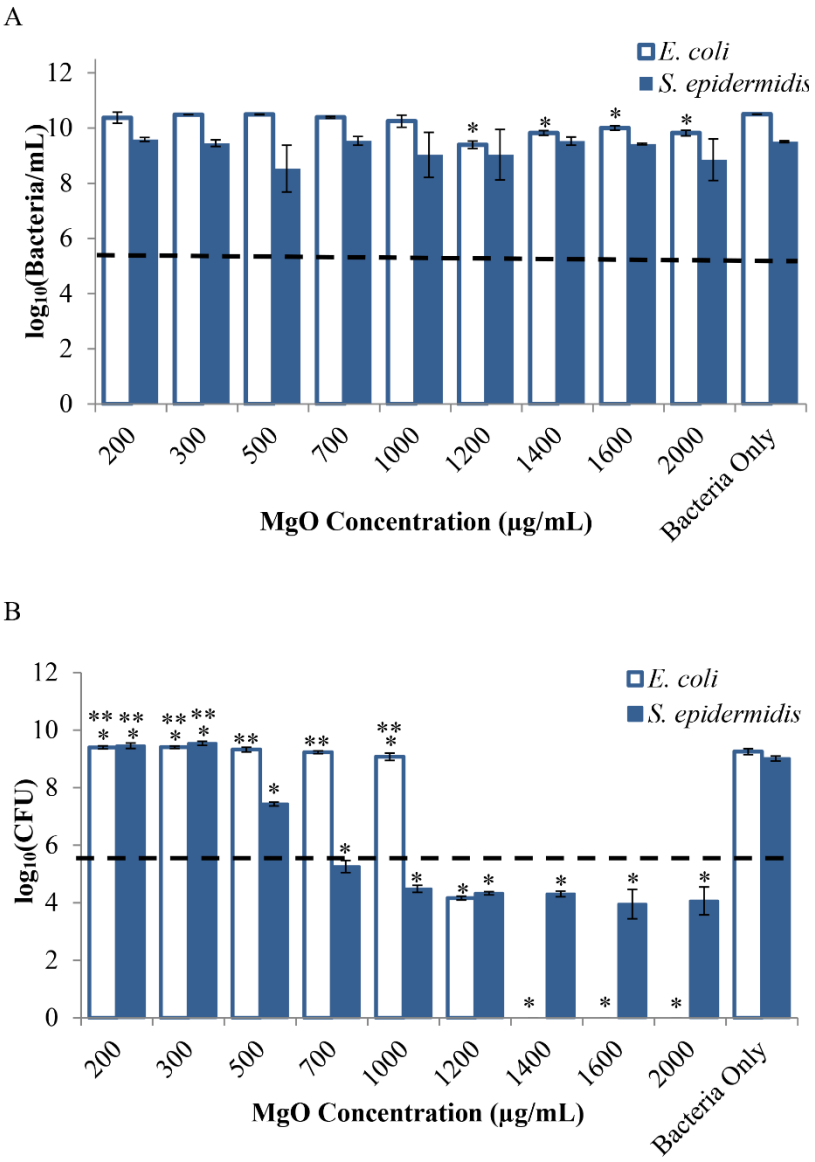

Figure 2.10: Bacterial density after they were cultured in respective LBB and TSB with MgO nanoparticles at concentrations of 200 – 2000 µg/mL for 24 hours, as quantified from (A) absorbance and (B) colony forming unit (CFU). Bacteria were seeded at a concentration of $5x10^5$ bacteria/mL as indicated by the black dashed line. Values are mean ± standard deviation; n=3 for A and n=9 for B. *p<0.05 compared to the Bacteria Only control of respective bacteria type, **p<0.05 compared to1200-2000 µg/mL for *E. coli* or compared to 500-2000 µg/mL for *S. epidermidis*.

Collectively, our results suggested that MgO nanoparticles at certain concentrations not only reduced bacterial viability in broth, but also reduced bacterial adhesion density onto glass surfaces. Inhibiting bacterial adhesion onto an implant surface is important to reduce implant-associated infections, because adhered bacteria are much harder to treat and systemic administration of antibiotics is often ineffective [31].

The pH of the LBB for *E. coli* culture and TSB for *S. epidermidis* culture was plotted in Figure 2.11A. The pH of the *E. coli* culture with 200 to 1000 µg/mL of MgO all showed that average pH increased to 8.8 or greater, significantly greater than the Broth Only controls. When compared with the Bacteria Only control, the pH of the *S. epidermidis* culture did not change much when cultured with 200 to 300 µg/mL of MgO, and started to increase steadily as the MgO concentration increased to and above 500 µg/mL. When comparing the pH of the MgO-free LBB controls with and without *E. coli*, it appeared that *E. coli* increased pH to 8.7, which is alkaline. When comparing the pH of the MgO-free TSB controls with and without *S. epidermidis*, it appeared that the *S. epidermidis* reduced pH to 5.7, which is acidic.

Both the LBB for *E. coli* culture and TSB for *S. epidermidis* culture showed increasing Mg^{2+} and Ca^{2+} concentrations with increasing MgO (Figure 2.11 B,C). At 2000 µg/mL of MgO, Mg^{2+} concentration reached 42 mM for *E. coli* culture and 36mM for *S. epidermidis* culture, respectively.

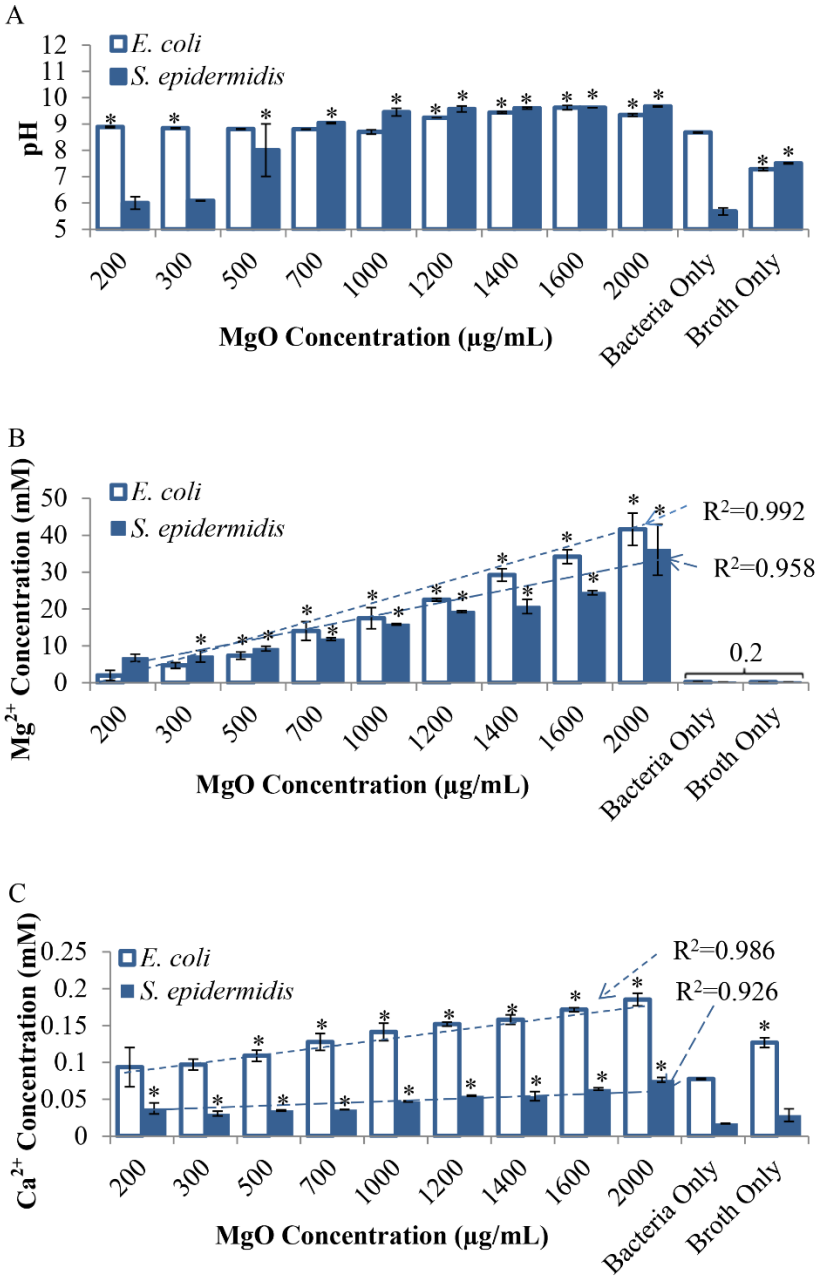

Figure 2.11: Broth analyses after bacteria were cultured in respective LBB and TSB with MgO nanoparticles at concentrations of 200 – 2000 µg/mL for 24 hours. (A) post-culture broth pH at each prescribed MgO concentration, (B) Mg^{2+} ion concentration in the post-culture broth at each prescribed MgO concentration, and (C) Ca^{2+} ion concentration in the post-culture broth at each prescribed MgO concentration. A short-dashed line and long-dashed line indicate the linear fit for the data corresponding to 200-2000 µg/mL MgO for *E. coli* and *S. epidermidis*, respectively. Values are mean ± standard deviation; n=3. **p*<0.05 compared to the Bacteria Only control of respective bacteria type.

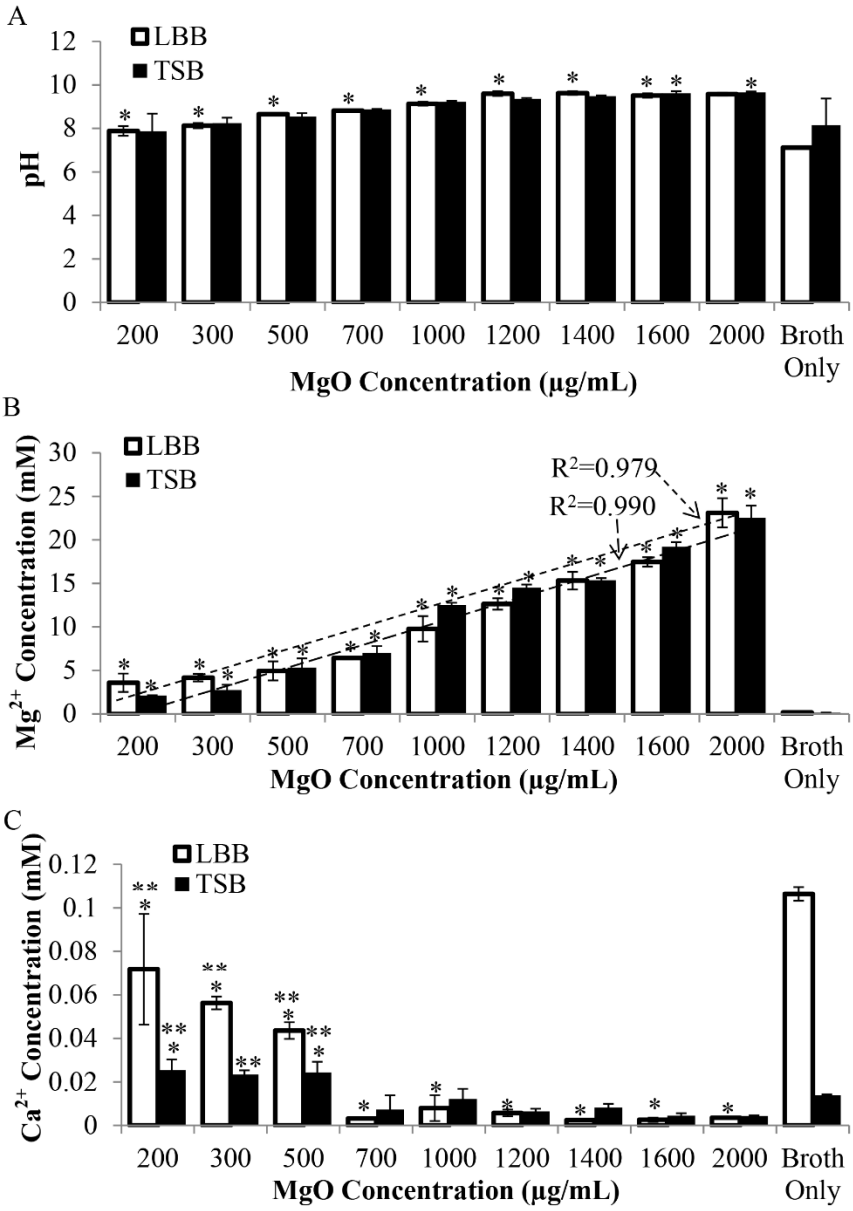

Figure 2.12: Broth analyses after MgO nanoparticles at concentrations of 200 – 2000 µg/mL were cultured in respective LBB and TSB for 24 hours without bacteria. (A) post-culture broth pH at each prescribed MgO concentration, (B) Mg^{2+} ion concentration in the post-culture broth at each prescribed MgO concentration, and (C) Ca^{2+} ion concentration in the post-culture broth at each prescribed MgO concentration. A short-dashed line and a long-dashed line indicate the linear fit for the data corresponding to 200-2000 µg/mL MgO for LBB and TSB, respectively. Values are mean ± standard deviation; n=3. *p<0.05 compared to the Broth Only control for respective broth type, **p<0.05 compared to 700-2000 µg/mL MgO in respective broth type.

2.3.3b The Effects of MgO Nanoparticles on LBB and TSB in Acellular Conditions

In acellular conditions, the pH and Mg^{2+} concentration showed increasing trends for both LBB and TSB as MgO concentration increased (Figure 2.12). The average pH of the Broth Only controls was 7.1 for LBB and 8.1 for TSB. Each group with MgO resulted in higher average pH when compared with the Broth Only control. Statistically significant increased pH was found in all groups of LBB with MgO. The pH of TSB groups with MgO did not show statistically significant difference when compared with the Broth Only control until MgO concentration increased to 1600 µg/mL due to the large deviation in the Broth Only control. All groups with MgO showed statistically higher Mg^{2+} concentration than the Broth Only controls. Mg^{2+} concentration steadily increased with increasing MgO concentrations. In the groups with MgO, Ca^{2+} concentration generally decreased with increasing MgO for both broth types. For LBB, all groups with MgO had significantly less Ca^{2+} compared to the Broth Only control. In the case of TSB, we observed greater average Ca^{2+} concentration in the groups with 200-500 µg/mL of MgO than the Broth Only control, but only statistically significant at 200 and 500 µg/mL. At and above 700 µg/mL, the average Ca^{2+} concentration in TSB was lower than the Broth Only control, but not statistically significant.

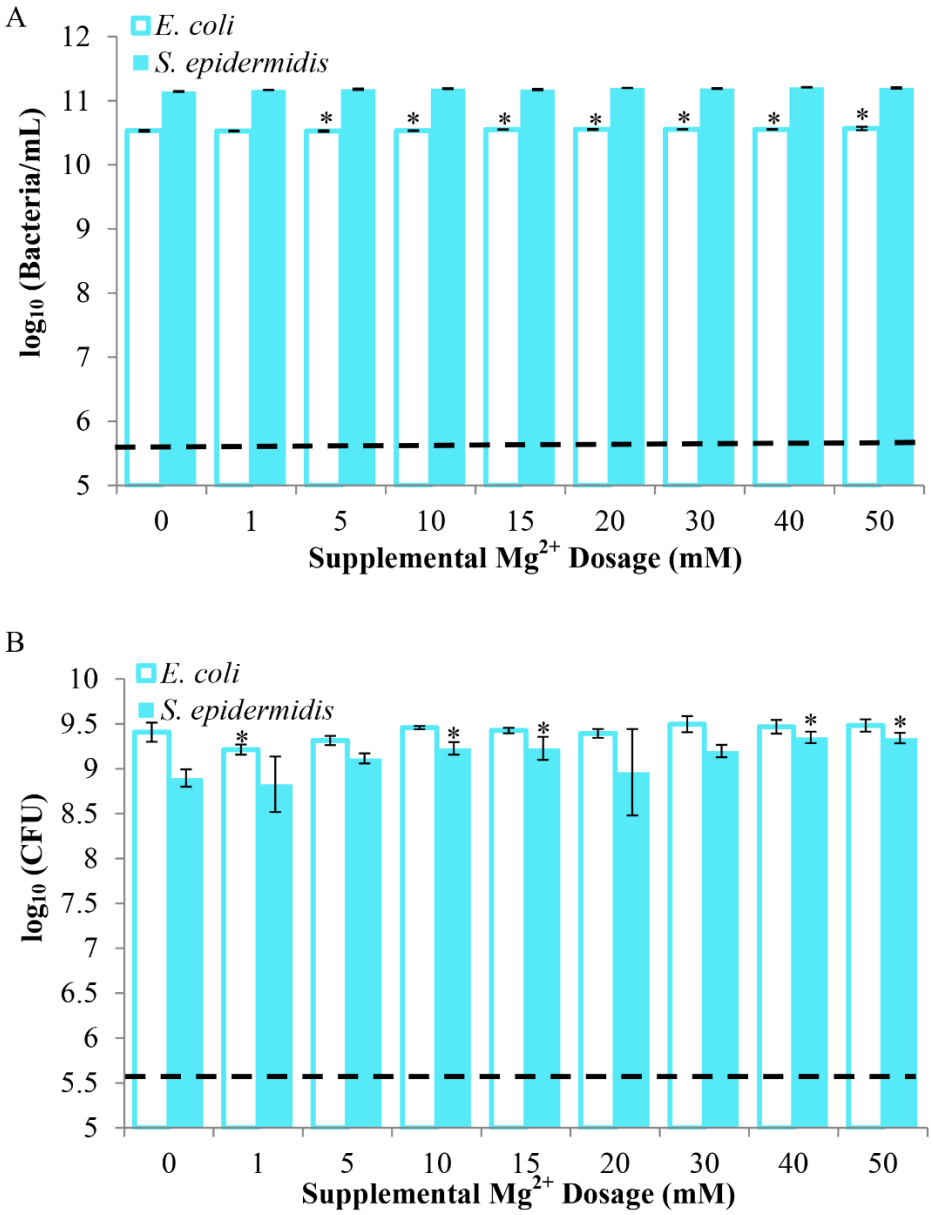

Figure 2.13: Bacterial density after they were cultured in respective LBB and TSB supplemented with 0 –50 mM Mg^{2+} ions for 24 hours, as quantified from (A) absorbance and (B) colony forming units (CFU). Bacteria were seeded at a concentration of $5x10^5$ bacteria/mL as indicated by the black dashed line. Values are mean ± standard deviation; n=3 for A and n=9 for B. *p<0.05 compared to the control without supplemental Mg^{2+} dosage (0 mM), for respective bacteria type.

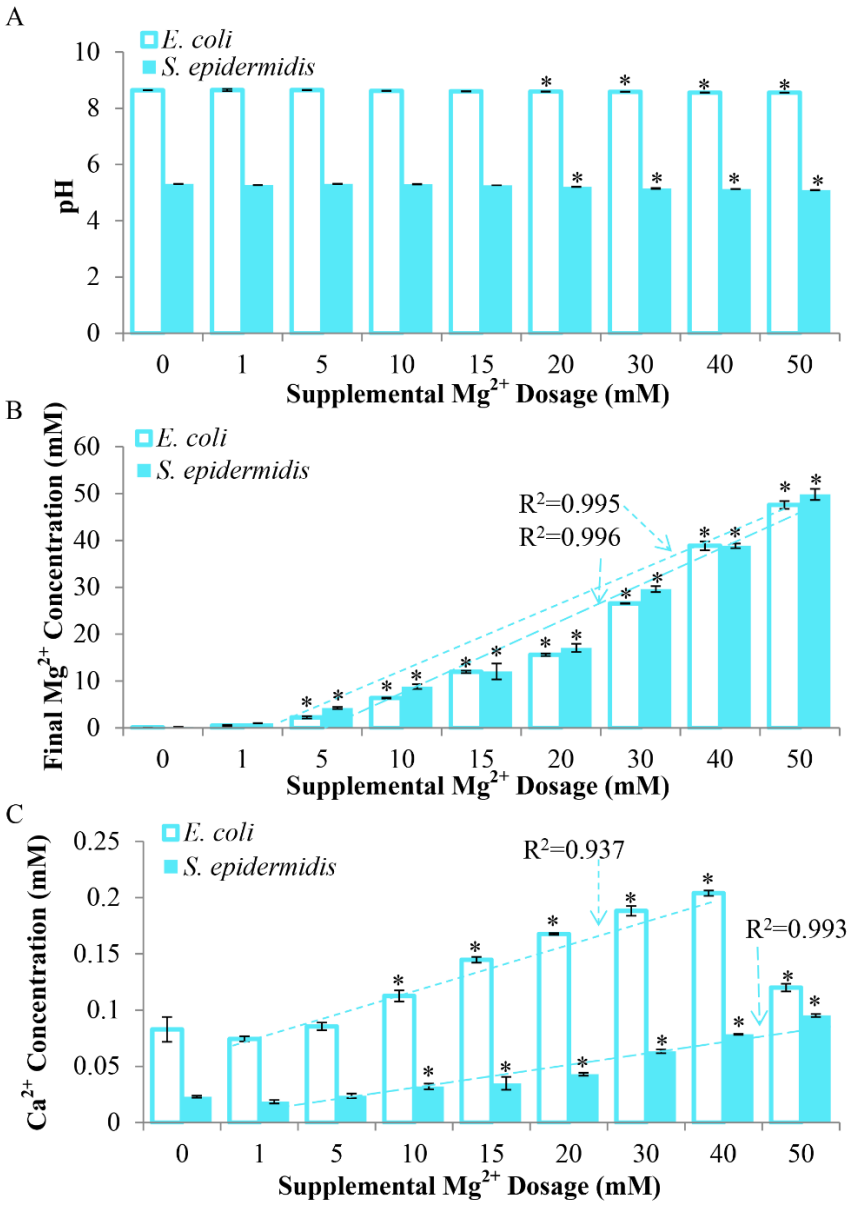

Figure 2.14: Broth analyses after bacteria were cultured in respective LBB and TSB supplemented with 0-50 mM Mg^{2+}+ for 24 hours. (A) post-culture broth pH at each prescribed supplemental Mg^{2+} dosage, (B) Mg2+ ion concentration in the post-culture broth at each prescribed supplemental Mg2+ dosage, and (C) Ca^{2+} ion concentration in the post-culture broth at each prescribed supplemental Mg^{2+} dosage. A short-dashed line indicates the linear fit for the data corresponding to 1-50mM supplemental Mg^{2+} dosage in graph B and 1-40mM supplemental Mg^{2+} dosage in graph C for *E. coli*. A long-dashed line indicates the linear fit for the data corresponding to 1-50 mM supplemental Mg^{2+} dosage for *S. epidermidis*. Values are mean ± standard deviation; n=3.*p<0.05 compared to the control without supplemental Mg^{2+} dosage (0 mM), for respective bacteria type.

2.3.3c The Effects of Mg^{2+} Ion Dosing on Bacteria Viability and Growth

Bacterial culture with supplemental Mg^{2+} ions did not lead to bactericidal or bacteriostatic effects on *E. coli* or *S. epidermidis* because all of the evaluated groups with supplemental Mg^{2+} dosages resulted in significant bacterial growth since seeding, similar to the 0mM dosage group (Figure 2.13). CFU quantification showed similar results with significant bacterial growth for the groups with supplemental Mg^{2+}dosages, similar to the 0mM group (no supplemental dosage). The groups supplemented with 10, 15, 40, and 50mM Mg^{2+} ions showed statistically significant increase in viable *S. epidermidis* (Figure 2.13).

The pH of the broths with supplemental Mg^{2+} dosages remained relatively unchanged with only a slight decrease in pH at dosages of 20mM or higher for both *E. coli* and *S. epidermidis* (Figure 2.14A). With increasing Mg^{2+} concentration, we observed the expected increase in final Mg^{2+} concentration for both LBB and TSB (Figure 2.14 B). Ca^{2+} concentration of the LBB with *E. coli* increased with increasing supplemental Mg^{2+} dosage but had a sharp decrease at 50mM (Figure 2.14 C). For TSB with *S. epidermidis*, Ca^{2+} concentration increased with increasing supplemental Mg^{2+} dosage.

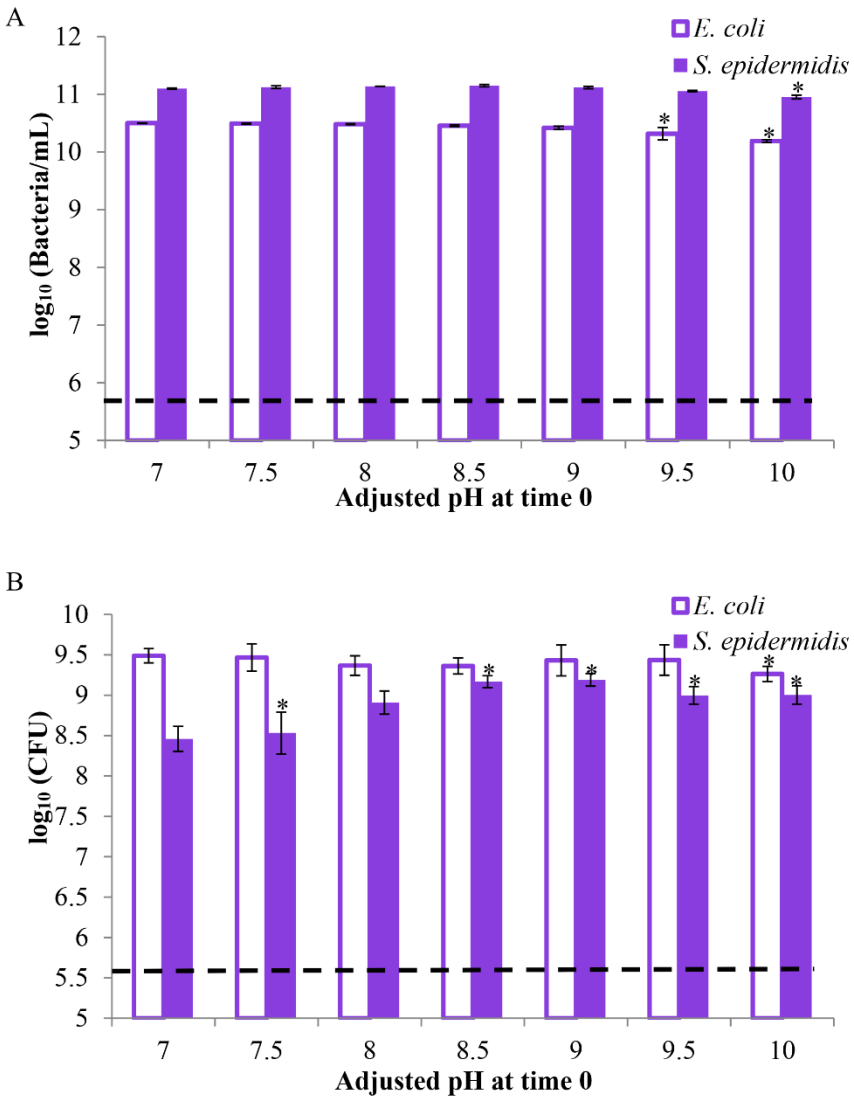

Figure 2.15: Bacterial density after they were cultured for 24 hours in respective LBB and TSB with initial pH adjusted to 7-10, as quantified from (A) absorbance and (B) colony forming units (CFU). Bacteria were seeded at a concentration of $5x10^5$ bacteria/mL as indicated by the black dashed line. Values are mean ± standard deviation; n=3 for A and n=9 for B. *p<0.05 compared to the control with an initial pH 7 for respective bacteria type.

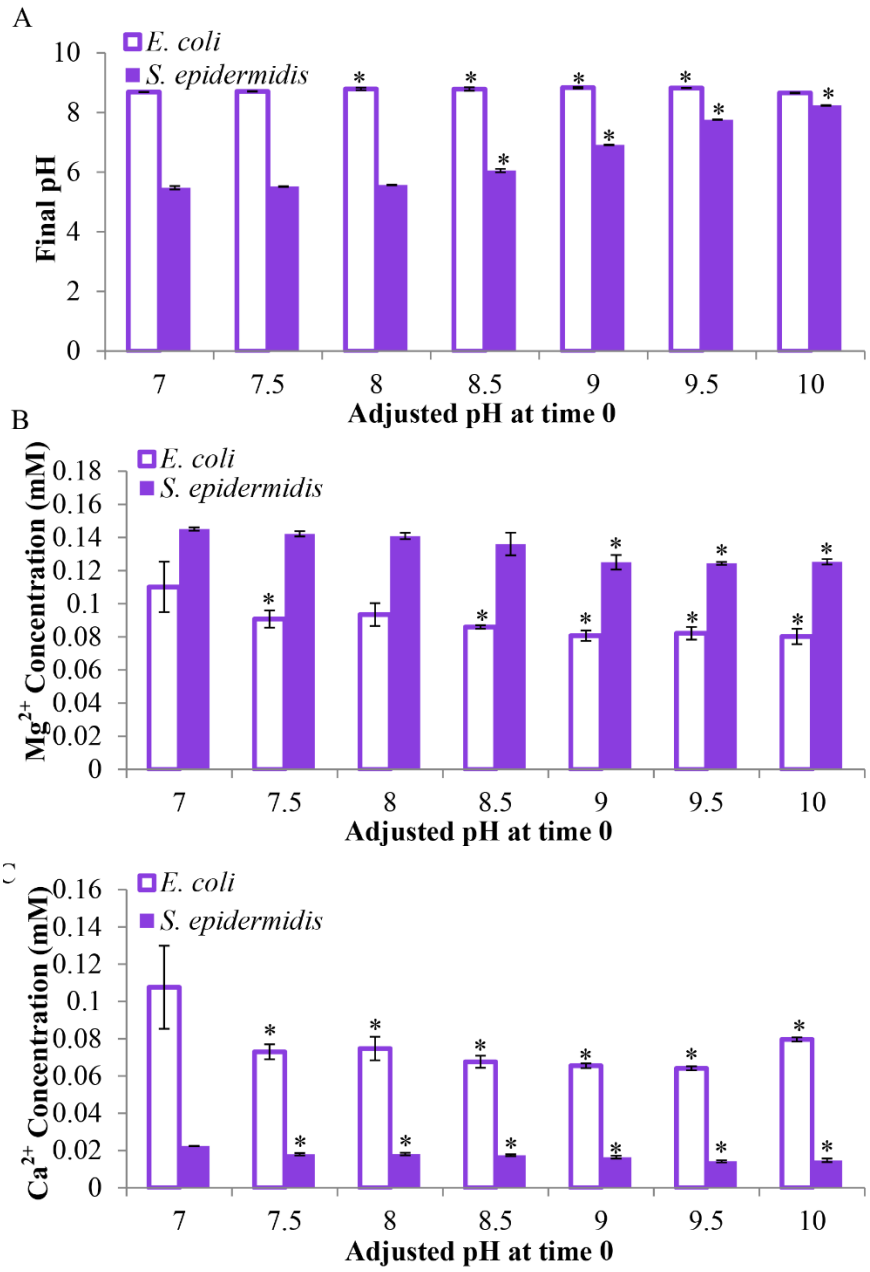

Figure 2.16: Broth analyses after bacteria were cultured for 24 hours in respective LBB and TSB with initial pH adjusted to 7-10. (A) post-culture broth pH at each prescribed initial pH, (B) Mg^{2+} ion concentration in the post-culture broth at each prescribed initial pH, and (C) Ca^{2+} ion concentration in the post-culture broth at each prescribed initial pH. Values are mean ± standard deviation; n=3. *p<0.05 compared to the control with an initial pH 7 for respective bacteria type.

2.3.3d The Effects of Initial pH on Bacteria Viability and Growth

Increasing initial broth pH up to 10 did not lead to bactericidal or bacteriostatic effects on *E. coli* or *S. epidermidis* because all of the evaluated groups with increased pH resulted in significant bacterial growth since seeding, similar to the control group with initial pH of 7 (Figure 2.15). CFU quantification showed similar bacterial concentrations for the groups with initial pH adjusted to greater than 7.5 and the control group with initial pH of 7 (Figure 2.15). Statistically significant but slight decrease in *E. coli* CFUs was observed at pH of 10; some *S. epidermidis* groups with initial pH adjusted to greater than 7.5 showed statistically greater CFUs than the control group with initial pH of 7.

The final pH of LBB for *E. coli* culture changed to a narrow range of 8.7 - 8.8 and the final pH of TSB for *S. epidermidis* culture decreased to 5.5 - 8.2, even though their initial pH values were adjusted to 7-10, respectively (Figure 2.16A). Adjusting the initial broth pH to higher values led to decreasing trends in Mg^{2+} concentrations, with some statistical significance at pH 7.5, 8.5 and above for *E. coli* and at pH 9 and above for *S. epidermidis* (Figure 2.16B). Ca^{2+} concentration decreased when the initial broth pH values were adjusted to 7.5 - 10 as compared with the control group at initial pH 7, for both types of bacteria (Figure 2.16C).

2.4 Discussion

2.4.1 BMSC Viability

The effects of MgO nanoparticles on BMSC adhesion density and viability depend on MgO concentration and *in vitro* culture methods. With the co-seeding method, BMSC adhesion density all decreased when cultured with MgO, as compared with the

Cells Only control, because BMSCs were likely to have more direct-contact with MgO nanoparticles during co-seeding when the cells were not yet adhered to the substrates and not yet established in culture, which might have made the BMSCs more vulnerable to MgO nanoparticles. MgO nanoparticles were also reported to increase bacterial death with more direct-contact via shaking [9], which suggested that direct-contact with MgO might be a key factor causing cell death. In contrast, with the sequential-seeding method, BMSC density was significantly greater than the Cells Only control at 72 hours when cultured with 200 µg/mL of MgO. Moreover, the BMSCs with sequentially seeded 300 µg/mL of MgO showed similar cell density as the Cells Only control at 72 hours. These results suggested that BMSCs were less vulnerable to the effects of MgO under the sequential-seeding method, because they adhered to the culture plates and established themselves in the culture before exposure to MgO. Thus, MgO nanoparticles, in small dosages, such as 200 µg/mL, are beneficial for bone regeneration, because they could enhance proliferation of the BMSCs. The sequential-seeding method represents how the cells would interact with newly implanted MgO more closely than the co-seeding method, and, thus, will be the focus of the following discussion. For the purposes of this study, we define CCC as the concentration of the material of interest, in our case of MgO, which results in 50+% cell deaths with respect to the seeding density. Our results suggested that the CCC for 20nm MgO nanoparticles to BMSCs were between 300 and 500 µg/mL under the sequential-seeding method. Figure 2.17 summarizes the critical MgO concentrations and their effects on BMSCs under the sequential-seeding method.

MgO nanoparticles resulted in increase of media pH; intuitively, the pH increase might be a factor contributed to the observed BMSC death at or above 500 µg/mL of MgO. The monitoring of pH change over a 24-hour period showed that the pH increase occurred rapidly within the first 15 min and then decreased (Figure 2.8). The peak pH of media with 200 µg/mL of MgO was 8.57 and the peak pH of media with 1000 µg/mL of MgO was 9.37. The reduction in the pH values at 48 and 72 hours in the sequentially seeded culture (Figure 2.6A) indicated that most of the MgO nanoparticles dissociated in the first 24 hours and thus released more OH-during that initial 24 hours. Previous work from our lab has shown that there was no statistical difference in BMSC density when cultured in DMEM with initial pH values adjusted up to 9.0 [28]. It is possible that pH was a factor contributing to the cell death observed at and above 1000 µg/mL of MgO, considering the peak pH reached 9.37, above 9.0. However, the fact that the BMSC death was observed at 200 µg/mL of MgO in the co-seeded condition but not in the sequentially seeded condition indicated that there might be other reasons for the cytotoxic effects of MgO nanoparticles at these low concentrations of MgO where the peak pH was below 9.0.

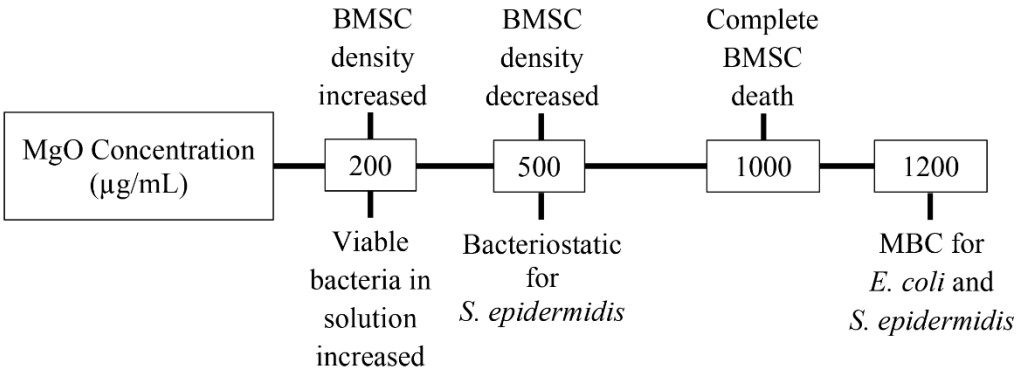

Figure 2.17: Summary diagram of critical MgO concentrations and their effects on BMSCs, *E. coli*, and *S. epidermidis.*

Our results are in agreement with the theoretical dissolution of MgO, which resulted in increase in pH and release of Mg^{2+} ions [20-23]. When exposed to water, MgO absorbs water to form $Mg(OH)_2$ due to its hygroscopic nature [20]. MgO is only slightly soluble in water, with a solubility of 0.086 g/L at 30 °C, which is much greater than the solubility of 0.012 g/L for $Mg(OH)_2$. Despite the low solubility, MgO can dissociate in water by the overall reaction: $MgO + H_2O \rightarrow Mg^{2+} + 2OH^-$ [21]. $Mg(OH)_2$ molecules dissolved in water also dissociate and release Mg^{2+} ions and hydroxide anions (OH^-) [22]. It is important to mention that the actual chemical interactions of MgO with physiological fluids are very complex, due to the presence of calcium, phosphate, carbon dioxide, and other ions and proteins. MgO and $Mg(OH)_2$ also form on the surface of Mg-base metallic alloys when exposed to aqueous physiological solutions, resulting in the release of OH^- and Mg^{2+} ions [23, 24].

It is clear that the cells do have an effect on the Mg^{2+} concentrations. Specifically, the average Mg^{2+} concentrations in media with 2000 μg/mL of MgO were similar for both co-seeding and sequential-seeding conditions (44 mM), which were greater than that for acellular conditions at 24 hours (34 mM). It is speculated that either the BMSCs promoted MgO dissociation or their death led to the release of intracellular Mg^{2+} ions; as a result, Mg^{2+} concentrations increased as compared with the acellular conditions. Intracellular magnesium concentrations range from 5 to 20 mmol/L [32, 33]. The release of right amount of Mg^{2+} ions at the right moment might have contributed to the enhanced proliferation at 200 μg/mL of MgO in the sequentially-seeded culture. Figure 2.18A plots the correlation between Mg^{2+} concentrations and BMSC density at 24 hours for both co-

seeding and sequential-seeding conditions. As Mg^{2+} concentrations increased with increasing MgO nanoparticles, a drop in cell density occurred. However, it is unlikely that Mg^{2+} ions caused BMSC death, since a recent study showed no adverse effects with supplemental Mg^{2+} ions up to 27mM [34]. Another recent study reported that Mg^{2+} ions enhanced osteogenic activity of BMSCs [35]. The release of right amount of Mg^{2+} ions at the right time through MgO dissociation could be beneficial for promoting bone regeneration.

The increase in Mg^{2+} concentrations with increasing MgO correlated with a decrease in Ca^{2+} concentration; this trend was observed in 24 hours of co-seeding, sequential-seeding, and acellular culture conditions. The decrease in Ca^{2+} ions with increasing MgO concentrations might indicate that the release of Mg^{2+} ions promoted the precipitation of Ca^{2+} ions. It has been reported that the incorporation of MgO into bioactive glasses resulted in formation of thicker apatite layers [36], most likely due to the increased precipitation of Ca^{2+} ions that promoted apatite layer formation. If the increase in Mg^{2+} ions caused the precipitation of calcium-containing salts during the first 24 hours, it is possible that the precipitated salts were rinsed away during the media exchange at the end of the 24-hour and 48-hour time points in the sequential-seeding method. This would explain why the Ca^{2+} concentration remained the same as the control for the samples with MgO at 48 and 72 hours. The Ca^{2+} concentrations at the MgO concentrations of 200-2000 μg/mL were different in the sequential-seeded culture versus acellular condition; the presence of BMSCs increased the Ca^{2+} concentrations at low MgO concentrations when they were viable and decreased the Ca^{2+} concentrations at high

MgO concentrations when they were dead. The intracellular concentration of calcium ions is 10,000 times lower than that in the plasma, i.e., <0.0002 mmol/L intracellularly, compared with ~2 mmol/L in the plasma [37]. Thus, the release of intracellular Ca^{2+} is negligible, and it is more likely that higher MgO concentrations promoted Ca^{2+} deposition, which resulted in lower Ca^{2+} concentrations in the media.

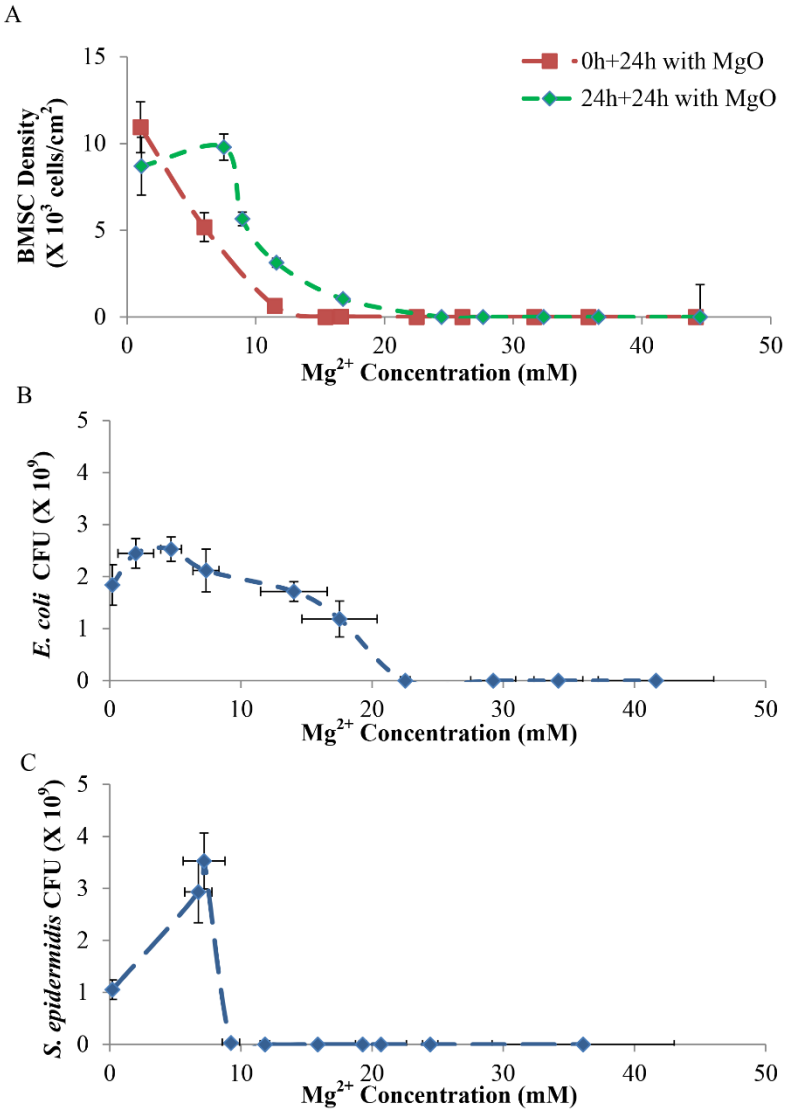

Figure 2.18: Correlation plots relating the post culture Mg^{2+} concentration to (A) BMSC density, (B) *E. coli* CFU and (C) *S. epidermidis* CFU after respective culture with MgO nanoparticles. (A) Data from Figure 2.5 and 2.6B. (B, C) Data from Figure 2.10B and 2.11B, Values are mean ± standard deviation.

In order to take full advantage of the benefits provided by MgO nanoparticles, it may be necessary to use MgO in a composite or as a coating, rather than using it alone. The CCC for 20nm MgO nanoparticles was determined to be between 300 and 500 µg/mL. MgO nanoparticles in the 200 µg/mL dosage in the sequentially seeded culture were found to enhance BMSC proliferation. This may be due to the release of Mg^{2+} ions from MgO dissociation, and Mg^{2+} ions were known to enhance osteogenic activity of BMSCs [35]. The composites incorporating MgO nanoparticles can potentially utilize the benefits of MgO, while mitigating the toxicity. For example, a recent *in vitro* study showed that MgO nanoparticles enhanced bone cell adhesion and proliferation when MgO was incorporated into a polymer to form a composite [38]. *In vivo* studies also indicated that MgO-containing pastes and scaffolds led to enhanced bone formation [5, 6, 39]. Additionally, using MgO nanoparticle as a coating material could also decrease bacterial adhesion, thereby reducing biofilm formation and infection.

2.4.2 Bacteria Viability

Clearly, MgO nanoparticles at the concentrations at and above 1200 µg/mL are bactericidal to both *E. coli* and *S. epidermidis*. That is, MBC of MgO nanoparticles for *S. epidermidis* and *E. coli* are 1200 µg/mL, which is well above the tolerable levels for BMSCs. This suggests that bare MgO nanoparticles may not be optimal to be used directly as an antimicrobial agent in solutions or body fluids. It is important to emphasize that MBC defines the bactericidal effect to the bacteria suspended in the fluid, and MgO nanoparticles reduced the adhesion and cluster size of both *E. coli* and *S. epidermidis* when the concentration was as low as 200µg/mL (Figure 2.9). Bacterial clusters are far

more likely to develop a biofilm than individual bacterial cells, and bacterial colonies in biofilm are more difficult to treat. Reduction in bacterial cluster number and size is beneficial because it decreases the risk of bacterial biofilm formation. Collectively, the right amount of MgO nanoparticles, e.g., 200µg/mL, could provide dual benefits, i.e., promoting BMSC proliferation while reducing bacterial adhesion and infections.

A previous study showed that MIC of MgO nanoparticles for *E.* coli was 500µg/mL based on a microtitre plate-based assay [19]. However, our CFU quantification suggested that there were no statistically significant decrease in *E. coli* viability in broth at 500µg/mL of MgO. This might be due to the difference between the microtitre plate-based assay and CFU quantification from agar plating.

The exact mechanisms for the antimicrobial properties of MgO nanoparticles are not yet confirmed. Since MgO nanoparticles caused increase in pH and Mg^{2+} concentration, we examined whether pH or Mg^{2+} concentration are the main factors contributing to bacterial death. It turns out the increase in pH and Mg^{2+} concentration did not reduce bacterial viability. The pH of LBB and TSB increased more with respect to their controls with increasing MgO concentration, than the pH of the DMEM. This is likely because the buffering effect of LBB and TSB in the bacterial culture environment is not as good as DMEM in the BMSC culture environment. Both *E. coli* and *S. epidermidis* proliferated significantly when cultured in LBB and TSB, respectively, up to a pH of 10. The pH at the end of 24 hours showed that both *E. coli* and *S. epidermidis* could adjust the pH of their environment (Figure 2.16). *E. coli* tended to adjust pH to 8.6 to 8.8 no matter what initial pH was, and *S. epidermidis* adjusted pH to 5.5 when the

initial pH was 7-8, and gradually increased to 8.2 when the initial pH increased to 10. LBB for *E. coli* culture contains no buffering agents. TSB contains dipotassium hydrogen phosphate at a concentration of 14mM as a buffering agent. The pKa of hydrogen phosphate buffer is 7.21. *S. epidermidis* produced acidic waste products that could mediate pH increase induced by MgO dissociation. The ability of these bacteria to adjust their environment makes them resilient to pH effects. The viability of both types of bacteria showed initial increase followed by a sharp decrease with increasing Mg^{2+} concentration from increasing MgO concentration (Figure 2.18 B, C). However, the release of Mg^{2+} from MgO, is unlikely to be the source of antimicrobial properties of MgO nanoparticles, because both *E. coli* and *S. epidermidis* proliferated significantly when cultured with supplemental Mg^{2+} dosage up to 50mM.

When *E. coli* and *S. epidermidis* were cultured with MgO, both LBB and TSB showed an increase in Ca^{2+} concentration over the native amount in each broth. In gram negative bacteria, such as *E. coli*, the polysaccharides that make up most of the biofilms are either neutral or poly-anionic [31]. Presence of calcium and magnesium cations could enhance biofilm formation for such bacteria because these cations could cross link with polymer strands, thus strengthening binding force. However, we found that the increase of calcium did not enhance biofilm formation of *E. coli*. This further showed effectiveness of MgO against bacterial infection. Even though there were more cations present with increasing MgO, the cations did not increase bacterial adhesion or biofilm formation. The SEM images showed fewer adhered bacteria as MgO concentration increased. For gram positive bacteria, including staphylococci, the polysaccharides are

cationic [31]. The presence of cations would have no enhancing effect on the formation of *S. epidermidis* biofilm.

CFU quantification in a prior study showed lower *E. coli* viability when the bacteria were cultured with magnesium-yttrium alloy that had oxide layers on the surface compared to those that lacked initial oxide layers [40], which suggested oxide layers on the surface played an important role on the antimicrobial activity of magnesium and its alloys.

One proposed mechanism for the antimicrobial activities of MgO suggested that the interaction of MgO and bacterial cell wall/membrane caused damage to the cell wall/membrane, leading to leakage of minerals, proteins, and genetic material resulting in cell death [41]. Previous studies also indicated that metal oxide nanoparticles could spontaneously produce reactive oxygen species (ROS) [9, 42, 43]. MgO, in particular, has been shown to enhance lipid peroxidation [19]. It is believed that superoxides, hydrogen peroxide, and/or hydroxyl radicals may be produced from consecutive oxidation-reduction reactions occurring at the MgO surface. Superoxide is also stable under alkaline conditions and has higher diffusion distance with increasing pH [44]. Superoxide from MgO can interact with the carbonyl group in the peptide and cause degradation of proteins [45]. If this were the case, ROS would be responsible for the antimicrobial properties of MgO. A recent study, however, suggested that MgO exhibited antimicrobial activity against *E. coli*, in the absence of ROS, through membrane damage [46]. According to Leung *et al*., there was no expression of ROS-related proteins, which indicated ROS production was not part of the bactericidal properties of MgO. This study

measured the protein levels in the first 20 minutes of exposure to MgO. Longer studies in the absence of ROS may be necessary to confirm this mechanism. We believe direct contact with MgO nanoparticles was important for bactericidal effect; however, further research is necessary to determine the exact mechanisms to take full advantage of MgO nanoparticles for antimicrobial applications.

2.5 Conclusions

This chapter reported the dose-dependent responses of BMSC, *E. coli,* and *S. epidermidis* toward MgO nanoparticles for the first time. The two *in vitro* culture methods used, i.e., co-seeding and sequential-seeding, affected the BMSC response at low concentrations of MgO nanoparticles. MgO nanoparticles at a concentration of 200 μg/mL enhanced BMSC adhesion density and proliferation up to 72 hours *in vitro* when sequentially-seeded. MgO nanoparticle concentrations at or above 500 μg/mL caused near to complete BMSC death independent of the culture methods. The bacterial culture showed that MBC of MgO nanoparticles for *E. coli* and *S. epidermidis* was 1200 μg/mL, and reduced bacterial adhesion was observed at and above 200 μg/mL of MgO nanoparticles. The exact mechanisms for the bactericidal effects of MgO nanoparticles remained elusive, but were most likely due to direct-contact induced cell wall/membrane damage. Collectively, these *in vitro* results suggested that MgO nanoparticles at a concentration of 200 μg/mL provided dual benefits of promoting BMSC proliferation while reducing bacterial adhesion, which should be further studied for potential medical applications. The use of free MgO nanoparticles yielded detrimental effects to BMSCs in

concentrations above 300μg/mL. We recommend further study into MgO nanoparticles as a coating material or as a part of a composite.

2.6 Acknowledgement

The authors thank the support from the U.S. National Science Foundation (NSF award CBET 1512764), the Burroughs Wellcome Fund (1011235), the Hellman Faculty Fellowship (HL), NIH SBIR program (6R43DE023287), and the University of California (UC) Regents Faculty Fellowship (HL). The authors appreciate the Central Facility for Advanced Microscopy and Microanalysis (CFAMM) for the use of SEM FEI XL30 at the University of California at Riverside. The authors also thank the undergraduate student researchers (Vannessa Guzman, Hakikat Gill, and Jimmy Tran) for their assistance with pH measurements and ImageJ analysis.

Any opinions, findings, and conclusions or recommendations expressed in this material are those of the author(s) and do not necessarily reflect the views of the National Science Foundation.

2.7 References

1. Fielding, G.A., W. Smoot, and S. Bose, *Effects of SiO2, SrO, MgO, and ZnO dopants in tricalcium phosphates on osteoblastic Runx2 expression.* J Biomed Mater Res A, 2014. **102**(7): p. 2417-26.
2. Kum, C.H., et al., *A poly(lactide) stereocomplex structure with modified magnesium oxide and its effects in enhancing the mechanical properties and suppressing inflammation.* Small, 2014. **10**(18): p. 3783-94.
3. Patel, M.K., et al., *Biocompatible nanostructured magnesium oxide-chitosan platform for genosensing application.* Biosens Bioelectron, 2013. **45**: p. 181-8.
4. Pourdanesh, F., et al., *In vitro and in vivo evaluation of a new nanocomposite, containing high density polyethylene, tricalcium phosphate, hydroxyapatite, and magnesium oxide nanoparticles.* Mater Sci Eng C Mater Biol Appl, 2014. **40**: p. 382-8.
5. Tarafder, S., et al., *SrO- and MgO-doped microwave sintered 3D printed tricalcium phosphate scaffolds: Mechanical properties and in vivo osteogenesis in a rabbit model.* J Biomed Mater Res B Appl Biomater, 2014.
6. Nygren, H., et al., *Increase of Compact Bone Thickness in Rat Tibia after Implanting MgO into the Bone Marrow Cavity.* J Funct Biomater, 2014. **5**(3): p. 158-66.
7. Carpenter, T.O., et al., *A randomized controlled study of effects of dietary magnesium oxide supplementation on bone mineral content in healthy girls.* J Clin Endocrinol Metab, 2006. **91**(12): p. 4866-72.
8. Khandaker, M., Y. Li, and T. Morris, *Micro and nano MgO particles for the improvement of fracture toughness of bone-cement interfaces.* J Biomech, 2013. **46**(5): p. 1035-9.
9. Sawai, J., *Antibacterial characteristics of magnesium oxide powder.* World Journal of Microbiology and Biotechnology, 2000. **16**: p. 187-194.
10. Sawai, J., *Quantitative evaluation of antibacterial activities of metallic oxide powders (ZnO, MgO and CaO) by conductimetric assay.* J Microbiol Methods, 2003. **54**(2): p. 177-82.
11. Webster, T.J. and H. Liu, *Nanomedicine for implants: A review of studies and necessary experimental tools.* Biomaterials, 2007. **28**(2): p. 354-369.
12. Liao, J., et al., *Investigating the role of hematopoietic stem and progenitor cells in regulating the osteogenic differentiation of mesenchymal stem cells in vitro.* J Orthop Res, 2011. **29**(10): p. 1544-53.
13. Grayson, W.L., et al., *Stromal cells and stem cells in clinical bone regeneration.* Nat Rev Endocrinol, 2015. **11**(3): p. 140-150.
14. Sales, V.L., et al., *Endothelial progenitor and mesenchymal stem cell-derived cells persist in tissue-engineered patch in vivo: application of green and red fluorescent protein-expressing retroviral vector.* Tissue Eng, 2007. **13**(3): p. 525-35.
15. Lee, J.Y., et al., *Directing hepatic differentiation of embryonic stem cells with protein microarray-based co-cultures.* Integr Biol (Camb), 2009. **1**(7): p. 460-8.

16. Honda, M.J., et al., *The sequential seeding of epithelial and mesenchymal cells for tissue-engineered tooth regeneration.* Biomaterials, 2007. **28**(4): p. 680-9.
17. Cremet, L., et al., *Orthopaedic-implant infections by Escherichia coli: molecular and phenotypic analysis of the causative strains.* J Infect, 2012. **64**(2): p. 169-75.
18. Lew, D.P. and F.A. Waldvogel, *Osteomyelitis.* N Engl J Med, 1997. **336**(14): p. 999-1007.
19. Krishnamoorthy, K., *Antibacterial activity of MgO nanoparticles based on lipid peroxidation by oxygen vacancy.* Journal of Nanoparticle Research, 2012. **14**(9).
20. Yanagisawa, Y., *Interaction of Oxygen Molecules with Surface Centers of UV-Irradiated MgO.* Journal of Physics Society Japan, 1981. **50**(1): p. 209-216.
21. Ito, T., et al., *Oxygen Species Adsorbed on Ultraviolet-irradiated Magnesium Oxide.* Journal of the Chemical Society, Faraday Transactions 1, 1985. **81**: p. 10.
22. Iskandar, M.E., A. Aslani, and H. Liu, *The effects of nanostructured hydroxyapatite coating on the biodegradation and cytocompatibility of magnesium implants.* J Biomed Mater Res A, 2013. **101**(8): p. 2340-54.
23. Cipriano, A.F., et al., *Investigation of magnesium-zinc-calcium alloys and bone marrow derived mesenchymal stem cell response in direct culture.* Acta Biomaterialia, 2015. **12**: p. 298-321.
24. Simchi, A., et al., *Recent progress in inorganic and composite coatings with bactericidal capability for orthopaedic applications.* Nanomedicine, 2011. **7**(1): p. 22-39.
25. US Nanomaterials Research, Inc. Magnesium Oxide (MgO) Nanopowder, http://www.us-nano.com/inc/sdetail/242 28 September 2015
26. Donlan, R.M., *Biofilms: microbial life on surfaces.* Emerg Infect Dis, 2002. **8**(9): p. 881-90.
27. Mejias, J.A., *The kinetics and mechanism of MgO dissolution.* Chemical Physics Letters, 1999. **314**: p. 558-563.
28. Fruhwirth, O., *Dissolution and Hydration Kinetics of MgO.* Surface Technology, 1985. **24**: p. 301-317.
29. Zheng, Y., *Biodegradable Metals.* Materials Science and Engineering: R, 2014. **77**.
30. Mueller, W.D., et al., *Degradation of magnesium and its alloys: dependence on the composition of the synthetic biological media.* J Biomed Mater Res A, 2009. **90**(2): p. 487-95.
31. Liu, H., *The effects of surface and biomolecules on magnesium degradation and mesenchymal stem cell adhesion.* J Biomed Mater Res A, 2011. **99**(2): p. 249-60.
32. Jahnen-Dechent, W. and M. Ketteler, *Magnesium basics.* Clin Kidney J, 2012. **5**(Suppl 1): p. i3-i14.
33. Rude, R., *Magnesium disorders,* in *Fluids and electrolytes*, T.R. Kokko J, Editor. 1996, Saunders Company: Philadelphia, PA. p. 421-445.
34. Cipriano, A., *Investigation of magnesium–zinc–calcium alloys and bone marrow derived mesenchymal stem cell response in direct culture.* Acta Biomateriala, 2014.

35. Yoshizawa, S., et al., *Magnesium ion stimulation of bone marrow stromal cells enhances osteogenic activity, simulating the effect of magnesium alloy degradation.* Acta Biomaterialia, 2014. **10**(6): p. 2834-42.
36. Vallet-Regi, M., A.J. Salinas, J. Roman, M. Gil, *Effect of magnesium content on the in vitro bioactivity of CaO-MgO-SiO_2-P_2O_5 sol-gel glasses.* Journal of Materials Chemistry, 1998. **9**: p. 4.
37. Goldstein, D.A., *Serum Calcium*, in *Clinical Methods: The History, Physical, and Laboratory Examinations*, H.W. Walker HK, Hurst JW, Editor. 1990, Butterworths: Boston.
38. Hickey, D.J., et al., *Adding MgO nanoparticles to hydroxyapatite-PLLA nanocomposites for improved bone tissue engineering applications.* Acta Biomaterialia, 2015. **14**: p. 175-84.
39. Tarafder, S., et al., *Microwave-sintered 3D printed tricalcium phosphate scaffolds for bone tissue engineering.* J Tissue Eng Regen Med, 2013. **7**(8): p. 631-41.
40. Lock, J.Y., et al., *Degradation and antibacterial properties of magnesium alloys in artificial urine for potential resorbable ureteral stent applications.* J Biomed Mater Res A, 2014. **102**(3): p. 781-92.
41. Montero, M., et al., *Escherichia coli glycogen metabolism is controlled by the PhoP-PhoQ regulatory system at submillimolar environmental Mg2+ concentrations, and is highly interconnected with a wide variety of cellular processes.* Biochem J, 2009. **424**(1): p. 129-41.
42. Dong, C., *Antibacterial study of Mg(OH)2 nanoplatelets.* Materials Research Bulletin, 2011. **46**: p. 576-582.
43. Xia, T., et al., *Comparison of the abilities of ambient and manufactured nanoparticles to induce cellular toxicity according to an oxidative stress paradigm.* Nano Lett, 2006. **6**(8): p. 1794-807.
44. Yamamoto, O., *Change in antibacterials characteristics with doping amount of ZnO in MgO-ZnO solid solution.* Nano Letters, 2000. **6**(8): p. 1794-17807.
45. Al-Hazmi, F., *A new large-scale synthesis of magnesium oxide nanowires: Structural and antibacterial properties.* Superlattices and Microstructures, 2012. **52**: p. 200-209.
46. Leung, Y.H., et al., *Mechanisms of antibacterial activity of MgO: non-ROS mediated toxicity of MgO nanoparticles towards Escherichia coli.* Small, 2014. **10**(6): p. 1171-83.

Chapter 3: Dissociation of MgO and $Mg(OH)_2$ in Physiologically Relevant Solutions

3.1 Introduction

Magnesium oxide (MgO) and magnesium hydroxide [$Mg(OH)_2$] are widely used compounds in different industries, and their properties are increasingly attractive for biomedical applications [1-4]. MgO is very stable at high temperatures in oxidizing atmospheres and reducing atmospheres up to 2300 °C and 1700 °C, respectively[5]. Its stability at these conditions led to the general statement in reference texts that MgO is generally 'stable' and 'relatively inert' [6, 7]. However, the conditions under which MgO is 'stable' and 'relatively inert' were not clearly discussed. It is also well accepted that MgO is hygroscopic and hydrates at room temperature to produce $Mg(OH)_2$, which is why MgO is rarely found in natural mineral deposits. The hygroscopic nature of MgO and its transition to $Mg(OH)_2$ are often mentioned alongside a statement that MgO is generally stable [8-10]. Additionally, $Mg(OH)_2$ is conventionally known to be insoluble in water and stable at temperatures up to 300 °C [5].

Recently, MgO and $Mg(OH)_2$ have become more popular for biomedical applications due to their bioactivity. Magnesium oxide and magnesium hydroxide have long been used as dietary supplements to improve bone density[11, 12]. In physiological conditions, both magnesium oxide and magnesium hydroxide release magnesium ions, which have been shown to be osteoconductive, *in vitro*[13, 14]. Additionally, it has been shown that MgO nanoparticles significantly increase bone marrow derived mesenchymal stem cell (BMSC) adhesion and proliferation in low concentrations, e.g. at 200 μg/mL [15]. MgO nanoparticles have also been shown to exhibit antimicrobial properties, which

are beneficial for reducing the risk of infection associated with any implantable material [15-17]. MgO is hygroscopic and will adsorb water and react to form $Mg(OH)_2$ [9, 10, 18]. It has been widely accepted that MgO is stable and is a model for crystalline cubic structure, with a high degree of perfection. However nano-sized MgO in simulated biological environments dissociates and can be detrimental to mesenchymal stem cells, particularly in concentrations exceeding 300 µg/mL [15]. Additionally, MgO and $Mg(OH)_2$ are both formed during passivation and degradation of metallic magnesium, which is a biodegradable metal of interest for orthopedic applications. As such, it is important to fully understand the dissociation of MgO and $Mg(OH)_2$ in physiologically-relevant solutions.

This article reports the effect of physiologically relevant media, Dulbecco's Modified Eagle's Media (DMEM), simulated body fluid (SBF), and its sub-components (mainly Cl^-), on MgO and $Mg(OH)_2$ nanoparticles. Observing the dissociation of MgO and $Mg(OH)_2$ in this media, with and without FBS and P/S supplements, could provide insight into the degradation of magnesium. SBF is a solution designed to mimic biological fluid, having ion concentrations almost equivalent to those found in human blood plasma [19]. To evaluate the dissociation of MgO and $Mg(OH)_2$ in biological conditions, SBF was used. One of the buffers in SBF is 4-(2-hydroxyethyl)-1-piperazineethanesulfonic acid (HEPES). HEPES buffer is a synthetic biological buffer that is effective in regulating pH between 6.8 and 8.2. HEPES regulates the local pH at the surface of magnesium leading to increased degradation rate [20, 21]. The increased corrosion caused by HEPES activity is partly due to the cracks formed in the particle

boundaries on the surface layer which provide a pathway for HEPES to continuously degrade the internal portions of magnesium [20]. Due to the specific activity of HEPES, a solution of HEPES in water was included as well, to better elucidate which component of SBF may have the greatest effect on MgO and $Mg(OH)_2$ dissociation. As previously mentioned, studies have suggested that Cl^- is a key component in the corrosion of Mg metal by interacting with $Mg(OH)_2$ at the surface of the metal. To evaluate the suggested effects that Cl^- has on MgO and $Mg(OH)_2$, two different Cl^- sources, $MgCl_2$ and NaCl, were included. The use of $MgCl_2$ allowed for the delivery of Cl^- without the addition of another component, as Mg^{2+} is released from MgO and $Mg(OH)_2$. NaCl was used as a comparison to evaluate if the cations, Mg^{2+} and Na^+, showed any difference in dissociation of our nanoparticles. The concentration of the chloride salts was 103 mM, the same concentration of Cl^- found in SBF. An additional concentration at 200 mM of $MgCl_2$ was used to further explore the possible effect of chloride on dissociation of MgO and $Mg(OH)_2$. NaCl would provide another excellent source of Cl^- based on previous studies that found that intermediate species of MgO were formed in solutions with NaCl [22, 23].

Until roughly the past decade, MgO and $Mg(OH)_2$ have been largely relegated to industrial applications[5, 8, 22]. As such, the vast majority of literature on these compounds focuses on their activity and applications in non-biological environments. It is necessary to re-build a library of the fundamental properties of MgO and $Mg(OH)_2$ in physiological environments to fully understand and explore the potential of these

compounds in biomedical applications. Herein, we investigated the effects of DMEM, SBF and chloride on dissociation of MgO and $Mg(OH)_2$ nanoparticles.

3.2 Materials and Methods

3.2.1 Preparation of MgO and $Mg(OH)_2$ Nanoparticles

MgO nanoparticles were procured from US Research Nanomaterials Inc. (US3310, 99+% purity, 20nm diameter). In order to mimic the in vivo conditions under which the nanoparticles are used and make the results comparable to other in vitro studies, MgO nanoparticles were sterilized in a glass container via heating at 200°C in an oven for one hour prior to immersion in physiologically relevant solutions.

MgO cannot be sterilized through UV irradiation because the UV affects the surface chemistry of the MgO particles by causing adsorption of O_2 and production of superoxide ions [24, 25]. MgO nanoparticles were sterilized prior to characterization so that the particles would be in the same condition during characterization as they were prior to use in *in vitro* experiments.

The MgO nanoparticles were weighed in autoclaved and labeled microcentrifuge tubes. For each solution, the MgO weights are organized into triplets of 0.6, 3.0, and 6.0 mg. With 3 mL of total solution added to the MgO nanoparticles, the resulted concentrations were 200, 1000, and 2000 μg/mL.

The $Mg(OH)_2$ nanoparticles (US3320, 99+% purity, 20nm diameter, US Nanomaterials, Inc.) were prepared similarly to the MgO nanoparticles, and were sterilized in a glass jar and heated in the oven at 100°C for 1 hour. This temperature was selected to be much lower than the dehydration temperature of $Mg(OH)_2$ at 300 °C to

ensure that transition to MgO would not occur. These particles were organized by weight into autoclaved and labeled microcentrifuge tubes. For each solution, the weights were organized into triplets of 0.6, 3.0, 6.0, and 9.0 mg. With 3 mL of total solution added to the $Mg(OH)_2$ nanoparticles, the concentrations were at 200, 1000, 2000, and 3000 μg/mL. The concentration of 3000 μg/mL had a similar molar concentration to that of MgO at 2000 μg/mL. By using 3000 μg/mL of $Mg(OH)_2$ we obtained 51.44 μmol/mL of Mg^{2+} which is comparable to that of 2000 μg/mL of MgO which yielded 49.62 μmol/mL of Mg^{2+}. This was included to make results between MgO and $Mg(OH)_2$ comparable by both mass and molar concentration.

3.2.2 Preparation of Biologically Relevant Solutions

3.2.2a Preparation of $MgCl_2$ Solution

Previous studies suggested that Cl^- is a key component in the corrosion of metallic Mg by interacting with $Mg(OH)_2$ formed at the surface of the metal during degradation [9]. To evaluate the effects of Cl^- on MgO and $Mg(OH)_2$ without adding any additional components, $MgCl_2$ was used as the Cl^- source at two concentrations of 103 and 200 mM Cl^- in deionized water (DI, QGARD00D2, Millipore). The concentration of 103mM was selected because this is the same concentration of chloride found in SBF. Since Cl^- has been indicated as impacting Mg degradation, we also wanted to evaluate the effects of excess of Cl^-, hence the concentration of 200 mM was included. Both solutions were prepared the day prior to use in the experiment. To obtain an initial stock solution, 3g of $MgCl_2 \cdot 6H_2O$ were added to a glass bottle of 100 mL of DI, which was stirred with a stir bar to dissolve any salt clumps. The $MgCl_2$ solution was sterilized by filtration through a

0.45μm vacuum filter (Nalgene PES Filter 168, Thermo Scientific) in a laminar flow hood. The Mg^{2+} concentration was evaluated through induced coupled plasma-optical emission spectrometry (ICP-OES, Optima 8000, Perkin Elmer). The Mg^{2+} concentration was determined to be 135 mM. The expected concentration from 3 g of $MgCl_2 \cdot 6H_2O$ in 100 mL of DI was 147.6 mM. This discrepancy could occur if the $MgCl_2 \cdot 6H_2O$ had hydrated further before use. However, this was compensated for by measuring with ICP-OES and making necessary dilutions for the desired concentration. In $MgCl_2$, the ratio of Mg^{2+} to Cl^- is 1:2. Therefore, the resulting Cl^- concentration in the stock solution was 270 mM. Dilutions were made so that resulting Cl^- amount would be 103 and 200 mM for the dissociation study.

3.2.2b Preparation of NaCl

To further investigate the effects that Cl- has on the corrosion of Mg, NaCl was used as an alternative Cl- source because it is one of the key physiological salts and it can serve as a suitable source of Cl^- ions without Mg^{2+} for comparison. Additionally, it is thought that Cl^- ions initiate the dissociation of MgO and $Mg(OH)_2$. A solution of 103 mM of Cl- was prepared in the same manner as that of $MgCl_2$. As previously mentioned, 103 mM is the concentration of Cl^- in SBF, and SBF mimics ionic concentrations of blood plasma.

3.2.2c Preparation of SBF

To evaluate the dissociation of MgO and $Mg(OH)_2$ in a body fluid, revised simulated body fluid (SBF) was used to mimic a human blood serum, via established protocols[26]. In brief, 700 mL of deionized (DI) water was placed in a 1000 mL

polypropylene beaker. Then, 5.377g of NaCl, 0.420 g of $NaHCO_3$, 2.332 g of Na_2CO_3, 0.224 g of KCl, 0.228 g of $K_2HPO_4*3H_2O$, 0.305 g of $MgCl_2*6H_2O$, 11.928 g of 4-(2-hydroxyethyl)-1-piperazineethanesulfonic acid (HEPES, Sigma Aldrich) in 100mL of DI water, 0.277 g of $CaCl_2$, and 0.071 g of Na_2SO_4, were added sequentially, making sure that each component was fully dissolved before added the next. The solution was then titrated with 1 M NaOH solution, with approximately 0.8mL to bring the pH to 7.4. The pH was confirmed with a pre-calibrated pH meter (Symphony SB70P, VWR). If pH was not at the target of 7.4, it was adjusted with 1M NaOH to increase it or HEPES to decrease it. The solution was then transferred to a 1000 mL volumetric polypropylene flask and the total volume was brought up to 1000 mL by the addition of DI water. In a sterile laminar flow hood, the SBF solution was sterilized via vacuum filtration (Nalgene PES Filter 168, Thermo Scientific).

3.2.2d Preparation of HEPES

HEPES is a zwitterionic buffering agent that can maintain a biological pH between 6.8 and 8.2 and is not dependent on CO_2 concentration. A HEPES solution in DI water was made to match the same concentration of HEPES found in SBF. Specifically, to evaluate the effects of HEPES on MgO and $Mg(OH)_2$, 1.193 g of HEPES was added to 100 mL of DI water to achieve this concentration of 50 mM. Then, the solution was sterilized using the same vacuum filtration (Nalgene PES Filter 168, Thermo Scientific) in a sterile laminar flow hood.

3.2.2e Preparation of Complete and un-supplemented DMEM

Dulbecco's Modified Eagle's Medium (DMEM, Corning) is a common media for *in vitro* studies that utilize adherent cell lines. It is common to supplement DMEM with 10% fetal bovine serum (FBS, Hyclone) and 1% penicillin/streptomycin (P/S, Hyclone), which is known as complete DMEM (cDMEM). To understand the effects of DMEM, as well as the supplemental proteins from FBS and P/S, we evaluated cDMEM as well as un-supplemented DMEM, which will herein be referred to as 'DMEM'. The purchased solutions were mixed in a laminar flow hood to maintain sterility.

3.2.3 Dissociation of MgO and $Mg(OH)_2$ Nanoparticles within Solution

3.2.3a Preparation of MgO and $Mg(OH)_2$ Nanoparticle Incubation

All solutions and nanoparticles were handled in a biosafety II laminar flow hood to maintain sterility and to keep consistency with cell culture practices. Nanoparticles at 0 mg, 0.6 mg, 3 mg, 6 mg, and 9 mg (for $Mg(OH)_2$ only) were introduced into wells of a 12-well polystyrene plate (Corning, Falcon® 351143) with 3 mL of solution to achieve concentrations of 0 μg/mL, 200 μg/mL, 1000 μg/mL, 2000 μg/mL, and 3000 μg/mL.

To transfer the particles, 1 mL of each solution was added to the micro-centrifuge tubes with the measured MgO or $Mg(OH)_2$ particles and thoroughly suspended through pipetting. The solution/MgO particle mixture was transferred to the assigned wells. Then, an additional 2 mL of respective solution was added resulting in a total volume of 3 mL for each well.

The polystyrene plates with nanoparticles and solutions were placed in an incubator (MCO-19AIC, Sanyo Scientific), at standard cell culture conditions, 37°C, 5%

CO_2 for 24 hours to allow nanoparticles to dissociate in conditions that closely mimic a physiological environment.

3.2.3b Post-Incubation Processing

After 24 hours, the plates were removed from the incubator. Solution and remaining particles were collected in 15 mL conical tubes. Each tube was then centrifuged at 3000 rpm for 2 min to collect the particles as a pellet. The solutions from the tubes were transferred into new 15 mL conical tubes, without disturbing the pellet. To rinse the particles, the pellet was suspended in 100% ethanol and centrifuged at 3000rpm for 1 minute. The ethanol was then aspirated out and new 100% ethanol was added for storage of the particles prior to further analysis.

3.2.4 Analysis of Solutions after MgO and $Mg(OH)_2$ Dissociation

3.2.4a Measuring pH

The pH of each solution was measured immediately after separation from the particles, to minimize the changes due to temperature and atmospheric CO_2, using a benchtop pH meter (Symphony SB70P, VWR).

3.2.4b ICP-OES Measurements

Each solution was diluted 1:200 in DI water to prepare for analysis via induced-coupled plasma optical emission spectrometry (ICP-OES, Optima 8000) in order to measure Mg^{2+} concentration. The Mg^{2+} concentration of the solutions without nanoparticles was used to determine the baseline concentration. This concentration was subtracted from Mg^{2+} concentrations at 200-2000 μg/mL (or 3000 μg/mL for $Mg(OH)_2$) and reported values are of Mg^{2+} released from MgO and $Mg(OH)_2$, respectively.

3.2.5 Characterization of MgO and $Mg(OH)_2$ Particles post-incubation

3.2.5a SEM and EDS Analysis

After culture, the collected particles from the 2000 µg/mL concentration of MgO and the 3000 µg/mL concentration of Mg(OH)2 for each solution was mounted on a pin mount and coated with platinum and palladium (Pt/Pd) using a sputter-coater (108 Auto, Cressington) for SEM and EDS analysis. Most samples were imaged using a secondary electron detector with a spot size of 3, a working distance of 10 mm, at an accelerating voltage of 30 kV and a magnification of 10,000x. However, due to the presence of proteins which will burn at 30 kV, MgO and Mg(OH)2 in the cDMEM solution were imaged at an accelerating voltage of 5 kV.

3.2.5b Preparation for X-Ray Diffraction Analysis

As previously described, the particles left over from the 24-hour incubation were stored in 100% ethanol. The particles from the highest concentration samples (2000 µg/mL for MgO and 3000 µg/mL were transferred in 100% ethanol to a zero-diffraction silicon wafer (SiZero24D10C1, MTI). The ethanol evaporated at room temperature leaving the particles, which were then evaluated using X-Ray diffraction (XRD, Empyrean, PANalytical). The XRD spectrums for MgO and $Mg(OH)_2$ were obtained using Cu Kα radiation (45 kV, 40 mA) at a step size of 0.006^o and dwelling time of 50 seconds using a PIXcel 1D detector (PANalytical). Phase identification was performed using the HighScore software (PANalytical).

3.2.6 Statistical Analysis

All experiments were run in triplicate. All data sets were analyzed using one-way analysis of variance (ANOVA) followed by the Tukey highest significant difference post hoc test. Statistical significance was considered at $p < 0.05$.

3.3 Results

3.3.1 Morphological change in remaining MgO and $Mg(OH)_2$ particles

Exposure to each physiological media caused morphological change of the remaining particles (Figure 3.1). Prior to exposure to physiological solutions, both MgO and $Mg(OH)_2$ maintained individual spherical particles in the nanometer size range. Exposure to cDMEM resulted in large amorphous micro-agglomerates in both MgO and $Mg(OH)_2$, which is likely evidence of proteins from the media. Exposure to DMEM for both MgO and $Mg(OH)_2$ showed similar evidence of amorphous proteins. However, the remaining particles for MgO in DMEM also shows flake structures reminiscent of interlaced spiral crystal growth. Similar structures were also seen in MgO in SBF. However, these structures were absent from $Mg(OH)_2$, which showed particle agglomeration primarily. MgO and $Mg(OH)_2$ in HEPES solution showed spherical flaked structures and flaked layered structures, respectively. In NaCl, MgO and $Mg(OH)_2$ showed particle agglomeration with some sheet structures but without larger organized patterns. In both (103 mM and 200 mM) $MgCl_2$ solutions, MgO showed interlaced flaked, flower-like, structures, while $Mg(OH)_2$ showed agglomerated needle-like structures. These same structures present in the $MgCl_2$ solutions were present in DI water for both MgO and $Mg(OH)_2$.

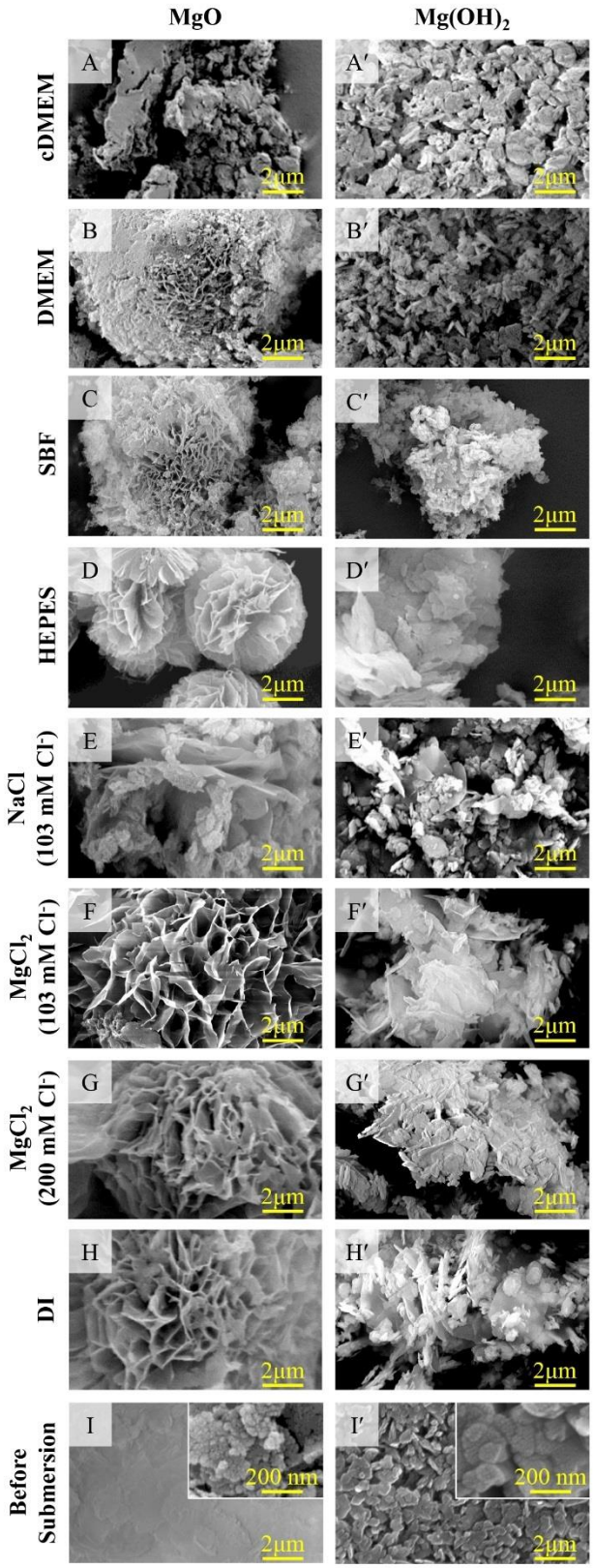

Figure 3.1: SEM images of (A-H) MgO and (A′-H′) $Mg(OH)_2$ nanoparticles before and after immersion in physiologically relevant solutions for 24 hours. SEM images were taken at an original magnification of 10,000x. For inset on H- H′, the original magnification is 150,000x and the Scale bar is 2 µm.

A

Atomic % MgO								
Element	cDMEM	DMEM	SBF	HEPES	NaCl (103 mM Cl^-)	$MgCl_2$ (103 mM Cl^-)	$MgCl_2$ (200 mM Cl^-)	DI
Mg	8.58	23.32	9.66	8.37	36.55	34.59	24.2	34.18
O	15.19	47.99	31.76	27.43	62.21	64.52	47.81	65.82
C	70.14	27.39	54.74	63.85	0	0	27.07	0
P	2.98	0	2.24	0	0	0	0	0
S	0.22	0	0	0.35	0	0	0	0
Cl	0	1.18	0	0	0.51	0.90	0.92	0
Na	0.73	0.13	0.30	0	0.74	0	0	0
Ca	2.16	0	1.31	0	0	0	0	0

B

Atomic % $Mg(OH)_2$								
Element	cDMEM	DMEM	SBF	HEPES	NaCl (103 mM Cl^-)	$MgCl_2$ (103 mM Cl^-)	$MgCl_2$ (200 mM Cl^-)	DI
Mg	77.85	20.38	3.36	4.56	37.22	38.58	41.43	40.36
O	15.98	42.25	13.17	20.37	62.13	61.35	57.87	59.64
C	4.58	34.01	80.72	75.06	0	0	0	0
P	0	1.69	1.89	0	0	0	0	0
S	0	0.17	0	0	0	0	0	0
Cl	0	0.08	0	0	0.20	0.07	0.16	0
Na	1.63	0.49	0.07	0	0.45	0	0	0
Ca	0	0.93	0.38	0	0	0	0	0

Table 3.1: EDS analysis of (A) MgO and (B) $Mg(OH)_2$ after submersion in physiologically relevant solutions, corresponding with SEM images in Figure 3.1.

3.3.2 Elemental and Crystalline phase change in MgO and $Mg(OH)_2$

EDS analysis was used to obtain elemental information on the remaining particles in order to inform XRD analysis (Table 3.1). Presence of Mg, O, C, P, S, Na, and Ca, was observed for the MgO in cDMEM condition. However, the atomic percent for MgO in cDMEM was only 8.58%. For $Mg(OH)_2$, cDMEM resulted in presence of Mg, O, C, and Na, where 77.85% of the atoms were Mg. For MgO in DMEM, Mg, O, C, P, Cl, and Na were observed with 23.32% Mg. For $Mg(OH)_2$ in DMEM, Mg, O, C, P, S, Cl, Na, and Ca were observed with 20.38% Mg. For both MgO and $Mg(OH)_2$ in SBF, Mg, O, C, P, Na, and Ca were observed with 9.66% and 3.36% Mg, respectively. In HEPES solution, MgO yielded residual particles with Mg, O, C, and S, while $Mg(OH)_2$ yielded residual particles

with Mg, O, and C, present. In each chloride solution, the elements from the salts were present along with Mg and O for MgO and $Mg(OH)_2$, as expected.

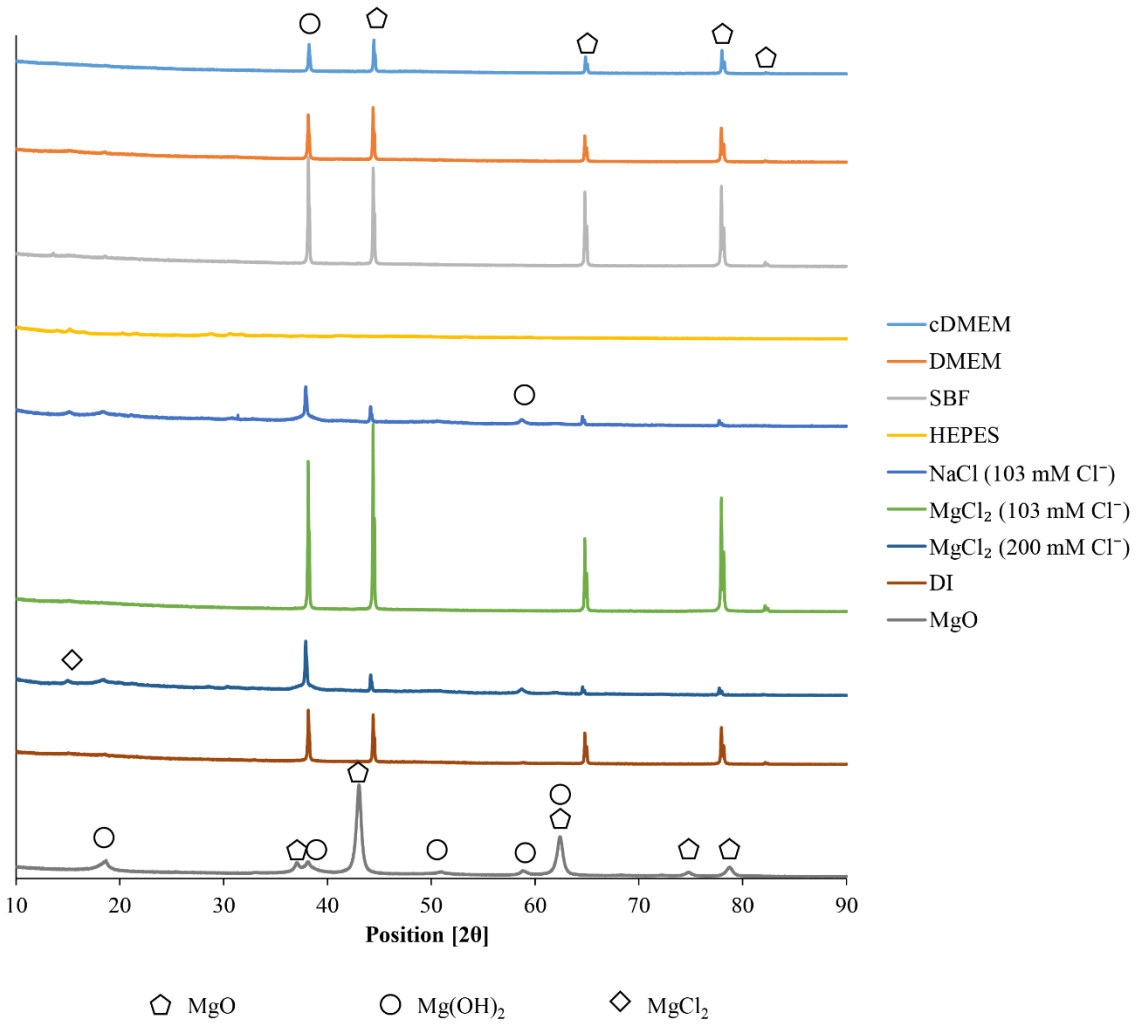

Figure 3.2: XRD analysis of MgO after submersion in physiologically relevant solutions.

XRD revealed that for each solution with MgO, the characteristic peaks of MgO shifted from 42° and 62° to 44° and 64°, respectively, indicating crystal change due to hydration (Figure 3.2). A $Mg(OH)_2$ peak at 38° was also present in all samples, except HEPES solution, after 24 hours of incubation. Additionally, residual $MgCl_2$ was found in

MgO particles exposed to $MgCl_2$ solution with 200 mM Cl^-. The residual MgO particles in HEPES solution resulted in no detectable peaks.

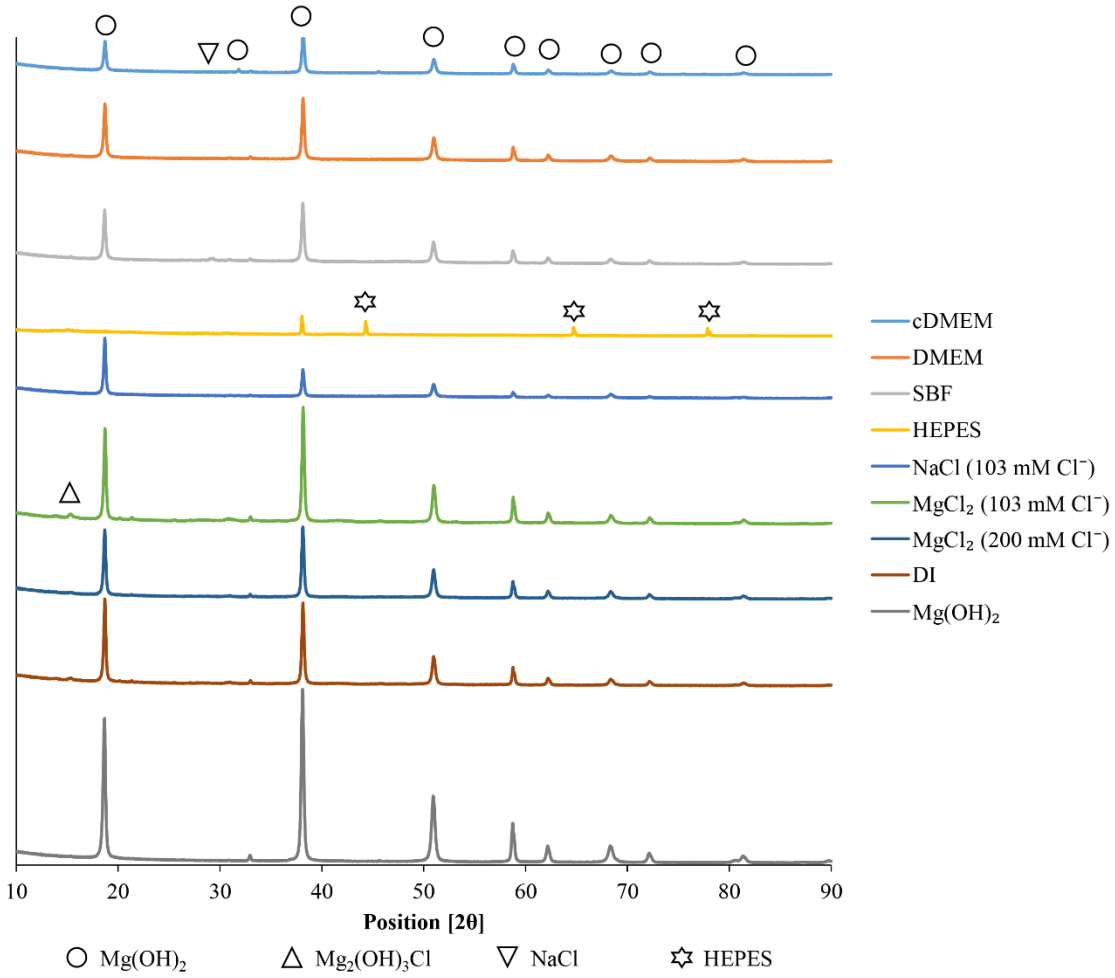

Figure 3.3: XRD analysis of $Mg(OH)_2$ after submersion in physiologically relevant solutions.

After 24 hours of exposure to physiological solutions, the remaining particles from $Mg(OH)_2$ samples still exhibited characteristic peaks of $Mg(OH)_2$, with some decrease in intensity in all solutions except HEPES (Figure 3.3). In the HEPES solution, all characteristic peaks for $Mg(OH)_2$ were missing and only small peaks of residual

HEPES were present. In solutions containing only $MgCl_2$, a small peak corresponding with $Mg_2(OH)_3Cl$ was detected.

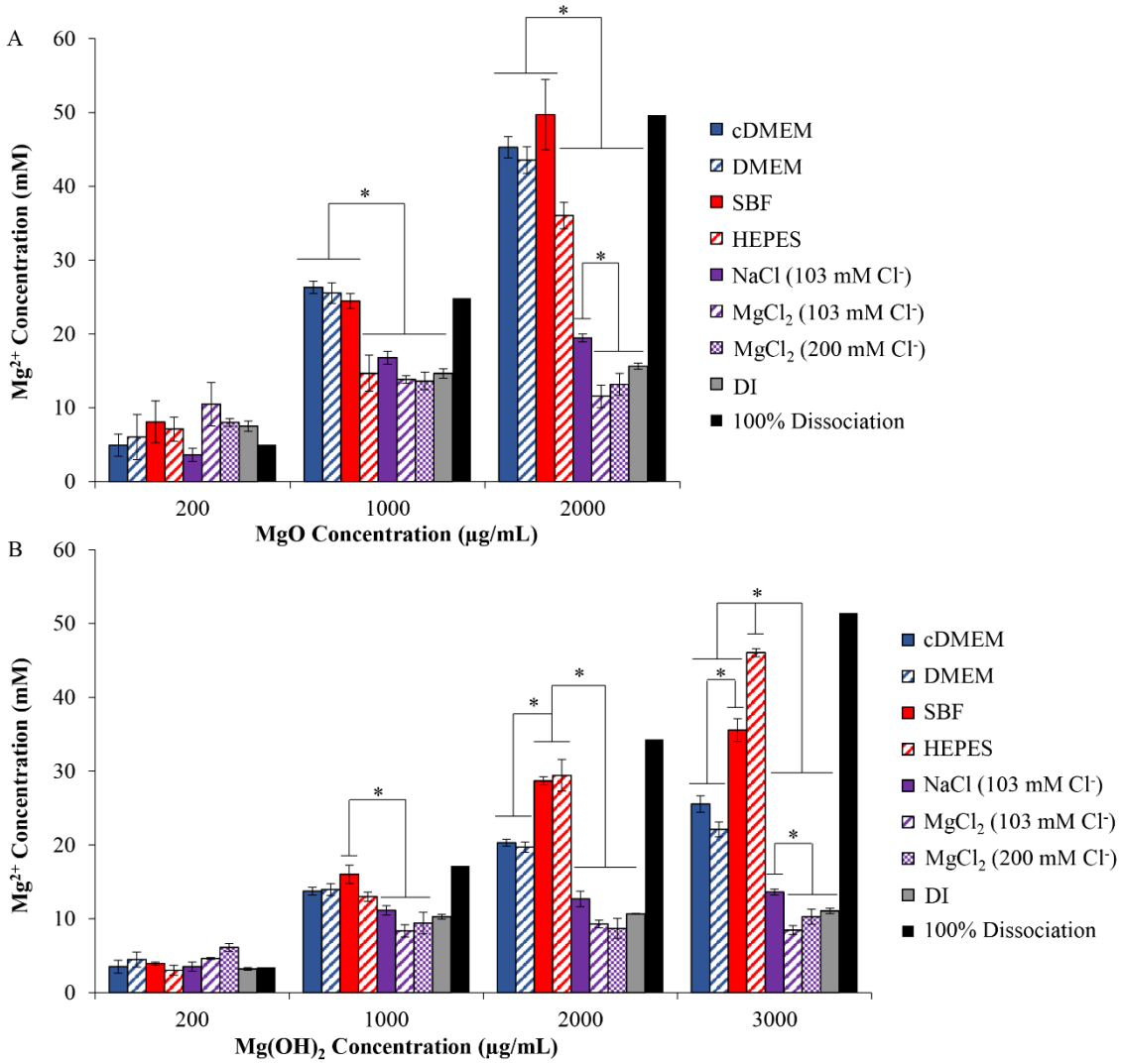

Figure 3.4: Mg^{2+} ion release from (A) MgO and (B) $Mg(OH)_2$ after submersion in physiologically relevant solutions for 24 hours. Values are mean ± standard deviation; n = 3. *p<0.05

3.3.3 Mg^{2+} release and pH change in physiological media

Figure 3.4 shows the change in Mg^{2+} concentration for MgO and $Mg(OH)_2$ after exposure to physiologically relevant solutions. All values were compared with the

expected values that were calculated if 100% dissociation occurred, which is plotted as the black bar in each condition. At 200 μg/mL, both MgO and $Mg(OH)_2$ showed 100% dissociation in all solutions. Solutions that exceeded the 100% dissociation level are attributed to the deviation in initial mass measurement of the nanoparticles. Additionally, MgO at 1000 μg/mL and 2000 μg/mL in cDMEM, DMEM, and SBF showed significantly higher dissociation than in DI water, HEPES buffer, NaCl, and $MgCl_2$ (103 and 200 mM) (Figure 3.4A). $Mg(OH)_2$ at higher concentrations of 1000, 2000, and 3000 μg/mL in SBF and HEPES resulted in higher concentrations of Mg^{2+} ions when compared with the solutions of just chloride salts, indicating higher dissociation (Figure 3.4B). This is more apparent at the concentrations of 2000 and 3000 μg/mL of $Mg(OH)_2$. Additionally, at 1000, 2000, or 3000 μg/mL, none of the nanoparticles reached 100 percent dissociation, i.e., the theoretical value of Mg^{2+} at 100% dissociation. It is clear that the solution with $MgCl_2$ (200 mM Cl^-) showed the least amount of Mg^{2+} release while the HEPES solution showed the highest amount of Mg^{2+} release.

Figure 3.5 shows the pH of the media after 24 hours of exposure to MgO and $Mg(OH)_2$. In the 0 μg/mL condition, for both particles, the pH of cDMEM, DMEM, and SBF was between 7.6 and 8.2. The pH of the HEPES, NaCl, $MgCl_2$ (103 mM), and $MgCl_2$ (200 mM) was between 5 and 5.32. The pH of DI water was approximately 5.6. At 200 μg/mL, the pH of cDMEM and DMEM was approximately 8.2 for both MgO and $Mg(OH)_2$, while the pH of SBF was 7.8 for both nanoparticles. The pH of the HEPES solution was 6.6 and 7 for MgO and $Mg(OH)_2$, respectively. The pH of the NaCl solution was 7.7 for both particles. For both MgO and $Mg(OH)_2$, the pH for $MgCl_2$ at 103 mM

and 200 mM concentrations was approximately 8.4 and 8, respectively. General trends continued when comparing the pH of different solutions as the amount of nanoparticles increased; and generally for each solution, its pH continued to increase with increasing MgO or $Mg(OH)_2$, up to 2000 µg/mL and 3000 µg/mL, respectively.

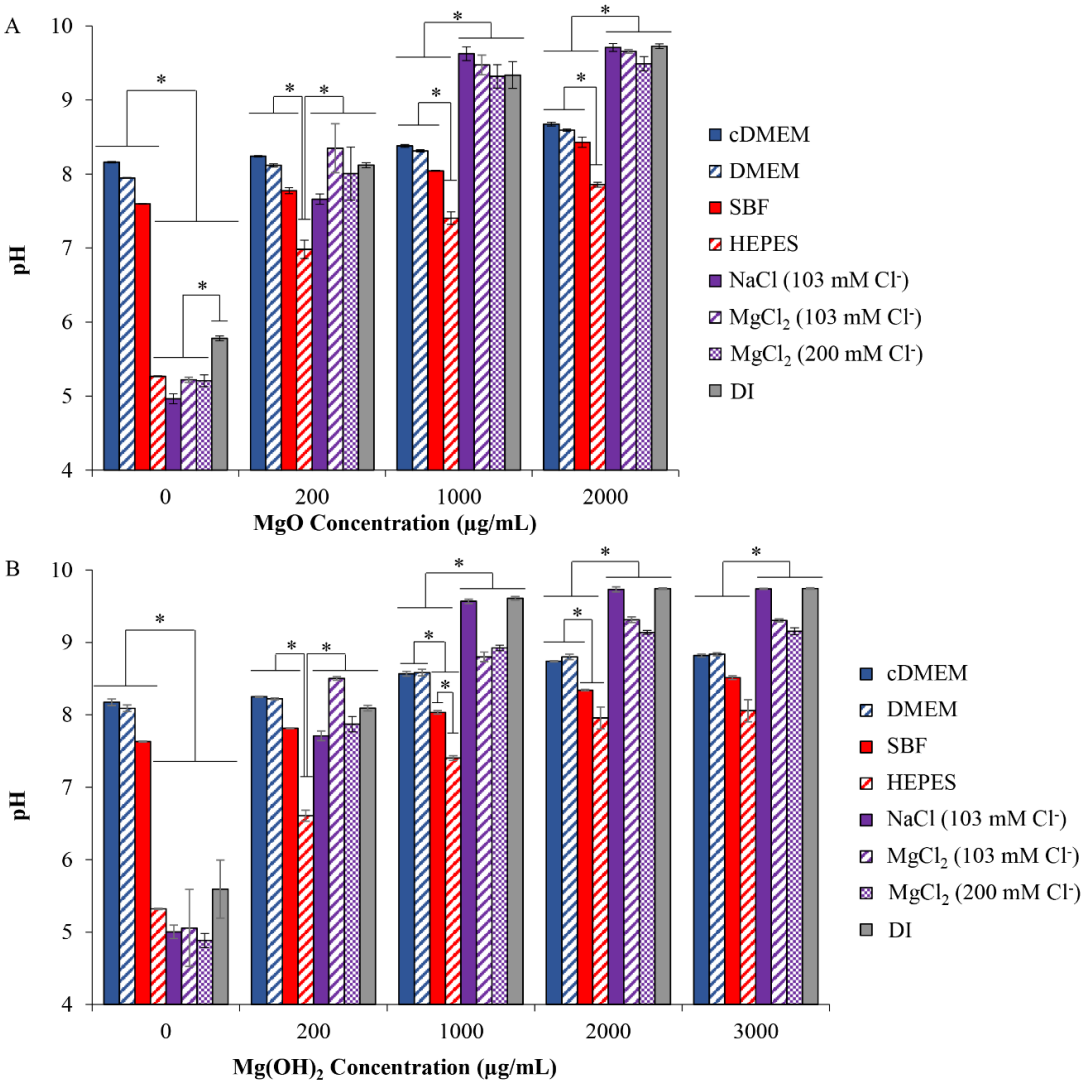

Figure 3.5: Resulting pH after submersion of (A) MgO and (B) $Mg(OH)_2$ in physiologically relevant solutions for 24 hours. Values are mean ± standard deviation; n = 3. *p<0.05

3.4 Discussion

3.4.1 Morphological change in remaining MgO and $Mg(OH)_2$ particles

The flaked and flower-like structures observed for MgO and $Mg(OH)_2$ are consistent with previous studies of $Mg(OH)_2$ precipitation [27, 28]. These structures formed during precipitation and crystal growth of $Mg(OH)_2$, the presence of which is confirmed by XRD. Previous studies have suggested that the MgO transition to $Mg(OH)_2$ occurs along a shared crystal face[8, 9]. However, in our study, given the increase in particle size, it appears that MgO dissociated and then $Mg(OH)_2$ formed resulting in crystal growth. It is also likely that there is a combination of MgO to $Mg(OH)_2$ transition and re-deposition, causing size growth of the particles.

3.4.2 Elemental and Crystalline phase change in MgO and $Mg(OH)_2$

EDS for MgO and $Mg(OH)_2$ in cDMEM, DMEM, and SBF showed presence of expected elements from salts within these solutions. The carbon (C) and sulfur (S) that were detected in HEPES samples are likely from the HEPES itself. The sodium and chloride present in the NaCl solutions, as well as the chloride present in $MgCl_2$ solutions, are also expected from salt residues. However, the amount of chloride remaining in NaCl was 0.5% and 0.2%, in MgO and $Mg(OH)_2$ respectively. This indicates that over 99% of remaining particles did not contain chloride, which supports the lack of formation of $MgCl_2$. Similar trends are observed in the $MgCl_2$ solutions which showed about 0.9% and less than 0.2% for MgO and $Mg(OH)_2$ respectively. It is likely that the measured chloride remaining from the NaCl and $MgCl_2$ solutions are residues from the solution as opposed to indicative of formation of compounds containing chloride.

From the XRD results, it is evident that MgO hydrates to form $Mg(OH)_2$ within 24 hours in each of the solutions evaluated (Figure 3.2). This is expected as this reaction is well established [8-10]. Residual MgO particles from the HEPES solution showed no peaks, indicating that crystalline particles were not detected in XRD. However, the microstructures in SEM showed some ordered flower-like structures for MgO. Previous studies showed that the degradation rate of metallic magnesium is increased by HEPES exposure [20]. As it degrades, a passivation layer of MgO and $Mg(OH)_2$ forms on metallic magnesium. It is likely that the increased degradation of metallic magnesium when exposed to HEPES is due to HEPES interaction with MgO and $Mg(OH)_2$, resulting in disruption of the passivation layer. The $MgCl_2$ peak detected in the MgO samples from $MgCl_2$ solutions is likely due to residual $MgCl_2$ from the solution as opposed to nucleophilic substitution of O^{2-} or OH^-. The energy in Mg=O and Mg-OH bonds is greater than that in Mg-Cl, making nucleophilic substitution by chloride energetically unfavorable.

Studies into the degradation of metallic magnesium can give insight into the dissociation of MgO and $Mg(OH)_2$ with respect to Cl^-. Metallic magnesium's mechanical properties, biodegradability, and biocompatibility have made magnesium a promising material for orthopedic implants. It has been shown that magnesium based implants for orthopedic purposes will degrade *in vivo* suggesting it could lead to the activation of bone cells [30]. However, metallic magnesium-based biomaterials have a rapid degradation rate, which greatly reduce the mechanical properties required for bone applications [12]. Recent work has utilized coatings of MgO and $Mg(OH)_2$ to slow the degradation rate of

metallic magnesium[30]. Despite these advances and problems with Mg based biomaterials, the reactions of MgO and $Mg(OH)_2$ in physiological solutions are not well understood. Previous studies suggest that degradation of magnesium metal is mediated by the presence of Cl^- ions[31]. It has been suggested that chloride ions replace hydroxide in the $Mg(OH)_2$ that forms on the surface of metallic magnesium as it degrades. This would result in the formation of $MgCl_2$, which is highly soluble, and would then allow for the release of Mg^{2+}. However, as $Mg(OH)_2$ (solubility ~1 x 10^{-4} g/l) has significantly lower solubility than $MgCl_2$ (solubility ~5.5 g/l), the replacement of the hydroxide groups by chloride is energetically unfavorable. Since the 1930s, $Mg(OH)_2$ has been produced on a large scale by precipitation through addition of $Ca(OH)_2$ to a solution of $MgCl_2$, which further demonstrates that the proposed chloride attack on $Mg(OH)_2$ is unfounded[5, 6].

Very few changes occurred in the crystal structure of $Mg(OH)_2$ after exposure to physiological solutions (Figure 3.3). However, in HEPES, fewer and smaller peaks of $Mg(OH)_2$ were detected, and some peaks of HEPES were detected, likely because of the interaction of $Mg(OH)_2$ with HEPES. Most interestingly, the small peak of $Mg_2(OH)_3Cl$ was detected in $Mg(OH)_2$ exposed to $MgCl_2$ solutions. Actual nucleophilic substitution of OH^- by Cl^- is unlikely, as previously described. However, it is possible that Cl^- can bind to the intermediate $MgOH^+$, that formed during dissociation of $Mg(OH)_2$. Furwirth et. al, described formation of $MgOH^+$ as a rate limiting step in the dissociation of MgO. It is likely a rate limiting step for the dissociation of $Mg(OH)_2$ as well, considering that MgO readily hydrates to form $Mg(OH)_2$. The presence of chloride could stabilize the charge in $MgOH^+$ groups; removing charge interactions could decrease the adsorption of H^+ to

nearby $Mg(OH)_2$, thus enhancing dissociation of $Mg(OH)_2$. Previous studies indicated that metallic magnesium degrades more rapidly in solutions containing NaCl [22, 23]. While direct nucleophilic substitution is unlikely as described by the aforementioned reasons, the interactions between Cl^- and $MgOH^+$ are a possible explanation for the increased degradation of metallic magnesium when exposed to chloride containing solutions.

3.4.3 Mg^{2+} release and pH change in physiological media

While the XRD results showed what precipitates are present after exposure to different solutions, the change in Mg^{2+} concentration is the true measure of dissociation of MgO and $Mg(OH)_2$. At 200 µg/mL, for both MgO and $Mg(OH)_2$, the observed 100% dissociation in all solutions indicated that these nanoparticles were fully degraded at this concentration. This would equate to solubility at 0.2 g/L, much higher than the solubility of MgO (0.0086 g/L) and $Mg(OH)_2$ (1×10^{-4} g/L) [5, 6]. These solubility values were determined at 25 °C in ambient conditions in distilled water, while our solutions were kept at 37 °C under cell culture conditions (5% CO_2). The difference in temperature is likely a factor in the observed increase in solubility. Another reason for this increased solubility is the fact that these particles are nano-sized. Nanoparticles have higher surface energy because of their increased surface area to volume ratio. The increase in exposure surface area may allow for dissociation more readily. In the HEPES, NaCl, $MgCl_2$ (103 mM), $MgCl_2$ (103 mM), and DI solutions, the pH was around 4 for each, which is acidic. These solutions were made in DI water, which is filtered to result in super-purified water. Super-purified water is acidic because the lack of salts results in complete lack of

buffering. As a result, CO_2 from the atmosphere dissolves in the water, producing carbonic acid and decreasing pH. Both MgO and $Mg(OH)_2$ are basic solids and the acidic media would cause these particles to dissolve more readily.

At concentrations of 1000 µg/mL and above for MgO and $Mg(OH)_2$, more varied phenomena were observed. No statistically significant difference was found for concentrations of 1000 µg/mL and above between cDMEM and DMEM for MgO and $Mg(OH)_2$, indicating that the presence of FBS and P/S did not affect dissociation. DMEM consists of salts in similar concentrations as SBF, amino acids, and bicarbonate buffer. It is likely the pH and buffering action within DMEM that causes the dissociation of MgO and $Mg(OH)_2$ [8]. The dissociation of MgO in SBF, which was not significantly different from that of cDMEM or DMEM, further supports this notion. However, the dissociation of $Mg(OH)_2$ in SBF is significantly higher at than that of cDMEM and DMEM. This may be due to the presence of HEPES buffer. As can be seen in the HEPES solution, $Mg(OH)_2$ readily dissociated in presence of HEPES alone. However, this may have been aided by the acidic pH in the HEPES-only solutions. Additionally, HEPES has been shown to have an affinity for metallic ions in blood plasma, which further supports the possibility of HEPES-mediated dissociation of $Mg(OH)_2$ [20]. As a synthetic buffer, however, the effects of HEPES-containing solutions do not necessarily correlate to how MgO and $Mg(OH)_2$ may behave *in vivo*. The dissociation in cDMEM, DMEM, and SBF is far greater than that of the NaCl, $MgCl_2$, and DI solutions. Previous studies into the hydration kinetics and dissolution of MgO at room temperature showed a non-linear pH effect. The dissociation of MgO and $Mg(OH)_2$ is heavily influenced by pH and

temperature [8, 18, 32]. Both MgO and $Mg(OH)_2$ are basic. At a pH less than 5, magnesium oxide can freely dissociate as $MgO+2H^+ \rightarrow Mg^{2+}+H_2O$, with the rate dependent upon the concentration of H^+ and Mg^{2+} already present in the solution. At a pH 7-8.5, MgO can dissociate in an overall reaction of $MgO+H_2O \rightarrow Mg^{2+}+2OH^-$ [8]. The dissociation rate in this case is dependent upon OH^- adsorption and subsequent Mg^{2+} and OH^- desorption. However, $Mg(OH)_2$ will precipitate at the surface of MgO, slowing this reaction. Since the pH of physiological fluids such as blood are buffered at pH 7.4 that falls between the 7-8.5 range, the latter reaction is likely representative of MgO behavior that explains why dissociation of MgO may occur in physiological fluids and conditions. The proposed mechanism for this was adsorption of protons, producing $MgOH^+$, which was then vulnerable to OH^- attack. The buffering agents present in cDMEM, DMEM, and SBF aim to keep pH between 7.2 and 8.2, which is the biological range that also results in increased dissociation from this proposed mechanism.

The dissociation of MgO and $Mg(OH)_2$ in the chloride solutions indicated no increase in dissociation when compared to the DI water. This is to be expected, as the energy of the bonds in MgO and $Mg(OH)_2$ is higher than that of $MgCl_2$, which indicates that substitution is not favored. Additionally, the presence of Mg^{2+} has also been shown to decrease dissociation of MgO, which is consistent with diffusion kinetics [8]. However, at 2000 µg/mL of MgO and 3000 µg/mL of $Mg(OH)_2$, the NaCl solution showed higher Mg^{2+} release than $MgCl_2$ solutions or DI water. As the solutions containing $MgCl_2$ evaluated the same Cl^- concentration, as well as roughly double that concentration, it is unlikely that it is the chloride alone that is causing this effect. The pH

measurements indicated that NaCl and DI water had greater pH increase than $MgCl_2$ solutions. It may be that $MgCl_2$ had a slightly greater ability to buffer the pH than NaCl, leading to decreased dissociation in $MgCl_2$ solutions.

3.5 Conclusion

While biological environments and solutions are extremely complex and dynamic, it is likely that pH still plays the largest part in the dissociation of MgO and $Mg(OH)_2$. The buffering effect of physiological medias allows for contact with H^+ and OH^- necessary for dissociation of these nanoparticles to occur. It is also unlikely that Cl^- can perform nucleophilic substitution on MgO or $Mg(OH)_2$, but it is possible that Cl^- plays another role in stabilizing intermediate forms of MgO and $Mg(OH)_2$ during dissociation. When applying well-established materials from industrial fields to biological fields, it is extremely important to understand the material in each specific environment and application. MgO has long been referred to as stable. However, this is not the case for nano-sized MgO in physiologically relevant solutions. The presented information is meant to encourage deeper understanding of how MgO and $Mg(OH)_2$ behave in body fluids to facilitate potential biomedical applications of these nanoparticles.

3.6 Acknowledgements

The authors thank partial support from the U.S. National Science Foundation (NSF award 1512764, 1125801, 1545852), the Burroughs Wellcome Fund (1011235), the Hellman Faculty Fellowship (HL), and the University of California (UC) Regents Faculty Development Award (HL. The authors appreciate the Central Facility for Advanced

Microscopy and Microanalysis (CFAMM) for the use of SEM FEI XL30 at the University of California at Riverside.

3.7 References

1. Fielding, G.A., W. Smoot, and S. Bose, *Effects of SiO2, SrO, MgO, and ZnO dopants in tricalcium phosphates on osteoblastic Runx2 expression.* J Biomed Mater Res A, 2014. **102**(7): p. 2417-26.
2. Kum, C.H., et al., *A poly(lactide) stereocomplex structure with modified magnesium oxide and its effects in enhancing the mechanical properties and suppressing inflammation.* Small, 2014. **10**(18): p. 3783-94.
3. Patel, M.K., et al., *Biocompatible nanostructured magnesium oxide-chitosan platform for genosensing application.* Biosens Bioelectron, 2013. **45**: p. 181-8.
4. Pourdanesh, F., et al., *In vitro and in vivo evaluation of a new nanocomposite, containing high density polyethylene, tricalcium phosphate, hydroxyapatite, and magnesium oxide nanoparticles.* Mater Sci Eng C Mater Biol Appl, 2014. **40**: p. 382-8.
5. Amundsen, K., et al., *Magnesium*, in *Ullmann's Encyclopedia of Industrial Chemistry*. 2000, Wiley-VCH Verlag GmbH & Co. KGaA.
6. Cotton, F.A. and G. Wilkinson, *Advanced inorganic chemistry*. 5th ed. 1988, New York: Wiley. xvii, 1455.
7. Atkins, P.W., *Shriver & Atkins' inorganic chemistry*. 5th ed. 2010, Oxford ; New York: Oxford University Press. xxiv, 824 pages.
8. Fruhwirth, O., et al., *Dissolution and Hydration Kinetics of Mgo.* Surface Technology, 1985. **24**(3): p. 301-317.
9. Láska, M., J. Valtýni, and P. Fellner *Influence of pH on the Crystal Size Distribution of Mg(OH)2 Prepared by the Hydration of MgO Crystal Research and Technology Volume 28, Issue 7*. Crystal Research and Technology, 1993. **28**, 931-936.
10. Refson, K., et al., *Water chemisorption and reconstruction of the MgO surface.* Phys Rev B Condens Matter, 1995. **52**(15): p. 10823-10826.
11. Carpenter, T.O., et al., *A randomized controlled study of effects of dietary magnesium oxide supplementation on bone mineral content in healthy girls.* J Clin Endocrinol Metab, 2006. **91**(12): p. 4866-72.
12. Stendig-Lindberg, G., R. Tepper, and I. Leichter, *Trabecular bone density in a two year controlled trial of peroral magnesium in osteoporosis.* Magnes Res, 1993. **6**(2): p. 155-63.
13. Yoshizawa, S., et al., *Role of magnesium ions on osteogenic response in bone marrow stromal cells.* Connect Tissue Res, 2014. **55 Suppl 1**: p. 155-9.
14. Yoshizawa, S., et al., *Magnesium ion stimulation of bone marrow stromal cells enhances osteogenic activity, simulating the effect of magnesium alloy degradation.* Acta Biomater, 2014. **10**(6): p. 2834-42.
15. Wetteland, C.L., N.Y. Nguyen, and H. Liu, *Concentration-dependent behaviors of bone marrow derived mesenchymal stem cells and infectious bacteria toward magnesium oxide nanoparticles.* Acta Biomater, 2016. **35**: p. 341-56.

16. Sawai, J., *Quantitative evaluation of antibacterial activities of metallic oxide powders (ZnO, MgO and CaO) by conductimetric assay.* J Microbiol Methods, 2003. **54**(2): p. 177-82.
17. Sawai, J. and T. Yoshikawa, *Quantitative evaluation of antifungal activity of metallic oxide powders (MgO, CaO and ZnO) by an indirect conductimetric assay.* J Appl Microbiol, 2004. **96**(4): p. 803-9.
18. Mejias, J.A., et al., *The kinetics and mechanism of MgO dissolution.* Chemical Physics Letters, 1999. **314**(5-6): p. 558-563.
19. Oyane, A., et al., *Preparation and assessment of revised simulated body fluids.* J Biomed Mater Res A, 2003. **65**(2): p. 188-95.
20. Dezfuli, S.N., et al., *Influence of HEPES buffer on the local pH and formation of surface layer during in vitro degradation tests of magnesium in DMEM.* Progress in Natural Science-Materials International, 2014. **24**(5): p. 531-538.
21. Ferguson, W.J., et al., *Hydrogen-Ion Buffers for Biological-Research.* Analytical Biochemistry, 1980. **104**(2): p. 300-310.
22. Johnson, I. and H. Liu, *A study on factors affecting the degradation of magnesium and a magnesium-yttrium alloy for biomedical applications.* PLoS One, 2013. **8**(6): p. e65603.
23. Peng, Q.M., et al., *Degradation behavior of Mg-based biomaterials containing different long-period stacking ordered phases.* Scientific Reports, 2014. **4**.
24. Yanagisawa, Y., *Interaction of Oxygen Molecules with Surface Centers of UV-Irradiated MgO.* Journal of Physics Society Japan, 1981. **50**(1): p. 209-216.
25. Ito, T., et al., *Oxygen Species Adsorbed on Ultraviolet-Irradiated Magnesium-Oxide.* Journal of the Chemical Society-Faraday Transactions I, 1985. **81**: p. 2835-2844.
26. Tian, Q.M., et al., *Cytocompatibility of Magnesium Alloys with Human Urothelial Cells: A Comparison of Three Culture Methodologies.* Acs Biomaterials Science & Engineering, 2016. **2**(9): p. 1559-1571.
27. Press, C., *CRC Handbook of Chemistry and Physics*. 98 ed. 2017, Boca Raton, Fla.: CRC Press : Taylor & Francis.
28. Li, C., et al., *Recycling rare earth elements from industrial wastewater with flowerlike nano-Mg(OH)(2).* ACS Appl Mater Interfaces, 2013. **5**(19): p. 9719-25.
29. Jadhav, S.A., *Interesting nanoshapes by "nano artwork".* Advanced Materials Letters, 2014. **5**(10): p. 4.
30. Cipriano, A.F., et al., *Investigation of magnesium-zinc-calcium alloys and bone marrow derived mesenchymal stem cell response in direct culture.* Acta Biomater, 2015. **12**: p. 298-321.
31. Mueller, W.D., et al., *Degradation of magnesium and its alloys: dependence on the composition of the synthetic biological media.* J Biomed Mater Res A, 2009. **90**(2): p. 487-95.
32. Fedorockova, A. and P. Raschman, *Effects of pH and acid anions on the dissolution kinetics of MgO.* Chemical Engineering Journal, 2008. **143**(1-3): p. 265-272.

Chapter 4: Use of Dual-Asymmetric Centrifugal Mixing to Increase Dispersion of Ceramic Nanoparticles in Polymer Solutions

4.1 Introduction

Homogeneous dispersion of nanoparticles in polymer matrices has been challenging theoretically and practically, because nanoparticles have a strong tendency to agglomerate (or aggregate) in polymers [1, 2]. When the weight and volume percentages of nanoparticles in polymers increase, it becomes even more difficult to achieve uniform dispersion. A surface modifier (e.g., surfactant) is often utilized to improve dispersion of nanoparticles by acting as a mediator between the nanoparticles and polymers during mixing [3, 4]. However, surfactants often raise concerns on toxicity and other associated complications for medical implant applications. Therefore, the objective of this research is to circumvent surfactants and investigate the use of mechanical mixing methods, particularly Dual-Asymmetric Centrifugal (DAC) mixing, to improve dispersion of polymer based nanocomposites with 30 wt.% of nanophase magnesium oxide (nMgO) or 30 wt.% of nanophase hydroxyapatite (nHA), and the effects of dispersion on the optical and biological properties of these nanocomposites for potential biomedical applications.

For this study, we selected biodegradable poly(lactic-co-glycolic acid) (PLGA) as the model polymer matrix because PLGA was approved by the U.S. Food and Drug Association (FDA) and the European Medicine Agency (EMA) for various medical applications, e.g., as sutures and drug delivery carriers. PLGA is a co-polymer composed of units of lactide and glycolide and degrades through hydrolysis of its ester bonds inside the human body. To retain the benefits of biodegradability of PLGA in the resulted nanocomposites, we selected nMgO and nHA as the model nanoparticles because they

are biodegradable inside the human body. Specifically, we are interested in these nanocomposites for bone applications as coatings to improve osseointegration of implants or as 3D printed synthetic bone matrix. Magnesium oxide (MgO) is a promising material for biomedical applications due to its bioactivity and mechanical properties [5-9]. For example, MgO has been shown to be beneficial for bone repair. Clinically, MgO has been used as an oral supplement to improve bone density [10]. As an implantable paste, MgO exhibited stimulatory effects on bone healing in rats [11]. MgO has also been used as an additive in bone cements to increase fracture toughness of the bone-cement interface [12]. Moreover, in the nanoparticle form, nMgO showed attractive antibacterial properties for potentially reducing hospital-acquired infections [13]. In small amounts, e.g., 200 μg/mL, nMgO enhanced adhesion and proliferation of bone marrow derived mesenchymal stem cells (BMSCs) in direct culture [13]. However, in amounts exceeding 500 μg/mL, nMgO significantly decreased the adhesion density of BMSCs *in vitro*, indicating possible cytotoxicity of nMgO at higher concentrations, especially when nMgO is in direct contact with cells. Therefore, dispersing nMgO in a polymer such as PLGA could potentially lead to a new class of nanocomposites that harvest the beneficial properties of nMgO, such as improved BMSC proliferation and ductility, while avoiding its cytotoxicity and brittleness. Hydroxyapatite (HA) is a naturally occurring ceramic material present in human bone and is known to enhance bone regeneration because of its osteoconductivity and osteoinductivity [14, 15]. In its nanophase form, nHA improved osteoblast cell adhesion and long-term functions *in vitro* and *in vivo* [16]. Similar to nMgO, nHA is also brittle when used alone and does not meet mechanical requirements

for most medical applications. The nHA/polymer composites, including nHA/PLGA, demonstrated attractive bioactivity and mechanical properties due to the complementary effects of nHA phase and PLGA matrix [17-19]. We used nHA/PLGA in this study as a comparison to nMgO/PLGA nanocomposites. We focused on 30 wt.% of nanoparticles and 70 wt.% of PLGA in this study because this high ceramic/polymer ratio presents a significant challenge in nanoparticle dispersion and this ratio showed promising mechanical and biological properties for biomedical applications [19-22]. For example, A PLGA composite with 10-50 wt % beta calcium phosphate nanoparticles was reported to have the highest yield strength at 30% nanoparticles by weight [22].

Degree of dispersion of nanoparticles in composites has great impact on its optical, mechanical, chemical, and biological properties. For this study, we were interested in the optical and biological properties of the nanocomposites. To confirm increased dispersion, transmission measurements in visible and infrared region were taken. The effect of dispersion on BMSC adhesion was evaluated as well, to demonstrate changes to biological properties. BMSCs were selected due to their use for bone applications. The comparison between composites with improved dispersion and agglomerated nanoparticles demonstrates the changes to these properties resulting from use of DAC mixing. Herein, we investigated the effects of dispersion on the optical and biological properties of nMgO/PLGA and nHA/PLGA with a ceramic/polymer ratio of 30/70.

4.2 Materials and Methods

4.2.1 Preparation and Characterization of Nanoparticles

4.2.1a Preparation of Magnesium Oxide Nanoparticles

Nanophase MgO in a powder form with a reported diameter of 20 nm was procured from US Research Nanomaterials Inc. (US3310). The nMgO powder was dehydrated and disinfected through heating in an oven at 200°C for one hour, prior to its use in preparing polymer-based nanocomposites and in cell culture. The common methods of sterilization or disinfection, such as autoclave and UV radiation, were not used for nMgO in this study, because of the hygroscopic nature of nMgO and its ability of absorbing UV to produce superoxide.

4.2.1b Preparation of Hydroxyapatite Nanoparticles

Nanophase hydroxyapatite (nHA) was synthesized through the wet precipitation method followed by hydrothermal treatment, as published previously [21]. Briefly, 40 mL each of 0.6 M $(NH_4)_2HPO_4$ and 1M $Ca(NO_3)_2$ solutions with alkaline pH were prepared in separate beakers at 40°C. The pH of each solution was measured using a pre-calibrated pH meter (Symphony SB70P, VWR) and adjusted to above pH 10 with 10 M NH_4OH, as necessary. The 0.6M $(NH_4)_2HPO_4$ solution was transferred to a 500mL beaker and a burette was used to add the 1M $Ca(NO_3)_2$ solution drop-wise into the 0.6M $(NH_4)_2HPO_4$ solution, while the temperature was kept at 40°C. The dispense rate of the 1M $Ca(NO_3)_2$ solution could affect the size of HA particles formed, and was controlled at 30 drops per minute to produce nano-sized HA particles. The resulting mixture was stirred for 20 hours to allow formation of nHA. After 20 hours, we obtained the nHA

suspension containing residual ammonia, since ammonium hydroxide (NH_4OH; Sigma Aldrich) was used to adjust the pH of reactant solutions to alkaline region. The product of this reaction was transferred into a centrifuge tube and centrifuged at 3000 rpm for 1 minute. The supernatant was discarded and the pellet was resuspended in 100mL of deionized (DI) water. Rinsing cycles of centrifugation and resuspension were repeated three times to remove the ammonia and excess reactants. After the final rinse, the pellet was resuspended in 100mL of DI water and transferred into an acid digestion bomb for hydrothermal treatment. Hydrothermal treatment was performed at 200°C for 20 hours to produce more crystalline hydroxyapatite nanoparticles[23]. After that, the suspension of nHA in DI water was centrifuged at 3000 rpm for 10 minutes, and the pellet was collected and dried under vacuum at 80°C for 12 hours. The dried particles were ground using a mortar and pestle to separate soft agglomerates that formed during the drying process. The nHA was sterilized by heating in an oven at 200°C for 1 hour, prior to its use in preparing polymer-based nanocomposites and in cell culture.

4.2.1c Characterization of nMgO and nHA nanoparticles

The nMgO and nHA particles were characterized prior to their use in the polymer-based nanocomposites. The morphology of both nMgO and nHA nanoparticles was visualized using a field emission scanning electron microscope (SEM; Philips XL30), with a secondary electron detector, at an accelerating voltage of 30 kV and a working distance of 10 mm. The original magnifications of 300,000x for nMgO and 100,000x for nHA were used for SEM imaging. Elemental composition of the nMgO and nHA nanoparticles was confirmed using the energy dispersive x-ray spectroscopy (EDS,

EDAX Leap detector attached to Philips XL30 SEM) at a spot size of 3 and an accelerating voltage of 30 kV. Crystalline phases of nMgO and nHA nanoparticles were characterized using x-ray diffraction (XRD, Empyrean, PANalytical). The XRD spectra for nMgO and nHA were obtained using Cu Kα radiation (45 kV, 40 mA) at a step size of 0.006° and dwelling time of 50 seconds using a PIXcel 1D detector (PANalytical). Phase identification was performed using the HighScore software (PANalytical). The particle size and distribution of nMgO and nHA were quantified based on their respective SEM images using the quantitative image analysis tools in ImageJ.

4.2.2 Preparation of Polymer-based Nanocomposites with nMgO or nHA nanoparticles

The ceramic/polymer ratio for nMgO/PLGA and nHA/PLGA was kept to be the same in this study, that is, 30% nMgO or nHA and 70% PLGA by weight, to study the effects of dispersion on optical and biological properties of a nanocomposite with the same composition. We created a new process involving only mechanical mixing (sonication plus dual asymmetric centrifugal mixing) to improve dispersion of nMgO and nHA in PLGA matrix, and the resulted nanocomposites were referred to as nMgO/PLGA_D and nHA/PLGA_D. For the purpose of comparison, we used a previously established mixing protocol (sonication only) to make the nanocomposites with more agglomerated nanoparticles, which were referred to as nMgO/PLGA_A and nHA/PLGA_A. PLGA was prepared as a polymer control using the same solvent casting method without adding nanoparticles.

4.2.2a The New Process for Making Nanocomposites with Improved Dispersion of Nanoparticles

The new process of nanocomposites integrated ultrasonic energy and dual asymmetric centrifugal mixing (also called speed mixing) in multiple steps to achieve improved dispersion of nanoparticles. Specifically, we developed and validated the protocols for nanocomposites of nMgO/PLGA and nHA/PLGA respectively.

The New Process for Dispersed nMgO/PLGA: In a 20mL vial, we added 4.5mL of chloroform ($CHCl_3$, Fisher Scientific) to 0.441g of PLGA (50:50 LA:GA, MW: 100 kDa, AP36, Polyscitech) to give a PLGA/solvent ratio of 0.098 g/mL (~ 0.1 g/mL). This ratio was selected after several trials for optimizing the viscosity to reduce the size and number of agglomerates effectively during sonication. Specifically, effective sonication prefers that the suspension has low viscosity so that the energy is not absorbed into the surrounding solvent and polymer. The PLGA solution was first sonicated in a low power ultrasonic bath (Symphony, VWR) at 40 °C for 1 hour to ensure the polymer is fully dissolved. The nMgO powder of 0.189g was added into the polymer solution to achieve a 30/70 nMgO/PLGA ratio and the resulting mixture was sonicated for an additional hour in the low-power ultrasonic bath at 40 °C. The suspension of nMgO/PLGA was then loaded into a Teflon vial in a speedmixer (DAC 150.1 FVZ-K, FlackTek, Inc.) for dual asymmetric centrifugal mixing (DAC, also referred to as speed mixing hereafter) at 2500 rpm for 5 minutes. Following the speed mixing, the nMgO/PLGA suspension was sonicated using a high-power sonicator (Qsonica, Q125) with a microprobe at 100% amplitude (16-18W) for 10 minutes with pulses of 5 seconds on and 5 seconds off. The vial containing the nanocomposite suspension was placed in

ice during high-power sonication to minimize heating of the suspension. The nMgO/PLGA nanocomposite suspension underwent two additional rounds of speed mixing and high-power sonication followed by another 5 minutes of speed mixing. The suspension was then cast into an 8.3cm by 4 cm Teflon dish, and placed under the chemical fume hood to allow the solvent to evaporate in air at room temperature for 24 hours. The air-dried nanocomposites were carefully removed from the Teflon mold using forceps, placed in a 20 mL glass vial, and re-suspended in 4 mL of chloroform. The re-suspended nanocomposites were sonicated in the low-power ultrasonic bath for 1 hour at 40^{o}C, and then went through the same combined steps of speed mixing and high-power sonication using the same parameters as described above. The dispersed suspension was again poured into the Teflon mold and dried in air at room temperature for 24 hours. The dried nanocomposites were re-suspended in 3.5 mL of chloroform in a 20mL glass vial. The suspension underwent two rounds of speed mixing and high-power sonication using the same parameters as described above. The multiple rounds of dissolution and re-suspension resulted in visibly higher dispersion compared to single cycles. Lastly, the suspension went through 5 minutes of speed mixing to remove the trapped gas bubbles, was cast in the Teflon mold, and dried in air for 24 hours and in vacuum for additional 48 hours to ensure complete removal of chloroform. The resulting nMgO/PLGA_D nanocomposites had a thickness of 0.1 mm and were cut to 10 mm by 10 mm squares for characterization of dispersion and use in cell culture.

The New Process for Dispersed nHA/PLGA: The well dispersed nHA/PLGA nanocomposites were prepared following a similar procedure to that of nMgO/PLGA.

However, it was necessary to modify the polymer/solvent ratio to disperse nHA nanoparticles because the size and density of nHA was different from nMgO. For nHA/PLGA, 0.433g of PLGA was dissolved in 3.5 mL of chloroform to give a PLGA/solvent ratio of 0.12 g/mL. The addition of 0.186g of nHA to PLGA solution was to achieve a 30/70 nHA/PLGA ratio. The density of nHA is 3.16 g/mL and the density of MgO is 3.58 g/mL. The slight difference in the densities of these nanoparticles resulted in the slight difference in the mass of PLGA and nanoparticles to keep the volume of the final composite the same between the nMgO/PLGA_D and nHA/PLGA_D samples. The nHA/PLGA suspension underwent the same multiple cycles of low-power sonication, speed-mixing and high-power sonication as the nMgO/PLGA. However, the volume of chloroform for nHA/PLGA was 3.25 mL and 3 mL on the second and third repeating rounds of mixing, respectively. The resulting nHA/PLGA nanocomposites had a thickness of 0.1 mm and were cut to 10 mm by 10 mm squares for characterization of dispersion and use in cell culture.

4.2.2b Nanocomposites with Agglomerated Nanoparticles for Comparison

The nMgO/PLGA_A and nHA/PLGA_A nanocomposites with agglomeration were prepared using a previously established protocol for comparison. Briefly, PLGA (50:50, MW 100,000 Da; Polyscitech) was dissolved in chloroform at a concentration of 0.1g/mL in a low-power sonication bath at 40 °C for 1 hour. The nMgO and nHA powders were then dispersed into the dissolved polymer using high power sonication at 100% amplitude (16-18W) for 10 minutes, with pulses of 5 seconds on and 5 seconds off to give a ceramic/polymer ratio of 3:7. Immediately after sonication, the suspension was

poured into an 8.3cm by 4cm Teflon dish in a chemical fume hood, and dried at room temperature in air for 24 hours and then in vacuum for additional 48 hours. The resulting nMgO/PLGA_A and nHA/PLGA_A nanocomposites were 0.1mm thick and were cut into 10mm by 10mm squares for material characterization and use in cell culture.

4.2.3 Characterization of Dispersed versus Agglomerated Nanocomposites

4.2.3a Macroscopic Images of the Nanocomposites

Macroscopic images for both nMgO/PLGA and nHA/PLGA nanocomposites, as well as PLGA control, were captured using a digital single-lens reflex camera (Rebel XTi, Canon) with a macroscopic lens (EF 50mm f/2.5, Canon). The nanocomposite samples were placed directly on top of a piece of paper with black "UCR" print to compare their optical transparency.

4.2.3b Microscopic Images of the Nanocomposites

The microstructures of nMgO/PLGA and nHA/PLGA nanocomposites were characterized using field emission scanning electron microscopy (SEM, Philips XL30). Prior to SEM imaging, the nanocomposite samples were secured onto a SEM pin mount using copper tape, and coated with platinum and palladium (Pt/Pd) using a sputter-coater (108 Auto, Cressington). Both the top surface and bottom side of the as-cast nanocomposites were imaged under SEM to evaluate the dispersion or agglomeration of nanoparticles. All of the SEM images were taken using a secondary electron detector at an accelerating voltage of 2kV, a spot size of 3, and a working distance of 10 mm.

4.2.3c Optical Characterization of the Nanocomposites

The optical transparency of the nanocomposites was quantified by transmittance of light at the wavelength of 300 to 900nm in increments of 50 nm using a spectrophotometer (Infinite M200 Pro, Tecan). Both the nMgO/PLGA and nHA/PLGA nanocomposites, as well as the PLGA control, were compared for optical transmission. Each sample was cut into the same dimension, i.e., a thin cylinder with a radius of 3.1 mm and a thickness of 0.1 mm to fit into a well of a 96-well plate. Absorbance readings were taken from the center of each well under dry conditions. Three blank wells were also evaluated to determine the absorbance of the plate without any samples. The readings from the blank wells were averaged and subtracted from the sample readings to isolate the absorbance of the nanocomposites. The absorbance readings were converted to the percentage of transmission using the well-defined relationship between absorbance and transmission as described by Beer's law, $A=2-\log_{10}(\%T)$, where A is the absorbance and %T is the percent transmission. Fourier transform infrared spectroscopy (FTIR, Optical 8000, Bruker) was used to evaluate the transmittance of the nanocomposites, as well as the nMgO, nHA, and PLGA controls in the infrared region, with a wavenumber range of 4000 to 500 cm^{-1} (equivalent to wavelength of 2.5 μm to 20 μm). FTIR analysis was performed using the transmission mode with 64 scans.

4.2.4 Cytocompatibility of the Nanocomposites with BMSCs In Vitro

4.2.4a Preparation of the Nanocomposite Samples and Controls for BMSC Culture

All samples were disinfected prior to cell culture using a customized method appropriate for the material type. PLGA, nMgO particles, and nHA particles were used as

controls for the nanocomposites, and titanium (Ti), glass slide, and tissue culture treated plate (TCTP) was used as the references. Specifically, the nMgO/PLGA and nHA/PLGA nanocomposites and PLGA controls were disinfected by soaking in 100% ethanol for an hour, and then dried at room temperature in a laminar flow hood. Ultraviolet (UV) radiation was not used for disinfecting PLGA and PLGA based nanocomposites, because PLGA is a UV absorber and UV causes degradation of the ester bonds [24]. The nMgO and nHA nanoparticles were sterilized through heating in an oven at 200°C for one hour. The nMgO and nHA were then weighed in respective sterile microcentrifuge tubes with 4.9 mg in each tube for a final concentration of 1.6 mg/mL. This concentration of nanoparticles was selected for nMgO and nHA particle controls because it is calculated to be the amount of nanoparticles present in the 10 mm x 10 mm x 0.1 mm nanocomposite scaffold. The 10 mm x 10 mm x 0.5 mm Ti and 10mm x 10mm x 0.1 mm glass references were cleaned in 100% acetone for 10 minutes and then in 100% ethanol for 30 minutes under low-power sonication. After drying in air at room temperature, the Ti and glass reference samples were sterilized using an autoclave (Biomedical Sterilizer 20", Beta Star Life Sciences Equipment).

4.2.4b Bone Marrow Derived Mesenchymal Stem Cell Culture with the Nanocomposites

Rat bone marrow derived mesenchymal stem cells (BMSCs) were used as the model cell to evaluate the cytocompatibility of the nanocomposites of interest. Mesenchymal stem cells can differentiate into muscle, bone, cartilage, and other connective tissue cells and as such, provide a model cell for a wide variety of tissues. BMSCs were extracted from the femur and tibia of juvenile rats according to the

previously established protocols approved by the Institutional Animal Care and Use Committee (IACUC) at the University of California at Riverside [25, 26]. BMSCs were cultured in Dulbecco's Modified Eagle Medium (DMEM) supplemented with 10% fetal bovine serum (FBS) and 1% penicillin/streptomycin (P/S) by volume under standard cell culture conditions in an incubator (MCO-19AIC, Sanyo Scientific), that is, a sterile, 5%CO_2/95% air, 37°C, humidified environment. The pH of media was adjusted to 7.4 before their use in cell culture. The sterilized nanocomposites and PLGA controls were placed into a tissue culture treated 12-well plates (Corning, Falcon® 353043) and equilibrated with DMEM under sterile conditions in a biosafety II laminar flow hood (Class II Type A2, Labconco). BMSCs at the second passage were seeded at a density of 10,000 cells/cm^2 directly onto the nanocomposite scaffolds, PLGA controls, nMgO and nHA controls, and the references, and incubated under standard cell culture conditions for 24 hours.

For the agglomerated nanocomposites, the BMSC culture was extended to 48 and 72 hours based on the results of 24-hour culture. At every 24 hours, the media were collected for pH measurements and analyses of Mg^{2+} and Ca^{2+} ion concentrations using inductively coupled plasma - optical emission spectrometry (ICP-OES). At the end of each prescribed time point, each well with the sample was rinsed with 2 mL of phosphate buffer saline (PBS) to remove non-adherent cells. Adherent cells were fixed using 4% paraformaldehyde, and stained with 4',6-Diamidino-2-Phenylindole, Dihydrochloride (DAPI, Life Technologies) and Alexa Fluor® 488 phalloidin (Life Technologies) to visualize the nuclei of the cells and F-actin in cytoskeleton under a fluorescence

microscope (Nikon Eclipse Ti), respectively. The number of adherent BMSCs were counted based on 10 fluorescence images for each sample, and the cell adhesion density was calculated as the number of adherent cells per unit area. The nanocomposites with well dispersed versus agglomerated nanoparticles were cultured in triplicate with BMSCs at different times. Cell adhesion density from each culture study was normalized by the respective TCTP reference and averaged for comparison.

4.3 Results

4.3.1 Characterization of nMgO and nHA

Figure 4.1 shows material characterization for nMgO and nHA particles. SEM images of nMgO and nHA in Figure 4.1A,B revealed their near-spherical morphology and confirmed the size of these nanoparticles. EDS results confirmed the elemental composition of nMgO and nHA (Figure 4.1C,D). The XRD spectra of the nMgO and nHA nanoparticles showed the peaks matching each peak of their respective standards, indicating that each nanoparticle exhibited the expected crystalline phase (Figure 4.1E,F). However, nMgO showed additional peaks in the XRD pattern for the nMgO sample indicated the presence of $Mg(OH)_2$ phase. MgO is hygroscopic and can readily react with water in the atmosphere to form $Mg(OH)_2$, which is most likely the cause of the $Mg(OH)_2$ peaks in the XRD spectra. The expected peaks for nHA were all present and matched the HA standard. The average particle diameters and standard deviation for nMgO and nHA samples were 23 ± 5 nm and 47 ± 12 nm, respectively (Figure 4.1G).

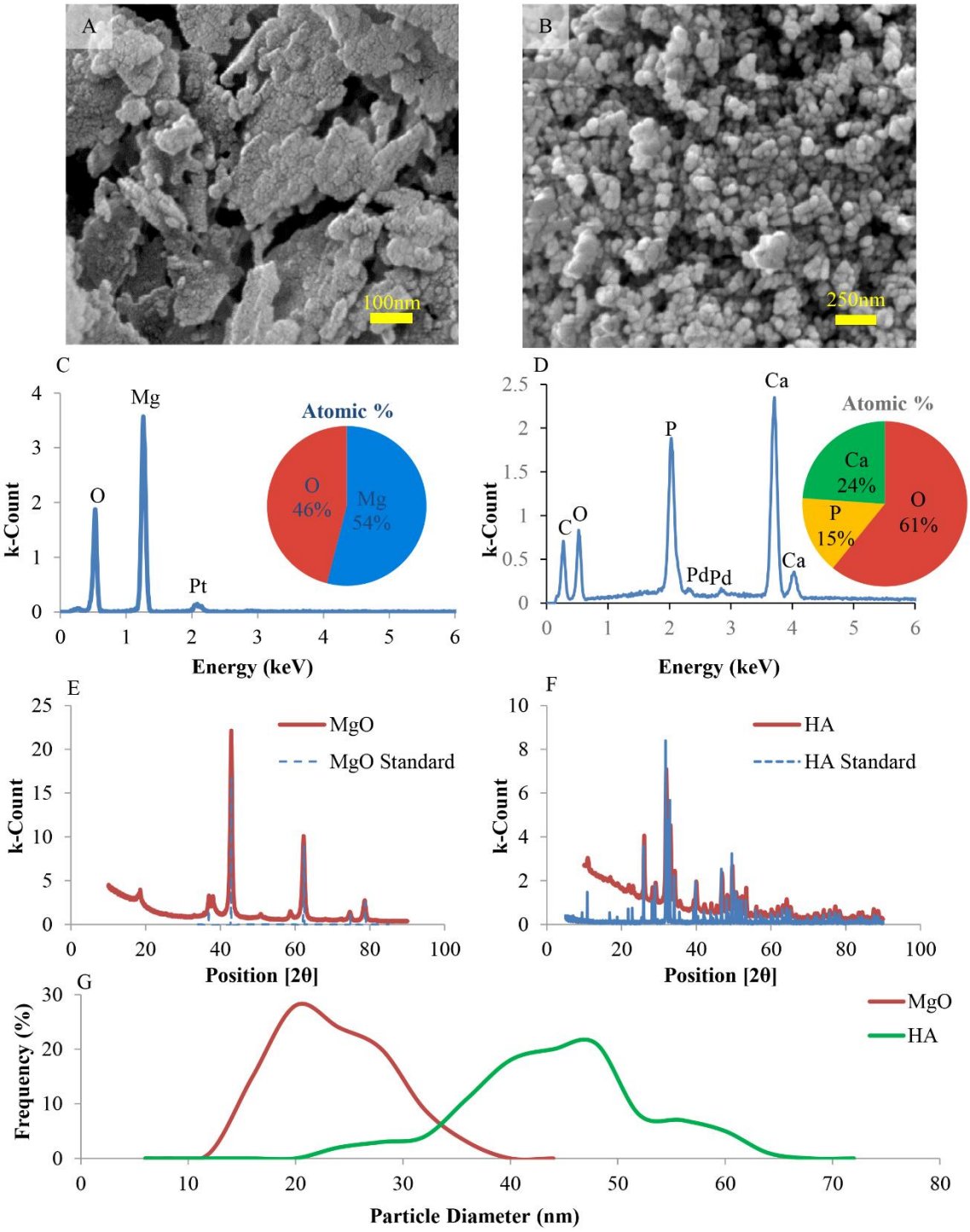

Figure 4.1: Characterization of MgO and HA nanoparticles. (A) SEM image of nMgO, (B) SEM image of nHA, and the corresponding (C, D) EDS analyses, (E, F) XRD analysis, and (G) particle size distribution for nMgO and nHA.

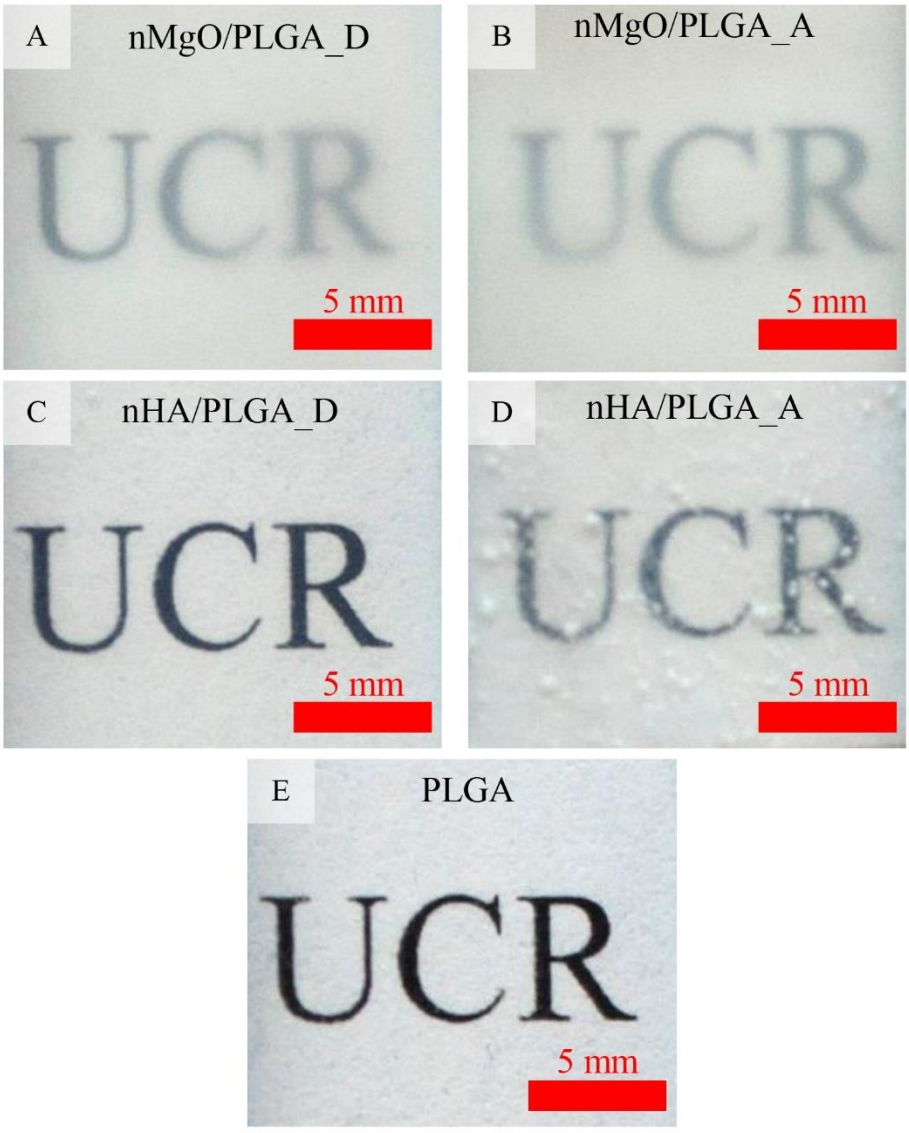

Figure 4.2: Macro-scale photographs of the dispersed versus agglomerated nanocomposites, showing the differences in their optical transparency when compared with the polymer alone and each other. (A) nMgO/PLGA_D, (B) nMgO/PLGA_A, (C) nHA/PLGA_D, (D), nHA/PLGA_A, and (E) PLGA. The nanocomposites with improved dispersion are denoted with _D, and the nanocomposites with agglomeration are denoted with _A. Scale bar is 5mm.

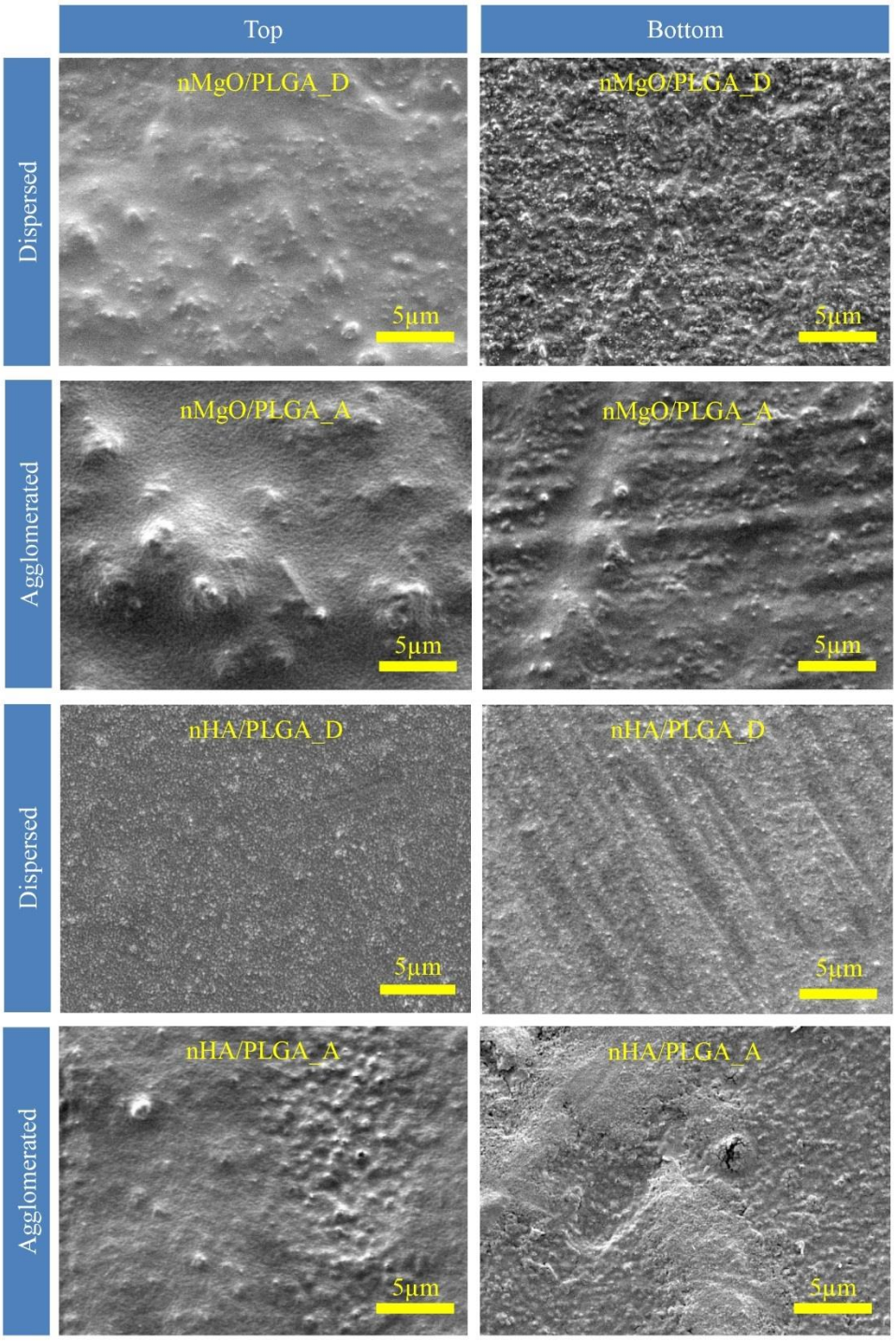

Figure 4.3: SEM images of the dispersed versus agglomerated nanocomposites, showing the differences in their microstructures. SEM images were taken using a secondary electron detector with a spot size of 3, a working distance of 10 mm, and an original magnification of 40,000x.

4.3.2 Macroscopic and Microscopic Comparison of the Nanocomposites with Dispersed versus Agglomerated Nanoparticles

Figure 4.2 shows the macroscopic appearance of the nanocomposites with nMgO or nHA. Macroscopic images of the dispersed nMgO/PLGA nanocomposites showed better optical transparency when compared with the agglomerated nMgO/PLGA; and both nMgO_PLGA_D and nMgO/PLGA_A showed no visible agglomerates at the macroscopic view. Similarly, macroscopic images of the dispersed nHA/PLGA nanocomposites appeared optically more transparent than the agglomerated counterpart; and nHA/PLGA_A showed visible agglomerates while nHA/PLGA_D did not at the macroscopic view. Improved dispersion was also achieved for the samples at a larger size, as demonstrated by consistent optical transparency shown in larger samples of nanocomposites (Figure A1, Appendix A). When comparing different nanocomposites and the PLGA control macroscopically, the nHA/PLGA_D showed an optical transparency very similar to PLGA and appeared more transparent than the nMgO/PLGA_D.

Figure 4.3 shows the microstructure of the nanocomposites with nMgO or nHA. SEM images revealed that the top and bottom surfaces of the well-dispersed nanocomposites were generally more homogenous in microstructure, with fewer and smaller agglomerates when compared with their agglomerated counterparts. Specially, although the top and bottom surface appeared different for nMgO/PLGA_D, it consistently showed that the agglomerates were smaller and fewer than nMgO/PLGA_A. Interestingly, the top and bottom surface for nHA/PLGA_D microscopically appeared more homogenous than nMgO/PLGA_D, in agreement with the greater optical

transparency of nHA/PLGA_D than nMgO/PLGA_D macroscopically. Although individual nanoparticles were visible under SEM prior to incorporation into the nanocomposites, the presence of the PLGA matrix limited resolution of nanoparticles in the nanocomposites under SEM. When the nanoparticles were embedded in the polymer, the polymer's sensitivity to heating of high energy electron beam required using lower voltage resulting in lower resolution. The topographical features shown on the bottom surface of some samples were caused by defects and scratches on the surface of the Teflon mold used for casting the nanocomposites.

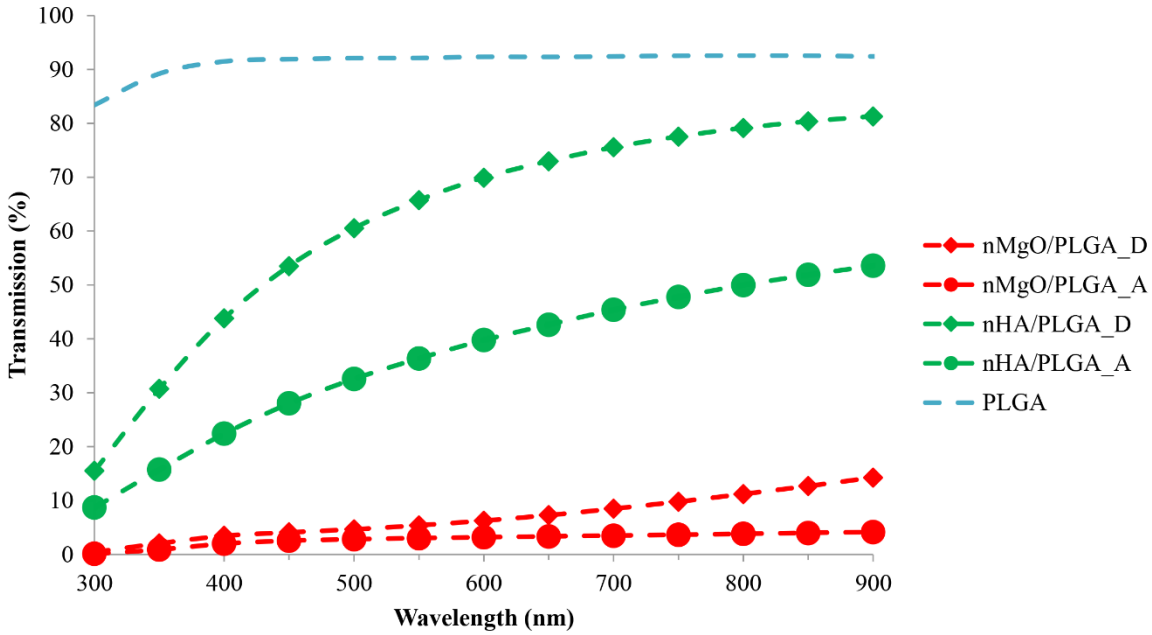

Figure 4.4: Optical transmission through the dispersed versus agglomerated nanocomposites at the wavelengths ranging from 300 to 900 nm when compared with the polymer alone. The nanocomposites with improved dispersion are denoted with _D, and the nanocomposites with agglomeration are denoted with _A.

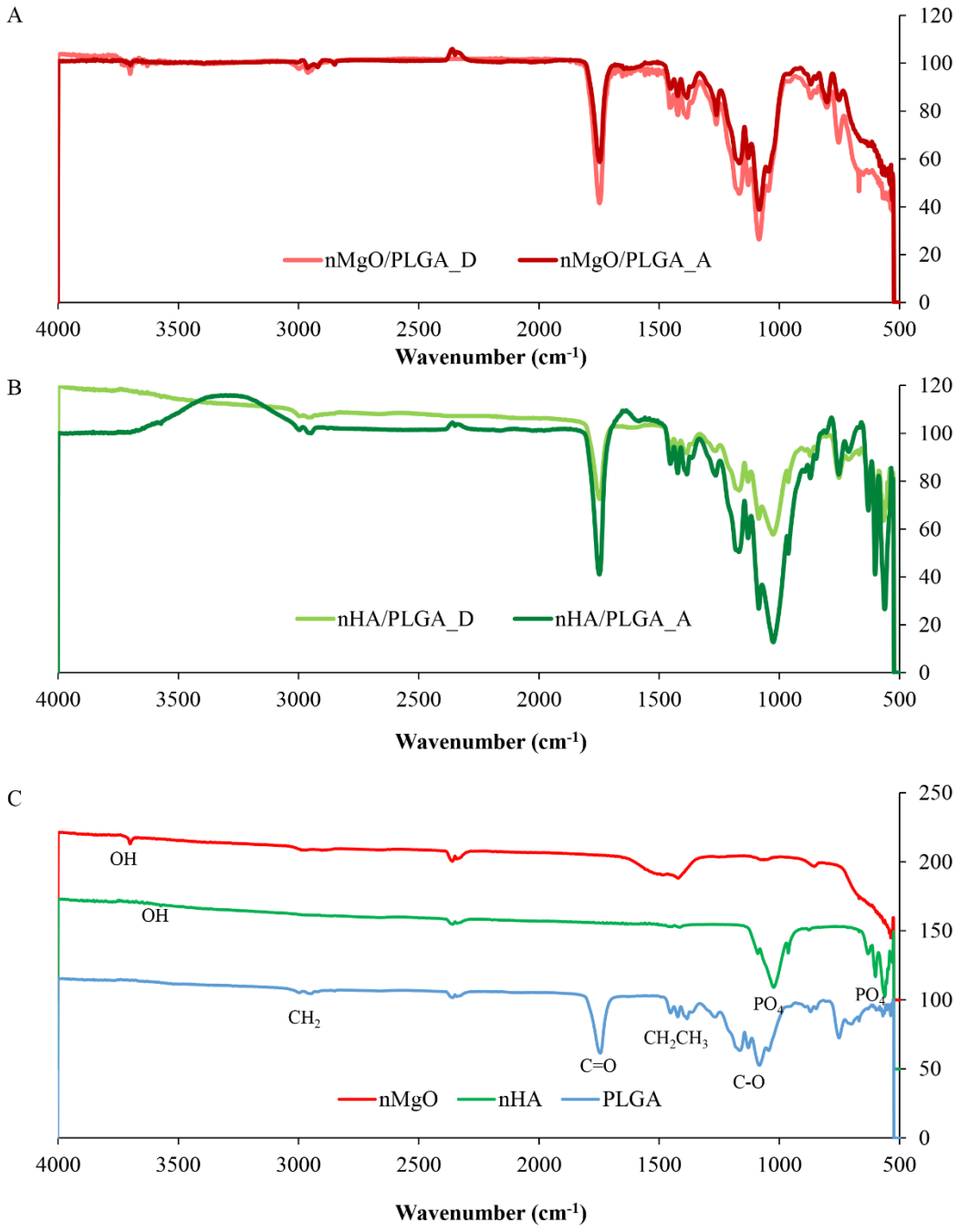

Figure 4.5: FTIR spectrum of the dispersed versus agglomerated nanocomposites when compared with the respective controls. (A) nMgO/PLGA_D, nMgO/PLGA_A, (B) nHA/PLGA_D, nHA/PLGA_A (B), and (C) single phase controls of nMgO, nHA, and PLGA.

4.3.3 Optical Properties of the Nanocomposites with Dispersed versus Agglomerated Nanoparticles

Figure 4.4 shows the quantified optical transmission at 300-900 nm through the nanocomposites with dispersed versus agglomerated nanoparticles, and the PLGA control. In general, optical transmission of the nanocomposites and PLGA control increased when the wavelength increased from 300nm to 900nm; and, the nanocomposites with dispersed nanoparticles showed greater optical transmission than their counterpart with agglomerated nanoparticles at 300-900nm wavelength. Both nMgO/PLGA_D and nMgO/PLGA_A nanocomposites showed near 0% transmittance at 300nm, which is in the range of ultraviolet wavelength. However, at 900 nm (infrared wavelength), nMgO/PLGA_D showed 14% transmittance in contrast to 4% transmission for nMgO/PLGA_A. Similarly, nHA/PLGA_D showed a greater transmittance of 15.5% and 81% at 300nm and 900 nm, respectively when compared with 8.7% and 54% transmittance of the nHA/PLGA_A at respective wavelength. PLGA was the most transparent, showing 83% transmittance at 300nm and 92% transmittance at 900 nm. The optical properties of the nanocomposites and PLGA control showed the following order from the greatest transmission to lowest transmission: PLGA > nHA/PLGA_D > nHA/PLGA_A > nMgO/PLGA_D > nMgO/PLGA_A.

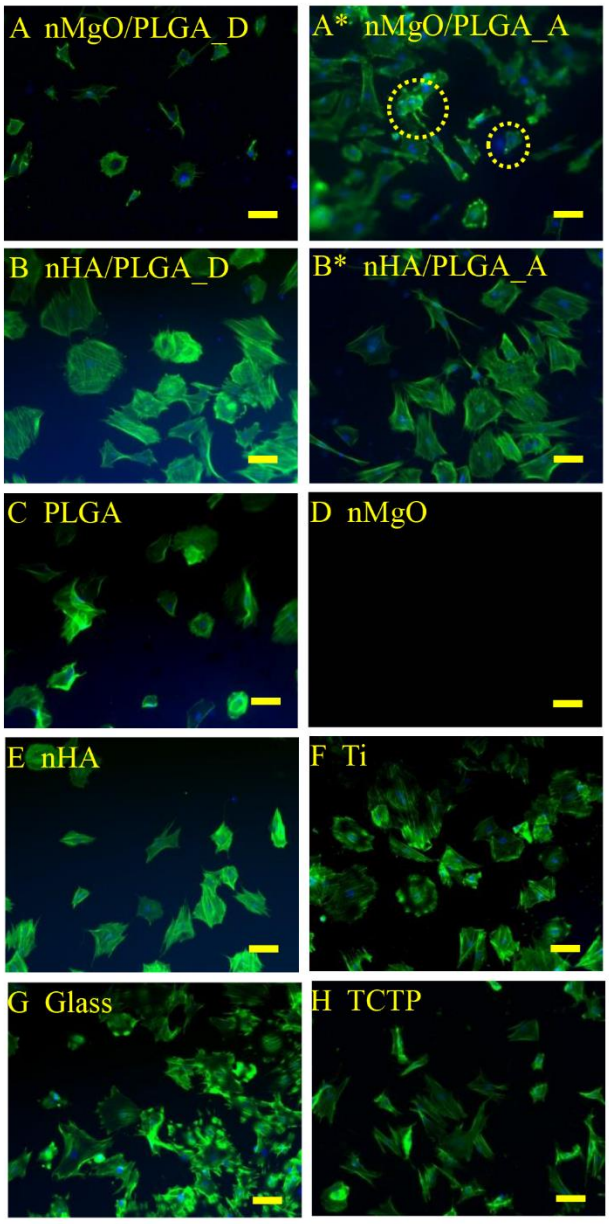

Figure 4.6: Representative fluorescence images of BMSCs that were directly cultured on the dispersed versus agglomerated nanocomposites for 24 hours compared with the single phase controls of PLGA, nMgO, and nHA, and the references of Ti, glass, and TCTP. TCTP is the Cells Only reference cultured on the plate. Yellow dashed circles highlight abnormal cell morphology. Blue stains nuclei and green stains F-actin. Scale bar = 100 μm.

Figure 4.5 shows the FTIR results of the nanocomposites with dispersed versus agglomerated nanoparticles, as well as the controls of PLGA, nMgO and nHA. The peaks for expected chemical groups were present. The peak at 1740 cm^{-1} is representative of C=O and was used as the main peak of PLGA. At the main PLGA peak, nMgO/PLGA_D, nMgO/PLGA_A, nHA/PLGA_D, and nHA/PLGA_A showed transmittance of 40%, 60%, 72% and 46%, respectively. The vibration of the main bond of Mg-O in nMgO cannot be detected at wavenumbers ranging from 500 to 4000 cm^{-1}. However, MgO is hygroscopic and it hydrates to form $Mg(OH)_2$ and the O-H bond was detected at 3700 cm^{-1}. The O-H peak at 3700 cm^{-1} is present in the nMgO sample and was used to detect nMgO in PLGA. At 3700 cm^{-1}, nMgO/PLGA_D and nMgO/PLGA_A showed the transmittances of 99% and 95%, respectively. The peak for phosphate, at 1000 cm^{-1}, was the representative peak for nHA. A small peak around 3550 cm^{-1} is present representing the hydroxide group of hydroxyapatite, which is consistent with previously published spectra from HA. At the 1000 cm^{-1} peak for nHA, nHA/PLGA_D and nHA/PLGA_A showed transmittance of 58% and 13% respectively.

4.3.4 Biological Properties of the Nanocomposites with Dispersed versus Agglomerated Nanoparticles

4.3.4a BMSC Adhesion and Morphology

BMSC morphology on nMgO/PLGA_D and nHA/PLGA_D appeared normal, though fewer cells were observed on nMgO/PLGA_D than on nHA/PLGA_D (Figure 4.6). While many cells were present on nMgO/PLGA_A and most of them appeared healthy with normal morphology, a few cells exhibited abnormal morphology, indicating signs of stress, as highlighted in Figure 4.6A*. Both nHA/PLGA_D and nHA/PLGA_A

samples exhibited well spread cells with healthy morphology. BMSCs cultured with PLGA controls, nHA particle controls, and the references of Ti and glass showed healthy morphology. However, the nMgO particle controls showed very few or no attached cells in the culture well.

BMSC adhesion density was calculated and normalized by the cell adhesion density for TCTP reference, as plotted in Figure 4.7. Specifically, cell adhesion density (CD) for each sample group (referred to as CD_x, where x is the sample type), was divided by the cell adhesion density on the TCTP reference (CD_{TCTP}), to achieve a unitless ratio, CD_x/CD_{TCTP}. The nMgO/PLGA_D exhibited significantly lower normalized cell density than the Ti and Glass references, while nMgO/PLGA_A exhibited significantly greater cell density than all the other groups and controls. Both nHA/PLGA_D and nHA/PLGA_A showed no statistically significant difference between each other and when compared with the Ti and Glass references.

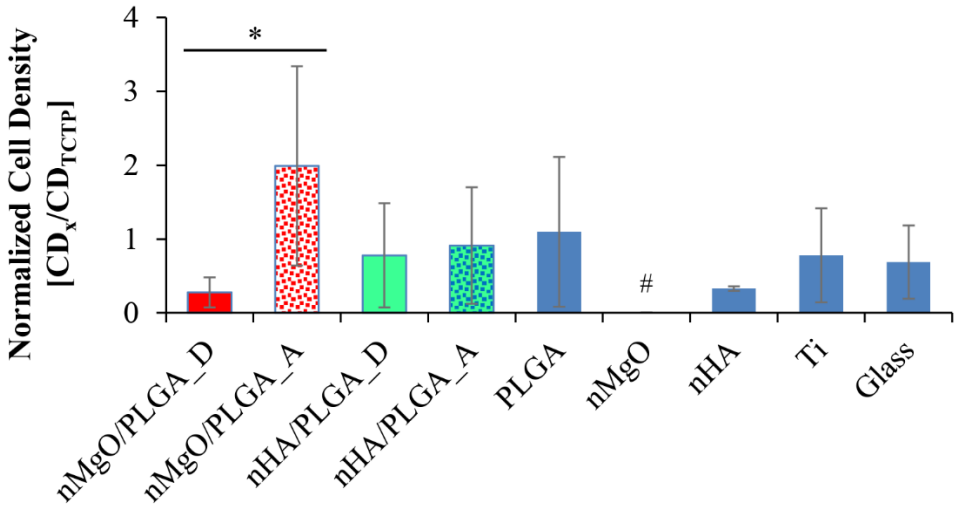

Figure 4.7: Normalized cell adhesion density of BMSCs after they were directly cultured on the dispersed versus agglomerated nanocomposites for 24 hours when compared with the single-phase controls of PLGA, nMgO, and nHA, and the references of Ti and glass. Values were normalized by the average cell density on TCTP reference. Values are mean ± standard error; n=15. #p<0.05 compared to the respective glass control for each time point. *p<0.05 compared to agglomerated counterpart.

The cell density ratio normalized by TCTP reference group is useful for comparing the respective nanocomposites with dispersed versus agglomerated nanoparticles directly, and the actual raw cell density values was reported in supplementary figures (Figure A2, Appendix A). For the nanocomposites with agglomerated nanoparticles, BMSC culture was extended to 48 and 72 hours in order to further evaluate BMSC responses to the nMgO/PLGA_A since we observed abnormal BMSC morphology at 24 hours. The raw cell adhesion density values and representative fluorescence images of the cells at 24, 48 and 72 hours for the nanocomposites with agglomerates were shown in Appendix A, Figure A2 and A3, respectively. At 24 hours, the average cell adhesion density on nMgO/PLGA_D was 2.3 x 10^3 cells/cm^2 and was 6.6

x 10^3 cells/cm^2 on nHA/PLGA_D. The average cell adhesion densities at 24 hours for the agglomerated samples, nMgO/PLGA_A and nHA/PLGA_A were 5.1 x 10^3 cells/cm^2 and 2.3 x 10^3 cells/cm^2, respectively. When comparing the nanoparticle controls of nMgO and nHA, the nMgO group showed almost no viable cells, while the nHA group showed some viable cells with a lower average cell density than the TCTP reference but not statistically significant. As the BMSC culture continued, we observed steady decrease in cell density after 48 and 72 hours of culture with nMgO/PLGA_A (Figure A2). The fluorescence images revealed a change in morphology of the BMSCs on the nMgO/PLGA_A after 48 and 72 hours as well (Figure A3, A″-A‴). The average cell density on nMgO/PLGA_D was significantly less than nMgO/PLGA_A; however, the average cell density for nHA/PLGA_D was significantly more than nHA/PLGA_A (Figure A2). The average spreading area of BMSCs on nMgO/PLGA_A decreased at 48 hours, when compared with the same cells at the 24-hour time point (Figure A3). At 72 hours, the few remaining cells showed little to no spreading on nMgO/PLGA_A.

4.3.4b Media Analyses of BMSC Culture

The degradation products of each component of the composites affects pH and thus, the first indication of possible degradation of the polymer nanocomposites is shown by pH in Figure 4.8A. Specifically, PLGA has acidic degradation products while MgO dissociates to release hydroxide. The pH of the media from nMgO/PLGA_D and nMgO/PLGA_A were both 8.3, which was a small but statically significant increase when compared to the TCTP reference. The pH from nMgO group was around 8.5-8.6 at

24-hour culture, greater than TCTP reference. The pH for all the other groups at 24 hours of culture, including nHA/PLGA_D ranged from 8.1 to 8.3 after 24 hours of culture.

To evaluate release and dissociation of nMgO, Mg^{2+} concentration in the post-culture media was measured, as shown in Figure 4.8B. The only samples that exhibited increase in Mg^{2+} concentration in media was nMgO/PLGA_D, nMgO/PLGA_A and nMgO, which had Mg^{2+} concentrations of 14.6 ± 1.4 mM, 12.1 ± 4.9 mM, and 36.2 ± 4.2 mM, respectively.

To evaluate release and dissociation of nHA, Ca^{2+} ion concentration in the post-culture media was measured, as shown in Figure 4.8C. Ca^{2+} concentrations in the media after culture with nMgO/PLGA_D and nMgO/PLGA_A were 1.30 ± 0.04 mM and 1.46 ± 0.06 mM, respectively. Ca^{2+} concentration in the media after culture with nHA/PLGA_D and nHA/PLGA_A were 1.37 ± 0.04 mM and 0.37 ± 0.01 mM, respectively, suggesting a statistically significant difference between them. Ca^{2+} concentrations in the control groups showed a large deviation, and no statistically significant differences were detected when compared with the TCTP reference with a Ca^{2+} concentration of 0.97 ± 0.69 mM. Both nMgO and nHA control groups showed lower average Ca^{2+} concentrations at 0.58 ± 0.4 mM and 0.49 ± 0.2 mM, respectively.

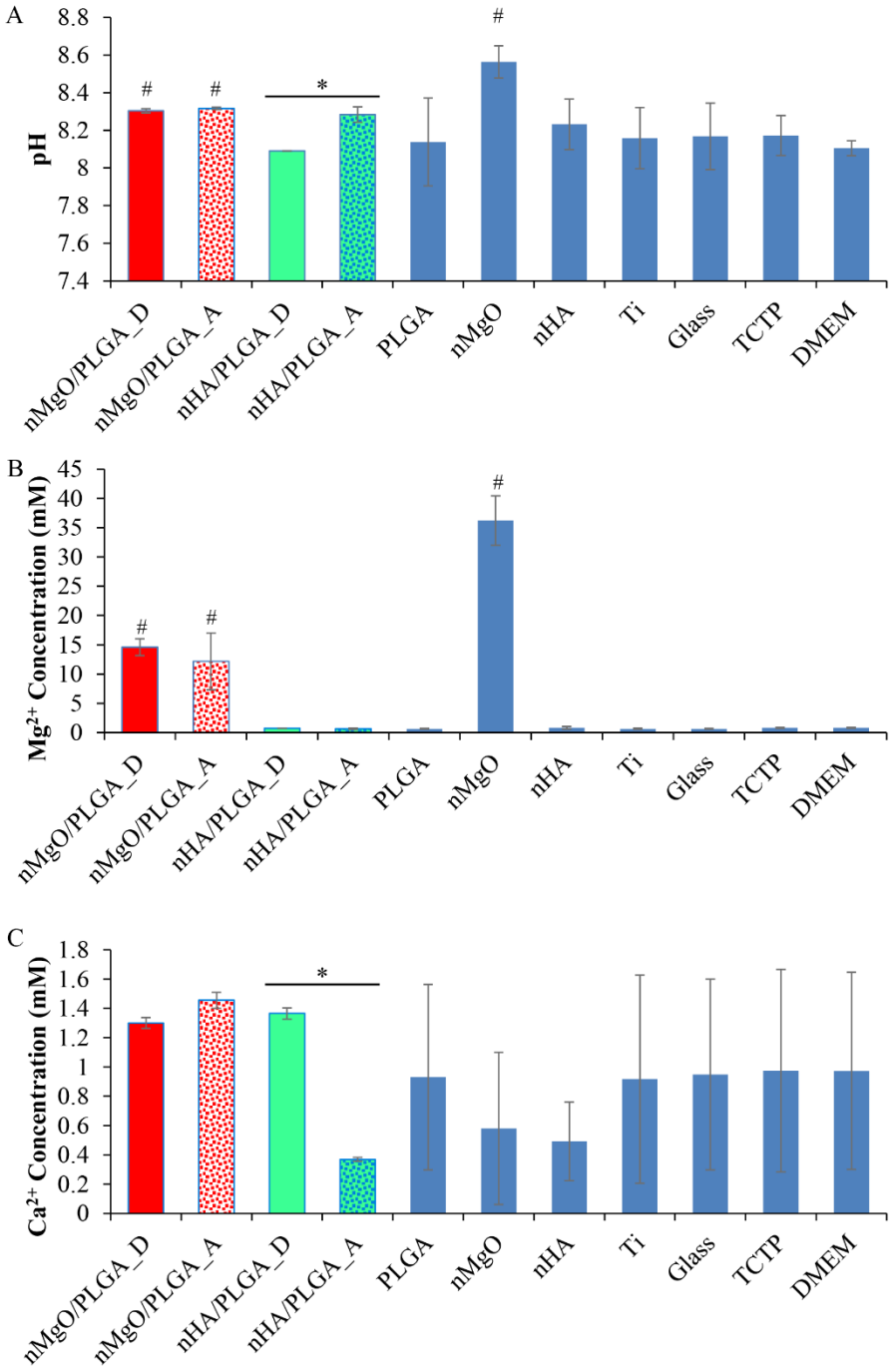

Figure 4.8: Media analyses after BMSCs were cultured with the nanocomposites and controls for 24 hours. (A) post-culture media pH, (B) Mg^{2+} ion concentration in the post-culture media, and (C) Ca^{2+} ion concentration in the post-culture media. Values are mean ± standard deviation; n=3. #p<0.05 compared to the TCTP (Cells Only) control. *p<0.05 compared to agglomerated counterparts.

Trends in pH change remained consistent at 48 and 72 hours for the nMgO/PLGA_A sample (Figure A4, Appendix A). At 48 and 72 hours, the nMgO/PLGA_A composite resulted in media pH of 8.25 and 8.24, respectively. These values, while statistically significant, exhibited small increase with respect to the other samples which remained around 8.1 and 8.0 at 48 and 72 hours, respectively (Figure A4A). The increase in pH from nMgO at 24 hours, did not continue at 48 and 72 hours, resulting in no statistical difference from the TCTP reference at these latter time points. All other conditions maintained pH similar to the TCTP reference at 48 and 72 hours and were not statistically different. Extended culture of nMgO/PLGA_A at 48 and 72 hours showed continuous release and dissociation of nMgO, but in a decreasing trend in average (Figure A4B). Specifically, the media concentration of Mg^{2+} in nMgO/PLGA_A, was 7.8 ± 1.3 mM and 6.9 ± 0.6 mM at 48 and 72 hours, respectively. Additionally, nMgO showed Mg^{2+} concentration of 2.8 mM at 48 hours, which was significantly less than the Mg^{2+} concentration of 36.2 ± 4.2 mM at 24 hours, suggesting that nMgO had a burst release of Mg^{2+} in the first 24 hours. The other groups exhibited no statistical difference in Mg^{2+} concentration when compared with the TCTP reference at 24, 48, and 72-hour time points with a Mg^{2+} concentration around 0.7 mM.

Ca^{2+} concentration showed no statistically significant difference after 48 hours of incubation with the nanocomposites and controls when compared with the TCTP reference (Figure A4C). However, at 72 hours, nHA exhibited significantly higher Ca^{2+} concentration at 0.7 ± 0.01 mM than the TCTP reference, possibly because nHA released detectable Ca^{2+} ions at the later time points. All the other samples at 48 and 72-hour time

points showed no statistically significant difference in Ca^{2+} concentration with respect to the TCTP reference.

4.4. Discussion

4.4.1 Methods for Dispersion of Nanoparticles in Polymers

Homogenous dispersion of nanoparticles in polymers typically involves mechanical mixing methods, modifications of surface chemistry of nanoparticles, or a combination of both. In this study, we focused on mechanical mixing methods to avoid additional concerns on chemical toxicity of surface modifiers for biomedical applications. The combination of high-power sonication and DAC mixing is the key for improved dispersion of nanoparticles in polymers for solvent casting because these two methods complement each other in breaking agglomerates in suspensions. High-power sonication works more effectively for suspensions of lower viscosity while DAC mixing works more effectively for suspensions of higher viscosity. By controlling the viscosity of polymer suspension, both high-power sonication and DAC mixing can be taken advantage of. Generally, more solvent should be used to dissolve the polymer to reduce the viscosity for high-power sonication, and less solvent should be used to increase the viscosity for DAC mixing. The ultrasonic energy produced around the probe of high-power sonicator can reduce local agglomeration effectively, and dispersion is more effective for the suspension closer to the probe of sonicator [28, 29]. However, sonication often induces air bubbles in the suspension, which leads to bubbles in as-cast composites. In contrast, DAC mixing can remove the bubbles with degassing. Furthermore, more viscous suspensions used for DAC mixing can decrease particle settling during the

solvent casting process according to Stokes law. Therefore, it is beneficial to include a DAC mixing step after sonication. The same combined methods of high-power sonication and DAC mixing were used for improving the dispersion of nMgO/PLGA and nHA/PLGA nanocomposites, but slight modification on the polymer/solvent ratio were needed for each type of nanocomposites. The combined methods of high-power sonication and DAC mixing not only can be used for improving dispersion of nanoparticles in polymer suspension for solvent casting, but also can be used to improve dispersion of nanoparticles in melted polymer for thermal extrusion or injection molding.

4.4.2 Comparison of the Nanocomposites with Dispersed versus Agglomerated Nanoparticles

Macroscopic and microscopic images of the nanocomposites confirmed the improvement of nanoparticle dispersion in the nanocomposites prepared by the new combined mechanical mixing process. Interestingly, SEM images of the top and bottom side of the solvent-cast nanocomposites showed different distribution of agglomerates in the nMgO/PLGA versus nHA/PLGA composite system. Both nMgO/PLGA_D and nMgO/PLGA_A showed larger agglomerates on the top side than on the bottom side of the scaffold after solvent casting, likely because the drag force (i.e., frictional force) prevented these agglomerates from settling downwards in the solvent casting process. Stokes' law describes the rate of settling of a particle in a viscous fluid under the assumptions that (1) the particle is in a spherical shape and does not interfere with other particles and (2) the fluid is homogeneous in composition and has a laminar flow. If the Stokes' law and its assumptions are applied to describe the settling of nanoparticles or their agglomerates during the solvent casting process, their terminal (i.e., settling)

velocity v (m/s) in the respective nanocomposite suspension can be expressed as the following:

$$v = \frac{2}{9}\frac{(\rho_p - \rho_f)gR^2}{\eta}$$

where ρ_p is the density of the particle (kg/m^3), ρ_f is the density of the fluid (kg/m^3), g is the gravitational acceleration (m/s^2), R is the radius of the particle (assumed as a sphere), and η is the dynamic viscosity (Pa·s). The settling velocity of the particle v is reached when the Stokes' drag force F_d balances the gravitational force F_g, i.e., $F_d = 6\pi\eta Rv = F_g = (\rho_p - \rho_f)g(\frac{4}{3}\pi R^3)$.

Stokes' law suggests that the particle would move vertically downwards if $\rho_p > \rho_f$ and upwards if $\rho_p < \rho_f$ and the larger agglomerates would have higher velocity than smaller agglomerates. The theoretical density of nMgO (3.58 g/cm^3) is greater than that of solvent (chloroform, 1.49 g/cm^3 at 25 °C) and PLGA (1.34 g/cm^3), and thus the smaller agglomerates of nMgO should have settled down slower than the larger agglomerates if the viscosity remained constant. However, the viscosity of polymer suspension increased after nMgO was added, likely because MgO has been shown to be a thickening agent for polyester resin [30]. The increased viscosity of nMgO/PLGA suspension could have increased the drag force, and trapped the larger agglomerates near the top surface of the suspension because of rapid solvent evaporation after casting. Moreover, MgO could react with carboxyl groups of polyesters to yield higher molecular weight polymeric salt, which could increase the density of the polymer suspension and further reduce the settling velocity [30]. Excess MgO was previously reported to increase

the viscosity of polyester resin by reacting with the polymeric salt and possibly form an interchain bonding through dipole interactions between MgO and salt units [30]. For further optimizing the polymer/solvent ratio and improving nanoparticle dispersion, viscosity of polymer solution and suspension with nanoparticles should be measured in the future.

In comparison, the nHA/PLGA_D shows smaller agglomerates than nMgO/PLGA_D on the top and bottom surface, despite the fact that nHA has an average diameter of 47 nm and a density of 3.16 g/cm^3, while nMgO has an average diameter of 23 nm and a density of 3.58 g/cm^3. The size (or diameter) and shape of the agglomerates in polymer suspension during casting might have played more significant role on homogeneity of nanocomposites than the theoretical density and particle size of nMgO and nHA because of $v \propto \Delta \rho$ in contrast to $v \propto R^2$(radius of agglomerates). Moreover, smaller particles might have higher surface energy and thus tend to agglomerate via Van der Waals forces and electrostatic interactions to lower their surface energy [31, 32], which might have contributed to the variance in agglomerate size of nMgO and nHA. However, it is more likely that the greater physicochemical interactions with the polymer, and the cubic crystal structure of nMgO caused the difference in the size and distribution of agglomerates in the nanocomposites and the formation of larger agglomerates, when compared with nHA under the same processing conditions.

4.4.3 Optical Properties of the Nanocomposites with Dispersed versus Agglomerated Nanoparticles

The nanocomposites with better dispersion of nanoparticles showed better optical transparency visually and quantitatively than their agglomerated counterparts. Larger

particles or agglomerates were reported to decrease optical transparency in the composites, while small individual nanoparticles could fit within the free volume of a polymer matrix and lead to enhanced optical transparency [32]. Well-dispersed nMgO/PLGA was 10% more transparent than its agglomerated counterpart, while well-dispersed nHA/PLGA was 27% more transparent that its agglomerated counterpart. It is possible that well dispersed nanoparticles filled the 'free volume' between polymer molecules and allowed for maximal optical transmission. For example, at the longer wavelengths, the optical transmission of nHA/PLGA_D was very close to PLGA control.

Between the two nanocomposite systems, nHA/PLGA_D and nHA/PLGA_A showed greater optical transmission than nMgO/PLGA_D and nMgO/PLGA_A. The smaller size of agglomerates in nHA/PLGA_D than in nMgO/PLGA_D likely contributed to its greater optical transmission. It is possible that the size of the nMgO agglomerates precluded them from entering the free volume in polymer and thus decreasing optical transparency, even though the individual nMgO had an average diameter of 23nm. The difference in optical properties of nMgO and nHA is probably another important factor that contributed to the different levels of optical transmission by the respective nanocomposites. MgO is capable of absorbing light, especially the UV light, which was confirmed in this study by the near zero transition of nMgO_PLGA at the UV range. At 900 nm, the nMgO/PLGA_D showed 67% less transmission than nHA/PLGA_D. Further research on the optical absorption, scattering and transmission of nMgO versus nHA would be useful. In the infrared (IR) region, nMgO/PLGA_D showed lower transmittance than nMgO/PLGA_A and nHA/PLGA_D showed higher

transmittance than nHA/PLGA_A, which differed from the transmittance at 300-900 nm. The vibration of the Mg-O bond after IR exposure did not result in defined peaks at wavenumbers ranging from 4000 to 500 cm^{-1}. However, the O-H bond was detected, possibly because MgO nanoparticles were hydrated to $Mg(OH)_2$ due to its hygroscopic nature. The lower transmittance of nMgO/PLGA_D than nMgO/PLGA_A, especially at the defined PLGA peaks, might be caused by greater nMgO interference with PLGA bond vibration. The FTIR results for nHA/PLGA was in agreement with optical transmittance in the 300-900 nm range; characteristic peaks of both nHA and PLGA showed lower transmission in nHA/PLGA_D than in nHA/PLGA_A.

4.4.4 The Effects of Dispersion on Biological Properties of the Nanocomposites

Degree of dispersion or agglomeration of nanoparticles in polymers affected BMSC adhesion and morphology even when the composition of nanocomposites, i.e., the weight ratio of nanoparticles to the polymer (30/70), remained the same. Many factors, including the chemistry, size, shape, and distribution of nMgO versus nHA nanoparticles, could have contributed to the observed BMSC adhesion and morphology on nMgO/PLGA and nHA/PLGA nanocomposites. While the nMgO/PLGA_D showed significantly lower cell density than nMgO/PLGA_A, the nHA/PLGA_D showed no statically significant difference in cell density when compared with nHA/PLGA_A (Figure 4.7). The increase of pH and Mg^{2+} released were not likely to be the cause of decreased cell density on the nMgO/PLGA nanocomposites because nMgO/PLGA_D and nMgO/PLGA_A showed similar effects on the pH and Mg^{2+}concentration in post-culture media (Figure 4.8) but drastically different cell density (Figure 4.7). Considering

that the control group of nMgO nanoparticles at 1600 μg/mL (equivalent to the amount added to the nanocomposites) induced significant cell death, it is possible that BMSCs had more direct contact with nMgO on the top surface of nMgO/PLGA_D than its agglomerated counterpart. Better dispersed nMgO on the surface of nMgO/PLGA_D increased its direct exposure (Figure 4.3), and thus increased its direct contact with BMSCs. The nMgO nanoparticles were previously reported to increase BMSC adhesion at a low concentration of 200 μg/mL and induced the death of BMSCs at the concentrations greater than 500 μg/mL [13]. The nMgO/PLGA_A increased cell density at the first 24 hours of culture likely because agglomeration reduced direct contact of nMgO with BMSCs and the concentration of nMgO on the top surface was at a low level beneficial to cells. However, the cell density on nMgO/PLGA_A steadily decreased at the 48 and 72 hours of culture (Figure A2, Appendix A), likely because nMgO was released when PLGA started to degrade, and the concentration of nMgO on the top surface reached a higher level that was toxic to cells.

In contrast to nMgO/PLGA, the nHA/PLGA_D showed similar cell density as nHA/PLGA_A, both similar to the cell density on the glass reference. The cell density in the nHA control group was lower in average, but nHA in the form of sintered devices or coatings was known to be cytocompatible [34-36]. The reduced cell density in the nHA control group was most likely because it was in the form of free particles in the media rather than a sintered bulk sample. Free flowing of nanoparticles in the media might interfere with cell adhesion because their motion on the bottom of the culture well could induce shear force and detach the cells.

In addition to the chemistry difference between nMgO and nHA, the surface roughness induced by their dispersion in respective nanocomposites could also differ and thus affect cell adhesion. For example, enhanced osteoblast adhesion and long-term functions were previously reported when titanium oxide (TiO_2) nanoparticles were ultrasonically dispersed in PLGA and produced nanometer surface roughness similar to bone [37]. Interestingly, osteoblast adhesion and functions initially increased when the sonication power used for dispersing TiO_2 nanoparticles in PLGA suspension increased and then decreased to some degree when the sonication power continued to increase and dispersion of TiO_2 nanoparticles continued to improve. This was attributed to the surface roughness of TiO_2/PLGA nanocomposites being the closest to bone when the sonication power and the dispersion was at the intermediate level [37]. This suggested that there was a threshold at which cells no longer exhibit favorable responses to increased dispersion when the resulting surface roughness passed the optimal level [37]. The lack of statistically significant difference in normalized cell density on nHA/PLGA_D and nHA/PLGA_A (Figure 4.7) seems to be in agreement with this. The nHA/PLGA nanocomposites prepared in this study had a higher level of dispersion than the previous studies on nHA/polymer nanocomposites [38, 39] based on the higher degree of optical transmission.

Interestingly, Hickey et. al evaluated the cell adhesion and growth on nMgO/PLLA (with 20% and 10% MgO) composites up to 5 days, and reported that nMgO/PLLA exhibited greater cell growth than HA/PLLA and PLLA alone [40]. The SEM images of these composites in literature [40] were very similar to our

nMgO/PLGA_A, indicating that the nMgO/PLGA_D prepared in our study had a higher level of dispersion. This might be one of the reasons contributing to different cell responses observed. In contrast with our nMgO/PLGA_A sample, Hickey, et. al. did not show cell death up to 5 days. This might be because of the lower loading of nMgO, which was at 10% and 20%, as opposed to 30% for our study. Moreover, PLGA is known to degrade faster than PLLA, which probably caused more rapid release of nMgO from the nMgO/PLGA in the first 3 days.

Currently, there are no standard methods to quantify the dispersion of nanoparticles in polymer matrix; and thus it is difficult to directly compare the properties of ceramic/polymer nanocomposites across different studies in literature. In particular, cell responses to nanocomposites could be affected by many other factors in addition to the level of nanoparticle dispersion. The optical absorbance/transmission measurements reported in our study could be good candidates to fulfill the need for standard quantification of nanoparticle dispersion in polymers, considering that most biodegradable polyesters used in biomedical applications have a high degree of transparency.

4.5 Conclusion

This chapter reported the combination of DAC mixing and high-powered sonication for improving dispersion of ceramic nanoparticles in polymer based nanocomposites, specifically for nMgO/PLGA and nHA/PLGA systems. Microstructural characterization confirmed that our new mechanical mixing processes improved nanoparticle dispersion in nMgO/PLGA and nHA/PLGA nanocomposites. Improved

nanoparticle dispersion increased the optical transparency of the nanocomposites visually and enhanced optical transmission for both nHA/PLGA and nMgO/PLGA nanocomposites. Improved dispersion of the nanoparticles enhanced cell adhesion on nHA/PLGA but decreased cell viability on nMgO/PLGA. This difference is likely because the chemistry of nHA and nMgO had different effects on cells. Increased direct contact with nHA may be beneficial for cells while increased direct contact with nMgO may not. This study provided a new process for enhancing dispersion of nanoparticles in a polymer matrix and revealed the effects of improved dispersion on optical properties and cell responses for potential biomedical applications. The homogenously dispersed nanoparticles in polymers may be used for a wide variety of applications, e.g., as coating materials for medical implants or as an ink material for 3D printing of different implantable devices.

4.6 Acknowledgements

The authors thank the support from the U.S. National Science Foundation (NSF award CBET 1512764), the Burroughs Wellcome Fund (1011235), the Hellman Faculty Fellowship (HL), and the University of California (UC) Regents Faculty Development Award (HL). The authors appreciate the Central Facility for Advanced Microscopy and Microanalysis (CFAMM) for the use of SEM FEI XL30 at the University of California at Riverside. The authors would also like to recognize Qiaomu Tian for assistance with FTIR measurements.

Any opinions, findings, and conclusions or recommendations expressed in this material are those of the author(s) and do not necessarily reflect the views of the National Science Foundation.

4.7 References

1. Kickelbick, G., *The search of a homogeneously dispersed material - the art of handling the organic polymer/metal oxide interface.* Journal of Sol-Gel Science and Technology, 2008. **46**(3): p. 281-290.
2. Wong, S.G., Mai, Y.W., *Performance Synergism in Polymer-Based Hybrid Materials*, in *Advanced Polymeric Materials: Structure Property Relationshhips*, G.O. Shonaike, Advani, S.G., Editor. 2003, CRC Press. p. 439-471.
3. Suslu, A., et al., *Effect of surfactant types on the biocompatibility of electrospun HAp/PHBV composite nanofibers.* J Mater Sci Mater Med, 2014. **25**(12): p. 2677-89.
4. Nguyen, V.S., D. Rouxel, and B. Vincent, *Dispersion of nanoparticles: from organic solvents to polymer solutions.* Ultrason Sonochem, 2014. **21**(1): p. 149-53.
5. Fielding, G.A., W. Smoot, and S. Bose, *Effects of SiO2, SrO, MgO, and ZnO dopants in tricalcium phosphates on osteoblastic Runx2 expression.* J Biomed Mater Res A, 2014. **102**(7): p. 2417-26.
6. Kum, C.H., et al., *A poly(lactide) stereocomplex structure with modified magnesium oxide and its effects in enhancing the mechanical properties and suppressing inflammation.* Small, 2014. **10**(18): p. 3783-94.
7. Patel, M.K., et al., *Biocompatible nanostructured magnesium oxide-chitosan platform for genosensing application.* Biosens Bioelectron, 2013. **45**: p. 181-8.
8. Pourdanesh, F., et al., *In vitro and in vivo evaluation of a new nanocomposite, containing high density polyethylene, tricalcium phosphate, hydroxyapatite, and magnesium oxide nanoparticles.* Mater Sci Eng C Mater Biol Appl, 2014. **40**: p. 382-8.
9. Tarafder, S., et al., *SrO- and MgO-doped microwave sintered 3D printed tricalcium phosphate scaffolds: Mechanical properties and in vivo osteogenesis in a rabbit model.* J Biomed Mater Res B Appl Biomater, 2014.
10. Carpenter, T.O., et al., *A randomized controlled study of effects of dietary magnesium oxide supplementation on bone mineral content in healthy girls.* J Clin Endocrinol Metab, 2006. **91**(12): p. 4866-72.
11. Nygren, H., et al., *Increase of Compact Bone Thickness in Rat Tibia after Implanting MgO into the Bone Marrow Cavity.* J Funct Biomater, 2014. **5**(3): p. 158-66.
12. Khandaker, M., Y. Li, and T. Morris, *Micro and nano MgO particles for the improvement of fracture toughness of bone-cement interfaces.* J Biomech, 2013. **46**(5): p. 1035-9.
13. Wetteland, C.L., N.Y. Nguyen, and H. Liu, *Concentration-dependent behaviors of bone marrow derived mesenchymal stem cells and infectious bacteria toward magnesium oxide nanoparticles.* Acta Biomater, 2016. **35**: p. 341-56.
14. da Cunha, M.R., et al., *Osteoconductive capacity of hydroxyapatite implanted into the skull of diabetics.* J Craniofac Surg, 2011. **22**(6): p. 2048-52.

15. Lin, L., Chow, K.L., Leng, Y., *Study of hydroxyapatite osteoinductivity with an osteogenic differentiation of mesenchymal stem cells.* Journal of Biomedical Materials Research Part A, 2009. **89A**(1): p. 326-335.
16. Liu, H. and T.J. Webster, *Nanomedicine for implants: a review of studies and necessary experimental tools.* Biomaterials, 2007. **28**(2): p. 354-69.
17. Lock, J., T.Y. Nguyen, and H. Liu, *Nanophase hydroxyapatite and poly(lactide-co-glycolide) composites promote human mesenchymal stem cell adhesion and osteogenic differentiation in vitro.* J Mater Sci Mater Med, 2012. **23**(10): p. 2543-52.
18. Lock, J. and H. Liu, *Nanomaterials enhance osteogenic differentiation of human mesenchymal stem cells similar to a short peptide of BMP-7.* Int J Nanomedicine, 2011. **6**: p. 2769-77.
19. Liu, H., Webster, T.J., *Mechanical properties of dispersed ceramic nanoparticles in polymer composites for orthopedic applications.* Int J Nanomedicine, 2010. **5**: p. 299-313.
20. Liu, H., Webster, T.J., *Enhanced Biological and Mechanical Properties of Well-Dispersed Nanophase Ceramics in Polymer Composites: From 2D to 3D Printed Structures.* Materials Science and Engineering: C, 2011. **31**(2): p. 14.
21. Johnson, I., K. Akari, and H. Liu, *Nanostructured hydroxyapatite/poly(lactic-co-glycolic acid) composite coating for controlling magnesium degradation in simulated body fluid.* Nanotechnology, 2013. **24**(37): p. 375103.
22. Ebrahimian-Hosseinabadi, M., et al., *Evaluating and Modeling the Mechanical Properties of the Prepared PLGA/nano-BCP Composite Scaffolds for Bone Tissue Engineering.* Journal of Materials Science & Technology, 2011. **27**(12): p. 1105-1112.
23. Loo, S.C., et al., *Synthesis and hydrothermal treatment of nanostructured hydroxyapatite of controllable sizes.* J Mater Sci Mater Med, 2008. **19**(3): p. 1389-97.
24. Yixiang, D., et al., *Degradation of electrospun nanofiber scaffold by short wave length ultraviolet radiation treatment and its potential applications in tissue engineering.* Tissue Eng Part A, 2008. **14**(8): p. 1321-9.
25. Iskandar, M.E., A. Aslani, and H. Liu, *The effects of nanostructured hydroxyapatite coating on the biodegradation and cytocompatibility of magnesium implants.* J Biomed Mater Res A, 2013. **101**(8): p. 2340-54.
26. Cipriano, A.F., et al., *Investigation of magnesium-zinc-calcium alloys and bone marrow derived mesenchymal stem cell response in direct culture.* Acta Biomater, 2015. **12**: p. 298-321.
27. Malina, D., K. Biernat, and A. Sobczak-Kupiec, *Studies on sintering process of synthetic hydroxyapatite.* Acta Biochim Pol, 2013. **60**(4): p. 851-5.
28. Noroozi, M., Radiman, S. , and Zakaria, A., *Influence of Sonication on the Stability and Thermal Properties of Al_2O_3 Nanofluids.* Journal of Nanomaterials, 2014: p. 10.

29. Liu, H. and T. Webster, *Enhanced biological and mechanical properties of well-dispersed nanophase ceramics in polymer composites: from 2D to 3D printed structures.* Materials Science and Engineering, 2011. **31**(2): p. 77-89.
30. Alvey, F.B., *Study of Reaction of Polyester Resins with Magnesium Oxide.* Journal of Polymer Science Part a-1-Polymer Chemistry, 1971. **9**(8): p. 2233-&.
31. Tomas, J., *Adhesion of ultrafine particles--A micromechanical approach.* Chemical Engineering Science, 2006. **62**: p. 14.
32. Smith, G.D. and D. Bedrov, *Dispersing nanoparticles in a polymer matrix: are long, dense polymer tethers really necessary?* Langmuir, 2009. **25**(19): p. 11239-43.
33. Naganuma, T. and Y. Kagawa, *Effect of particle size on the optically transparent nano meter-order glass particle-dispersed epoxy matrix composites.* Composites Science and Technology, 2002. **62**(9): p. 1187-1189.
34. Ergun, C., et al., *Increased osteoblast adhesion on nanograined hydroxyapatite and tricalcium phosphate containing calcium titanate.* Journal of Biomedical Materials Research Part A, 2007. **80A**(4): p. 990-997.
35. Ergun, C., et al., *Increased osteoblast adhesion on nanoparticulate calcium phosphates with higher Ca/P ratios.* Journal of Biomedical Materials Research Part A, 2008. **85A**(1): p. 236-241.
36. Iskandar, M.E., A. Aslani, and H. Liu, *The effects of nanostructured hydroxyapatite coating on the biodegradation and cytocompatibility of magnesium implants.* Journal of Biomedical Materials Research Part A, 2013. **101A**(8): p. 2340-2354.
37. Liu, H., E.B. Slamovich, and T.J. Webster, *Increased osteoblast functions among nanophase titania/poly(lactide-co-glycolide) composites of the highest nanometer surface roughness.* Journal of Biomedical Materials Research Part A, 2006. **78A**(4): p. 798-807.
38. Lock, J., T.Y. Nguyen, and H. Liu, *Nanophase hydroxyapatite and poly(lactide-co-glycolide) composites promote human mesenchymal stem cell adhesion and osteogenic differentiation in vitro.* J Mater Sci Mater Med, 2012.
39. Lock, J. and H. Liu, *Nanomaterials enhance osteogenic differentiation of human mesenchymal stem cells similar to a short peptide of BMP-7.* Internation Journal of Nanomedicine, 2011(6): p. 1-9.
40. Hickey, D.J., et al., *Adding MgO nanoparticles to hydroxyapatite-PLLA nanocomposites for improved bone tissue engineering applications.* Acta Biomater, 2015. **14**: p. 175-84.

Chapter 5: Cell Response to Triphasic Polymer/Ceramic Nanocomposites with Hydroxyapatite and Magnesium Oxide

5.1 Introduction

Magnesium oxide nanoparticles (nMgO) are of increasing interest in the field of bone regeneration for their potential benefits on bone forming cells [1-5]. In low concentrations, such as 200 µg/mL, nMgO has been shown to improve proliferation of bone marrow derived mesenchymal stem cells (BMSCs). However, nMgO has negative effects on BMSCs at concentrations exceeding 300 µg/mL. It is necessary to decrease with the concentration of nMgO to mitigate potentially toxic effects while maintaining beneficial effects, like increased proliferation. Previous studies have utilized nMgO in composites with biodegradable polymers, poly (L-lactic acid) (PLLA) and poly (lactic-co-glycolic acid) (PLGA) for bone regeneration applications [2]. The dispersion of nMgO, as well as the degradation rate of the polymer matrix, play vital roles in cell-material behavior for these composites. It has been shown that 30% of nMgO dispersed in PLGA decreased cell viability. Therefore, tour goal was to make a triphasic nanocomposite of nMgO, nano-hydroxyapatite (nHA), and PLGA to decrease the percentage of nMgO while maintaining a particle to polymer weight ratio of 3/7, which has been shown to yield increased mechanical properties [6].

Hydroxyapatite is a well-established calcium phosphate similar to natural occurring bone mineral. Nano-hydroxyapatite has been shown to be both osteoconductive and osteoinductive [7-9], which is essential for bone regeneration. However, naturally occurring bone mineral is a calcium deficient form of hydroxyapatite, which is in contrast to hydroxyapatite synthetically produced via wet precipitation[10, 11]. As such, dopants

are sometimes added to synthesize hydroxyapatite to produce mineral more similar to that of natural bone, with Mg^{2+} as a common dopant. Studies show that cells exposed to calcium magnesium phosphate exhibited higher preosteoblast density and higher expression of RUNX2, osteopontin, and alkaline phosphatase (ALP) than hydroxyapatite alone [12]. Evidence supports a cooperative effect of Mg^{2+} and Ca^{2+} for increased cell proliferation and osteogenic activity of bone forming cells [12, 13]. Therefore, we investigated the effect a PLGA matrix loaded with nMgO, which dissociates to release Mg^{2+} in physiological solutions, and hydroxyapatite in order to evaluate potential cooperative effects between these materials on cell adhesion. Herein, we report the effect of PLGA/HA/MgO, with weight ratios of 70/20/10, 70/25/5, and 70/29/1 on BMSCs.

5.2 Materials and Methods

5.2.1 Preparation of MgO

MgO nanoparticles were procured from US Research Nanomaterials Inc. (US3310, 99+% purity, 20nm diameter). In order to compare our results to previous and future cell studies, the MgO was sterilized prior to exposure to physiologically relevant solutions. MgO nanoparticles were sterilized in a glass container via heating at 200°C in an oven for one hour.

5.2.2 Preparation of HA

Hydroxyapatite was synthesized through wet precipitation as previously published [14, 15]. Briefly, 1M $Ca(NO_3)_2$ was added drop-wise to 0.6M $(NH_4)_2HPO_4$ at 40°C at a rate of 30 drops per minute. This mixture underwent stirring for 20 hours to allow formation of nHA. The resulting particle and solution mixture was centrifuged at 3000

rpm for 1 minute. The supernatant was discarded and the particles were resuspended in deionized (DI) water. Centrifuging and rinsing in DI was repeated 3 times to remove excess ammonia. The pellet was then resuspended in DI and transferred to an acid digestion bomb for hydrothermal treatment at 200°C for 20 hours. The suspension was then collected and centrifuged, followed by removal of the supernatant. The resulting particles were dried under vacuum at 80°C for 12 hours and then ground using a mortar and pestle. Prior to use in composites or cell culture, the nHA was disinfected by heating in an oven at 200°C for 1 hour.

	Abbreviations	Material Components (mg)			Component Concentration in Culture (mg/mL)			Comments
		PLGA	HA	MgO	PLGA	HA	MgO	
Triphasic Nanocomposites	P70/H20/M10	12	3.4	1.7	4	1.13	0.56	
	P70/H25/M5	11.6	4.2	0.8	3.86	1.4	0.26	
	P70/H29/M1	11.4	4.7	0.2	3.8	1.56	0.06	
Biphasic Nanocomposites	P70/H20	12	3.4	0	4	1.13	0	P70/H20/M10-M10
	P70/H25	11.6	4.2	0	3.86	1.4	0	P70/H25/M5-M5
	P70/H29	11.4	4.7	0	3.8	1.56	0	P70/H29/M1-M1
	P70/H30	11.3	4.9	0	3.76	1.63	0	
	P70/M30	11.5	0	4.9	3.83	0	1.63	
	P70/M10	12	0	1.7	4	0	0.56	P70/H20/M10-H20
	P70/M5	11.6	0	0.8	3.86	0	0.26	P70/H25/M5-H25
	P70/M1	11.4	0	0.2	3.8	0	0.06	P70/H29/M1-H29
	H20/M10	0	3.4	1.7	0	1.13	0.56	P70/H20/M10-P70
	H25/M5	0	4.2	0.8	0	1.4	0.26	P70/H25/M5-P70
	H29/M1	0	4.7	0.2	0	1.56	0.06	P70/H29/M1-P70
Single-Phase Controls	P70	12	0	0	4	0	0	P70/H20/M10-H20-M10
	H20	0	3.4	0	0	1.13	0	P70/H20/M10-P70-M10
	H25	0	4.2	0	0	1.4	0	P70/H25/M5-P70-M5
	H29	0	4.7	0	0	1.56	0	P70/H29/M1-P70-M1
	H30	0	4.9	0	0	1.63	0	P70/301-P70
	M30	0	0	4.9	0	0	1.63	P70/M30-P70
	M10	0	0	1.7	0	0	0.56	P70/H20/M10-P70-H20
	M5	0	0	0.8	0	0	0.26	P70/H25/M5-P70-H25
	M1	0	0	0.2	0	0	0.06	P70/H29/M1-P70-H29

Table 5.1: Composition of PLGA/HA/MgO and subsequent biphasic and single-phase controls. Amounts of each component are given as mass in mg for a single 1 cm^2 scaffold. Relationships between composites and controls are shown in the "Comments" column. For example, the comment for P70/H20 is 'P70/H20/M10-M10', which indicates that P70/H20 is a control for P70/H20/M10 and is similar to that sample but subtracted the 10% MgO (M10).

5.2.3 Nanocomposites

5.2.3a Synthesis

Composites were synthesized via mechanical dispersion and solvent casting as previously described in Chapter 4. PLGA/HA/MgO composites maintained a weight ratio of 7/3 polymer/nanoparticles. The 30% nanoparticles were split between HA and MgO as 20/10, 25/5, and 29/1 and compared with biphasic nanocomposites of PLGA/MgO and PLGA/HA where each nanoparticle represented the whole 30%. Controls were developed for each triphasic composite. The amount of each component present in a scaffold is detailed in Table 5.1.

In a 20mL vial, 0.443g of PLGA (90:10 LA:GA, MW 125kDa, AP49, Polyscitech) was added to 3.5mL of chloroform ($CHCl_3$, Fisher Scientific). The resulting solution was sonicated in a low power ultrasonic bath (Symphony, VWR) at 40°C for 1 hour to fully dissolve the polymer. Then HA was added to the solution and incorporated by vortexing for 1 minute, followed by speedmixing (DAC 150.1 FVZ-K, FlackTek, Inc.) at 2500 rpm for 5 minutes. The suspension then underwent high-powered probe sonication (Qsonica, Q125) for 10 minutes, with pulses of 5 seconds on and 5 seconds off. The suspension underwent a total of 3 cycles of high-powered sonication and speedmixing, ending with speedmixing at 3500 rpm for 5 minutes. The suspension was then poured into a 8.3 cm by 4 cm Teflon dish, where the chloroform was allowed to evaporate in air for 24 hours. The nanocomposite was then placed back into a 20 mL vial and 4 mL of chloroform was added. Low-powered sonication, speedmixing, and high-powered sonication were performed using the same cycles as the previous day. The

suspension was then poured into a Teflon dish where chloroform was allowed to evaporate for 24 hours in ambient conditions followed by an additional 48 hours of evaporation under vacuum. All biphasic controls, including PLGA/HA, were synthesized using this same protocol. However, PLGA/MgO with 70/30 wt%, utilized 4.5 mL of chloroform for the first round of suspension and 4 mL of chloroform during the second round of suspension. This was necessary in samples with 30% MgO because of the interactions of MgO with polyesters that result in increase in viscosity [16].

The resulting scaffolds were cut to 10 mm by 10 mm squares with a thickness of 0.1 mm to be used in cell studies. Each scaffold was disinfected by soaking in 100% ethanol for 24 hours before use in cell culture.

5.2.3b Characterization

A representative scaffold from each group was characterized via scanning electron microscopy (SEM, Philips XL30) to evaluate surface topography and energy dispersive x-ray spectrometry (EDS) to confirm elemental composition. In preparation for SEM/EDS analysis, each composite was adhered to an aluminum SEM pin mount with copper tape. The mounted samples were then coated with platinum and palladium (Pt/Pd) using a sputter-coater (108 Auto, Cressington). All SEM images were taken using a secondary electron detector at an accelerating voltage of 2 kV, a spot size of 3, a working distance of 10mm, and at a magnification of 10,000x. EDS was performed on the entire image area under the same conditions, except accelerating voltage was raised to 10 kV.

5.2.4 BMSC culture

5.2.4a Cell Culture

Bone marrow derived mesenchymal stem cells (BMSCs) were extracted from the femur and tibia of Sprague Dawley rat weanlings according to previously established protocols, approved by the Institutional Animal Care and Use Committee (IACUC) at the University of California at Riverside [5, 14, 15]. BMSCs were cultured in Dulbecco's Modified Eagle's Medium (DMEM) with 10% fetal bovine serum (FBS) and 1% penicillin/streptomycin (P/S) by volume, herein referred to as just DMEM. BMSCs were cultured in standard cell culture conditions at 37°C, with 5% CO_2/95% air in a humidified environment (MCO-19AIC, Sanyo Scientific). BMSCs at their second passage were cultured to 90% confluency for use in cell experiments.

5.2.4b Culture on Nanocomposites

Nanocomposites were placed in wells of 12-well tissue culture treated plates (TCTP, Corning, Falcon® 353043). Each composite was placed into its respective well and then rinsed with 2 mL of phosphate buffered saline. Then 1 mL of DMEM was added to each composite well. Mass of nanoparticles and the resulting concentration for bare nanoparticles are shown in Table 5.1. Nanoparticles were suspended via pipetting in 1 mL of DMEM and transferred to their respective wells. BMSCs at the second passage were seeded at a density of 10,000 cells/cm^2 directly onto the disinfected scaffolds in 2 mL of DMEM, bringing the total media volume in each well to 3 mL. Cells were cultured for 24 hours on all scaffolds. PLGA/HA/MgO with a weight ratio of 70/20/10 (P70H20M10), PLGA/MgO with a weight ratio of 70/30 (P70M30), and the controls for

these samples were eliminated based on decreased cell adhesion at 24 hours. The remaining samples underwent culture to 48 hours. Media was exchanged every 24 hours. At the end of each respective time point, media was collected for further analysis. BMSCs were fixed with 4% paraformaldehyde in PBS and stained with 4',6-Diamidino-2-Phenylindole, Dihydrochloride (DAPI, Life Technologies) and Alexa Fluor® 488 phalloidin (Life Technologies) to image the nuclei and cytoskeleton, respectively. BMSCs were imaged under a fluorescence microscope (Nikon Eclipse Ti) and 10 images were collected for each well. Composite images were made and cells were counted using ImageJ. Then cell density was calculated as adherent cells per area.

5.2.4c Post-culture Media Analysis

Immediately after collection, the pH of the media was determined using a benchtop pH meter (Symphony SB70P, VWR) to limit effects of atmospheric CO_2 on the bicarbonate buffering system present in DMEM. Each media sample was then diluted 1:100 in DI water to prepare for analysis via induced coupled plasma – optical emission spectrometry (ICP-OES, Optima 8000, Perkin Elmer). ICP-OES analysis was used to obtain media concentrations of Mg^{2+} and Ca^{2+} in order to evaluate the release of ions from the composites. Solutions of Mg and Ca at concentrations of 0.5 ppm, 1 ppm, and 5 ppm in nitric acid were used to generate a calibration curve for all Mg and Ca measurements, respectively. Measurements were reported as mg/L for Mg and µg/L for Ca. These values were then converted to mM by dividing by the molecular weight of Mg (24.305 g/mol) and Ca (40.078 g/mol) for each and dividing by 1000 in the case of Ca to convert µM to mM.

5.2.5 Statistical Analysis

All experiments were run in triplicate. All data sets were analyzed using one-way analysis of variance (ANOVA) followed by the Tukey highest significant difference post hoc test. Statistical significance was considered at $p < 0.05$.

5.3 Results

5.3.1 Characterization of Nanocomposites

SEM was utilized to show surface topography of triphasic composites and controls (Figure 5.1). P70/H20/M10, P70/H25/M5, and P70/29/M1 exhibited fairly homogenous particle distribution, though P70/H20/M10 and P70/H25/M5 exhibited larger agglomerates than P70/H29/M1. PLGA/HA controls showed similar topographies to that of their PLGA/HA/MgO counterparts. PLGA/MgO controls exhibited even distribution of visible MgO particles. However, P70/M5 showed presence of larger agglomerates of MgO. P70/M1 also showed presence of ripples in PLGA that may have been formed during handling (i.e. removal from mold, cutting to size) of composite.

EDS was utilized to confirm the elemental composition of each composite (Figure 5.2). As expected, PLGA/HA/MgO composites showed measurable calcium, phosphorus, magnesium, oxygen, and carbon. PLGA is a source of carbon and oxygen, hydroxyapatite is a source of calcium, phosphorus, and oxygen, and MgO is a source of magnesium and oxygen. P70/H20/M10 showed 6.83% Ca, 6.09% P, 5.00% Mg, 21.73% O, and 60.35% C. P70/H25/M5 showed 5.66% Ca, 5.51% P, 2.71% Mg, 28.38% O, and 52.28% C. P70/H29/M1 showed 9.8% Ca, 6.85% P, 0.93% Mg, 28.14% O, and 54.28% C. All in atomic percent.

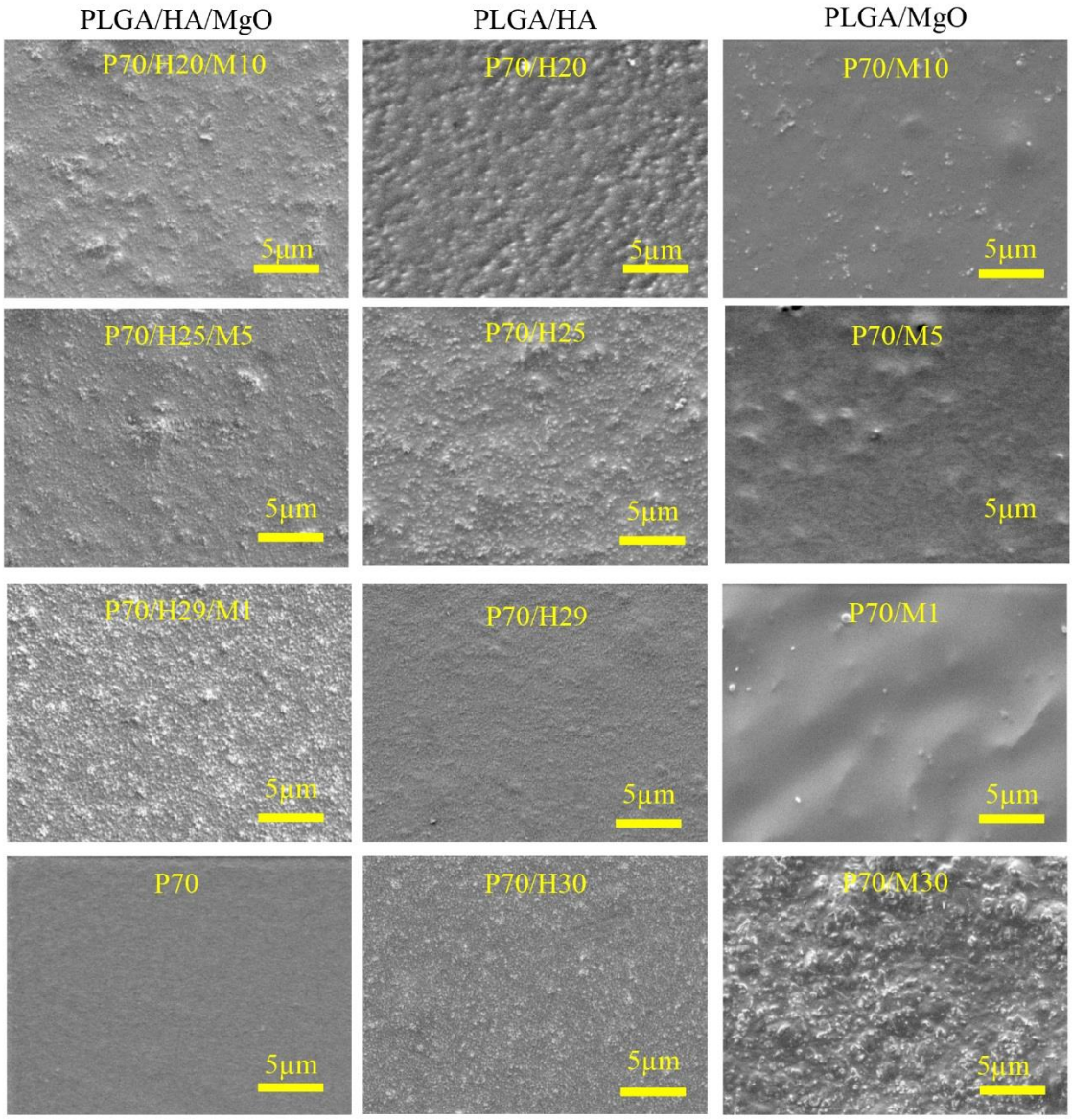

Figure 5.1: SEM micrographs of the surface of PLGA/HA/MgO scaffolds and subsequent controls.

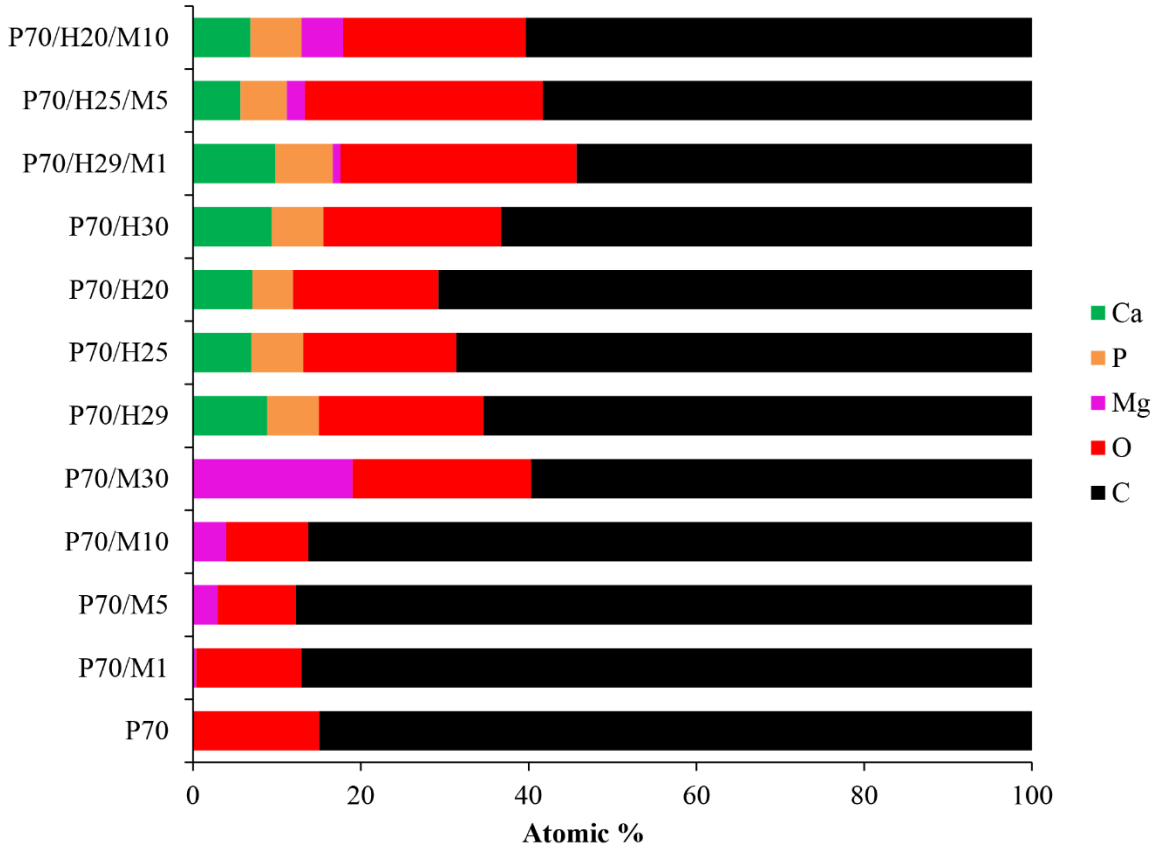

Figure 5.2: Quantified Atomic % of elements present in PLGA/HA/MgO and control scaffolds determined by EDS analysis.

5.3.2 BMSC culture

Fluorescence microscopy images of cells that were adhered to the sample after 24 hours of culture showed healthy cell morphology for each PLGA/HA/MgO composite (Figure 5.3). Each control and reference also showed cells with healthy morphology. However, P70/M30 (D′, Figure 5.3) showed visibly less cells with relatively smaller cell bodies. After 24 hours, cells adhered to the plate surrounding the samples also exhibited healthy morphology (Figure 5.4). Wells with nanoparticles showed less cells, with H20/M10 (D, Figure 5.4) and M30 (F‴, Figure 5.4) showing the least amount.

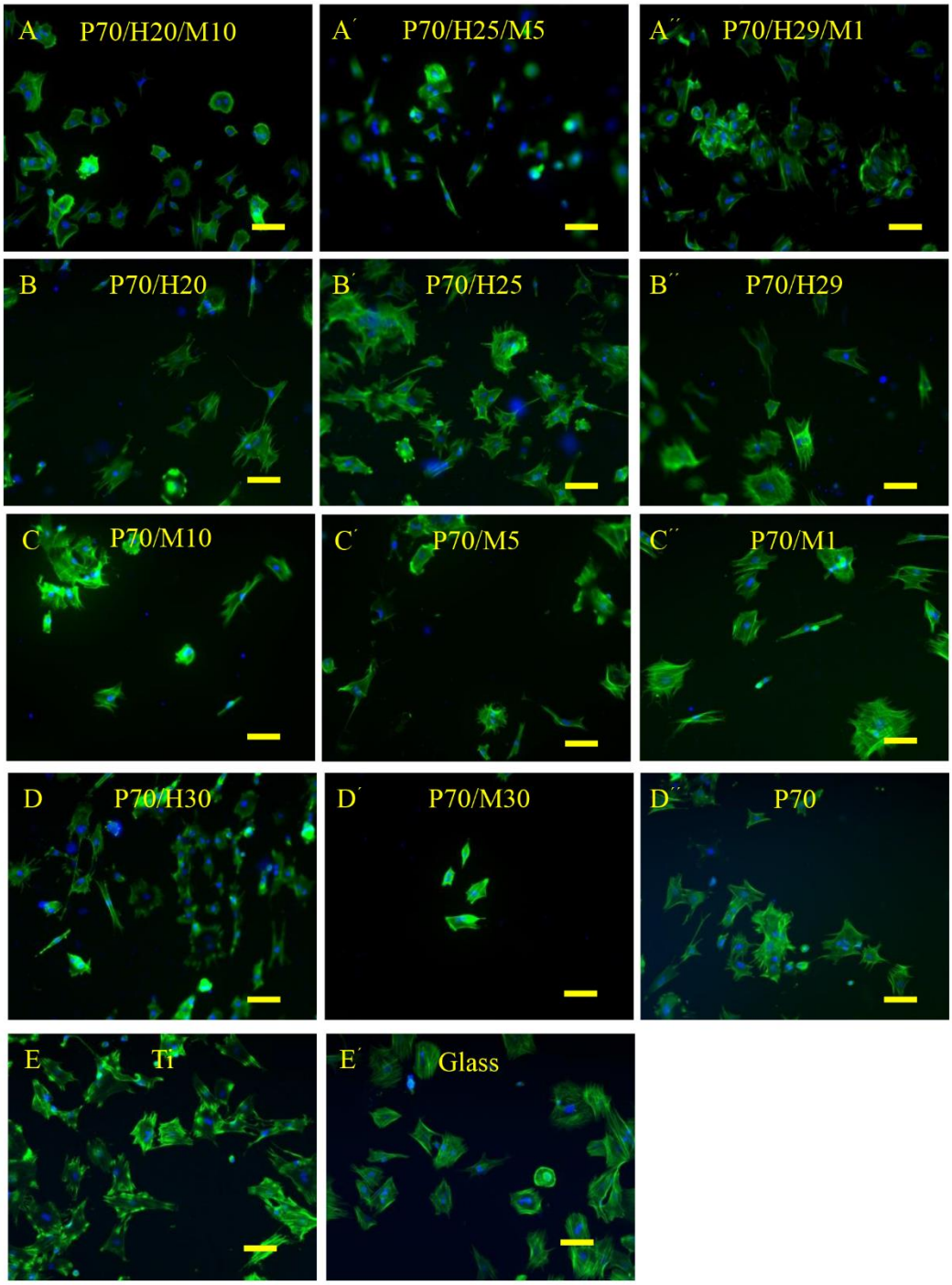

Figure 5.3: Fluorescence images of BMSCs adhered directly on scaffolds after 24 hours of direct culture. (A-A″) PLGA/HA/MgO, (B-B″) PLGA/HA, (C-C″) PLGA/MgO, (D-D″) additional polymeric controls and (E-E′) references. Scale bar is 100 µm.

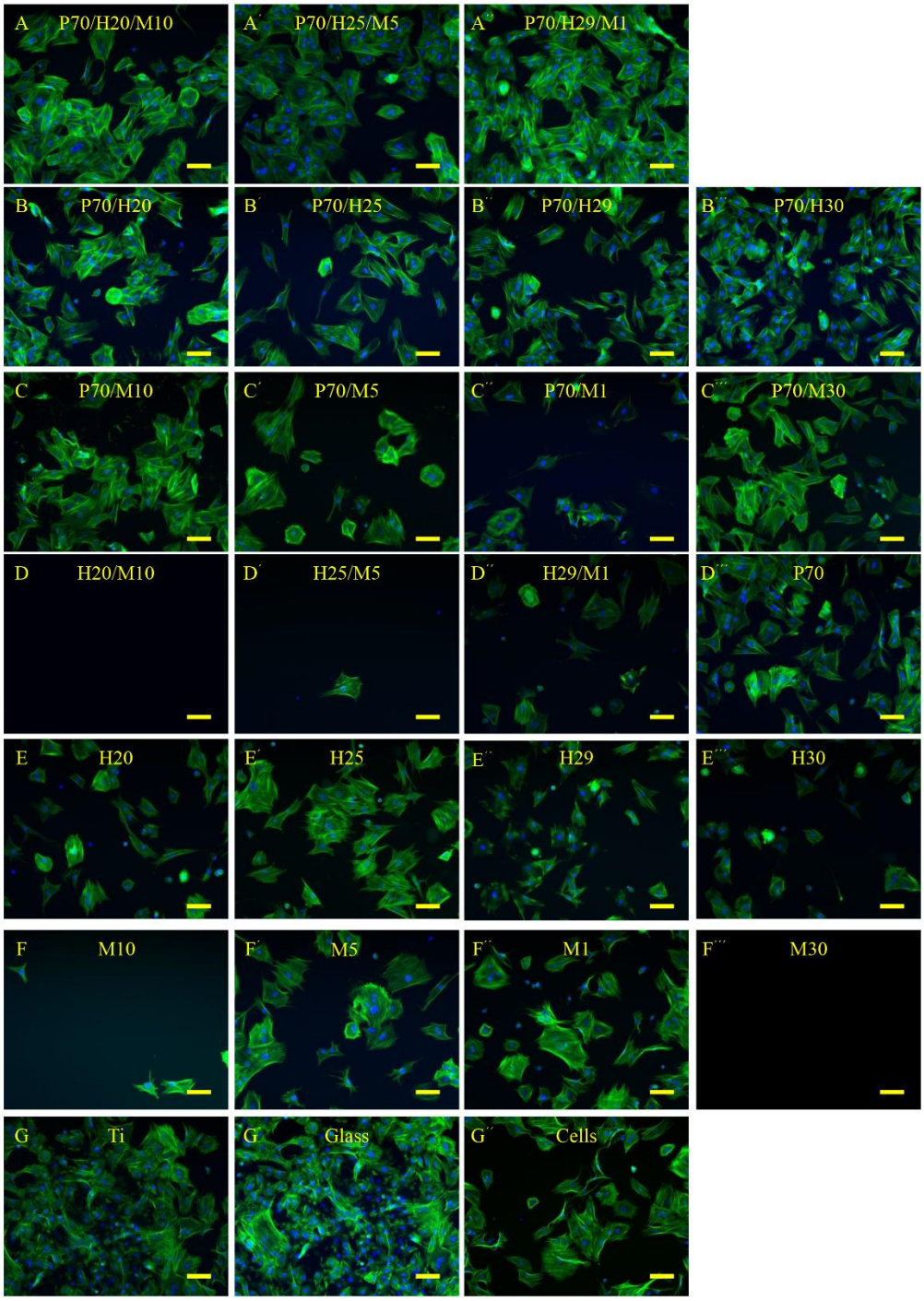

Figure 5.4: Fluorescence images of BMSCs adhered directly on TCTP surrounding scaffolds after 24 hours of direct culture. (A-A″) PLGA/HA/MgO, (B-B‴) PLGA/HA, (C-C‴) PLGA/MgO, (D-D‴) HA/MgO, (E-E‴) HA, (F-F‴) MgO, and (G-G″) references. Scale bar is 100 μm.

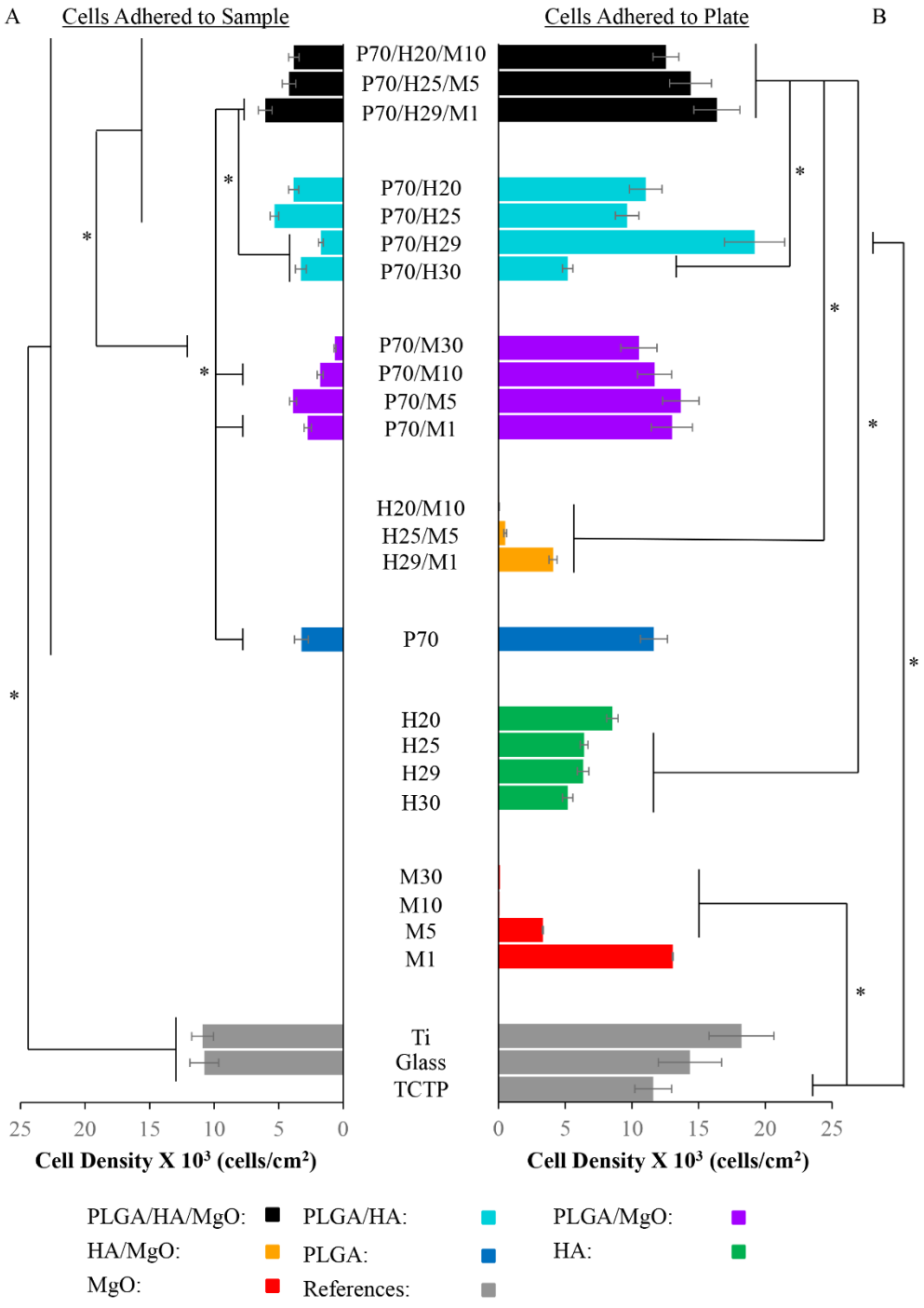

Figure 5.5: Adhesion density of BMSCs (left) adhered to sample and (right) adhered to plate after direct culture on PLGA/HA/MgO and controls for 24 hours. BMSCs were seeded at a density of 10,000 cells/cm^2. Values are mean ± standard deviation; n = 30. *p<0.05

Cell density was quantified for cells adhered to the sample (Figure 5A) and cells adhered to the plate (Figure 5.5B) after 24 hours of culture. P70/H20/M10 had 3.83 ± 0.40 x 10^3 cells/cm^2 and 12.55 ± 0.96 x 10^3 cells/cm^2 adhered to the sample and plate, respectively. P70/H25/M5 had 4.20 ± 0.52 x 10^3 cells/cm^2 and 14.4 ± 1.57 x 10^3 cells/cm^2 adhered to the sample and plate, respectively. Among the triphasic composites, P70/H29/M1 showed the highest average cell density with 6.04 ±0.53 x 10^3 cells/cm^2 adhered to the sample and 16.38 ± 1.73 x 10^3 cells/cm^2 adhered to the plate. PLGA/HA controls showed viable cells in each ratio type. P70/M30 showed significantly decreased cell density on the experimental samples, compared to the triphasic composites, with only 0.64 ± 0.07 x 10^3 cells/cm^2. All composites and polymers exhibited significantly lower cell density compared to Ti and Glass references. Cells adhered to the plate surrounding the triphasic composite were at significantly higher density compared to P70/H30, H20/M10, H25/M5, H29/M1, H25, H29, H30, M30, M10, M5, and M1. Cell density surround P70/H29 was significantly greater than the TCTP control. Remaining controls exhibited expected trends in cell density with nanoparticles showing less adherent cells, and M30 and M10 showing near to 0 viable cells.

Cells adhered to the sample (Figure 5.6) and to the plate (Figure 5.7) after 48 hours all exhibited healthy morphology. Cells adhered to all scaffold-type samples were abundant with approximate confluency ranging from 80-90%. However, visibly less cells were present on the plate surrounding P70/H30 (A″, Figure 5.7), P70/M5 (C, Figure 5.7), P70/M1 (C′, Figure 5.7), H25/M5 (D, Figure 5.7), and H29/M1 (D′, Figure 5.7). The quantified cell density after 48 hours of culture is shown in Figure 5.8. P70/H25/M5 had

$12.34 \pm 0.85 \times 10^3$ cells/cm^2 and $15.56 \pm 1.29 \times 10^3$ cells/cm^2 on the sample and plate, respectively. Once again, P70/H29/M1 showed the highest cell density of the triphasic composites with $14.44 \pm 1.43 \times 10^3$ cells/cm^2 and $20.12 \pm 1.52 \times 10^3$ cells/cm^2 on the sample and plate, respectively. Cell density on P70/H25/M5, P70/H29/M1, and Glass was significantly greater than the cell density on P70/M5. Cells adhered to the plate surrounding P70/H25/M5 and P70/H29/M1 were also significantly greater than the cell density on H25/M5, H29/M1. Additionally, the cell density surrounding P70/H29/M1 was greater than the P70/H30 reference. All bare nanoparticles, with the exception of M1 showed significant decrease in cell density when compared to Glass and TCTP.

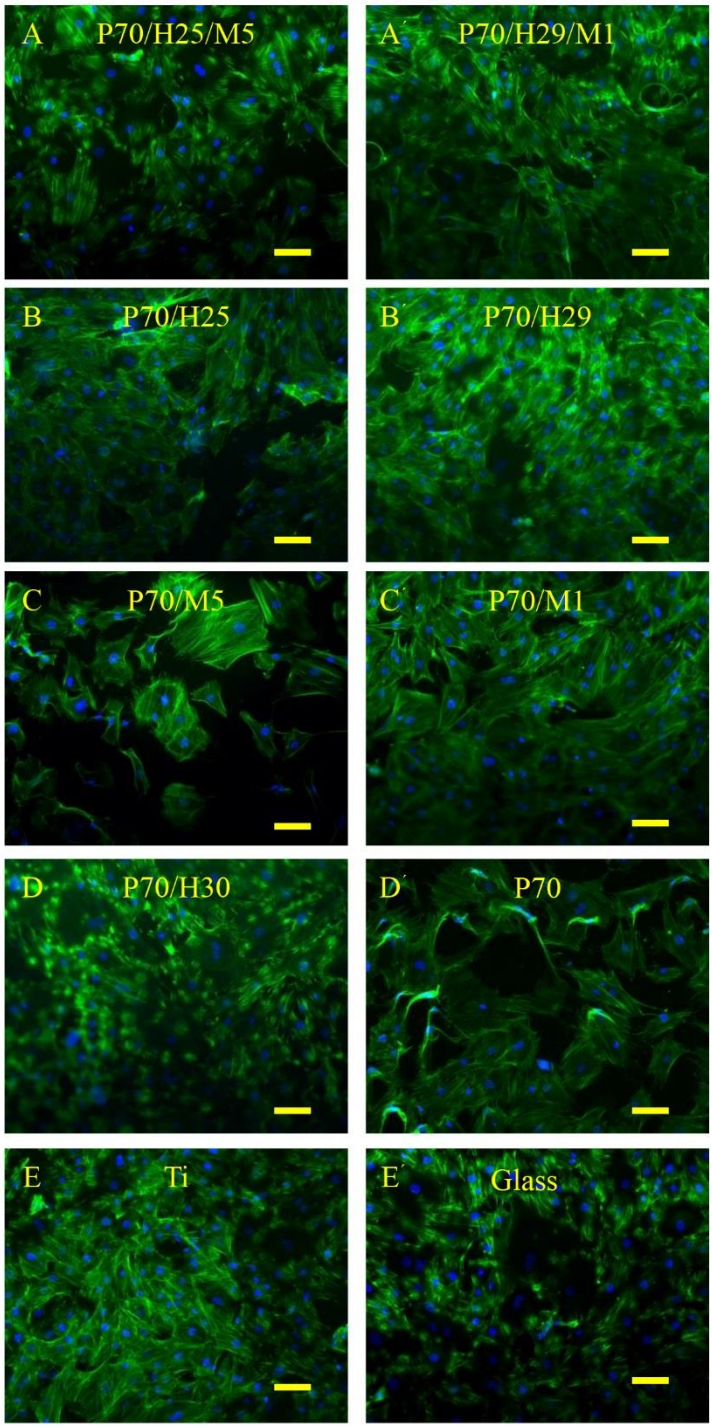

Figure 5.6: Fluorescence images of BMSCs adhered directly on scaffolds after 48 hours of direct culture. (A-A′) PLGA/HA/MgO, (B-B′) PLGA/HA, (C-C′) PLGA/MgO, (D-D′) additional polymeric controls and (E-E′) references. Scale bar is 100 µm.

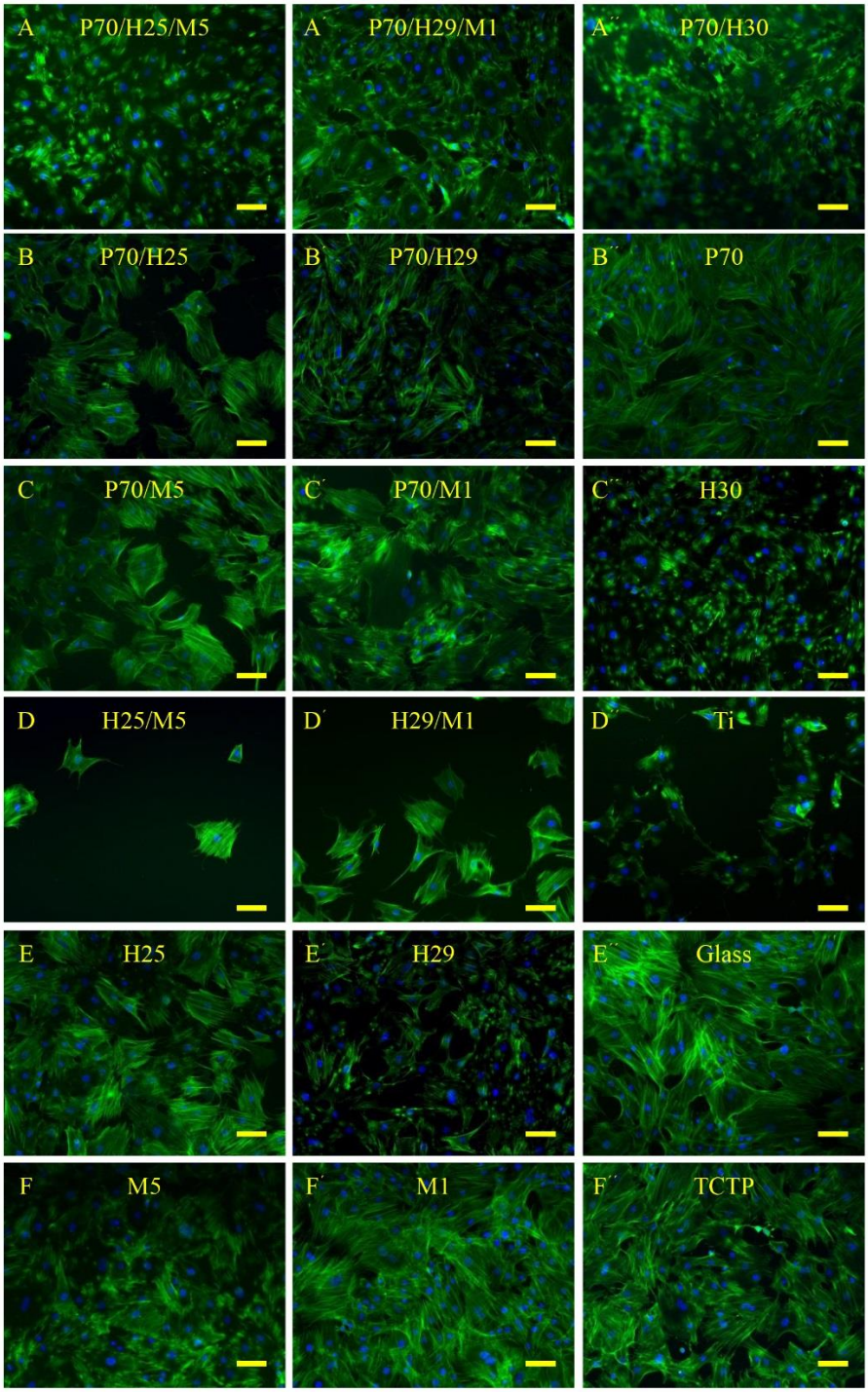

Figure 5.7: Fluorescence images of BMSCs adhered directly on TCTP surrounding scaffolds after 48 hours of direct culture. (A-A′) PLGA/HA/MgO, (B-B′) PLGA/HA, (C-C′) PLGA/MgO, (D-D′) HA/MgO, (E-E′) HA, (F-F′) MgO, and (A″-F″) references. Scale bar is 100 μm.

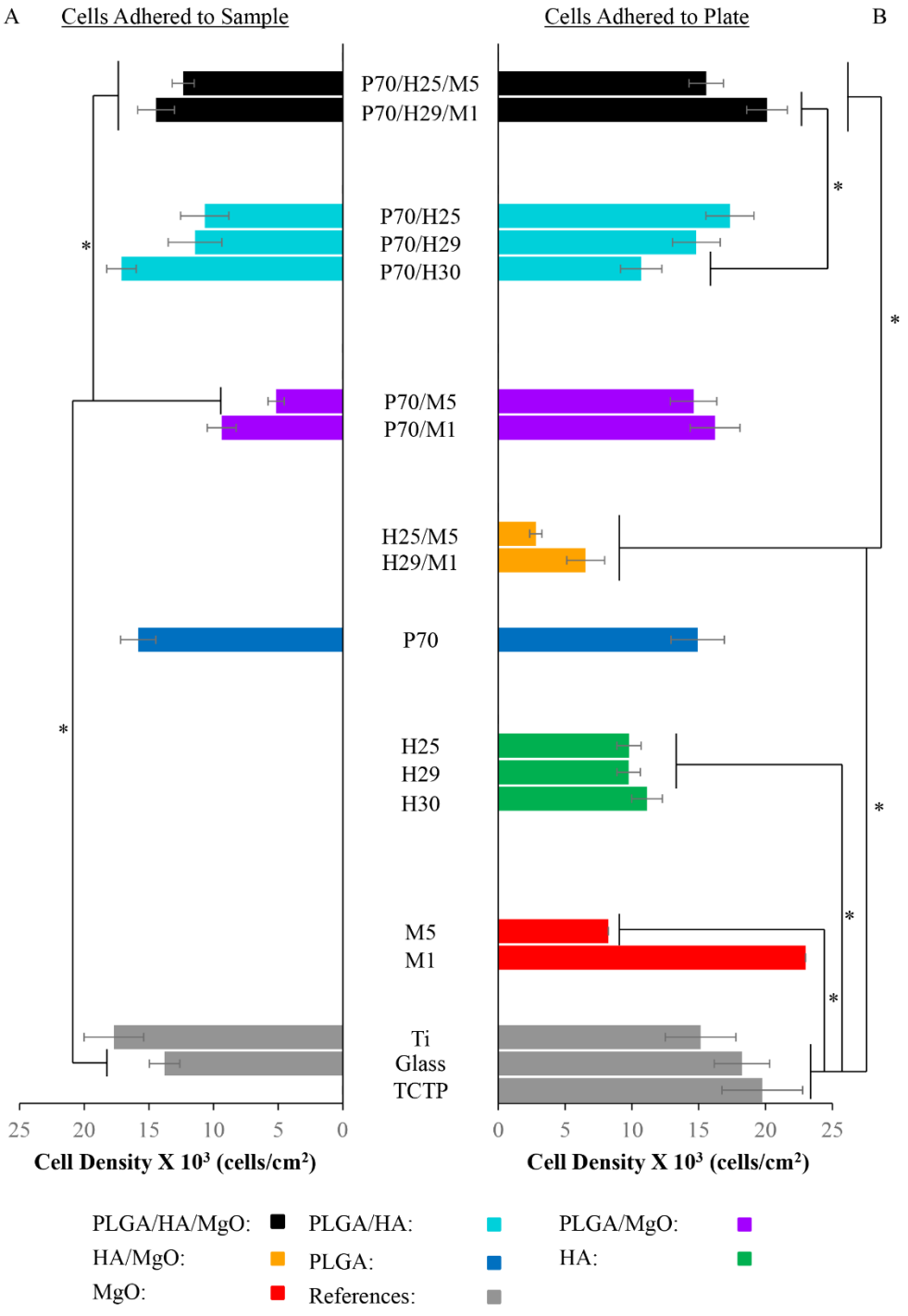

Figure 5.8: Adhesion density of BMSCs (left, A)) adhered to sample and (right, B) adhered to plate after direct culture on PLGA/HA/MgO and controls for 48 hours. BMSCs were seeded at a density of 10,000 cells/cm^2. Values are mean ± standard deviation; n = 30. *p<0.05

5.3.3 Post-culture Media Analysis

Change in pH showed small effect between samples at 24 hours (Figure 5.9A). After 24 hours of culture, the average pH of media cultured with P70/H20/M10, P70/H24/M5, and P70/H29/M1, was 8.37 ± 0.03, 8.32 ± 0.01, and 8.25 ± 0.02, respectively. P70/H29/M1 resulted in pH that was significantly lower than that of P70/H29/M10 and P70/H25/M5. H20/M10 had pH of 8.43 ± 0.01, which was statistically significant compared to TCTP and DMEM. M30 resulted in pH increase to 8.61 ± 0.04, which was statistically greater than all other samples. All other samples showed pH between 8.18 and 8.43, compared to TCTP and DMEM which had pH of 8.29 ± 0.02 and 8.31 ± 0.03, respectively.

Changes in pH after 48 hours of culture showed very minimal effects between samples (Figure 5.9B). After 48 hours, the pH of media cultured with P70/H25/M5 and P70/H29/M1 was 7.95 ± 0.03 and 7.88 ± 0.03, respectively. The pH of media from all other samples was between 7.82 and 7.95, compared to TCTP and DMEM which had media pH of 7.90 ± 0.03 and 7.93 ± 0.04, respectively. P70/H30 had a pH 7.82 ± 0.07 which was statistically lower than the pH of P70/H29/M1 and DMEM.

Release of Mg^{2+} ions corresponded with amount of MgO in samples cultured for 24 hours (Figure 5.10A). P70/H20/M10, P70/H25/M5, and P70/29/M1 had media Mg^{2+} concentrations of 6.36 ± 0.49 mM, 4.00 ± 0.48 mM, and 1.30 ± 0.06 mM, respectively. All PLGA/HA/MgO samples had statistically greater Mg^{2+} concentrations compared to TCTP and DMEM, which had Mg^{2+} concentrations of 0.95 ± 0.16 mM and 0.93 ± 0.07 mM, respectively. Additionally, P70/H20/M10 had significantly greater Mg^{2+}

concentration than P70/H29/M1 Bare MgO nanoparticles dissociated, releasing Mg^{2+}, which resulted in Mg^{2+} ion concentrations of 30.64 ± 1.09mM, 8.25 ± 1.29 mM, 6.27 ± 2.48 mM, 2.89 ± 0.94 mM from M30, M10, M5, and M1, respectively. P70/M30, all HA/MgO blends, M30, M10, and M5 resulted in significantly higher Mg^{2+} concentration compared to TCTP and DMEM.

Change in Mg^{2+} concentration at 48 hours was not as pronounced as that of 24 hours of culture (Figure 5.10B). Mg^{2+} concentration in media from P70/H25/M5 and P70/H29/M1 was 2.17 ± 0.12 mM and 1.24 ± 0.53 mM, respectively. The Mg^{2+} concentration of P70/M25/M5 was statistically greater than that of P70/H29/M1, P70/H25, P70/M29, H25/M5, H29/M1, TCTP and DMEM. The Mg^{2+} concentration of P70/M5 and P70/M1 was 2.02 ± 0.18 mM and 1.00 ± 0.13 mM, respectively. P70/M5, H25/M5, and M5 all resulted in Mg^{2+} concentrations that were statistically greater than TCTP and DMEM. All other samples were similar to that of the TCTP and DMEM references which were 0.82 ± 0.03 mM and 0.82 ± 0.01 mM, respectively.

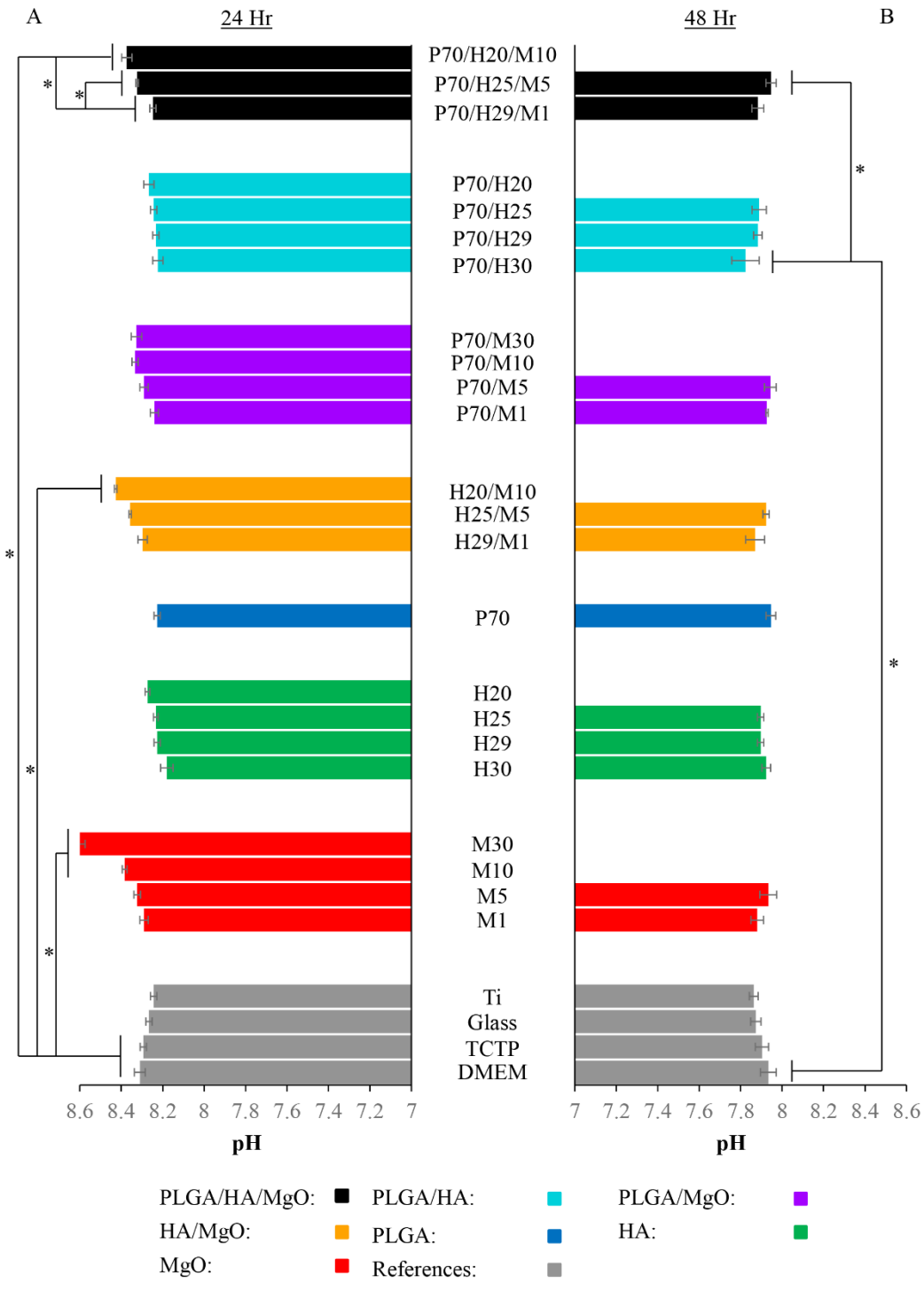

Figure 5.9: Media pH after BMSC culture on PLGA/HA/MgO and controls for (left, A) 24 hours and (right, B) 48 hours. Values are mean ± standard deviation; n = 3. *p<0.05

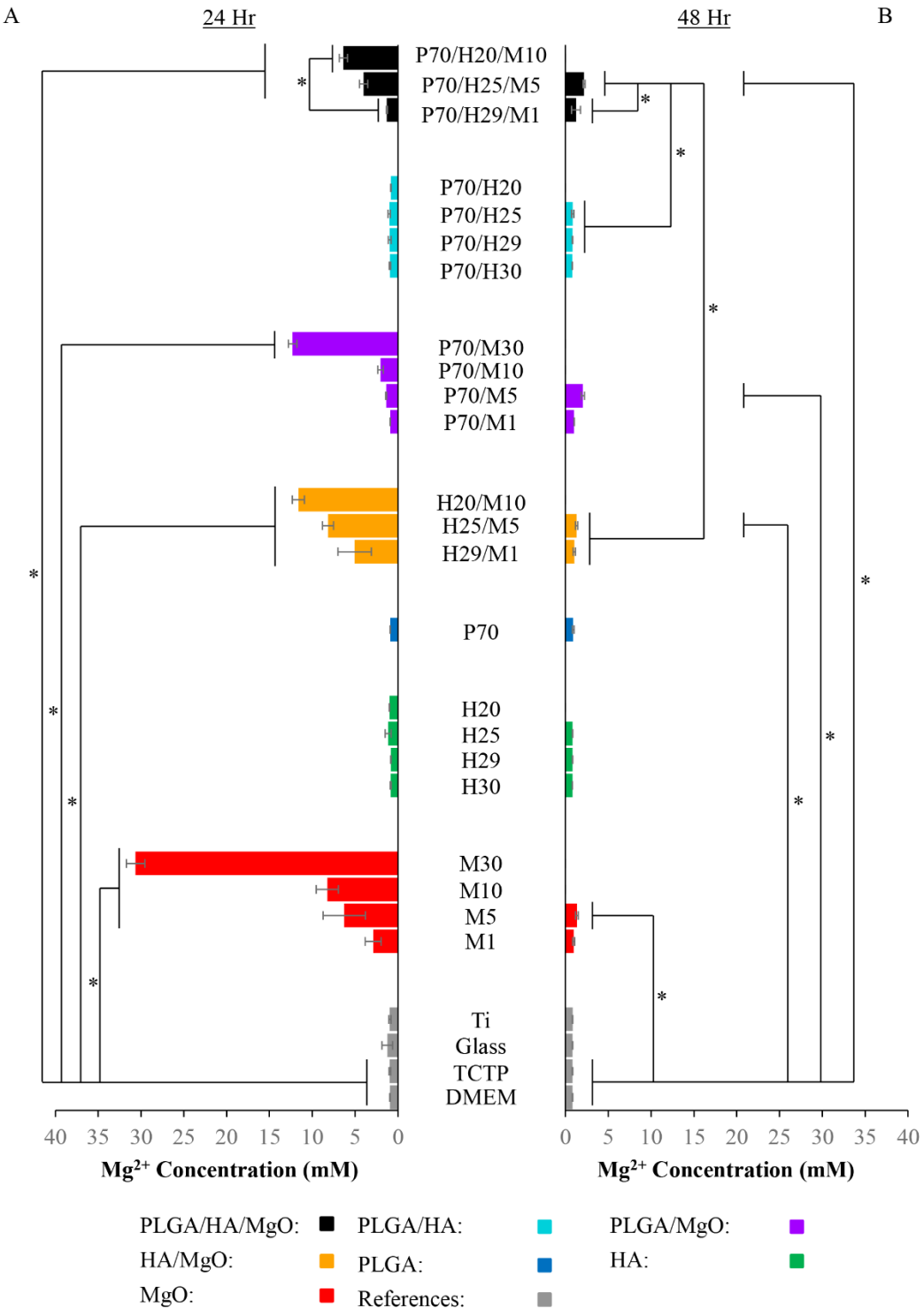

Figure 5.10: Concentration of Mg^{2+} in the media after BMSC culture on PLGA/HA/MgO and controls for (left, A) 24 hours and (right, B) 48 hours. Values are mean ± standard deviation; n = 3. *p<0.05

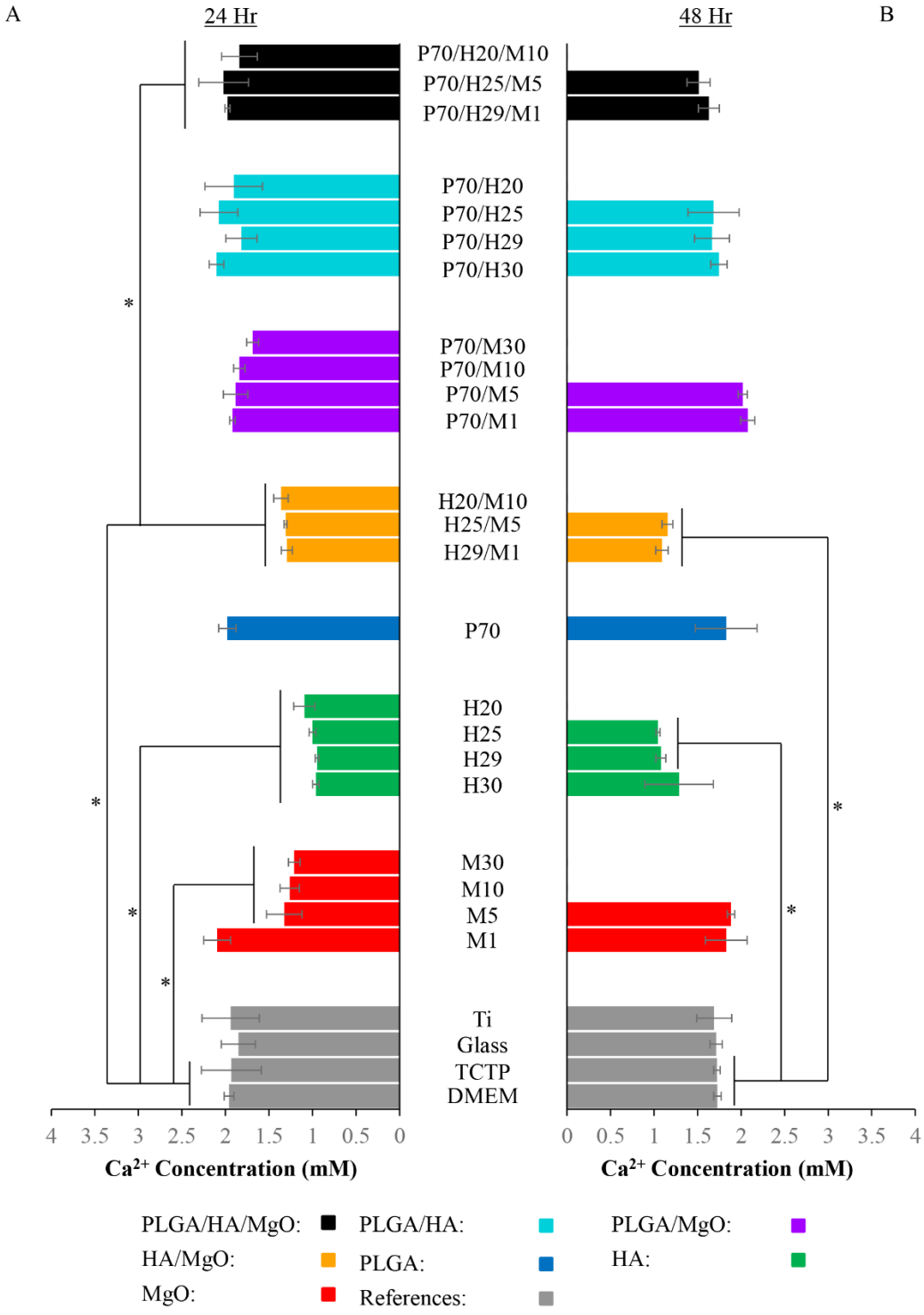

Figure 5.11: Concentration of Ca^{2+} in the media after BMSC culture on PLGA/HA/MgO and controls for (left, A) 24 hours and (right, B) 48 hours. Values are mean ± standard deviation; n = 3. *p<0.05

The amount of MgO and HA present correlated with changes in Ca^{2+} concentration at 24 hours (Figure 5.11A). Ca^{2+} concentration in media exposed to P70/H20/M10, P70/H25/M5, and P70/H29/M1 was 1.84 ± 0.21 mM, 2.02 ± 0.28 mM, and 1.98 ± 0.03 mM, respectively. The triphasic composites had statistically greater Ca^{2+} concentration than the HA/MgO nanoparticle mixtures. Bare particle mixes, H20/M10, H25/M5, and H29/M1 resulted in media Ca^{2+} concentrations of 1.36 ± 0.08 mM, 1.31 ± 0.02 mM, and 1.30 ± 0.06 mM, respectively. Similarly, bare HA, H20, H25, H29, and H30, resulted in Ca^{2+} concentrations of 1.09 ± 0.12 mM, 1.00 ± 0.04 mM, 0.95 ± 0.02 mM, and 0.96 ± 0.04 mM respectively. Bare MgO, M30, M10, and M5 resulted in Ca^{2+} concentrations of 1.21 ± 0.07 mM, 1.26 ± 0.11 mM, and 1.32 ± 0.20 mM, respectively. The HA/MgO nanoparticle mixtures, all HA nanoparticle concentrations, M30, M10, and M5 had statistically lower Ca^{2+} concentration compared to TCTP and DMEM. All other samples were not statistically different from TCTP and DMEM, which had Ca^{2+} concentrations of 1.93 ± 0.35 mM and 1.96 ± 0.05 mM, respectively.

After 48 hours, the effect of MgO and HA on Ca^{2+} concentration was greatly diminished. P70/H25/M5 and P70/H29/M1 had Ca^{2+} concentrations of 1.51 ± 0.13 mM and 1.63 ± 0.12 mM, respectively. P70/M5 and P70/M1 resulted in Ca^{2+} concentrations of 2.02 ± 0.05 mM and 2.08 ± 0.08 mM, respectively. Bare HA resulted in a decrease in Ca^{2+} concentration, compared to TCTP and DMEM references. HA25/M5, H29/M1, H25 and H29 had Ca^{2+} concentrations of 1.15 ± 0.06 mM, 1.09 ± 0.07 mM, 1.05 ± 0.02 mM and 1.08 ± 0.06 mM, respectively, which was statistically lower than that of TCTP and DMEM. H25 and H29 also exhibited statistically significant decrease in Ca^{2+}

concentration when compared to TCTP and DMEM. All other samples exhibited Ca^{2+} concentrations similar to that of TCTP and DMEM which were 1.72 ± 0.04 mM, and 1.73 ± 0.04, respectively.

5.4 Discussion

5.4.1 BMSC culture

While morphology of the cells adhered to experimental samples did not show much difference at 24 hours, the quantified cell density illuminated further differences (Figures 5.3, 5.5A). Glass and Ti references showed higher cell density on the sample than any other condition, despite the well-established biocompatibility of PLGA and HA [17-21]. Previous studies show that mechanical properties of ECM or scaffolding affect the behavior of mesenchymal stem cells. Specifically, materials with higher hardness or stiffness affected BMSC behavior resulting in increased cell adhesion, cell spreading, and osteogenic activity [22-24]. While the addition of nanoparticles increases the stiffness of the polymer matrix, Ti and Glass are metallic and ceramic, respectively, and have greater overall hardness [6]. It is likely that the difference in mechanical properties resulted in decrease in cell adhesion on polymeric substrates when compared to Ti and Glass. Of the polymeric samples, P70/H29/M1 showed the highest average cell density, even when compared to P70/H30, making this sample a promising candidate for bone applications.

Evaluation of cells adhered to the plate surrounding the experimental samples after 24 hours provided insight into how the chemistry of each material may affect surrounding BMSC behavior (Figures 5.4, 5.5B). The three blends of PLGA/HA/MgO performed similarly to Ti, Glass, and TCTP, indicating that the degradation products

released at 24 hours are cytocompatible with BMSCs. However, all bare nanoparticles resulted in significant decrease in cell adhesion. HA is well-established as a material for bone regeneration and is known to be biocompatible [4, 20, 21, 25]. It is likely that the decrease in cell density from exposure to just HA is from movement of loose nanoparticles affecting adhesion of the cells, rather than chemistry. The decrease in cell density when exposed to bare MgO is also consistent with previous studies, which identified the critical cytotoxic concentration of MgO to be 500 µg/mL for established cells and showed significant decrease in adherent BMSCs when co-seeded with MgO at concentrations as low as 200 µg/mL [5]. The amount of MgO in M10 and M5 resulted in MgO concentrations of 560 µg/mL and 260 µg/mL, which is higher than the concentrations of MgO nanoparticles identified to result in decrease cell adherence. Conversely, M1, which resulted in a MgO concentration of 6 µg/mL, resulted in increased cell density, confirming that low concentrations of MgO can be beneficial to BMSC function as seen with previous studies [5]. The absence of decrease in cell density of polymeric nanocomposites demonstrates that incorporation in a PLGA matrix mitigates negative effects of bare nanoparticles and more specifically, bare MgO nanoparticles.

Similar to the 24 hour study, at 48 hours cell morphology indicated little difference in BMSCs adhered to experimental samples, but quantified cell density help to better elucidate BMSC response (Figure 5.6, 5.8A). Cell density on P70/H29/M1 exceeded cell density adhered to the Glass reference at 48 hours when it was significantly less at 24 hours, indicating that the chemistry of this nanocomposite aided in

proliferation. However, no statistical difference was found between P70/H29/M1, P70/H30, and Ti. The benefit of addition of small amounts of MgO to nanocomposites for bone regeneration should be further investigated to determine if and at what concentration MgO is truly beneficial.

Evaluation of cells adhered to the plate surrounding experimental samples gave a more understanding of the effects of PLGA/HA/MgO and more specifically, the effects of components released by PLGA/HA/MgO and its effects on media (Figure 5.8B). P70/H29/M1 resulted in higher cell density on the plate compared to P70/H30, indicating that controlled release of small amount of MgO, and thus Mg^{2+} can increase cell proliferation. This is consistent with previous studies into the effect of bare MgO nanoparticles [5]. However, the lack of significance between the PLGA/HA/MgO samples and the TCTP reference makes the true benefit of these nanocomposites unclear. Cell activity, including expression of osteogenic proteins, should be further evaluated to fully understand what role MgO may play.

Previous studies of polymer/HA/MgO nanocomposite can give insight into the observed phenomena for our PLGA/HA/MgO blends. Hickey et. al. evaluated PLLA with 10% HA and 10% MgO and found increased primary human osteoblast density compared to composites with 20% HA and plain PLLA [2]. Conversely, PLGA/HA/MgO composites with 10% MgO did not out-perform our PLGA/HA composites. This may be due to differences in dispersion as shown in our previous studies described in Chapter 4. SEM images of the surface of the PLLA composites with 10% HA and 10% MgO showed inhomogeneous distribution of particles as well as agglomeration. The

differences between PLLA and PLGA composites with HA and MgO may also result in different cell response due to the fact that PLGA tends to degrade faster than PLLA and would result in higher release rate for MgO. Previous studies have also evaluated high-density polyethylene (HDPE) composites with 16% tri-calcium phosphate, 4% HA, and 0.1% MgO [4]. While this composite did not show much difference in the viability and proliferation of primary human osteoblasts compared to plain HDPE, this composite did result in higher expression of alkaline phosphatase, an essential protein for osteogenic activity. It is difficult to determine which component(s) of this composite resulted in increased ALP production because composites with just HA, MgO and tri-calcium phosphate were not evaluated. However, this does support the need for further investigation into the activity of MgO.

5.4.2 Media Analyses

Minimal pH effects were observed at 24 and 48 hours due to the buffering effect of bicarbonate within DMEM. Only M30 showed a somewhat substantial increase in pH. This is consistent with our previous studies into the activity of bare MgO nanoparticles [5]. MgO dissociates in biological media, releasing OH^- and Mg^{2+}, which is responsible for the observed pH increase. However, it has been previously shown that the cells may experience higher pH in the first few hours of exposure to MgO in comparison to pH at 24 hours due to the buffering of DMEM. This effect may be responsible for the observed cell death in the bare MgO nanoparticle groups.

Measurements of Mg^{2+} concentration in the media were more representative of MgO release and dissociation than pH because they were not affected by pH buffers. It is

clear that incorporation of MgO into a PLGA composite reduced the rate of release and dissociation of MgO, as seen with the difference in Mg^{2+} concentration. This is consistent with similar composites from previous studies in our lab. The fact that Mg^{2+} release diminished at 48 hours, indicates that there is bulk release and dissociation of MgO within the first 24 hours. Previous studies into the dissociation of MgO showed that 90-100% of bare MgO dissociates within 24 hours of culture in DMEM [5]. Previous studies also show that Mg^{2+} are not only safe for mammalian cells but also exhibit osteoinductive behavior [14, 26, 27]. Given that composites with MgO have also shown an increase in ALP expression in osteoblasts, this supports the use of MgO for bone regeneration [4].

Measurements of media Ca^{2+} concentration showed that HA and MgO affect calcium deposition but this activity is not detected in our PLGA composites. Each PLGA composite did not show much effect on Ca^{2+} concentration in the media. Conversely, bare HA/MgO, HA, and MgO (excluding M1), resulted in significant decrease in Ca^{2+} in the media. This may indicate that MgO and HA cause deposition of calcium-containing salts, which is consistent with our previous studies [5]. This effect was not detected for bare MgO at 48 hours, indicating that once MgO fully dissociated, it no longer affected deposition of calcium salts. However, decrease in Ca^{2+} concentration persisted up to 48 hours in the HA/MgO and HA nanoparticle conditions. The deposition of calcium salts is beneficial to the remineralization of bone, which is essential for bone regeneration and bone healing. This effect is well-described for HA, but not for MgO. As long as MgO, was still present in its crystal form, the beneficial effects on calcium deposition remained.

However, further analysis into the types of salts and minerals that are deposited would be essential to fully understand this effect.

5.5 Conclusion

P70/H29/M1 performed most favorably of the PLGA/HA/MgO composites, indicating it is viable for further study as a material for bone applications. However, we cannot make finite conclusions as to the effectiveness of this material without longer cell culture times and an evaluation into the protein expression of BMSCs. We reported the release of Mg^{2+} from polymer/HA/MgO composite and its effect on calcium deposition for the first time. The presence of MgO and HA is beneficial for deposition of calcium salts and composites of PLGA/HA/MgO may be beneficial for mineralization of bone.

5.6 Acknowledgements

The authors thank the support from the U.S. National Science Foundation (NSF award CBET 1512764), the Burroughs Wellcome Fund (1011235), the Hellman Faculty Fellowship (HL), and the University of California (UC) Regents Faculty Development Award (HL). The authors appreciate the Central Facility for Advanced Microscopy and Microanalysis (CFAMM) for the use of SEM FEI XL30 at the University of California at Riverside. The authors would also like to thank Chaoxing Zhang for his assistance with ICP-OES measurements.

5.7 References

1. Khandaker, M., Y. Li, and T. Morris, *Micro and nano MgO particles for the improvement of fracture toughness of bone-cement interfaces.* J Biomech, 2013. **46**(5): p. 1035-9.
2. Hickey, D.J., et al., *Adding MgO nanoparticles to hydroxyapatite-PLLA nanocomposites for improved bone tissue engineering applications.* Acta Biomater, 2015. **14**: p. 175-84.
3. Roh, H.S., et al., *Addition of MgO nanoparticles and plasma surface treatment of three-dimensional printed polycaprolactone/hydroxyapatite scaffolds for improving bone regeneration.* Mater Sci Eng C Mater Biol Appl, 2017. **74**: p. 525-535.
4. Pourdanesh, F., et al., *In vitro and in vivo evaluation of a new nanocomposite, containing high density polyethylene, tricalcium phosphate, hydroxyapatite, and magnesium oxide nanoparticles.* Mater Sci Eng C Mater Biol Appl, 2014. **40**: p. 382-8.
5. Wetteland, C.L., N.Y. Nguyen, and H. Liu, *Concentration-dependent behaviors of bone marrow derived mesenchymal stem cells and infectious bacteria toward magnesium oxide nanoparticles.* Acta Biomater, 2016. **35**: p. 341-56.
6. Ebrahimian-Hosseinabadi, M., et al., *Evaluating and Modeling the Mechanical Properties of the Prepared PLGA/nano-BCP Composite Scaffolds for Bone Tissue Engineering.* Journal of Materials Science & Technology, 2011. **27**(12): p. 1105-1112.
7. Huang, Y., et al., *Osteoconductivity and osteoinductivity of porous hydroxyapatite coatings deposited by liquid precursor plasma spraying: in vivo biological response study.* Biomed Mater, 2014. **9**(6): p. 065007.
8. Jang, C.H., et al., *Comparision of osteoconductivity of biologic and artificial synthetic hydroxyapatite in experimental mastoid obliteration.* Acta Otolaryngol, 2014. **134**(3): p. 255-9.
9. Lin, L., K.L. Chow, and Y. Leng, *Study of hydroxyapatite osteoinductivity with an osteogenic differentiation of mesenchymal stem cells.* J Biomed Mater Res A, 2009. **89**(2): p. 326-35.
10. Farzadi, A., et al., *Synthesis and characterization of hydroxyapatite/beta-tricalcium phosphate nanocomposites using microwave irradiation.* Ceramics International, 2011. **37**(1): p. 65-71.
11. Bellucci, D., et al., *A new hydroxyapatite-based biocomposite for bone replacement.* Materials Science and Engineering: C, 2013. **33**(3): p. 1091-1101.
12. Nabiyouni, M., Y. Ren, and S.B. Bhaduri, *Magnesium substitution in the structure of orthopedic nanoparticles: A comparison between amorphous magnesium phosphates, calcium magnesium phosphates, and hydroxyapatites.* Mater Sci Eng C Mater Biol Appl, 2015. **52**: p. 11-7.
13. He, L.Y., et al., *Effect of magnesium ion on human osteoblast activity.* Braz J Med Biol Res, 2016. **49**(7).

14. Cipriano, A.F., et al., *Investigation of magnesium-zinc-calcium alloys and bone marrow derived mesenchymal stem cell response in direct culture.* Acta Biomater, 2015. **12**: p. 298-321.
15. Johnson, I., K. Akari, and H. Liu, *Nanostructured hydroxyapatite/poly(lactic-co-glycolic acid) composite coating for controlling magnesium degradation in simulated body fluid.* Nanotechnology, 2013. **24**(37): p. 375103.
16. Alvey, F.B., *Study of Reaction of Polyester Resins with Magnesium Oxide.* Journal of Polymer Science Part a-1-Polymer Chemistry, 1971. **9**(8): p. 2233-&.
17. Kapoor, D.N., et al., *PLGA: a unique polymer for drug delivery.* Ther Deliv, 2015. **6**(1): p. 41-58.
18. Makadia, H.K. and S.J. Siegel, *Poly Lactic-co-Glycolic Acid (PLGA) as Biodegradable Controlled Drug Delivery Carrier.* Polymers, 2011. **3**(3): p. 1377-1397.
19. Ortega-Oller, I., et al., *Bone Regeneration from PLGA Micro-Nanoparticles.* Biomed Res Int, 2015. **2015**: p. 415289.
20. Cheng, L., et al., *Osteoinduction of hydroxyapatite/beta-tricalcium phosphate bioceramics in mice with a fractured fibula.* Acta Biomater, 2010. **6**(4): p. 1569-74.
21. Zakaria, S.M., et al., *Nanophase hydroxyapatite as a biomaterial in advanced hard tissue engineering: a review.* Tissue Eng Part B Rev, 2013. **19**(5): p. 431-41.
22. Guilak, F., et al., *Control of stem cell fate by physical interactions with the extracellular matrix.* Cell Stem Cell, 2009. **5**(1): p. 17-26.
23. Kshitiz, et al., *Control of stem cell fate and function by engineering physical microenvironments.* Integr Biol (Camb), 2012. **4**(9): p. 1008-18.
24. Park, J.S., et al., *The effect of matrix stiffness on the differentiation of mesenchymal stem cells in response to TGF-beta.* Biomaterials, 2011. **32**(16): p. 3921-30.
25. Lock, J., T.Y. Nguyen, and H. Liu, *Nanophase hydroxyapatite and poly(lactide-co-glycolide) composites promote human mesenchymal stem cell adhesion and osteogenic differentiation in vitro.* J Mater Sci Mater Med, 2012. **23**(10): p. 2543-52.
26. Yoshizawa, S., et al., *Role of magnesium ions on osteogenic response in bone marrow stromal cells.* Connect Tissue Res, 2014. **55 Suppl 1**: p. 155-9.
27. Yoshizawa, S., et al., *Magnesium ion stimulation of bone marrow stromal cells enhances osteogenic activity, simulating the effect of magnesium alloy degradation.* Acta Biomater, 2014. **10**(6): p. 2834-42.

Chapter 6: Thermogelling PLGA-PEG-PLGA Hydrogel Loaded with Hydroxyapatite and Mangesium Oxide for Bone Repair

6.1 Introduction

Thermogelling hydrogels have been of increasing interest to the field of tissue engineering due to their injectability. Ideally, a thermosensitive hydrogel for medical applications would be solution at room temperature and then gel at body temperature, 37 ºC. These hydrogels have the potential to be a minimally invasive and robust cell delivery system that could allow for the sustained and controlled release of various growth factors, drugs, cells, and other bioactive molecules [1-4]. These unique properties allow for the application of thermosensitive hydrogels in the regeneration of bone, cartilage, adipose tissue, neural tissue, and cardiovascular tissue [4]. Furthermore, thermosensitive hydrogels have the ability to fill unique shapes due to their *in situ* gelation, which makes then an ideal filler for porous bone [5]. Hydrogels could also be used in the treatment of severe microfractures caused by osteoporosis or overuse. The basic mechanism of thermosensitive hydrogel gelation is as follows: Once placed in an aqueous solution, interactions between the polymer molecules and water occur. An increase in temperature causes local changes in the hydrophobic interactions of the polymer chains, resulting in micelle formation. The micelle formation and aggregation results in formation of an opaque gel [6, 7].

Poly (D,L-lactide-co-glycolide)-poly (ethylene glycol)-poly (D,L-lactide-co-glycolide), PLGA-PEG-PLGA (PLGA-*b*-PEG, PbP) hydrogels have gained a lot of attention due to the well-established biocompatibility of their subcomponents, PLGA and PEG [6-15]. Stimuli responsive PbP hydrogels have been successfully developed for the

delivery of various biomedically relevant treatments such as anti-cancer drugs, vaccines, hydroxyapatite, simvastatin, etc. [7-10]. Additionally, a host of PLGA and PEG based constructs have been approved by the FDA for the use in drug delivery systems [13-15]. Despite its biocompatibility, PbP is not particularly bioactive and the use of a bioactive component may render them much more effective in a physiological setting [7-9, 16].

Hydroxyapatite (HA) is a biocompatible and bioactive ceramic material that is found in the hard tissues in the body [17]. It has been shown that HA is one of the most stable calcium phosphate salts under normal temperature and at pH between 4 and 12 [17, 18]. Furthermore, HA has been shown to be osteoinductive and osteoconductive, resulting in bone formation without the addition of osteogenic biomolecules [17-19].

The use of MgO in biomedical implants has also increased in recent years due to its ability to enhance mechanical properties of composite materials as well as its bioactivity [20-24]. At low concentrations (200 μg/mL), MgO has been shown to increase proliferation of bone marrow derived mesenchymal stem cells (BMSCs) [24]. MgO has also been shown to have antimicrobial activity towards gram position and gram-negative bacteria, which is beneficial for any implantable materials that can pose infection risk [24-26]. MgO is a hygroscopic mineral that absorbs water and reacts to form $Mg(OH)_2$, both of which are considered insoluble [27-31]. However, MgO and $Mg(OH)_2$ have been shown to dissociate under physiological conditions, releasing Mg^{2+} ions [32]. Magnesium ions have been shown to exhibit osteogenic activity, which is beneficial for bone regeneration [33, 34]. As a result, MgO is a prime candidate as an additive to materials for bone regeneration.

To determine the effects of a PbP hydrogel loaded with HA and MgO (PbP/HA/MgO), the direct exposure cell culture method was used [35]. In brief, BMSCs were cultured for 24 hours prior to addition of hydrogel composites. The direct exposure cell culture method was used to mimic the response of established cells to an injected hydrogel. Herein, we report the gelation behavior and bioactivity of PbP/HA/MgO.

6.2 Materials and Methods

6.2.1 Preparation of MgO

MgO nanoparticles were procured from US Research Nanomaterials Inc. (US3310, 99+% purity, 20nm diameter). MgO nanoparticles were sterilized in a glass container via heating at 200°C in an oven for one hour.

6.2.2 Preparation of HA

Hydroxyapatite was synthesized through wet precipitation as previously published [36, 37]. Briefly, 40 mL of 1M $Ca(NO_3)_2$ was added drop-wise to 40 mL of 0.6M $(NH_4)_2HPO_4$ at 40°C at a rate of 30 drops per minute. This mixture underwent stirring for 20 hours to allow formation of nHA. The resulting particle and solution mixture was centrifuged at 3000 rpm for 1 minute. The supernatant was discarded and the particles were resuspended in deionized (DI) water. Centrifuging and rinsing in DI was repeated 3 times to remove excess ammonia. The pellet was then resuspended in DI and transferred to an acid digestion bomb for hydrothermal treatment at 200°C for 20 hours. The suspension was then collected and centrifuged, followed by the removal of the supernatant. The resulting particles were dried under vacuum at 80°C for 12 hours and

then ground using a mortar and pestle. Prior to use in composites or cell culture, the nHA was disinfected by heating in an oven at 200°C for 1 hour.

6.2.3 Hydrogel Composites

6.2.3a Preparation of PLGA-PEG-PLGA

PLGA-PEG-PLGA (PbP) is a triblock polymer with thermoreversible gelling behavior. Two blends of PLGA-PEG-PLGA were purchased from PolySciTech (AK24, AK19, Akina Inc.). One of these blends of PLGA-PEG-PLGA starts to gel at 17°C, herein referred to as PbP17 and the second gels at 40°C, herein referred to as PbP40. A mixture of the two blends of PLGA-PEG-PLGA was developed with the aim of producing a thermoreversible hydrogel that gels at physiological temperature, 37°C. Specifically, hydrogel solutions with 20% by weight of PbP and 80% by weight of Dulbecco's Modified Eagle Medium (DMEM, MT10013CM, Fisher Scientific) were developed. For each, PbP17 and PbP40, 140 mg of PbP was added to an 8 mL glass vial (Fisher Scientific, 03-339-21D) with 560 µL of DMEM at 4°C. Dual-Asymmetric Centrifugal mixing, as referred to as speed-mixing (DAC 150.1 FVZ-K, FlackTek, Inc.), utilizes opposing rotational force to mix viscous suspensions and solutions via shear force. Speed-mixing at 2500rpm for 5 minutes was used to incorporate the PbP and DMEM. These mixtures were then stored at 4°C for 12 hours to facilitate complete dissolution of the PbP. After the 12 hours, the PbP/DMEM mixtures then underwent speed-mixing at 2500 rpm for 5 minutes to further homogenize the mixture. Each solution was then filtered through 0.2 µm syringe filters (Millex®, SLGV004SL,

Millipore) for sterilization. The resulting solutions were used as PbP17 and PbP40 stock to prepare hydrogel/ceramic composites.

6.2.3b PbP/HA/MgO Synthesis

All nanoparticles and PbP solutions were transferred in a laminar flow hood to maintain sterility. In a sterile 8 mL glass vial, 354 µL of PbP17 solution and 284.6 µL of PbP40 solution were added. The resulting mixture underwent two cycles of speedmixing at 2500 rpm for 5 minutes and cooling in a water bath at 4°C for 5 minutes. Under sterile conditions in a laminar flow hood, 12.9 mg of HA was added. This mixture then underwent 3 cycles of speedmixing and cooling as described for mixing of PbP17 and PbP40. Then, 1.3 mg of MgO was added and the resulting mixture underwent another 3 cycles of speedmixing and cooling. This resulted in PbP/HA/MgO suspension with a dry weight ratio of 90/9/1. PbP/HA, PbP/MgO, and PbP controls were made using the same procedure, except no MgO was added to PbP/HA, no HA was added to PbP/MgO and no nanoparticles were added to PbP.

To prepare uniform hydrogels, a silicone mold was developed, diagramed in Figure 6.1. This mold had wells with a depth of 5 mm and a diameter of 5.5 mm via 3D printing (3D Bioplotter, EnvisionTEC). The silicone mold was place atop a glass slide (Fisherbrand 12-544-1). The flexibility of the silicone mold edges and the removable bottom, made for easier removal of hydrogels. The glass was sterilized in 70% ethanol for 1 hour while exposed to a sonic bath (Symphony SB70P). Then the mold and glass bottom were sterilized in a quartz dish in a UV sterilizer (M-2036, Meishida). Under sterile conditions, each hydrogel mixture was injected into the wells of the silicone mold

to form cylinders with a diameter of 5.5 mm and a height of 4 mm. The mold was placed into an incubator under standard cell culture conditions, 37°C with 5% CO_2 for 1 hour to allow the gel to form. Composition of each gel is summarized in Table 6.1.

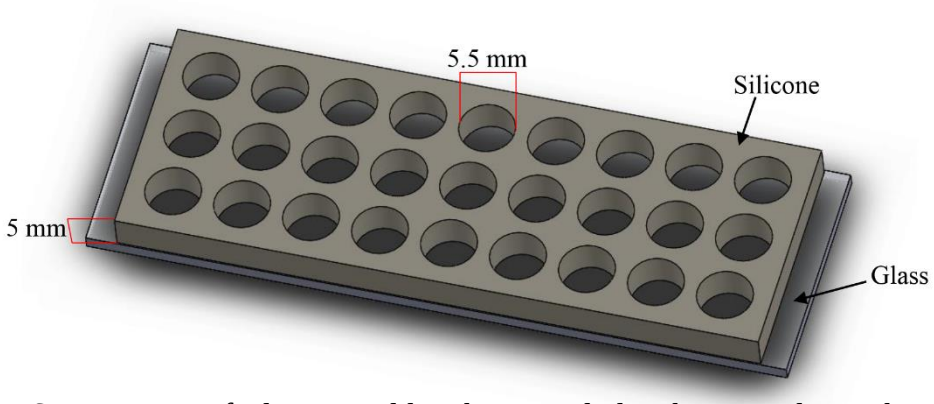

Figure 6.1: Diagram of silicone mold with removal glass base, used to make hydrogels of standard sizes.

6.2.4 Gelation Temperature

Gelation temperature of each composite was determined while the hydrogel suspensions were in 8 mL vials. The vial, containing composite hydrogels, was placed in a water bath and temperature was increased incrementally from 4°C to 37°C. The mixture was maintained at each 1°C increment for 10 minutes, at which point, the vial was inverted and flow or lack of flow was observed. If no flow occurred, the mixture was considered to have gelled and the sol-gel temperature was recorded (Table 6.1). Representative images were taken of each hydrogel when in solution, gelled, and at 37ºC (Figure 6.2). Each sample was held 90º from an upright position for 1 minute and then photographed to demonstrate representative flow behavior.

	PbP/HA/MgO	PbP/HA	PbP/MgO	PbP
PbP17 (mg)	10.4	10.4	10.4	10.5
PbP40 (mg)	8.4	8.5	8.5	8.5
HA (mg)	1.9	1.9	0	0
MgO (mg)	0.2	0	0.2	0
DMEM (μL)	76	76	76	76
Dry Weight ratio (PbP17/PbP40/HA/MgO)	50/40/9/1	50/40/9/0	55/44/0/1	55/45/0/0
Gelation Temperature (ºC)	30-35*	29-34	28-33*	27-33

Table 6.1: Composition of PbP/HA/MgO and hydrogel controls and resulting gelation temperature. *These composites lost thermoreversibility, meaning these composites did not transition back to the solution phase after cooling.

6.2.5 Effect of PbP/HA/MgO on BMSCs

6.2.5a BMSC Direct Exposure Culture

Bone marrow derived mesenchymal stem cells (BMSCs) isolated from Sprague Dawley rat weanlings were used to evaluate initial cytocompatibility of the PbP hydrogel composites [24, 37]. To better mimic how established cells surrounding a microfracture may interact with injected PbP composites, the direct exposure culture method was utilized [35]. In brief, BMSCs at their second passage were seeded at a density of 10,000 cells/cm^2 into wells of a 24 well tissue culture treated plate (TCTP, Corning, Inc. 353226). These cells were incubated for 24 hours prior to exposure to experimental materials under standard cell culture conditions, 37°C with 5% CO_2/95% air and humidity. After 24 hours of culture, three representative wells were fixed and quantified to obtain adherent cell density prior to introduction of experimental materials. For the remaining wells, fresh media was exchanged and PbP composites and nanoparticle controls were added to their respective wells. The BMSCs then underwent an additional

24 hours of incubation while exposed to PbP composites or nanoparticle controls. At the end of this culture, media was collected for analysis and BMSCs were fixed with 4% paraformaldehyde. The fixed BMSCs were then stained with AlexaFlour® 488 phalloidin (Life Technologies), an actin stain, and 4',6-Diamidino-2-Phenylindole, Dihydrochloride (DAPI, Life Technologies), a DNA/nuclei stain. BMSCs were imaged under a fluorescence microscope (Nikon Eclipse Ti) and 10 images were collected for each well for excitation of DAPI and excitation of AlexaFlour® 488. Composite images of DAPI and AlexaFlour® 488 excitation were made to fully evaluate cell morphology using ImageJ. Cells were counted and cell density was calculated as adherent cells per area.

6.2.5b Post-culture Media Analyses

Immediately after collection, each tube of media was centrifuged at 3000 rpm for 2 minutes to remove debris from PbP, HA, and MgO. The media was then separated from the resulting pellet and stored in sterile 15 mL conical tubes. Immediately following this, the pH of the media was determined using a pre-calibrated pH meter (Symphony SB70P, VWR) to limit effects of atmospheric CO_2 on the bicarbonate buffering system present in DMEM. Each media sample was then diluted 1:100 in DI water to prepare for analysis via induced coupled plasma – optical emission spectrometry (ICP-OES, Optima 8000, Perkin Elmer). ICP-OES analysis was used to obtain media concentrations of Mg^{2+} and Ca^{2+} in order to evaluate release of ions from composites. Solutions of Mg and Ca at concentrations of 0.5 ppm, 1 ppm, and 5 ppm in nitric acid were used to generate a calibration curve for all Mg and Ca measurements, respectively. Measurements were reported as mg/L for Mg and µg/L for Ca. These values were then converted to mM by

dividing by the molecular weight of Mg (24.305 g/mol) and Ca (40.078 g/mol) for each and dividing by 1000 in the case of Ca to convert µM to mM.

6.2.6 Statistical Analysis

All experiments were run in triplicate. All data sets were analyzed using one-way analysis of variance (ANOVA) followed by the Tukey highest significant difference post hoc test. Statistical significance was considered at $p < 0.05$.

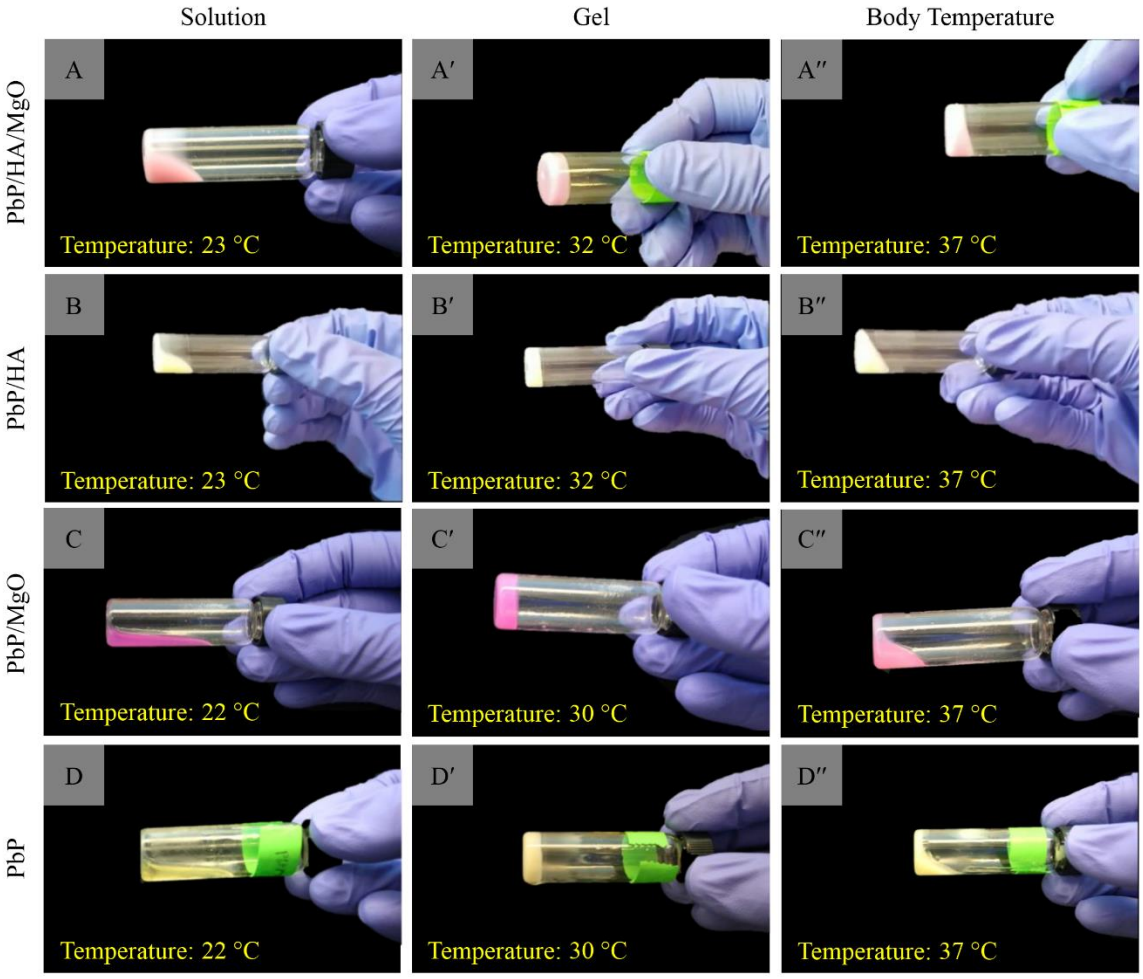

Figure 6.2: Photographs of hydrogels in (A-D) solution phase, (A′-D′) gel phase, and at (A″-D″) body temperature.

6.3 Results

6.3.1 Gelation Behavior of PbP/HA/MgO

Gelation temperature of PbP/HA/MgO was dependent heavily upon the amount of HA and MgO present as summarized in Table 6.1. The gelation temperature of PbP/HA/MgO was 30-35ºC. The gelation temperature of controls PbP/HA, PbP/MgO, and PbP were 29-34 ºC, 28-33 ºC, and 27-33 ºC, respectively. Representative images showing behavior in the solution and gel state are included in Figure 6.2. PbP/HA/MgO had slow flow in the solution phase and no flow in the gel phase. PbP/HA showed more flow than PbP/HA/MgO but less than PbP in the solution phase and no flow in the gel phase. PbP/MgO behaved similarly to PbP/HA/MgO as it also has little flow in the solution phase and no flow in the gel phase. PbP showed free flow in the solution phase and no flow in the gel phase. None of the gels showed no-flow at 37 ºC, but PbP/HA/MgO exhibited limited and very slow flow. It was also observed that PbP/HA/MgO and PbP/MgO did not reverse back to the solution state after cooling down to 22ºC, indicating a loss of the reversibility of the thermosensitive response. Color also varied between samples. All samples showed decrease in transparency in the gel phase when compared to the solution phase. The decrease in transparency is due to the hydrogen bonding and hydrophobic interactions that occur to cause micelle formation and aggregation [6, 7]. As micelles form, the resulting change in structure causes diffraction of light, leading to increased opacity. Additionally, PbP/HA/MgO and PbP/MgO were both pink in color while PbP/HA and PbP were yellow likely due to interactions with the pH indicator, phenol red, within DMEM.

6.3.2 Gel Behavior in Cell Culture

Images of the hydrogels at the start and end of cell culture are shown in Figure 6.3. There was difficulty removing PbP/HA/MgO from the mold resulting in a break in each of these gels. Otherwise, PbP/HA/MgO held shape when initially placed in culture and then degraded over 24 hours. PbP/HA and PbP/MgO also held shape initially and then degraded over the 24 hour cell culture. PbP had no structural integrity at 37 °C and as a result, could not be transferred to culture as a gel. Instead, PbP solution was added to cell culture for this control and no visible color or structural change was observed at the end of the 24 hour culture.

6.3.3 BMSC culture with PbP/HA/MgO

The morphology of cells after culture with PbP/HA/MgO and controls was evaluated via fluorescence microscopy (Figure 6.4). Cell size and morphology after exposure to PbP/HA/MgO, PbP/HA, PbP/MgO, PbP, and MgO were normal and comparable to the TCTP reference. Cell number and size visibly decreased for HA/MgO and HA nanoparticle controls.

These trends in cell number were quantified as cell density (Figure 6.5). Cell density prior to the addition of hydrogels and nanoparticles was $2.8 \times 10^3 \pm 230$ cells/cm^2. After 24 hours of exposure to PbP/HA/MgO the average cell density was $3 \times 10^3 \pm 277$ cells/cm^2. The average cell density of wells exposed to PbP/HA and PbP/MgO was $2.4 \times 10^3 \pm 328$ cells/cm^2 and $3.3 \times 10^3 \pm 374$ cells/cm^2, respectively. PbP/HA/MgO, PbP/HA, and PbP/MgO showed statistically lower cell density compared to PbP, which was $5 \times 10^3 \pm 677$ cells/cm^2. Average cell density after exposure to HA/MgO, HA, and

MgO was 788 ± 215 cells/cm^2, 1.1 x 10^3 ± 486 cells/cm^2, and 5 x 10^3 ± 957 cells/cm^2, respectively. Average cell density on the TCTP reference was 6 x 10^3 ± 784 cells/cm^2.

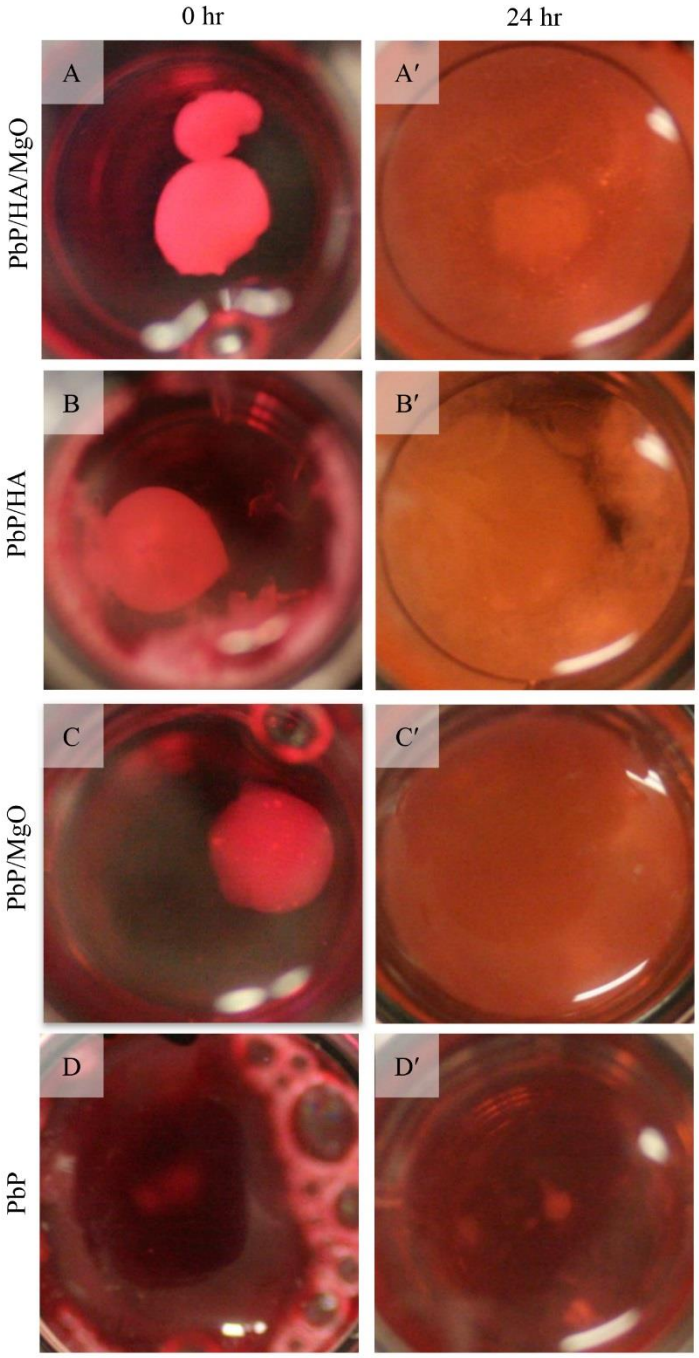

Figure 6.2: Photographs of hydrogels in BMSC culture at (A-D) 0 hours and (A′-D′) 24 hours.

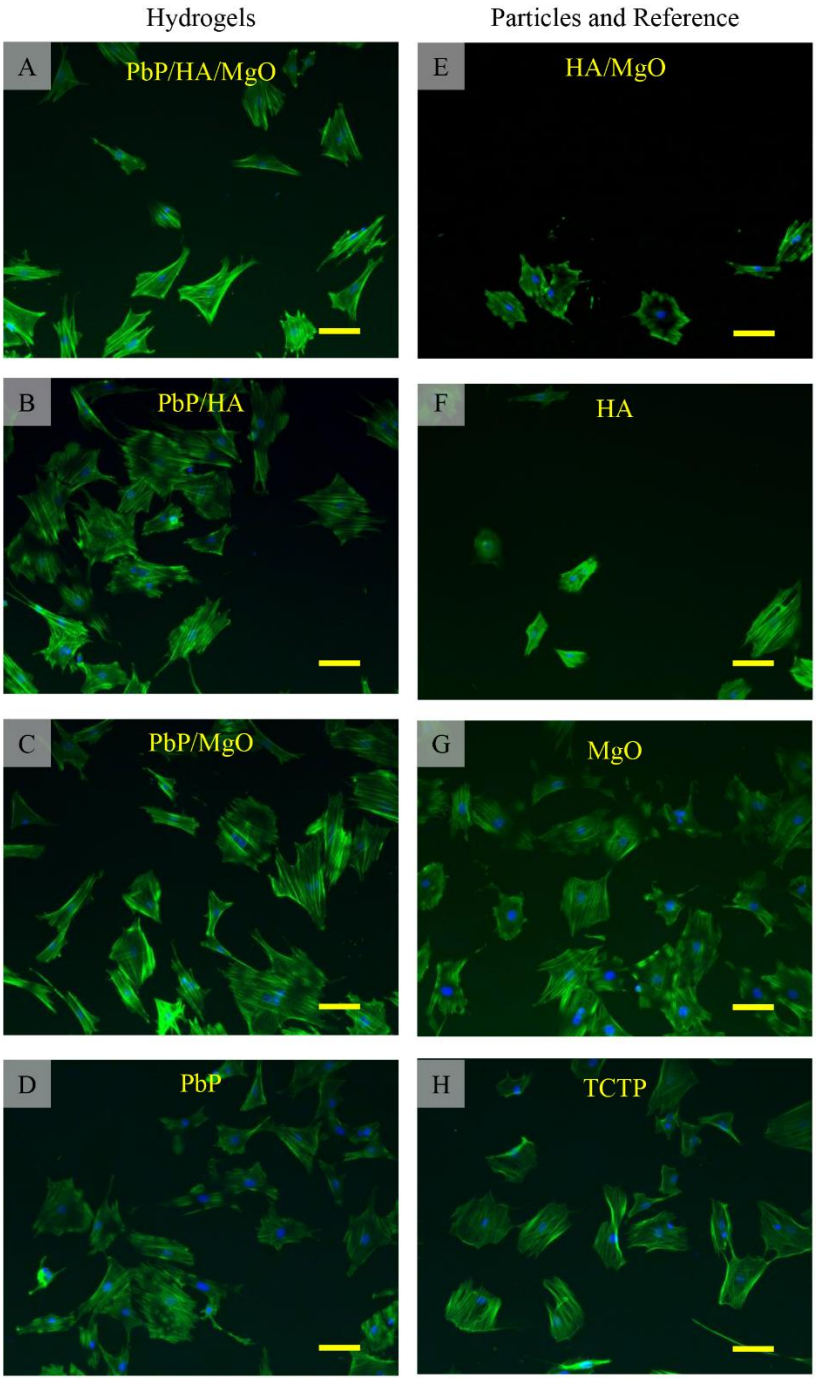

Figure 6.3: Fluorescence images of BMSCs after 24 hours of direct exposure to (A) PbP/HA/MgO and (B-G) controls compared to (H) TCTP reference. Scale bar is 100 µm.

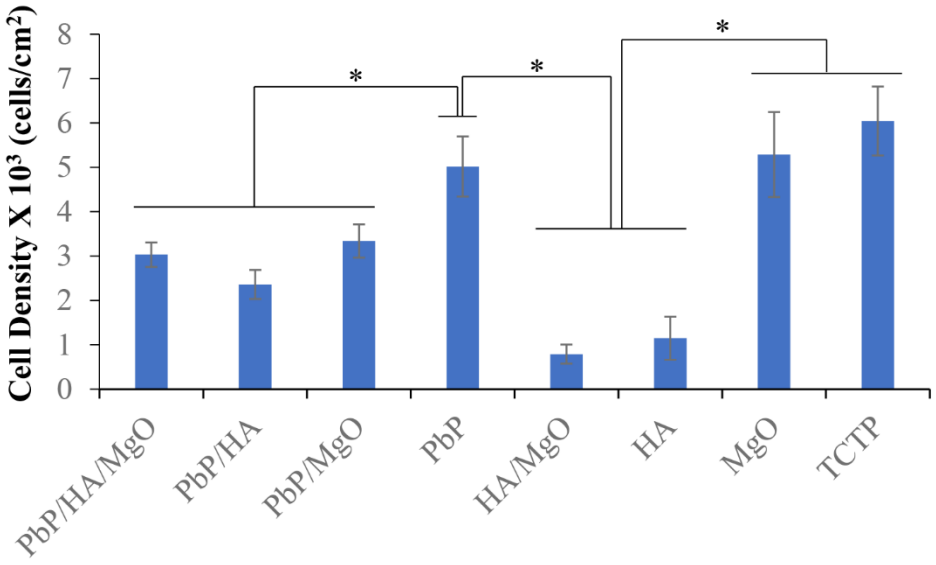

Figure 6.4: Adhesion density of BMSCs after direct exposure culture with PbP/HA/MgO and controls for 24 hours. BMSCs were seeded at a density of 10,000 cells/cm^2. Adherent cell density at introduction of experimental materials was 2.8 x 10^3 ± 230 cells/cm^2. Values are mean ± standard deviation; n = 30. *p<0.05

6.3.4 Post-culture Media Analyses

The presence of hydrogel and nanoparticles had minimal effect on pH (Figure 6.6A). The pH of every condition remained between 7.77 and 8.33. Specifically, the pH of wells with PbP/HA/MgO was 7.77 ± 0.03, which was statistically significant compared to most other conditions, excluding PbP/HA, PbP/MgO, and DMEM. The average pH's of PbP/HA and PbP/MgO were 7.87 ± 0.08 and 7.87 ± 0.06, respectively. The pH of wells containing just PbP was 8.00 ± 0.01. Bare nanoparticles seemed to have greater effect on pH with increases to 8.33 ± 0.05, 8.10 ± 0.03, and 8.22 ± 0.02 for HA/MgO, HA, and MgO, respectively. The average pH from reference wells, TCTP and DMEM, was 8.07 ± 0.13 and 7.95 ± 0.11, respectively.

Magnesium ion concentration in the media was measured to determine potential release from composite materials (Figure 6.6B). PLGA/HA/MgO was shown to increase free Mg^{2+} in the media to 3.47 ± 0.23 mM. PbP/HA, PbP/MgO, and PbP containing media had Mg^{2+} concentrations of 0.82 ± 0.03 mM, 3.10 ± 0.40 mM, and 0.85 ± 0.48 mM, respectively. Mg^{2+} concentration was 2.23 ± 0.21 mM, 0.76 ± 0.02 mM, and 3.83 ± 0.31 mM for the nanoparticles, HA/MgO, HA, and MgO, respectively. Reference wells of TCTP and DMEM had Mg^{2+} concentrations of 0.81 ± 0.01 mM and 0.80 ± 0.01 mM, respectively. All MgO containing samples showed statistically greater Mg^{2+} concentration in the media compared to all other conditions.

Calcium ion concentration in the media was also measured to determine how materials may affect deposition of calcium salts or release of free Ca^{2+} (Figure 6.6C). PLGA/HA/MgO containing wells had a Ca^{2+} concentration of 2.30 ± 0.33 mM. The Ca^{2+} concentration of PbP/HA, PbP/MgO, and PbP was 1.86 ± 0.05 mM, 2.16 ± 0.21 mM, and 1.86 ± 0.06mM, respectively. Nanoparticles, HA/MgO, HA, and MgO resulted in Ca^{2+} concentrations of 1.27 ± 0.07 mM, 1.17 ± 0.01 mM, and 1.80 ± 0.02 mM, respectively. The TCTP and DMEM references had Ca^{2+} concentrations of 1.80 ± 0.02 mM and 1.84 ± 0.03 mM, respectively.

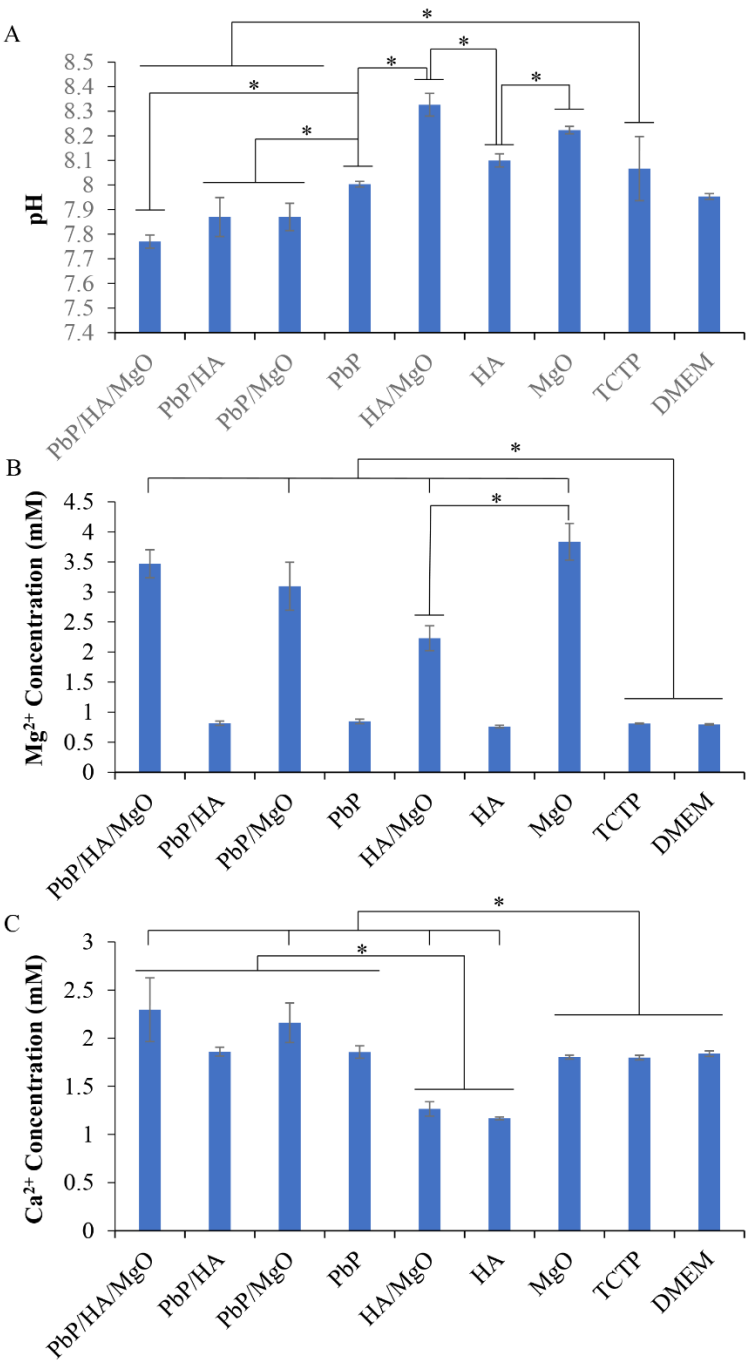

Figure 6.5: Media analyses after BMSC direct exposure culture with PbP/HA/MgO and controls. (A) Post-culture media pH, (B) Mg^{2+} ion concentration in the post-culture media, and (C) Ca^{2+} ion concentration in the post-culture media. Values are mean ± standard deviation; n = 3. *p<0.05

6.4 Discussion

6.4.1 Gelation Behavior of the PbP/HA/MgO

The composition of the polymer triblock, as well as the presence of nanoparticles, had great impact on gelation behavior of PbP (Table 6.1). As shown with PbP/HA/MgO and PbP/HA, the addition of HA increased gelation temperature due to an increase in hydrophilicity. This is consistent with similar HA-containing thermoreversible hydrogels [38, 39]. The addition of MgO also showed slight increase in gelation temperature, likely due to the increased hydrophilicity of the gel composite. However, it was also observed that the presence of MgO resulted in loss of thermoreversibility of gelation. It is possible, given the complementary electronegativity of each atom in the MgO crystal, that MgO is a suitable agent to allow hydrogen bonding and electrostatic interactions with the polymer to cause a crosslinking-like effect. Additionally, there are acidic residues within PbP that would readily interact with MgO, which is basic [27-32]. The crosslinking-like effect of MgO is likely the cause of loss of thermoreversibility. It has been previously shown that the addition of MgO to a carrageenan-based hydrogel resulted in increased stability and decreased burst release of drugs [40]. It is likely that the stabilizing factor observed in this study is similar to the crosslinking-like behavior observed with PbP. In 1971, Alvey demonstrated that the addition of MgO increases the viscosity of nonacid-terminated polyester resins [41]. This showed that MgO can interact with the polymer aside from acid/base reactions. It was also shown that the increase in viscosity is lost when MgO is exposed to water. This is in agreement with our observations of MgO in PLGA-PEG-PLGA hydrogels.

Color change was apparent during the shift from solution to gel phase for each sample (Figure 6.2). Generally, PbP composites in their solution phase tend to be more transparent and become more opaque as temperature is raised and the gel is formed. This is due to the fact that as temperature increases, micelles form and aggregate [7-12, 38, 39]. The micelles reflect more light, leading to the opaque color when gelled. In addition to change in opacity, PbP/HA/MgO and PbP/MgO were pink in color while PbP/HA and PbP were yellow. The DMEM used in the gels contains phenol red, a common pH indicator. In the physiological pH region, between 6.8 and 8.2, Phenol red remains a bright red color. However, phenol red turns yellow at pH below 6.8 and turns pink above pH 8.2. The acidic residues on PbP resulted in the shift of color to yellow, while the presence of MgO increased pH to shift color to the pink range. As MgO is very basic, the addition of MgO, even in small quantities, was enough to cause a shift in pH of the gel back to the physiological region.

6.4.2 Gel Behavior in Cell Culture

All gels lost shape during the 24 hour culture, indicating probable degradation of the PbP (Figure 6.3). The presence of MgO made PbP/HA/MgO and PbP/MgO the most stable gels going into cell culture, but this effect was lost in just 24 hours. This was likely caused by the loss of crosslinking-like behavior due to hydration and dissociation of MgO. MgO is known to hydrate to form $Mg(OH)_2$, which has a much less compact hexagonal crystal structure with a surface made up mostly of OH^- [29-32]. The chemistry and larger crystal size of $Mg(OH)_2$ makes it much less effective as a crosslinker, compared to MgO. MgO nanoparticles, particularly in small amounts (<200µg/mL),

readily dissociate in physiologically-relevant media [32]. As MgO dissociated, any stabilizing effects were lost. Since MgO is known to produce hydroxide as it dissociates, this would further have negative effects on the stability of PbP [16, 42-45]. Like most metal oxides, MgO is also thought to produce oxygen radicals. Oxygen radicals tend to increase degradation of polymeric hydrogels, including PEG [12]. It is possible that hydroxide and/or oxygen radical released from MgO resulted in increased degradation of PbP. The loss of shape in PbP/HA, however, is likely due to non-ideal gelation temperature. PbP/HA and PbP had upper temperature limits of 34 °C and 33 °C respectively, which is below body temperature, 37 °C. Above this upper temperature limit, syneresis, the separation of polymer and fluid, started to occur, resulting in loss of gel integrity. A different PbP17/PbP40 ratio may have resulted in a more stable gel for these conditions, however these samples needed to serve as controls for the PbP/HA/MgO. Additionally, gelation temperature of PLGA-PEG-PLGA is controlled by ratio of LA:GA:EG, as well as total chain length. The total length of PbP40 was greater than PbP17, which was why its gelation temperature was higher. However, we found that the PbP40 did not form a gel with no flow during inversion, up to 50°C. This is likely due to the fact that increasing chain length also increases instability of the gel as micelle formation is hindered in larger sizes [46]. Therefore, increasing PbP40 in our complete PbP mix resulted in loss of integrity of the gel and was not a viable option. As a result, PbP was not stable at 37 °C and could not be added in gel form to cell culture. It is likely that this caused rapid loss of structure in all of our hydrogel samples, as even PbP/HA/MgO exhibited slow flow at 37 °C.

6.4.3 BMSC culture with PbP/HA/MgO

While cells exposed to PbP/HA/MgO and composite controls exhibited healthy morphology, the decrease in cell density indicated potentially negative effects of PbP composites. Specifically, PbP/HA/MgO, PbP/HA, and PbP/MgO all performed similarly, resulting in statistically significant decrease in cell density when compared to the TCTP control, while PbP alone did not. This would indicate that PbP is cytocompatible but the release of nanoparticles decreased cell density. However, only HA/MgO and HA nanoparticle controls resulted in decrease in cell density, while MgO nanoparticles did not. Decrease in cell density from HA/MgO and HA is likely due to natural toxicity of nano-sized particles to cells, despite the chemical compatibility of HA. MgO dissociates within 24 hours, which would mitigate the toxicity associated with its nano-size [24]. The amount of MgO delivered in any MgO containing sample resulted in a MgO concentration of 650 μg/mL. This concentration was in the range, 500 μg/mL to 700 μg/mL, determined to cause decrease to cell viability in our previous study [24]. However, as the MgO nanoparticles can settle quickly, the cell culture are plays more of a role in determining contact between MgO and cells than just concentration by volume. This previous study utilized a 12 well plate with a culture area roughly double the culture area of a 24 well plate. This makes the PbP/MgO sample particularly interesting as each of its components yielded no ill effect. It is possible that the acid/base interactions between PbP and MgO resulted in rapid release of hydroxide, and potentially other reactive oxygen species, that caused more detrimental effects to cells than either component on its own. It is also possible that its encapsulation in PbP slowed the

dissociation of MgO, allowing for more direct exposure of MgO to cells which has been shown to increase toxicity [24-26].

6.4.4 Post-culture Media Analyses

The pH of the media post-culture gave insight into how the PbP may have changed pH and, thus, cell response (Figure 6.6A). All measured pH was within physiological range. However, the pH of media exposed to PbP/HA/MgO, PbP/HA, and PbP/MgO was significantly less than the TCTP reference, indicating that PbP degraded and released acidic residues. However, PbP alone showed no significant change in pH compared to the TCTP reference, which may be due to comparable cellular activity or lack of degradation of PbP. PbP alone was unable to form a gel but it may be that hydrolysis of its ester linkages occurred at a slower rate in absence of nanoparticles, meaning that it did not truly degrade and instead remained as soluble PLGA-PEG-PLGA chains. The observed increase in pH from HA/MgO and MgO can be largely attributed to dissociation of MgO, as was expected from a previous study [24]. However, it is important to note that the buffering activity of bicarbonate found within DMEM can hide initial effects, as well as potential ongoing local effects, of pH from materials. Specifically, pH during degradation of PbP could reach lower than the pH observed at 24 hours but the buffering activity takes time to adjust pH. Similarly, MgO was shown to increase pH within 5 minutes and sustain a higher pH in DMEM for at least 4 hours, despite returning to a physiological range after 24 hours [24]. This indicates that the pH measured at the end of the 24 hour culture may not be representative of the pH experienced by the cells, meaning that pH may play a role in the observed decrease in

cell density for PbP/HA/MgO. Previous studies with PLGA/PEG hydrogels loaded with HA have shown a slight increase in pH with increasing HA, which is in contrast to the trends with our PbP/HA sample [38, 39]. This may be due to difference in hydrogel media, in which previous studies utilized phosphate buffered saline and we used DMEM. The buffering capacity and interactions between media and PbP may cause the observed pH change with PbP/HA.

Measured Mg^{2+} concentration in the media showed an expected dissociation of MgO in PbP/HA/MgO (Figure 6.6B). PbP/HA/MgO and PbP/MgO showed comparable Mg^{2+} concentration to bare MgO nanoparticles, indicating that encapsulation in PbP did little to mitigate dissociation of MgO. However, HA/MgO showed lower Mg^{2+} concentration in the media indicating that the presence of HA with MgO may stabilize MgO to prevent MgO dissociation, or cause deposition of more stable Mg-salts.

Ca^{2+} concentration in the media gave an indication of how PbP/HA/MgO and control materials may affect the deposition of calcium salts, which is essential to bone healing (Figure 6.6C). PbP/HA/MgO and PbP/MgO showed a slight increase in Ca^{2+} concentration compared to the TCTP reference, however it was difficult to determine if this was due to the chemistry of the materials interacting with the media or from the release of intracellular calcium from BMSCs. Due to the lack of Ca^{2+} concentration change from PbP/HA, which also exhibited lower cell density, it is likely that the chemistry of PbP/HA/MgO and PbP/MgO caused the dissociation of calcium salts. Due to their shared valency Mg^{2+} can replace Ca^{2+} in calcium compounds, which may account for some of the observed Ca^{2+} release. However, bare HA/MgO showed an opposing

effect while bare MgO had no effect on Ca^{2+} concentration. It is possible that the difference in behavior of HA and MgO when loaded into PbP, or when bare, is due to difference in pH. Several studies suggest pH plays a role in solubility of calcium salts, including hydroxyapatite [47, 48]. While the pH between samples did not vary greatly, it is possible that pH vacillated more between samples at earlier timepoints in the study, as previously discussed. The acidic residues from PbP, combined with the effects of MgO, may have caused dissociation of calcium salts.

6.5 Conclusion

While PbP/HA/MgO may be beneficial as an injectable filler for bone defects and osteoporotic bone, significant improvement and optimization needs to occur to make it truly viable. Specifically, tailoring the ratio of LA:GA:EG in PbP is necessary to develop a more stable hydrogel matrix at body temperature, 37 ºC. Additionally, the reactivity of MgO in physiological media makes it detrimental to the structural integrity of PbP. If used in future hydrogels for medical applications, MgO should be coated or modified to mitigate rapid release of hydroxide and potentially other oxygen radicals. Combined, an improved PbP matrix loaded with HA and coated MgO may still provide a viable and minimally invasive treatment for small bone defects.

6.6 Acknowledgements

The authors thank the support from the U.S. National Science Foundation (NSF award CBET 1512764), the Burroughs Wellcome Fund (1011235), the Hellman Faculty Fellowship (HL), and the University of California (UC) Regents Faculty Development Award (HL). The authors appreciate the Central Facility for Advanced Microscopy and

Microanalysis (CFAMM) for the use of SEM FEI XL30 at the University of California at Riverside.

Any opinions, findings, and conclusions or recommendations expressed in this material are those of the author(s) and do not necessarily reflect the views of the National Science Foundation.

6.7 References

1. Drury, J.L. and D.J. Mooney, *Hydrogels for tissue engineering: scaffold design variables and applications.* Biomaterials, 2003. **24**(24): p. 4337-51.
2. Lee, K.Y. and D.J. Mooney, *Hydrogels for tissue engineering.* Chem Rev, 2001. **101**(7): p. 1869-79.
3. Tan, H.P. and K.G. Marra, *Injectable, Biodegradable Hydrogels for Tissue Engineering Applications.* Materials, 2010. **3**(3): p. 1746-1767.
4. Munarin, F., et al., *New perspectives in cell delivery systems for tissue regeneration: natural-derived injectable hydrogels.* J Appl Biomater Funct Mater, 2012. **10**(2): p. 67-81.
5. Polo-Corrales, L., M. Latorre-Esteves, and J.E. Ramirez-Vick, *Scaffold design for bone regeneration.* J Nanosci Nanotechnol, 2014. **14**(1): p. 15-56.
6. Chen, S., et al., *Triblock copolymers: synthesis, characterization, and delivery of a model protein.* Int J Pharm, 2005. **288**(2): p. 207-18.
7. Chen, X., et al., *PLGA-PEG-PLGA triblock copolymeric micelles as oral drug delivery system: In vitro drug release and in vivo pharmacokinetics assessment.* J Colloid Interface Sci, 2017. **490**: p. 542-552.
8. Feng, L., et al., *Assessment of PLGA-PEG-PLGA copolymer hydrogel for sustained drug delivery in the ear.* Curr Drug Deliv, 2014. **11**(2): p. 279-86.
9. Yan, Q., et al., *Controlled release of simvastatin-loaded thermo-sensitive PLGA-PEG-PLGA hydrogel for bone tissue regeneration: in vitro and in vivo characteristics.* J Biomed Mater Res A, 2015. **103**(11): p. 3580-9.
10. Wang, X., et al., *Thermo-sensitive hydrogel PLGA-PEG-PLGA as a vaccine delivery system for intramuscular immunization.* J Biomater Appl, 2016.
11. Fu, X., et al., *A PLGA-PEG-PLGA Thermosensitive Gel Enabling Sustained Delivery of Ropivacaine Hydrochloride for Postoperative Pain Relief.* Chem Pharm Bull (Tokyo), 2017. **65**(3): p. 229-235.
12. Reid, B., et al., *PEG hydrogel degradation and the role of the surrounding tissue environment.* J Tissue Eng Regen Med, 2015. **9**(3): p. 315-8.
13. Herndon, T.M., et al., *U.S. Food and Drug Administration Approval: peginterferon-alfa-2b for the adjuvant treatment of patients with melanoma.* Oncologist, 2012. **17**(10): p. 1323-8.
14. Jain, R.A., *The manufacturing techniques of various drug loaded biodegradable poly(lactide-co-glycolide) (PLGA) devices.* Biomaterials, 2000. **21**(23): p. 2475-90.
15. Marin, E., M.I. Briceno, and C. Caballero-George, *Critical evaluation of biodegradable polymers used in nanodrugs.* Int J Nanomedicine, 2013. **8**: p. 3071-90.
16. Jeong, B., et al., *Biodegradable block copolymers as injectable drug-delivery systems.* Nature, 1997. **388**(6645): p. 860-2.
17. Zakaria, S.M., et al., *Nanophase hydroxyapatite as a biomaterial in advanced hard tissue engineering: a review.* Tissue Eng Part B Rev, 2013. **19**(5): p. 431-41.

18. Koutsopoulos, S., *Synthesis and characterization of hydroxyapatite crystals: a review study on the analytical methods.* J Biomed Mater Res, 2002. **62**(4): p. 600-12.
19. Cheng, L., et al., *Osteoinduction of hydroxyapatite/beta-tricalcium phosphate bioceramics in mice with a fractured fibula.* Acta Biomater, 2010. **6**(4): p. 1569-74.
20. Fielding, G.A., W. Smoot, and S. Bose, *Effects of SiO2, SrO, MgO, and ZnO dopants in tricalcium phosphates on osteoblastic Runx2 expression.* J Biomed Mater Res A, 2014. **102**(7): p. 2417-26.
21. Kum, C.H., et al., *A poly(lactide) stereocomplex structure with modified magnesium oxide and its effects in enhancing the mechanical properties and suppressing inflammation.* Small, 2014. **10**(18): p. 3783-94.
22. Patel, M.K., et al., *Biocompatible nanostructured magnesium oxide-chitosan platform for genosensing application.* Biosens Bioelectron, 2013. **45**: p. 181-8.
23. Pourdanesh, F., et al., *In vitro and in vivo evaluation of a new nanocomposite, containing high density polyethylene, tricalcium phosphate, hydroxyapatite, and magnesium oxide nanoparticles.* Mater Sci Eng C Mater Biol Appl, 2014. **40**: p. 382-8.
24. Wetteland, C.L., N.Y. Nguyen, and H. Liu, *Concentration-dependent behaviors of bone marrow derived mesenchymal stem cells and infectious bacteria toward magnesium oxide nanoparticles.* Acta Biomater, 2016. **35**: p. 341-56.
25. Sawai, J., *Quantitative evaluation of antibacterial activities of metallic oxide powders (ZnO, MgO and CaO) by conductimetric assay.* J Microbiol Methods, 2003. **54**(2): p. 177-82.
26. Sawai, J. and T. Yoshikawa, *Quantitative evaluation of antifungal activity of metallic oxide powders (MgO, CaO and ZnO) by an indirect conductimetric assay.* J Appl Microbiol, 2004. **96**(4): p. 803-9.
27. Amundsen, K., et al., *Magnesium*, in *Ullmann's Encyclopedia of Industrial Chemistry*. 2000, Wiley-VCH Verlag GmbH & Co. KGaA.
28. Fedorockova, A. and P. Raschman, *Effects of pH and acid anions on the dissolution kinetics of MgO.* Chemical Engineering Journal, 2008. **143**(1-3): p. 265-272.
29. Láska, M., J. Valtýni, and P. Fellner *Influence of pH on the Crystal Size Distribution of Mg(OH)2 Prepared by the Hydration of MgO Crystal Research and Technology Volume 28, Issue 7*. Crystal Research and Technology, 1993. **28**, 931-936.
30. Mejias, J.A., et al., *The kinetics and mechanism of MgO dissolution.* Chemical Physics Letters, 1999. **314**(5-6): p. 558-563.
31. Refson, K., et al., *Water chemisorption and reconstruction of the MgO surface.* Phys Rev B Condens Matter, 1995. **52**(15): p. 10823-10826.
32. Fruhwirth, O., et al., *Dissolution and Hydration Kinetics of Mgo.* Surface Technology, 1985. **24**(3): p. 301-317.
33. Yoshizawa, S., et al., *Role of magnesium ions on osteogenic response in bone marrow stromal cells.* Connect Tissue Res, 2014. **55 Suppl 1**: p. 155-9.

34. Yoshizawa, S., et al., *Magnesium ion stimulation of bone marrow stromal cells enhances osteogenic activity, simulating the effect of magnesium alloy degradation.* Acta Biomater, 2014. **10**(6): p. 2834-42.
35. Tian, Q.M., et al., *Cytocompatibility of Magnesium Alloys with Human Urothelial Cells: A Comparison of Three Culture Methodologies.* Acs Biomaterials Science & Engineering, 2016. **2**(9): p. 1559-1571.
36. Guan, R.G., et al., *Electrodeposition of hydroxyapatite coating on Mg-4.0Zn-1.0Ca-0.6Zr alloy and in vitro evaluation of degradation, hemolysis, and cytotoxicity.* J Biomed Mater Res A, 2012. **100**(4): p. 999-1015.
37. Johnson, I., K. Akari, and H. Liu, *Nanostructured hydroxyapatite/poly(lactic-co-glycolic acid) composite coating for controlling magnesium degradation in simulated body fluid.* Nanotechnology, 2013. **24**(37): p. 375103.
38. Lai, M.C., et al., *In situ gelation of PEG-PLGA-PEG hydrogels containing high loading of hydroxyapatite: in vitro and in vivo characteristics.* Biomed Mater, 2014. **9**(1): p. 015011.
39. Lin, G., et al., *Injectable and thermosensitive PLGA-g-PEG hydrogels containing hydroxyapatite: preparation, characterization and in vitro release behavior*. Biomed Mater, 2012. **7**(2): p. 024107.
40. Hezaveh, H. and Muhamad, II, *Effect of MgO nanofillers on burst release reduction from hydrogel nanocomposites.* J Mater Sci Mater Med, 2013. **24**(6): p. 1443-53.
41. Alvey, F.B., *Study of Reaction of Polyester Resins with Magnesium Oxide.* Journal of Polymer Science Part a-1-Polymer Chemistry, 1971. **9**(8): p. 2233-&.
42. Han, S., C. Kim, and D. Kwon, *Thermal/oxidative degradation and stabilization of polyethylene glycol.* Polymer, 1997. **38**(2): p. 317-323.
43. Jeon, O., et al., *The effect of oxidation on the degradation of photocrosslinkable alginate hydrogels.* Biomaterials, 2012. **33**(13): p. 3503-14.
44. Lyu, S. and D. Untereker, *Degradability of polymers for implantable biomedical devices.* Int J Mol Sci, 2009. **10**(9): p. 4033-65.
45. Makadia, H.K. and S.J. Siegel, *Poly Lactic-co-Glycolic Acid (PLGA) as Biodegradable Controlled Drug Delivery Carrier.* Polymers, 2011. **3**(3): p. 1377-1397.
46. Chen, L., et al., *Effects of Molecular Weight and Its Distribution of PEG Block on Micellization and Thermogellability of PLGA-PEG-PLGA Copolymer Aqueous Solutions.* Macromolecules, 2015. **48**(11): p. 3662-3671.
47. Goss, S.L., et al., *Determination of calcium salt solubility with changes in pH and P-CO2, simulating varying gastrointestinal environments.* Journal of Pharmacy and Pharmacology, 2007. **59**(11): p. 1485-1492.
48. Moreno, E.C., T.M. Gregory, and W.E. Brown, *Preparation and Solubility of Hydroxyapatite.* Journal of Research of the National Bureau of Standards Section a-Physics and Chemistry, 1968. **A 72**(6): p. 773-80.

Appendix A: Supplementary Figures for Chapter 4

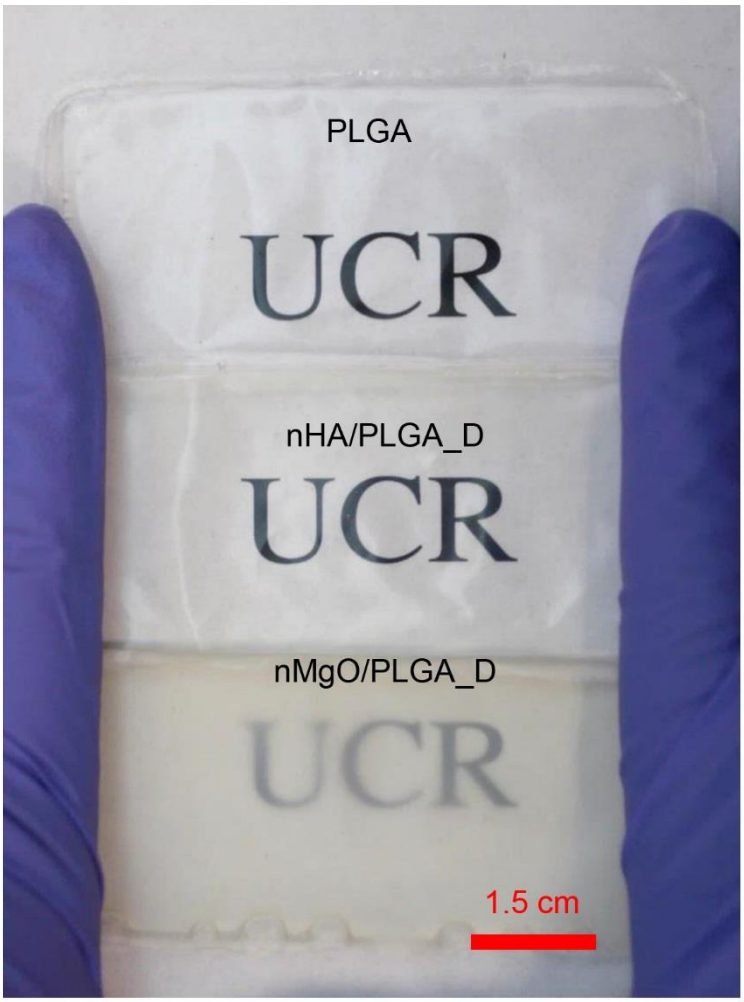

Supplementary Figure A1: Macro-scale photographs of the dispersed nanocomposites, showing the larger scale production of well-dispersed nanocomposites with optical transparency. (A) PLGA, (B) nHA/PLGA_D, and (C) nMgO/PLGA_D. Scale bar is 1.5 cm.

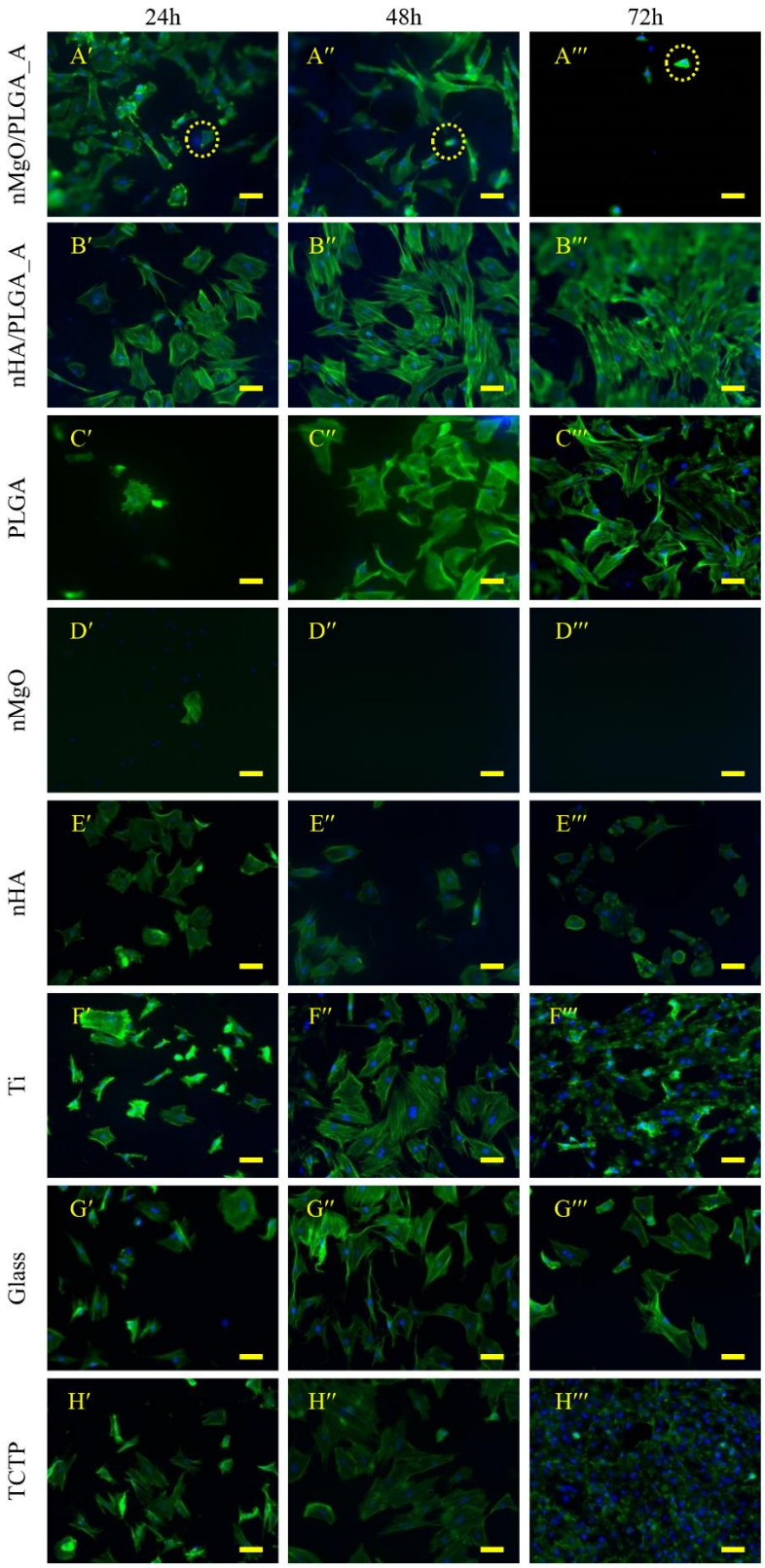

Supplementary Figure A2: Representative fluorescence images of BMSCs that were directly cultured on the agglomerated nanocomposites for up to 72 hours. (A′-G′) 24, (A″-G″) 48, and (A‴-G‴) 72 hours when compared with the (H-H‴) TCTP (Cells Only) reference. Blue stains nuclei and green stains F-actin. Scale bar = 100 µm.

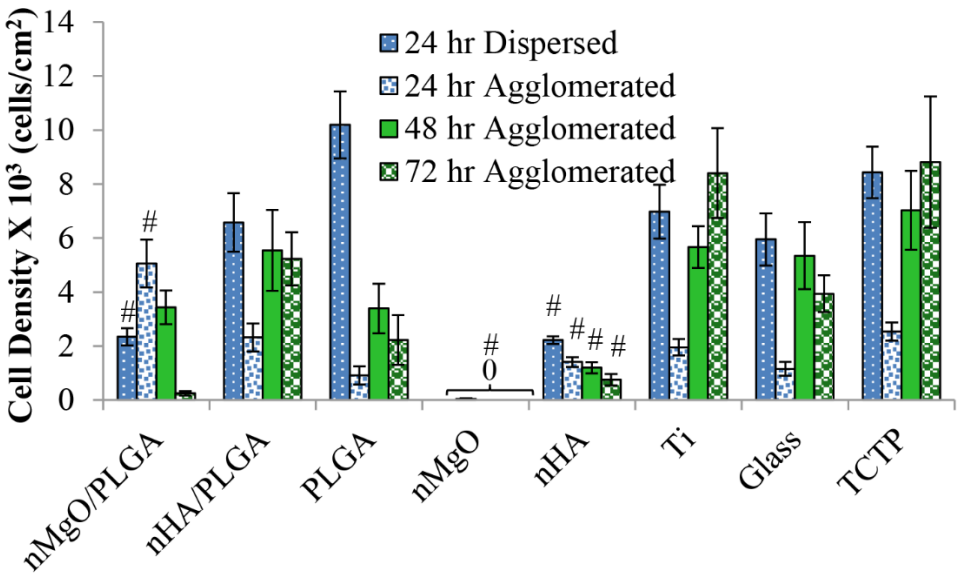

Supplementary Figure A3: The raw values of BMSC adhesion density after they were directly cultured on the nanocomposites for up to 72 hours, when compared with the controls and references. Values are mean ± standard error; n=15. *p<0.05 compared to the TCTP (Cells Only) control for the respective time points.

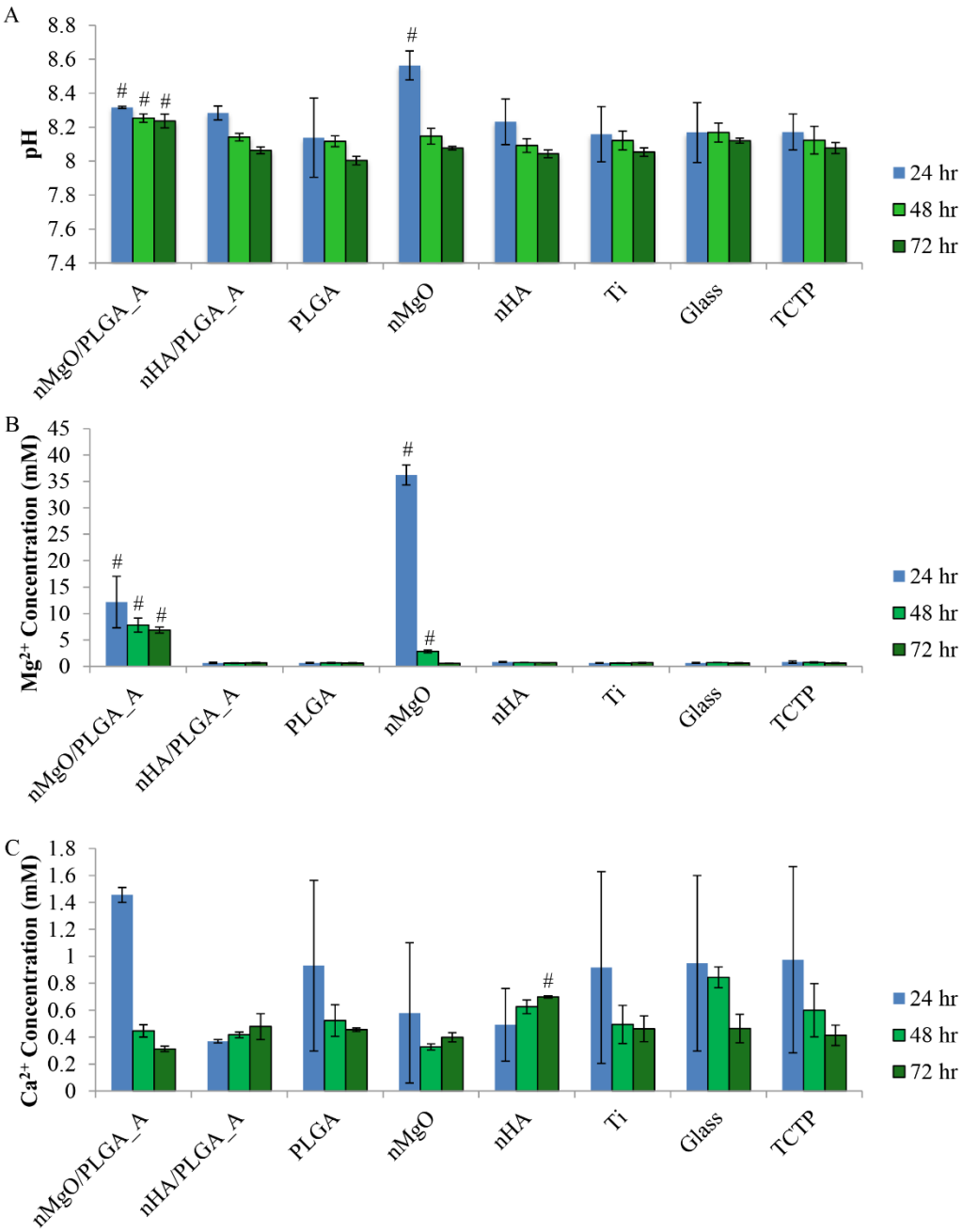

Supplementary Figure A4: Media analyses after BMSCs were cultured with the agglomerated nanocomposites and controls for up to 72 hours. (A) post-culture media pH at each time point, (B) Mg^{2+} ion concentration in the post-culture media at each prescribed time point, and (C) Ca^{2+} ion concentration in the post-culture media at each prescribed time point. Values are mean ± standard error; n=3. *p<0.05 compared to the TCTP (Cells Only) control for the respective time points.

Appendix B: Supplementary Tables for Chapter 5

Sample	Cell Density x 10^3 (cells/cm^2)			
	On Sample-24 hr	On Plate-24 hr	On Sample-48 hr	On Plate-48 hr
P70/H20/M10	3.83 ± 0.4$^{\Delta}$	12.55 ± 0.96	N/A	N/A
P70/H25/M5	4.2 ± 0.52$^{\Delta}$	14.4 ± 1.57	12.34 ± 0.85	15.56 ± 1.29
P70/H29/M1	6.04 ± 0.53$^{\Delta}$	16.38 ± 1.73	14.44 ± 1.43	20.12 ± 1.52
P70/H20	3.84 ± 0.39$^{\Delta}$	11.04 ± 1.22	N/A	N/A
P70/H25	5.33 ± 0.33$^{\Delta}$	9.64 ± 0.88	10.68 ± 1.87	17.34 ± 1.79
P70/H29	1.73 ± 0.19$^{\Delta\Diamond}$	19.2 ± 2.25$^{\square}$	11.43 ± 2.07	14.82 ± 1.79
P70/H30	3.28 ± 0.42$^{\Delta}$	5.19 ± 0.39	17.12 ± 1.14	10.69 ± 1.54$^{\square}$
P70/M30	0.64 ± 0.07$^{\Delta}$	10.52 ± 1.36	N/A	N/A
P70/M10	1.78 ± 0.23$^{\Delta}$	11.7 ± 1.28	N/A	N/A
P70/M5	3.88 ± 0.27$^{\Delta}$	13.67 ± 1.36	5.15 ± 0.63$^{\Delta\Diamond}$	14.62 ± 1.73
P70/M1	2.75 ± 0.28$^{\Delta}$	13 ± 1.54	9.37 ± 1.12	16.23 ± 1.87
H20/M10	N/A	0.04 ± 0.02$^{\square\Diamond}$	N/A	N/A
H25/M5	N/A	0.51 ± 0.11$^{\square\Diamond}$	N/A	2.81 ± 0.46$^{\square\Diamond}$
H29/M1	N/A	4.1 ± 0.31$^{\square\Diamond}$	N/A	6.54 ± 1.42$^{\square\Diamond}$
P70	3.24 ± 0.54$^{\Delta}$	11.65 ± 1.02	15.82 ± 1.37	14.92 ± 1.99
H20	N/A	8.54 ± 0.43	N/A	N/A
H25	N/A	6.42 ± 0.3$^{\Diamond}$	N/A	9.78 ± 0.9$^{\square}$
H29	N/A	6.34 ± 0.43$^{\Diamond}$	N/A	9.76 ± 0.87$^{\square\Diamond}$
H30	N/A	5.19 ± 0.39	N/A	11.14 ± 1.14
M30	N/A	0.11 ± 0.03$^{\square\Diamond}$	N/A	N/A
M10	N/A	0.06 ± 0.03$^{\square\Diamond}$	N/A	N/A
M5	N/A	3.32 ± 0.33$^{\square\Diamond}$	N/A	8.24 ± 1.49$^{\square}$
M1	N/A	13.06 ± 3.05	N/A	23 ± 1.72
Ti	10.89 ± 0.85	18.22 ± 2.43	17.71 ± 2.31	15.14 ± 2.65
Glass	10.76 ± 1.11	14.35 ± 2.38	13.79 ± 1.18	18.24 ± 2.08
TCTP	N/A	11.6 ± 1.38	N/A	19.76 ± 3.02

Table B1: Numerical values of Cell Density on experimental samples and on the tissue culture plate after 24 hour and 48 hours of culture. This Table corresponds to values represented in Figure 5 and Figure 8. Values are mean ± standard deviation; n = 3. ◊ $p<0.05$

Sample	Cell Culture Media Analyses					
	pH-24 hr	pH-48 hr	Mg^{2+}-24 hr	Mg^{2+}-48 hr	Ca^{2+}-24 hr	Ca^{2+}-48 hr
P70/H20/M10	8.37 ± 0.03□Δ	N/A	6.36 ± 0.49□Δ	N/A	1.84 ± 0.21◊	N/A
P70/H25/M5	8.32 ± 0.01	7.95 ± 0.03	4 ± 0.48□Δ	2.17 ± 0.12□Δ	2.02 ± 0.28	1.51 ± 0.13
P70/H29/M1	8.25 ± 0.02Δ	7.88 ± 0.03	1.3 ± 0.06	1.24 ± 0.53	1.98 ± 0.03	1.63 ± 0.12
P70/H20	8.27 ± 0.03◊	N/A	0.83 ± 0.02◊	N/A	1.9 ± 0.33	N/A
P70/H25	8.24 ± 0.02Δ◊	7.89 ± 0.03	1.01 ± 0.13◊	0.86 ± 0.13◊	2.08 ± 0.22	1.68 ± 0.29
P70/H29	8.23 ± 0.02Δ	7.88 ± 0.02	0.95 ± 0.16	0.83 ± 0.02	1.82 ± 0.18	1.67 ± 0.2
P70/H30	8.22 ± 0.03□Δ	7.82 ± 0.07Δ	0.93 ± 0.07	0.79 ± 0.03	2.1 ± 0.08	1.75 ± 0.09
P70/M30	8.33 ± 0.03	N/A	12.3 ± 0.49□Δ	N/A	1.69 ± 0.07	N/A
P70/M10	8.33 ± 0.02	N/A	2.02 ± 0.32◊	N/A	1.84 ± 0.07	N/A
P70/M5	8.29 ± 0.02	7.94 ± 0.03	1.37 ± 0.07◊	2.02 ± 0.18□Δ	1.88 ± 0.14	2.02 ± 0.05
P70/M1	8.24 ± 0.02Δ	7.93 ± 0.01	0.92 ± 0.03	1 ± 0	1.92 ± 0.03	2.08 ± 0.08
H20/M10	8.43 ± 0.01□Δ	N/A	11.61 ± 0.71□Δ◊	N/A	1.36 ± 0.08□Δ	N/A
H25/M5	8.36 ± 0.01□	7.92 ± 0.02	8.15 ± 0.65□Δ◊	1.31 ± 0.13□Δ◊	1.31 ± 0.02□Δ◊	1.15 ± 0.06□Δ
H29/M1	8.3 ± 0.02	7.87 ± 0.05	5.06 ± 1.95□Δ◊	1.04 ± 0.13	1.3 ± 0.06□Δ	1.09 ± 0.07□Δ◊
P70	8.23 ± 0.02□Δ	7.95 ± 0.02	0.91 ± 0.04	0.91 ± 0.1	1.98 ± 0.1	1.83 ± 0.35
H20	8.27 ± 0.01◊	N/A	0.99 ± 0.02◊	N/A	1.09 ± 0.12□Δ	N/A
H25	8.23 ± 0.01Δ◊	7.9 ± 0.02	1.15 ± 0.36◊	0.82 ± 0.01◊	1 ± 0.04□Δ◊	1.05 ± 0.02□Δ
H29	8.23 ± 0.02□Δ	7.9 ± 0.02	0.82 ± 0.02	0.82 ± 0.01	0.95 ± 0.02□Δ◊	1.08 ± 0.06□Δ◊
H30	8.18 ± 0.03□Δ	7.92 ± 0.02◊	0.84 ± 0.06	0.82 ± 0.01	0.96 ± 0.04□Δ◊	1.29 ± 0.39
M30	8.61 ± 0.04□Δ	N/A	30.64 ± 1.09□Δ◊	N/A	1.21 ± 0.07□Δ	N/A
M10	8.38 ± 0.01□Δ	N/A	8.25 ± 1.29□Δ	N/A	1.26 ± 0.11□Δ◊	N/A
M5	8.32 ± 0.02	7.93 ± 0.04	6.27 ± 2.48□Δ	1.32 ± 0.16□Δ◊	1.32 ± 0.2□Δ◊	1.88 ± 0.04
M1	8.29 ± 0.02	7.88 ± 0.03	2.89 ± 0.94	0.97 ± 0.11	2.09 ± 0.16	1.83 ± 0.24
Ti	8.24 ± 0.02Δ	7.86 ± 0.02	0.95 ± 0.12	0.84 ± 0.01	1.94 ± 0.33	1.69 ± 0.2
Glass	8.27 ± 0.02	7.87 ± 0.03	1.23 ± 0.63	0.83 ± 0.01	1.85 ± 0.2	1.71 ± 0.07
TCTP	8.29 ± 0.02	7.9 ± 0.03	0.95 ± 0.09	0.82 ± 0.03	1.93 ± 0.35	1.72 ± 0.04
DMEM	8.31 ± 0.03	7.93 ± 0.04	0.93 ± 0.03	0.82 ± 0.01	1.96 ± 0.05	1.73 ± 0.04

Table B2: Numerical values of pH, Mg^{2+} concentration, and Ca^{2+} concentration from post-culture media analyses after 24 hours and 48 hours of culture. Mg^{2+} and Ca^{2+} concentrations are given in mM. This Table corresponds to values represented in Figures 9-11. Values are mean ± standard deviation; n = 3. ◊ $p<0.05$ compared to corresponding PLGA/HA/MgO. □ $p<0.05$ compared to TCTP. Δ $p<0.05$ compared to Glass.